

DRA

N 84-20842

THEORETICAL AND EXPERIMENTAL ANALYSIS OF LASER
ALTIMETERS FOR BAROMETRIC MEASUREMENTS OVER THE OCEAN

by

B. M. Tsai
C. S. Gardner

RRL Publication No. 527

Technical Report
March 1984

Supported by
Contract No. NASA NSG-5049

NATIONAL AERONAUTICS & SPACE ADMINISTRATION
Goddard Space Flight Center
Greenbelt, Maryland 20771



RADIO RESEARCH LABORATORY
DEPARTMENT OF ELECTRICAL AND COMPUTER ENGINEERING
COLLEGE OF ENGINEERING
UNIVERSITY OF ILLINOIS
URBANA, ILLINOIS 61801

THEORETICAL AND EXPERIMENTAL ANALYSIS OF LASER
ALTIMETERS FOR BAROMETRIC MEASUREMENTS OVER THE OCEAN

by

B. M. Tsai
C. S. Gardner

RRL Publication No. 527

Technical Report
March 1984

Supported by
Contract No. NASA NSG-5049

NATIONAL AERONAUTICS & SPACE ADMINISTRATION
Goddard Space Flight Center
Greenbelt, Maryland 20771

RADIO RESEARCH LABORATORY
DEPARTMENT OF ELECTRICAL AND COMPUTER ENGINEERING
COLLEGE OF ENGINEERING
UNIVERSITY OF ILLINOIS
URBANA, ILLINOIS 61801

ABSTRACT

The optical path length from a satellite to the earth's surface is strongly dependent on the atmospheric pressure along the propagation path. Surface pressure can be determined by measuring the difference between the round-trip propagation times of laser pulses that are transmitted simultaneously at two wavelengths. Although pressure measurements can be made over the ground and water, the application of this technique to pressure measurements over the ocean is considered.

The statistical characteristics and the waveforms of the ocean-reflected laser pulses are studied. The received signal is found to be corrupted by shot noise and time-resolved speckle. The statistics of time-resolved speckle and its effects on the timing accuracy of the receiver are studied in the general context of laser altimetry.

For estimating the differential propagation time, various receiver timing algorithms are proposed and their performances evaluated. The results indicate that, with the parameters of a realistic altimeter, a pressure measurement accuracy of a few millibars is feasible.

The data obtained from the first airborne two-color laser altimeter experiment are processed and analyzed. The results are used to verify the pressure measurement concept.

ACKNOWLEDGEMENTS

The authors would like to acknowledge Dr. James B. Abshire at NASA-GSFC for his valuable help throughout the research, especially his work on the experiments and computer simulation.

Many thanks are also owed to Mrs. Jan F. McGarry for her work on the computer simulation and to Mr. H. Edward Rowe for his assistance throughout the experiments.

This research was supported by the National Aeronautics and Space Administration under the Grant NSG-5049.

TABLE OF CONTENTS

	Page
1. INTRODUCTION.	1
2. THEORY OF THE PRESSURE MEASUREMENT TECHNIQUE.	4
3. LASER BACKSCATTER FROM THE OCEAN.	10
4. TIME-RESOLVED SPECKLE	25
4.1. Introduction.	25
4.2. Statistics of the Detected Signal	26
4.3. Estimation of Arrival Time.	52
4.4. Computer Simulation	66
4.5. Partially Developed Speckle	70
4.6. Summary	79
5. ESTIMATION OF DIFFERENTIAL ARRIVAL TIME	90
5.1. Introduction.	90
5.2. Timing Algorithms	90
5.3. Frequency Domain Representation of Timing Error	103
5.4. Comparison of the Correlation and Centroid Algorithms	106
5.5. Transmitter Effects	112
5.6. Sampling Effects.	113
5.7. Summary	117
6. BANDWIDTH OF THE OCEAN REFLECTED PULSE.	120
7. LINK EQUATIONS.	125
8. AIRBORNE ALTIMETER EXPERIMENT DATA ANALYSIS	127
8.1. Introduction.	127
8.2. Data Analysis	132
8.3. Altitude Dependence of the Received Signal Energy	165
8.4. Summary	173
9. CONCLUSIONS	174
APPENDIX A: EVALUATION OF THE PERFORMANCE OF THE CORRELATION ALGORITHM FOR A GAUSSIAN MEAN RECEIVED PULSE SHAPE.	177
APPENDIX B: DERIVATIONS LEADING TO THE FREQUENCY DOMAIN REPRESENTATION OF TIMING ERROR	183
APPENDIX C: EXPANSION OF EQUATION (5.46)	187
APPENDIX D: DERIVATIONS LEADING TO EQUATION (5.53)	188

APPENDIX E: EXPECTED DIFFERENTIAL DELAY FOR THE AIRCRAFT EXPERIMENT	189
APPENDIX F: EFFECTS OF TELESCOPE CENTRAL OBSTRUCTIONS ON RECEIVED SIGNAL LEVEL.	191
REFERENCES.	199
CUMULATIVE LIST OF RADIO RESEARCH LABORATORY REPORTS PREPARED UNDER NASA GRANT NSG-5049	201
PAPERS PUBLISHED.	203

LIST OF FIGURES

Figure		Page
2.1.	Pressure measurement sensitivity to differential pathlength errors as a function of the satellite elevation angle.	8
3.1.	Mean received waveforms of the laser altimeter for different wind speed and SWH. Gaussian ocean surface, normal incidence. .	14
3.2.	Mean received waveforms for laser altimeters with different beam divergence angles. Gaussian ocean surface, normal incidence.	15
3.3.	Mean received pulse shape for reflection from an ocean wave with a height of 2 m (trough-crest). The laser altimeter is at an altitude of 400 km and the beam divergence is varied from 100 μ rad to 900 μ rad.	18
3.4.	Mean received pulse shape for reflection from ocean waves with different wave heights. Normal incidence.	19
3.5.	Mean received pulse shape for reflection from an ocean wave with a height of 2 m (trough-crest). The laser altimeter is slightly off normal, with a nadir angle of 1°.	21
3.6.	Comparison of sinusoidal and trochoidal waves.	23
3.7.	Mean received pulse shape from reflection from a trochoidal wave with a height of 2 m (trough-crest). The laser altimeter is at an altitude of 400 km.	24
4.1.	Example of time-resolved speckle	27
4.2.	Mean received pulse shape for reflection from an infinite flat diffuse target. Normal incidence. Magnitude scale is relative.	36
4.3.	Waveform of the variance for reflection from an infinite flat diffuse target. Normal incidence. Magnitude scale is relative.	37
4.4.	Number of speckle correlation cells for reflection from an infinite flat diffuse target. Normal incidence.	38
4.5.	Mean received pulse shape for reflection from an infinite flat diffuse target. Non-normal incidence. Magnitude scale is relative.	40
4.6.	Waveform of the variance for reflection from an infinite flat diffuse target. Non-normal incidence. Magnitude scale is relative	41
4.7.	Number of speckle correlation cells for reflection from an infinite flat diffuse target. Non-normal incidence.	42

Figure		Page
4.8.	Geometry of the finite size plate target	43
4.9.	Mean received pulse shape for reflection from a finite size plate. Magnitude scale is relative.	45
4.10.	Waveform of the variance for reflection from a finite size plate. Magnitude scale is relative.	46
4.11.	Number of speckle correlation cells for reflection from a finite size plate.	48
4.12.	Mean received pulse shape for reflection from a finite size plate. Magnitude scale is relative.	49
4.13.	Waveform of the variance for reflection from a finite size target. Magnitude scale is relative	50
4.14.	Number of speckle correlation cells for reflection from a finite size plate.	51
4.15.	Timing performance for reflection from an infinite flat diffuse target calculated using Eq. (4.63). Normal incidence. Mean received pulse shape corresponds to that in Figure 4.2.	59
4.16.	Timing performance for reflection from an infinite flat diffuse target calculated using Eq. (4.63). Non-normal incidence. Mean received pulse shape corresponds to that in Figure 4.5.	60
4.17.	Timing performance for reflection from a finite size plate calculated using Eq. (4.63). Mean received pulse shape corresponds to that in Figure 4.9.	61
4.18.	Slope of the mean pulse shape shown in Figure 4.9. Magnitude scale is relative.	62
4.19.	Slope of the mean pulse shape shown in Figure 4.12. Magnitude scale is relative.	64
4.20.	Timing performance for reflection from a finite size target. Calculated using Eq. (4.63). Mean received pulse shape corresponds to that in Figure 4.12	65
4.21.	Comparison of simulation and theory.	69
4.22a.	Schematic diagram of the laser and the retroreflectors on LAGEOS. Relative position in units of transmitted pulse width .	80
4.22b.	Simulated results for reflection from LAGEOS	81

Figure	Page
4.22c. Simulated results for reflection from LAGEOS for variance due to shot noise.	82
4.22d. Simulated results for reflection from LAGEOS for variance due to speckle	82
4.23a. Schematic diagram of the laser and the retroreflectors on LAGEOS. Relative position in units of transmitted pulse width.	83
4.23b. Simulated results for reflection from LAGEOS	84
4.23c. Simulated results for reflection from LAGEOS for variance due to shot noise.	85
4.23d. Simulated results for reflection from LAGEOS for variance due to speckle	85
4.24a. Schematic diagram of the laser and the retroreflector on LAGEOS. Relative position in units of transmitted pulse width.	86
4.24b. Simulated results for reflection from LAGEOS	87
4.24c. Simulated results for reflection from LAGEOS for variance due to shot noise.	88
4.24d. Simulated results for reflection from LAGEOS for variance due to speckle	88
5.1. Comparison of the correlation and centroid algorithms for a simulated received pulse shape from a Gaussian ocean surface . .	107
5.2. Comparison of the correlation and centroid algorithms for a simulated received pulse shape from a sinusoidal ocean surface .	109
5.3a. Power spectra of the mean received pulse shape shown in Figure 5.1	110
5.3b. Power spectra of the mean received pulse shape shown in Figure 5.2	110
5.4. Effects of speckle averaging on the correlation algorithm. The mean pulse shape corresponds to Figure 5.2	111
5.5. Performance of the correlation algorithm when the mean pulse shapes at two wavelengths are different. One wavelength has mean pulse shape corresponding to that in Figure 5.1. The other wavelenegth has mean pulse shape corresponding to that in Figure 5.2.	114

Figure		Page
8.1.	A picture of the NASA electra airplane.	128
8.2.	A picture of the computer system on board the airplane.	129
8.3.	A picture of the equipment rack on board the airplane	130
8.4.	A picture of the interior of the airplane showing the laser power supply, the laser and the transmitting optics	131
8.5.	A waveform recorded at 305 m (1000 ft) altitude	133
8.6.	A waveform recorded at 305 m (1000 ft) altitude	134
8.7.	Timing history and timing histograms for the 305 m altitude data, using the correlation algorithm. Correlation coefficient is curve fitted around its peak	137
8.8.	History plot and histogram of the correlation coefficient for the 305 m altitude data. Correlation coefficient is curve fitted around its peak.	138
8.9.	Two recorded waveforms at 1219 m (4000 ft) altitude	139
8.10.	Timing history and timing histogram for the 1219 m altitude data, using the correlation algorithm. Correlation coefficient is curve fitted around its peak	140
8.11.	History plot and histogram of the correlation coefficient for the 1219 m altitude data. Correlation coefficient is curve fitted around its peak.	141
8.12.	Two recorded waveforms obtained from ranging to a white plate . .	143
8.13.	Timing history and timing histogram for the data obtained from ranging to a white plate, using the correlation algorithm. Correlation coefficient is curve fitted around its peak.	144
8.14.	History plot and histogram of the correlation coefficient for the data obtained from ranging to a white plate. Correlation coefficient is curve fitted around its peak	145
8.15.	Two recorded waveforms obtained from ranging to a cube corner reflector	146
8.16.	Timing history and timing histogram for the data obtained from ranging to a cube corner reflector, using the correlation algorithm. Correlation coefficient is curve fitted around its peak	147

Figure		Page
8.17.	History plot and histogram of the correlation coefficient for the data obtained from ranging to a cube corner reflector. Correlation coefficient is curve fitted around its peak	148
8.18.	Timing history and timing histogram for the data obtained at 305 m altitude, using the separation between the two peaks as the differential arrival time estimate	151
8.19.	Timing history and timing histogram for the data obtained from ranging to a cube corner reflector, using the separation between the two peaks as the differential arrival time estimate	152
8.20.	Timing history and timing histogram for the data collected at 305 m altitude. Results obtained by calculating the centroids of 75 points around the peaks	154
8.21.	Timing history and timing histogram for the data collected from ranging to a cube corner reflector. Results obtained by calculating the centroids of 75 points around the peaks	155
8.22.	Timing history and timing histogram for the data collected from ranging to a cube corner reflector. Results obtained by calculating the centroids of 50 points around the peaks.	156
8.23.	Timing history and timing histogram for the data collected at 305 m altitude. Results obtained by correlating the UV pulse with the logarithm of the green pulse	157
8.24.	Two recorded waveforms and their logarithms. 305 m altitude data.	158
8.25.	Timing history and timing histogram for the data collected from ranging to a cube corner reflector. Results obtained by correlating the UV pulse with the logarithm of the green pulse	160
8.26.	Two recorded waveforms and their logarithms. Cube corner reflector data.	161
8.27.	Timing history and timing histogram for the data collected at 305 m altitude. Results obtained by correlating the logarithm of the UV pulse with the green pulse.	162
8.28.	Timing history and timing histogram for the data collected from ranging to a cube corner reflector. Results obtained by correlating the logarithm of the UV pulse with the green pulse	163
8.29.	Timing history and timing histogram for the data collected at 305 m altitude. Results obtained by correlating the logarithms of both pulses	164

Figure	Page
8.30. Timing history and timing histogram for the data collected from ranging to a cube corner reflector. Results obtained by correlating the logarithms of both pulses	166
8.31. Received signal level versus altitude for a telescope with central obstruction	168
8.32. Received signal level versus altitude for a telescope without central obstruction	170
8.33. Effects of telescope focusing on the received signal level. Telescope has central obstruction	171
8.34. Effects of telescope focusing on the received signal level. Telescope has no central obstruction.	172
F.1. Geometry of the optical setup	192
F.2. Ray tracing of the telescope.	194
F.3. Geometry of the detector plane and image plane.	195

1. INTRODUCTION

Global measurements of temperature and pressure are essential in all weather and climate predictions. Forecasting and modeling have been hampered by the lack of measurements in inaccessible regions of the earth's surface, particularly over the oceans. Consequently, there is considerable interest in developing remote-sensing techniques for measuring pressure and temperature from satellites. Pressure is probably the most difficult parameter to measure accurately. Korb et al. [1] have proposed a differential absorption (DIAL) technique for remote sensing of pressure and temperature by observing the near-IR absorption in the oxygen A band. The feasibility of their technique was demonstrated experimentally using CW lasers to make measurements over the horizontal paths. Unfortunately, the technique places severe constraints on the wavelength stability of the laser.

In a previous paper, Gardner [2] proposed a pressure measurement technique using a two-color short pulse laser altimeter. This technique was an extension of NASA's ongoing two-color ranging program to measure atmospheric pressure [3]. The technique makes use of the fact that the atmosphere is dispersive and the group refractivity is proportional to pressure; therefore, the difference between the optical path lengths from a satellite to the earth's surface is proportional to the surface pressure. The altimeter uses fixed frequencies rather than tunable lasers and is insensitive to laser wavelength changes. The theory on which the technique is based is reviewed in Chapter 2.

Although pressure measurements can be made over both the ground and water, pressure measurement over the ocean is of greatest interest. In a previous paper [4], we studied the statistics and waveforms of the ocean

reflected laser pulses. Parts of the results that are relevant to the pressure measurement technique are reviewed in Chapter 3. In addition, we also study the reflection of laser pulses from sinusoidal and trochoidal waves, because these waves give rise to glints that can improve the accuracies of the pressure measurements.

When a short laser pulse is reflected from the ocean surface, the reflected pulse will be broadened to about twice the width of the range spread of the wave height. Because the received pulse has a width longer than the transmitted laser pulse, speckle will cause random small-scale fluctuations within the received pulse which distort its shape. This effect is referred to as time-resolved speckle. In Chapter 4, we derive the statistics of time-resolved speckle. The problem of estimating the arrival time of laser pulses in the presence of time-resolved speckle is also considered. The results not only are important to the pressure measurement technique, but also have applications in general laser radar and ranging.

The pressure measurement technique requires accurate measurements of the differential propagation time of laser pulses at two wavelengths. If the altimeter uses the fundamental and tripled ND:YAG laser frequencies, picosecond timing accuracies are required to make millibar-level pressure measurements. The timing problem is complicated by the fact that, due to the random dynamic nature of the ocean, the mean reflected pulse shape cannot be predicted a priori. This means optimal estimators such as the maximum likelihood estimator cannot be used. In Chapter 5, we propose and study several suboptimal estimators that do not require knowledge of the pulse shape.

The timing accuracy of the receiver depends on the bandwidth of the received signal. The signal bandwidth is related to the surface profile

within the laser footprint. In Chapter 6, we investigate the relation between the surface profile and the bandwidth of the received signal.

In Chapter 7, we use the results obtained from previous chapters to estimate the expected timing accuracies of realistic system designs and to estimate the corresponding accuracies of the barometric measurements.

An airborne altimeter experiment was conducted by NASA personnel on September 7 and 8, 1983. This initial experiment was basically a shakedown flight for a series of more extensive flights to be conducted during the late summer 1984. To verify the theory, the data collected were processed by different timing algorithms. The results are discussed in Chapter 8.

2. THEORY OF THE PRESSURE MEASUREMENT TECHNIQUE

The optical path length is defined as the integral of the group refractive index along the ray path. Because the horizontal refractivity gradients in the atmosphere are small, the two-way optical path length between a satellite and the earth's surface for a pulsed laser system is given by [2]

$$R_o = 2 \int_{r_{\text{ocean}}}^{r_{\text{sat}}} \frac{(1 + 10^{-6} N_g)}{\sin \theta} dr \quad . \quad (2.1)$$

N_g is the group refractivity, r is the geocentric altitude, and θ is given by Snell's law for a spherically stratified medium. It is convenient to express Eq. (2.1) as the sum of the straight-line path length R_L and an atmospheric correction AC:

$$R_o = 2R_L + AC \quad (2.2)$$

where

$$AC = 2 \int_{r_{\text{ocean}}}^{r_{\text{sat}}} \frac{10^{-6} N_g}{\sin \theta} + 2 \left[\int_{r_{\text{ocean}}}^{r_{\text{sat}}} \frac{dr}{\sin \theta} - R_L \right] \quad . \quad (2.3)$$

The first term comprising AC is the velocity correction, while the second term is the difference between the geometric lengths of the ray and straight-line paths.

The atmospheric correction can be evaluated by using an appropriate model for the group refractivity. Although AC depends on the atmospheric pressure, temperature, and humidity along the propagation path, it is most sensitive to pressure. In fact, when the laser is pointed at nadir, AC is

approximately proportional to the atmospheric pressure at the earth's surface. Therefore, surface pressure can be computed from measurements of AC.

A pulsed laser altimeter measures the round-trip optical path length R_0 . If the straight-line distance (R_L) between the satellite and the laser footprint on the earth's surface is known, AC can be calculated by using Eq. (2.2). Because R_L must be known to within a few centimeters for the approach to be effective, it is probably not practical. As an alternative, a multicolor altimeter can be used to determine AC by calculating the difference between the round-trip optical path lengths measured at two different wavelengths:

$$\Delta R = R_1 - R_2 = AC_1 - AC_2 \quad . \quad (2.4)$$

A theoretical expression for ΔR can be obtained by evaluating the integrals in Eq. (2.3). This is done by using the perfect gas law, law of partial pressure, and the hydrostatic equation to obtain a suitable refractivity profile. Although the dominant variation of ΔR with respect to pressure is linear, there is a small quadratic variation which cannot be neglected. If Eqs. (2.3) and (2.4) are evaluated and then solved for atmospheric pressure at the earth's surface, we obtain [2]

$$P = \frac{-b + (b^2 - 4ad)^{1/2}}{2a} \quad , \quad (2.5)$$

$$a = 4.73 \times 10^{-8} \frac{f(\lambda_1) + f(\lambda_2)}{T \sin^2 E} \frac{2}{3 - 1/K} \quad , \quad (2.6)$$

$$b = -2.357 \times 10^{-3} + \frac{1.084 \times 10^{-8} \text{ TK}}{\tan^2 E} - \frac{1.5 \times 10^{-13} T^2}{\sin^4 E} \frac{K^2}{2 - K} \quad , \quad (2.7)$$

$$d = \frac{F(\theta, H) \Delta R \sin E}{2[f(\lambda_1) - f(\lambda_2)]} - 2.24 \times 10^{-4} e, \quad (2.8)$$

$$F(\theta, H) = 1 + 0.0026 \cos(2\theta) - 0.0003H, \quad (2.9)$$

$$K = 1.163 + 0.00968 \cos(2\theta) - 0.00104T + 0.00001435P, \quad (2.10)$$

$$f(\lambda) = 0.9650 + \frac{0.0164}{\lambda^2} + \frac{0.000228}{\lambda^4}, \quad (2.11)$$

where

λ = laser wavelength (μm),

e = water vapor pressure at the laser footprint (mbar),

P = atmospheric pressure at the laser footprint (mbar),

T = temperature at the laser footprint ($^{\circ}\text{K}$),

θ = colatitude of the laser footprint,

H = altitude of the laser footprint above sea level (km), and

E = satellite elevation angle.

The function $f(\lambda)$ accounts for atmospheric dispersion which is responsible for the difference in the measured pathlengths at the two wavelengths.

To compute the surface pressure it is necessary to know ΔR , E , e and T . Fortunately, only a crude estimate of the surface temperature is required. An accuracy of 20 – 30° is easy to obtain and should be adequate. A temperature error of 20°C would contribute less than a few tenths of a millibar to the pressure error for an elevation angle above 30° . Errors in the measured values of E are also only significant at the lower elevation angles. Above 50° elevation, the errors in E can be neglected provided

they are of the order of a millirad or less. The pressure sensitivity to errors in water vapor is constant with respect to elevation angle. A 10 mbar error in water vapor pressure will contribute ~1 mbar to the surface pressure error [2]. Since water vapor pressure can approach 40 mbar when the surface temperature and relative humidity are high, its effect cannot be ignored. Currently, satellite-based microwave sensors can provide water vapor pressure information accurate to about 10% [5]. For a maximum water vapor pressure of 40 mbar, a 10% error in water vapor pressure measurement corresponds to about 0.4 mbar error in surface pressure error. So, by using the information collected by the microwave sensor or by installing a microwave sensor together with the laser altimeter, the error due to water vapor can be reduced to an insignificant amount.

In an actual system, the dominant error source is likely to be the differential path-length measurement. The pressure sensitivity to differential path-length errors [2] is given by

$$\frac{\partial P}{\partial \Delta R} \cong \frac{0.212 \sin E}{f(\lambda_1) - f(\lambda_2)} \text{ (mbar/mm)} \quad (2.12)$$

This sensitivity depends both on the choice of wavelengths and on the elevation angle. At low-elevation angles the laser pulses travel through more of the atmosphere so the pressure effects are more significant. In addition, ΔR is greater for larger wavelength differences because of greater differences in group refractivity. $\partial P / \partial \Delta R$ is plotted vs. elevation angle in Fig. 2.1 for three possible wavelength combinations of fundamental (1064 nm), doubled (532 nm), and tripled (355 nm) ND:YAG laser frequencies. When ranging at nadir using the 355 and 1064 nm wavelengths,

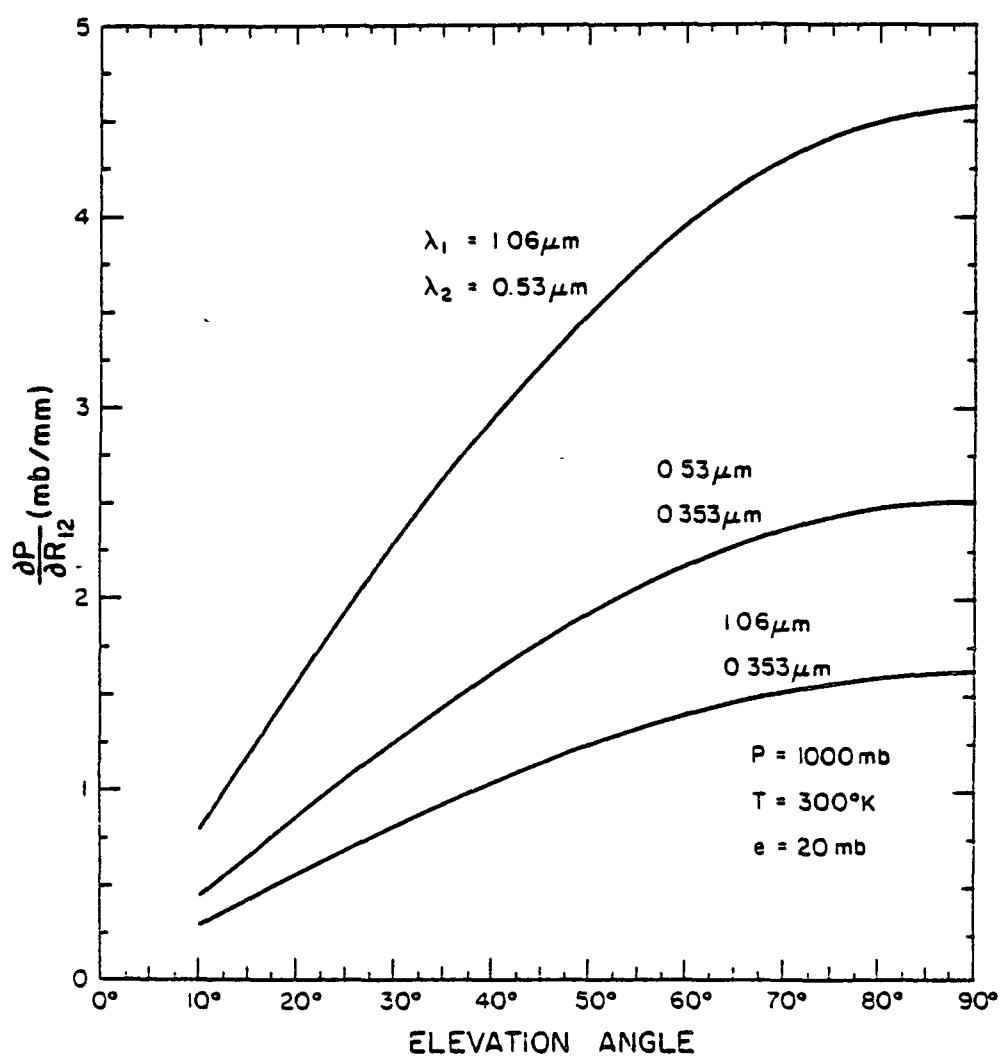


Figure 2.1. Pressure measurement sensitivity to differential pathlength errors as a function of the satellite elevation angle.

the required differential path-length accuracy is 0.6 mm/mbar, which requires a timing accuracy of 2 psec/mbar.

Although the pressure sensitivity to errors in ΔR decreases as the elevation angle is decreased, other error factors become more significant. The sensitivity to temperature and elevation-angle errors and the differential path-length errors increase as the elevation angle is decreased. Consequently, the best performance will be obtained with the laser pointed at nadir. When the laser is pointed to within a few degrees of nadir, Eq. (2.5) can be approximated by

$$P \approx -\frac{d}{b} \approx 2.12 \times 10^2 \frac{F(\theta, H) \sin E}{f(\lambda_1) - f(\lambda_2)} \Delta R - 0.095e \quad (2.13)$$

In this case, the rms pressure error is approximately

$$\sigma_p = \left[\left(\frac{\partial P}{\partial \Delta R} \sigma_{\Delta R} \right)^2 + \left(\frac{\partial P}{\partial e} \sigma_e \right)^2 + \left(\frac{\partial P}{\partial E} \sigma_E \right)^2 \right]^{1/2} \quad (2.14)$$

where $\sigma_{\Delta R}$, σ_e , and σ_E are the rms errors in ΔR , e , and E , respectively.

In Eq. (2.14),

$$\frac{\partial P}{\partial e} \approx 0.095 \text{ (mbar/mbar)} \quad (2.15)$$

$$\frac{\partial P}{\partial E} \approx \frac{10^{-3} P}{\tan E} \text{ (mbar/mrad)} \quad (2.16)$$

and $(\partial P)/(\partial \Delta R)$ is given by Eq. (2.12).

3. LASER BACKSCATTER FROM THE OCEAN

Although pressure measurements can be made over both the ground and water, pressure measurement over the ocean is of greatest interest. In a previous paper [4], we studied the statistics and waveforms of the ocean reflected laser pulses. Parts of the results that are relevant to the pressure measurement technique are reviewed in this chapter. In addition, we also study the reflection of laser pulses from sinusoidal and trochoidal waves, because these waves give rise to glints that can improve the accuracies of the pressure measurement.

For near normal incidence, the reflection of laser pulses from the ocean is due mainly to scattering by randomly distributed specular points on the surface. These specular points arise from ocean-wave structures with slopes oriented to reflect the signal back to the receiving telescope. Ocean waves are generated by the joint actions of wind as a disturbing force, and gravity and surface tension as restoring forces. The larger waves, with wavelengths greater than ~ 2 cm, are gravity waves. The smaller waves, for which surface tension is the restoring force, are capillary waves. The wavelengths of capillary waves are bounded at the small-scale end by viscous dissipation to ~ 1 mm. Since the wavelengths of even the smallest capillary waves are much larger than an optical wavelength, diffraction is not important, and the laser backscatter can be analyzed using geometric optics.

If the laser beam is pointed at nadir and the reflected pulses are detected by a direct-detection receiver, the mean received signal conditioned on a given ocean surface profile is given by [4], [6]

$$E[S(t)|\xi] = \overline{S}(t) = \langle N \rangle \int d^2 \underline{\rho} b_2(\underline{\rho}, z) |f(t - \psi)|^2 * h(t) , \quad (3.1)$$

where

$$b_n(\underline{\rho}, z) = |a(\underline{\rho}, z)|^n \beta_r^{n/2}(\underline{\rho}) / \int d^2 \underline{\rho} |a(\underline{\rho}, z)|^n \beta_r^{n/2}(\underline{\rho}) , \quad (3.2)$$

and

$$\psi = \frac{2z}{c} + \frac{\rho^2}{cz} - \frac{2\xi(\underline{\rho})}{c} . \quad (3.3)$$

Here

$\langle N \rangle$ = expected number of detected signal photons/pulse,

$\underline{\rho} = (x, y)$ = horizontal coordinate vector on the ocean surface
measured from the center of the footprint,

$a(\underline{\rho}, z)$ = complex amplitude cross section of the laser footprint,

$\beta_r(\underline{\rho})$ = power reflection coefficient of the ocean surface,

$\xi(\underline{\rho})$ = ocean surface profile,

z = altitude of the laser altimeter,

c = velocity of light,

$f(t)$ = transmitted pulse amplitude, and

$h(t)$ = impulse response of the receiver electronics.

In this equation ψ is the delay of the reflected pulse. The first term in Eq. (3.3) is the nominal distance of the target, the second term is the additional delay due to the curvature of the laser wavefront and the last term is from the range spread of the target. The power-reflection coefficient depends on the angle of incidence and sea state. For divergence angles of a few milliradians or less, $\beta_r(\underline{\rho})$ is essentially constant within the footprint.

The covariance function of the received signal, which describes the fluctuation of the received signal due to shot noise and speckle, is given by [4], [6]

$$C_s(t_1, t_2) = \langle N \rangle \int d^2 \underline{\rho} b_2(\underline{\rho}, z) \int_{-\infty}^{\infty} d\tau |f(\tau - \psi)|^2 h(t_1 - \tau) h(t_2 - \tau) \\ + \frac{\langle N \rangle^2}{K} \int d^2 \underline{\rho} b_4(\underline{\rho}, z) g(t_1 - \psi) g(t_2 - \psi) , \quad (3.4)$$

where

$$K = \frac{A_R [\int d^2 \underline{\rho} |a(\underline{\rho}, z)|^2 \beta_r(\underline{\rho})]^2}{\lambda^2 z^2 \int d^2 \underline{\rho} |a(\underline{\rho}, z)|^4 \beta_r^2(\underline{\rho})} \quad (3.5)$$

and

$$g(t) = |f(t)|^2 * h(t) . \quad (3.6)$$

In Eq. (3.4) K is the ratio of the receiver aperture area (A_R) to the speckle correlation area and $g(t)$ is the point target response of the system. The first term on the right-hand side of Eq. (3.4) is due to shot noise, while the second term is due to speckle noise. For a Gaussian laser cross section, K is given by [4], [6]

$$K = \pi A_R \left(\frac{2 \tan \theta_T}{\lambda} \right)^2 , \quad (3.7)$$

where θ_T is the beam divergence (half-angle measured at $\exp(-1/2)$ point). For typical laser altimeter configurations, K is of the order of a few thousand or larger.

The wave height at any given point on the ocean is the result of many wave components that have been generated by the wind in different regions and have propagated to the point of observation. Since the motions of different wave components are weakly correlated, the central limit theorem can

be used to argue that the wave height (i.e., surface profile) is Gaussian distributed. Therefore, over areas which are large compared to the longest waves on the ocean, $\xi(\rho)$ is usually assumed to obey Gaussian statistics. Experimental data tend to support this hypothesis. Consequently, the wave slopes are also Gaussian distributed and independent of the wave height [4]. Under these conditions, the power-reflection coefficient for normal incidence is given by [4], [7]

$$\beta_r = \frac{|R(0)|^2}{4\pi(S^2 + 2 \tan^2 \theta_T)} , \quad (3.8)$$

where $R(0)$ is the Fresnel backscatter coefficient and S^2 is the mean-square (MS) value of the total slope. The factor 4π is needed to convert scattering cross section to reflection coefficient. An empirical relationship between S^2 and wind speed was derived by Cox and Munk [8]:

$$S^2 = \left\langle \left(\frac{\partial \xi}{\partial x} \right)^2 \right\rangle + \left\langle \left(\frac{\partial \xi}{\partial y} \right)^2 \right\rangle = 0.003 + 0.00512W , \quad (3.9)$$

where W is the average wind speed in m/sec measured at 12.5 m above the mean sea level.

The expected received pulse can be calculated by taking the expectation of Eq. (3.1) over the probability distribution of the surface profile ξ . In Figs. 3.1 and 3.2, we show the mean received waveforms for a laser altimeter that has a Gaussian-shape point-target response $g(t)$. The point-target response is assumed to have a rms range width ($c\sigma_g$) of 1 cm. In Fig. 3.2, the mean waveforms are plotted for five different sea states. These figures show that the larger the significant wave height (SWH), the broader the return pulse. In Fig. 3.2, the sea state is fixed while the beam divergence is varied. As the beam divergence increases, the trailing

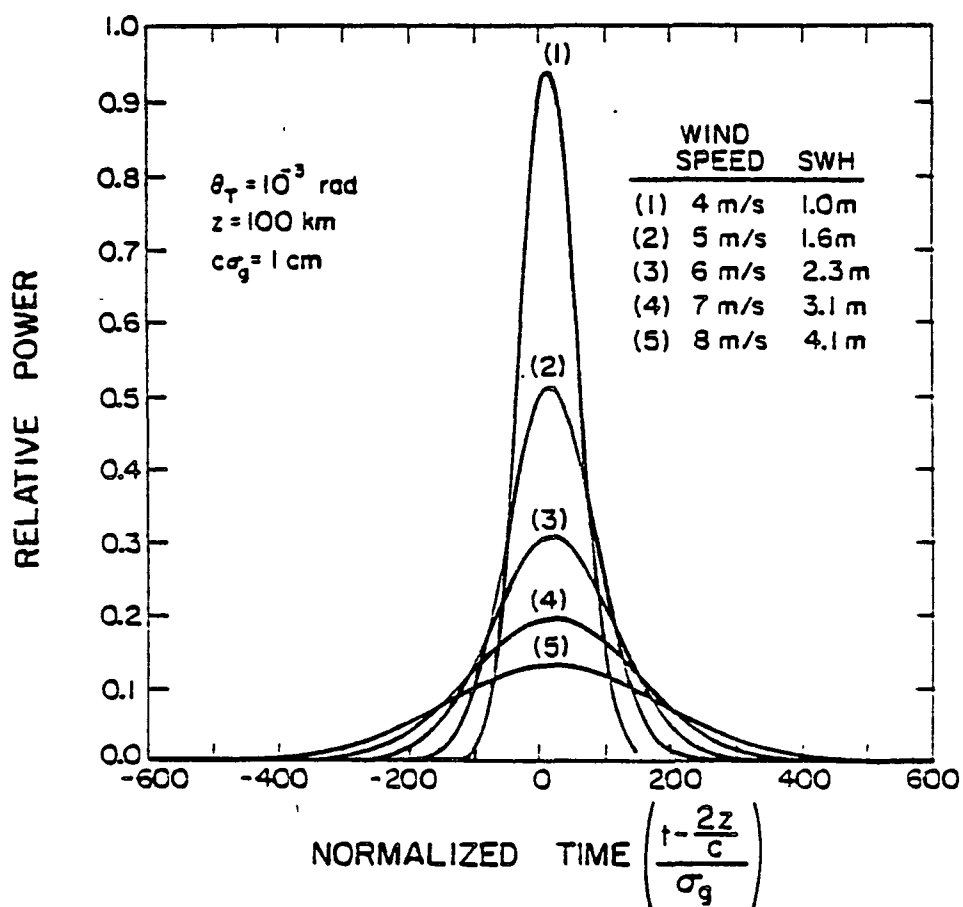


Figure 3.1. Mean received waveforms of the laser altimeter for different wind speed and SWH. Gaussian ocean surface, normal incidence.

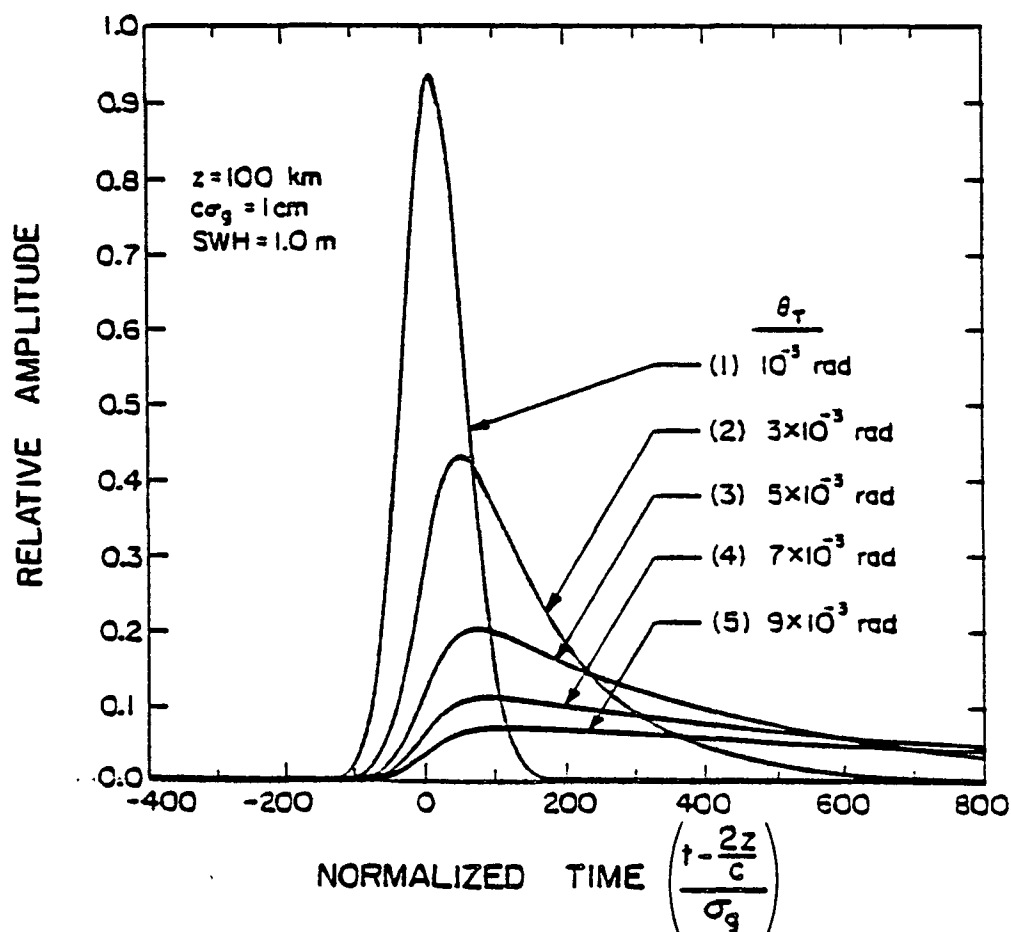


Figure 3.2. Mean received waveforms for laser altimeters with different beam divergence angles. Gaussian ocean surface, normal incidence.

edge of the pulse is broadened by the wavefront curvature effects, and the return pulse becomes asymmetric. To obtain the sharpest return pulses, it is necessary to have a small beam divergence which can be achieved relatively easily with laser altimeters. This is more difficult to achieve with radar altimeters due to their limitation in the antenna size.

The pulse shapes computed using the above approach will accurately predict the actual pulse shapes whenever the laser footprint is large compared to the periods of the waves. However, if the footprint is small, the local probability distribution of the surface profile within the footprint may be considerably different from Gaussian. For pressure-measurement applications, a small beam divergence angle is desired to minimize pulse broadening due to beam-curvature effects. As a consequence, the size of the footprint will be small and may not be significantly larger than the wavelength of the long-period ocean waves. Sea-wave records often reveal a sinusoidal or trochoidal profile for the dominant long-period waves which may extend over distances of a few hundred meters. In these areas, the surface profile is more suitably modeled as a large amplitude sinusoidal (or trochoidal) wave with superimposed small amplitude disturbances (capillary waves or small gravity waves) of short correlation length. For a sinusoidal wave model, we have

$$\begin{aligned}\xi(\underline{\rho}) &= \xi_0(\underline{\rho}) + \xi_1(\underline{\rho}) \\ &= A \cos\left(\frac{2\pi}{\Lambda} x + \beta\right) + \xi_1(\underline{\rho}) \quad ,\end{aligned}\tag{3.10}$$

where A is the amplitude of the sinusoidal wave, Λ is its wavelength, β is the phase angle and $\xi_1(\underline{\rho})$ is the small-scale disturbance. Using this model, the mean received signal can be expressed as

$$\begin{aligned}
E\{S(t)\} &= \int_{-\infty}^{\infty} d\xi_1 p(\xi_1) E\{S(t) | \xi_1\} \\
&= \langle N \rangle \int d\underline{\rho} b_2(\underline{\rho}, z) \int_{-\infty}^{\infty} d\xi_1 p(\xi_1) g\left(t - \frac{2z}{c} - \frac{\rho^2}{cz} + \frac{2}{c} \xi_0 + \frac{2}{c} \xi_1\right) .
\end{aligned}
\tag{3.11}$$

The integration over ξ_1 can be viewed as a convolution, so Eq. (3.11) can also be written as

$$E\{S(t)\} = \frac{c}{2} E\{S(t) | \xi_1 = 0\} * p_{\xi_1}\left(-\frac{c}{2} t\right) . \tag{3.12}$$

This equation implies that we need only evaluate the mean waveform for the ξ_1 equals zero case, i.e., $E\{S(t) | \xi_1 = 0\}$. The mean received waveform for any distribution of ξ_1 can be obtained by convolving the probability density function of ξ_1 with $E\{S(t) | \xi_1 = 0\}$.

Expected received pulse shapes were calculated for several values of beam divergence using the sinusoidal model. The results which are plotted in Fig. 3.3 show strong reflections from the wave crests and troughs. These reflections or glints occur because of the relatively large surface area at the crest and trough altitudes. The sharpness of the observed glints is directly related to the beam divergence. When the divergence is large, beam-curvature effects broaden the reflected pulses. The rise time of the crest reflection is limited only by the transmitted pulse width, beam divergence, and the receiver bandwidth. The tail at the trough reflections is primarily due to beam curvature effects. In Fig. 3.4, we calculated the results for three different ocean-wave heights. The wave height of the ocean can be inferred from the received pulse by measuring the separation between the crest and trough returns.

When the laser is pointed slightly off nadir in a direction normal to the wave fronts, the received pulse broadens, and multiple glints appear

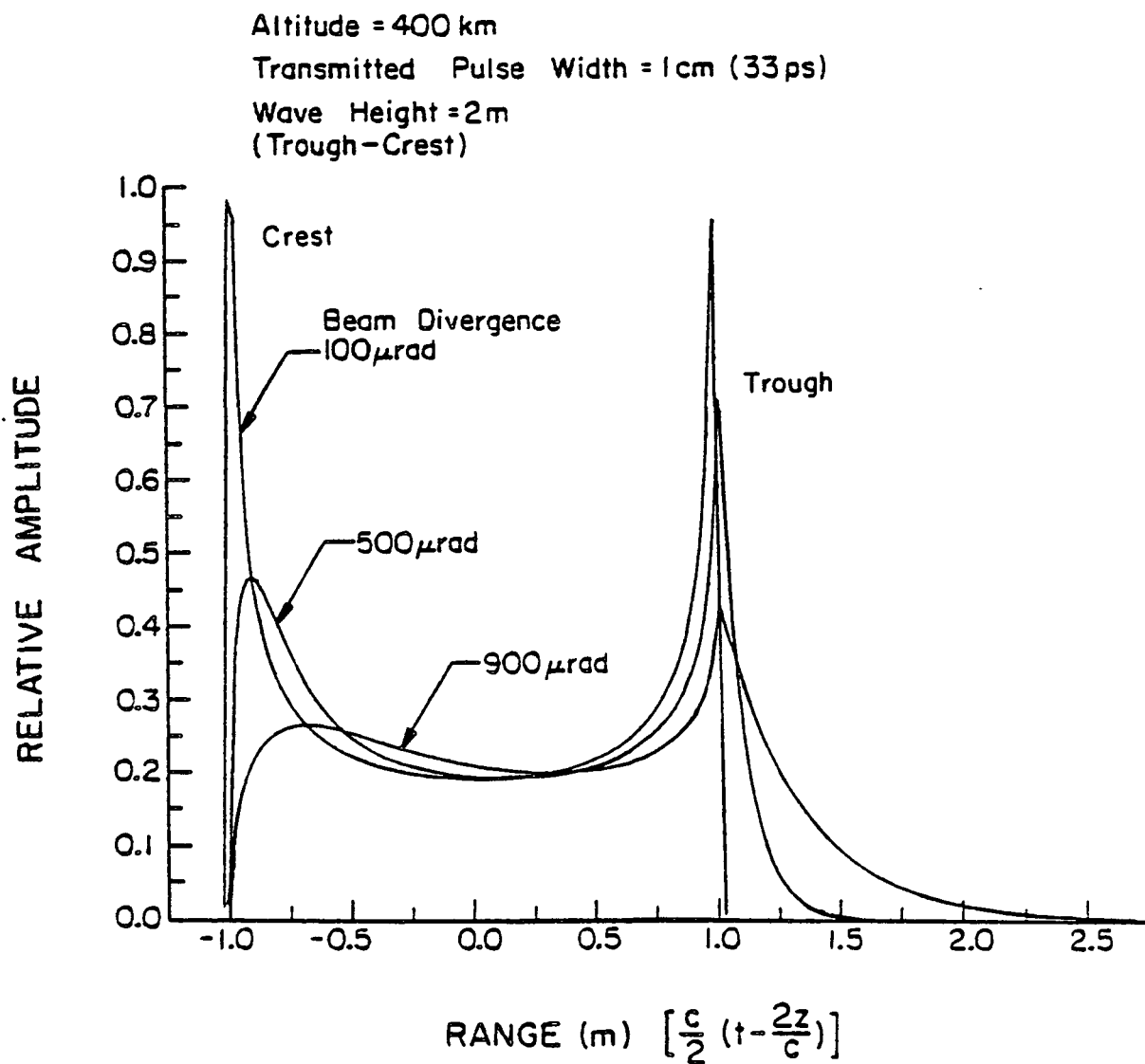


Figure 3.3. Mean received pulse shape for reflection from an ocean wave with a height of 2 m (trough-crest). The laser altimeter is at an altitude of 400 km and the beam divergence is varied from 100 μ rad to 900 μ rad.

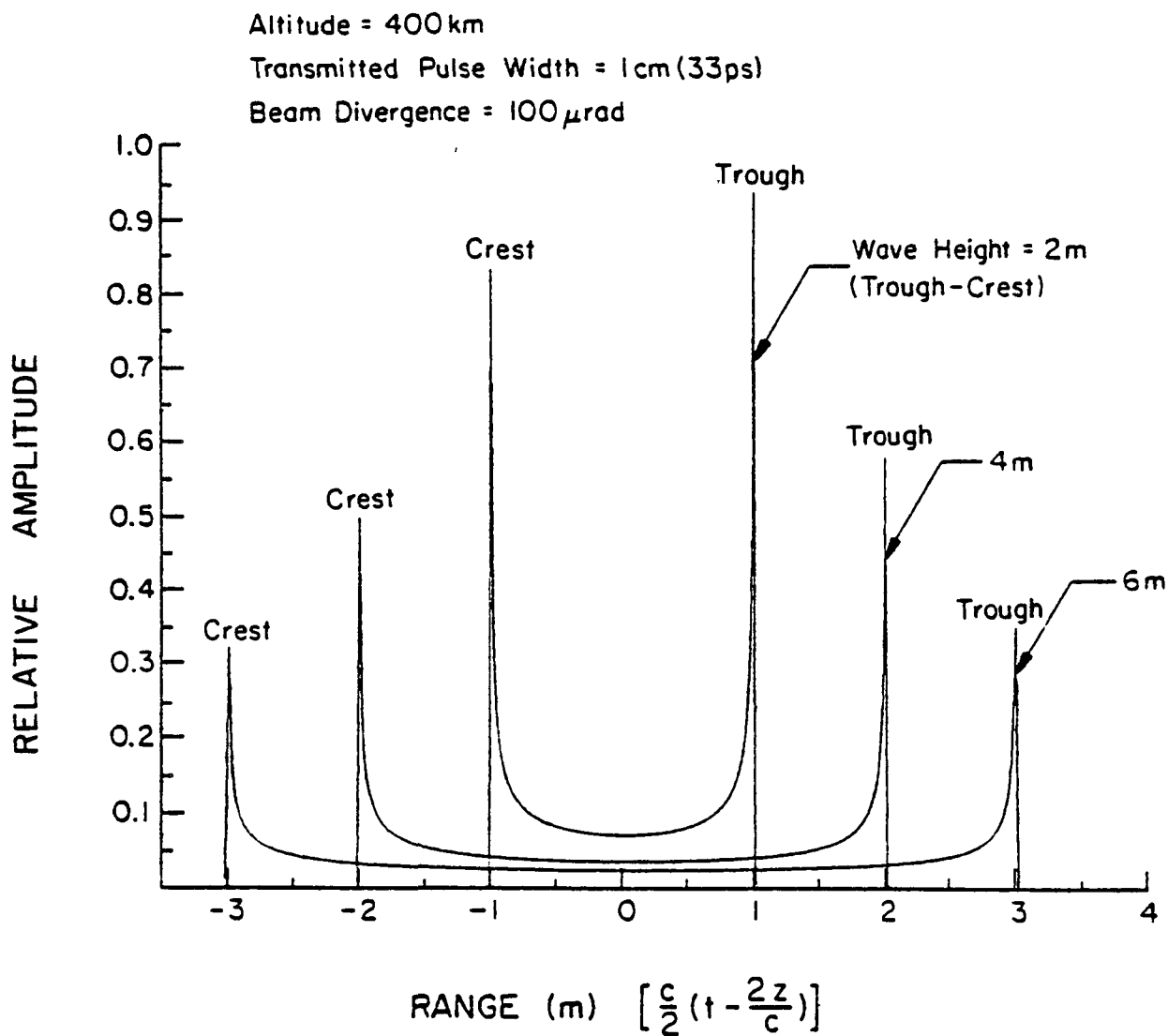


Figure 3.4. Mean received pulse shape for reflection from ocean waves with different wave heights. Normal incidence.

because of reflections from successive wave crests and troughs. This is illustrated in Fig. 3.5 for a nadir angle of 1° . A sinusoidal wave model was used with a wave height of 1 m (crest to trough) and a wave period of 10 m. Crest reflections are responsible for sharp peaks in the first half of the pulse, while trough reflections are responsible for the structure in the second half. At 1° off nadir for a 10-m wave period, the range difference between successive crests (or troughs) is ~ 17.5 cm. These results suggest that it may be possible to measure the crest-to-trough wave height and wave period as well as SWH using a short-pulse laser altimeter. This is not possible using microwave altimeters because the curvature effects due to the large beamwidths ($\sim 1-2^\circ$) obscure the crest and trough reflections.

In the actual ocean, the wave crests tend to be relatively high and sharp, while the wave troughs are comparably smooth and shallow. In some cases, the wave is more suitably modeled as a trochoid [9], i.e.,

$$\xi(\underline{\rho}) = \xi(x, y) = A \cos\left(\frac{2\pi}{\Lambda} x_0 + \beta\right) + \xi_1(\underline{\rho}) \quad (3.13)$$

and

$$x = x_0 - A \sin\left(\frac{2\pi}{\Lambda} x_0 + \beta\right) \quad (3.14)$$

For a sinusoid the profile depends sinusoidally on x , while for a trochoid the profile depends sinusoidally on x_0 , which is related to x by Eq. (3.14), a non-linear transformation. The difference between a trochoid and a sinusoid can be seen from the following reasoning. For simplicity, let $\beta = 0$, so the wave crest occurs at $x = x_0 = 0$. We have

$$\begin{cases} x_0 > x & -\Lambda/2 < x < \Lambda/2 \\ x_0 = x & x = \Lambda/2, -\Lambda/2 \\ x_0 < x & -\Lambda < x < -\Lambda/2, \Lambda/2 < x < \Lambda \end{cases} \quad (3.15)$$

Altitude = 400 km
 Transmitted Pulse Width = 1 cm (33ps)
 Beam Divergence = $100\mu\text{rad}$
 Wave Period = 10 m
 Wave Height = 1 m
 (Trough-Crest)
 Nadir Angle $\phi = 1^\circ$

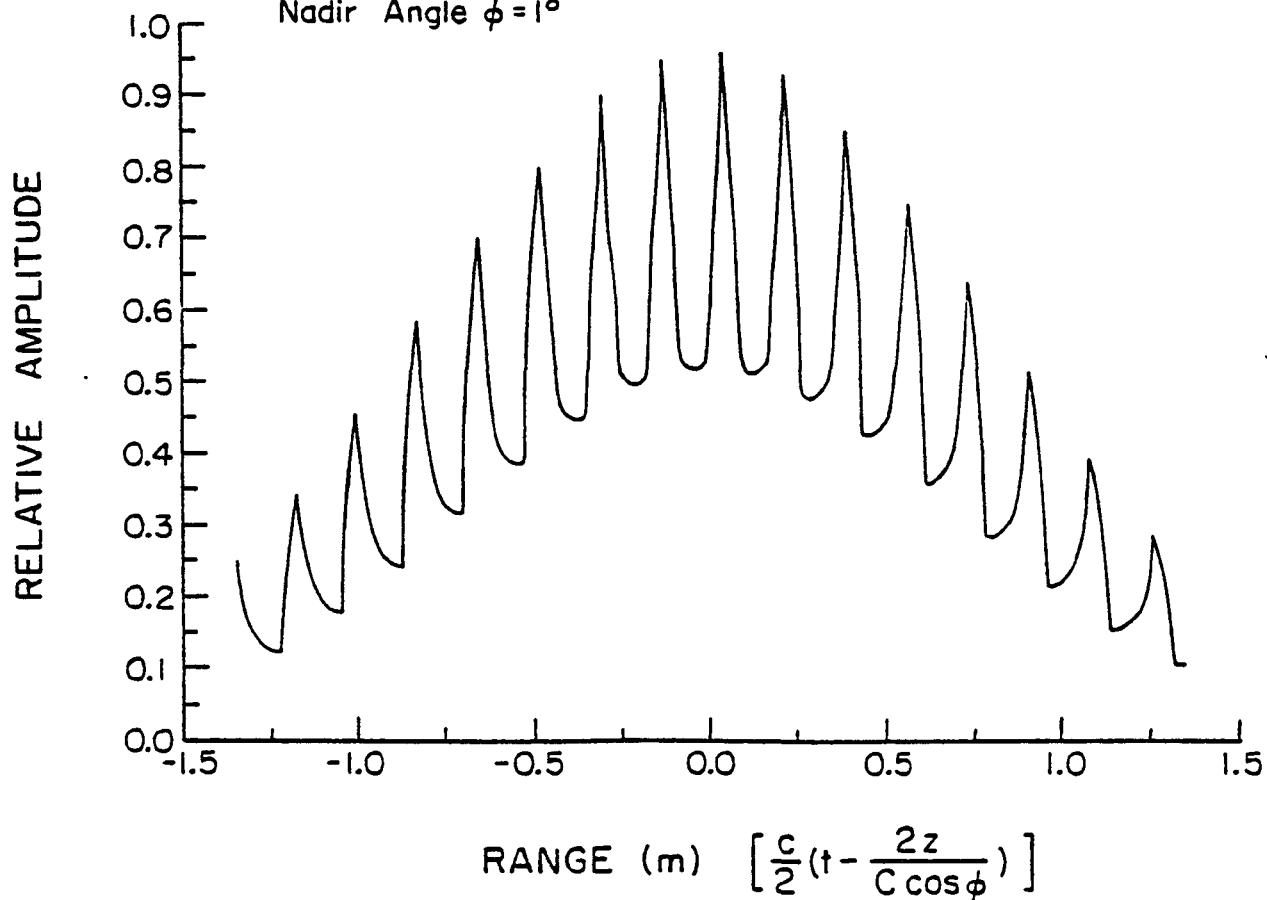


Figure 3.5. Mean received pulse shape for reflection from an ocean wave with a height of 2 m (trough-crest). The laser altimeter is slightly off normal, with a nadir angle of 1° .

For points around the crest, $x_0 > x$, the decay of a trochoid from its peak is faster than a sinusoid, so its peak is sharper. For points near the trough, $x_0 < x$ and the rise from the trough is slower, resulting in a smoother trough. In Fig. 3.6, we plot sinusoidal and trochoidal waves for a trough-crest wave height of 2 m and a wavelength of 10 m. Indeed, the trochoid is sharper around the crests and smoother around the troughs.

Since trochoids have sharper crests and smoother troughs, we expect the reflections from the crests to be weaker and the reflections from the troughs to be stronger than in the case of sinusoids. This is born out by the results shown in Fig. 3.7. For trochoidal waves, the reflections from the troughs are enhanced. These results should be compared with Fig. 3.3.

Obviously, the ocean-surface profile is not a perfect sinusoid or trochoid. The Gaussian model and the sinusoidal wave model can be viewed as the two extremes. The actual received pulse shapes are likely to lie somewhere between the broad smooth pulses, which result from the Gaussian model, and the highly structured shapes, which arise from the sinusoidal model. For the pressure-measurement application, a small laser beam divergence angle is desired to minimize pulse broadening due to beam-curvature effects. Therefore, the received pulses are expected to exhibit fine scale structure due to strong reflections within the laser footprint. Later we will see that this fine structure is an important factor in achieving the picosecond (i.e., millimeter) timing accuracies which are required for measuring atmospheric pressure.

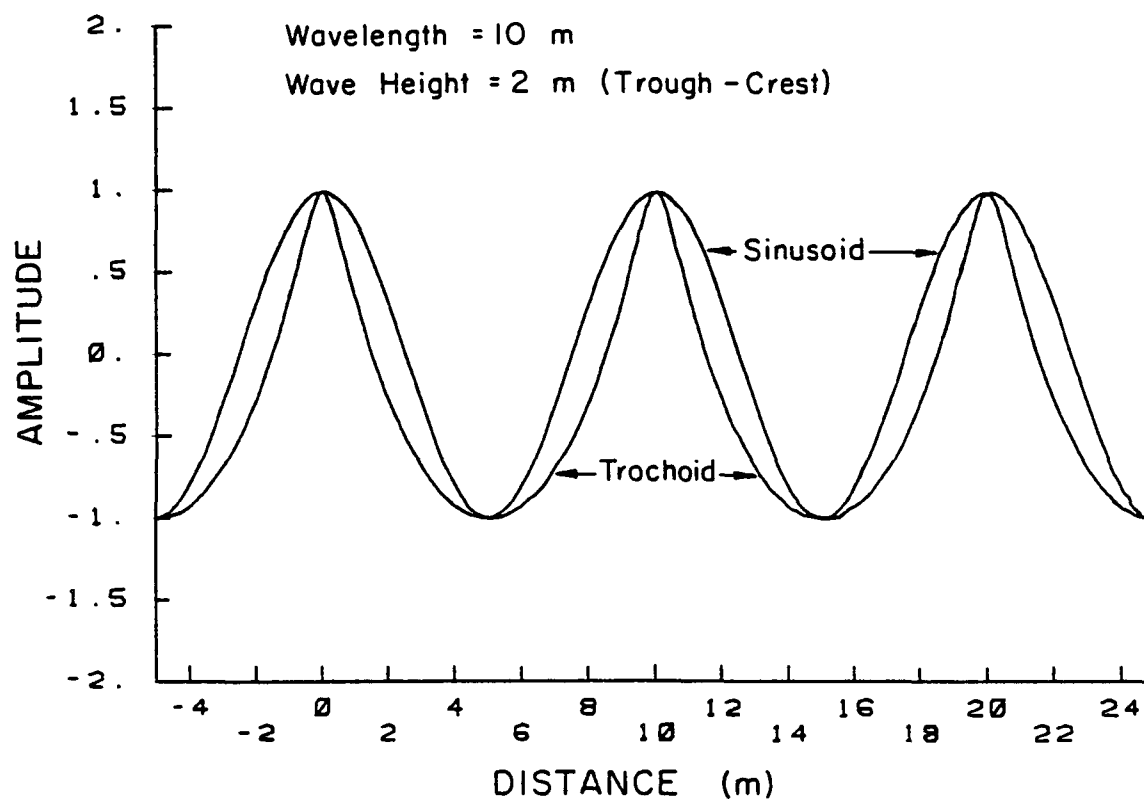


Figure 3.6. Comparison of sinusoidal and trochoidal waves.

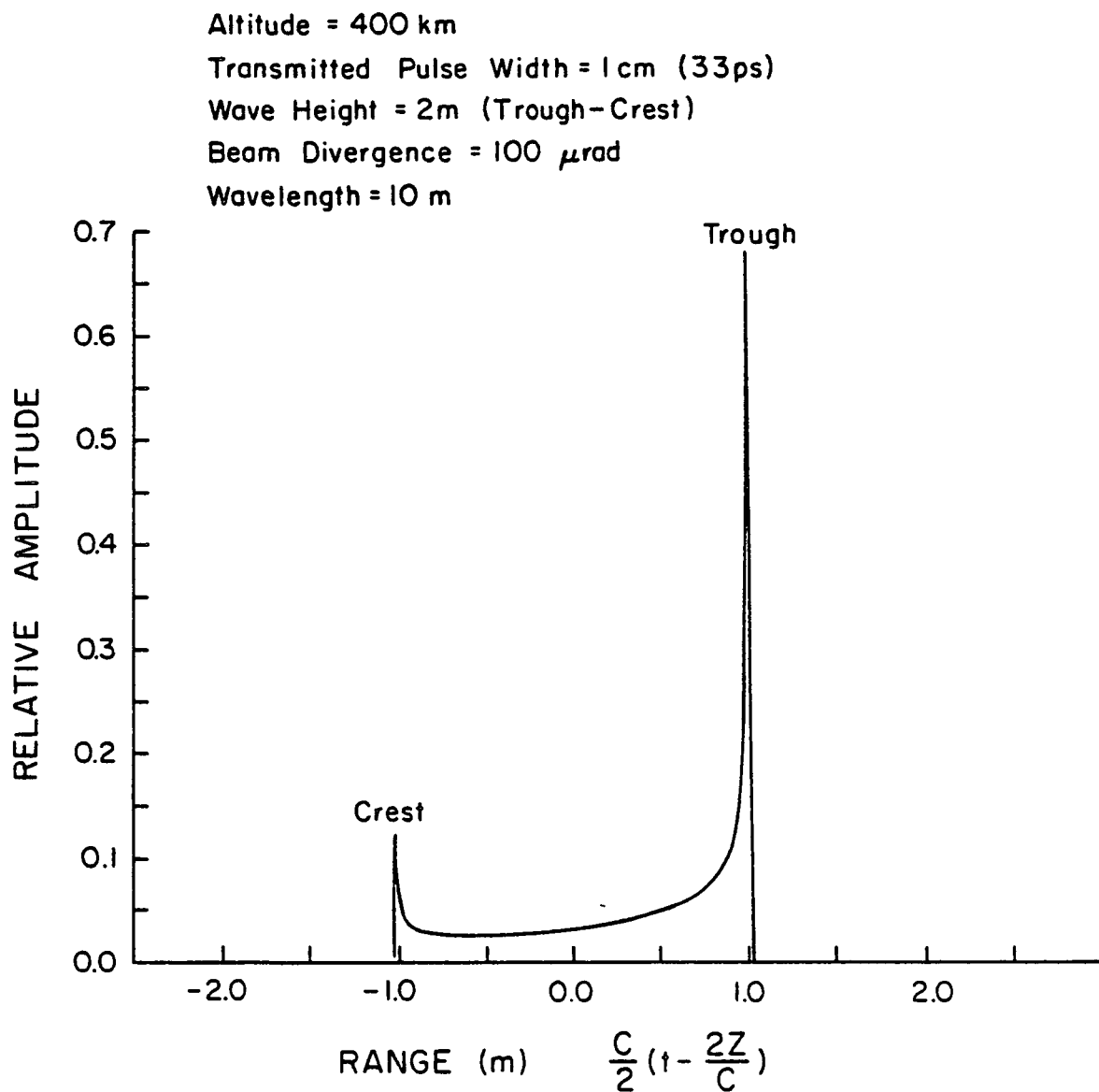


Figure 3.7. Mean received pulse shape from reflection from a trochoidal wave with a height of 2 m (trough-crest). The laser altimeter is at an altitude of 400 km.

4. TIME-RESOLVED SPECKLE

4.1. Introduction

For pressure measurements over the ocean, the ocean surface is the ranging target. Since the ocean surface is rough on the optical scale, the reflected laser pulses are corrupted by speckle. In this chapter, we study the statistical properties of speckle and its effects on the ranging accuracies of laser altimeters. The results not only are important to the pressure measurement technique, but also have applications in general laser radar and ranging.

Since the first discovery of the laser speckle phenomenon, there have been many studies treating its statistical properties. However, these studies have been either for CW laser illumination [10], [11], or for a pulsed laser where the width of the received pulse is comparable to the correlation length of the speckle-induced fluctuations [12]. This latter case applies when the reflecting surface, or target, is rough on the optical scale but has a range spread which is much smaller than the laser pulse width. The speckle causes random fluctuations of the total received energy and is an important noise phenomenon in target detection.

With the advent of mode-locking and Q-switching technologies, laser pulses of a few picoseconds in durations are common today. The narrowness of the transmitted pulse promises higher accuracies in applications like remote sensing and ranging. In practice, most targets will have range spreads that far exceed the width of the laser pulse. Such would be the case for reflections of short laser pulses from airplanes, the ocean surface and the ground. The received pulse will be broadened to about twice the range spread of the target. The pulse shape is related to the geometry

of the target. In this case, the received pulse has a width longer than the correlation length of the speckle-induced fluctuations. As a consequence, speckle will cause random small-scale fluctuations within the received pulse which distort its shape. Similar phenomena can also occur for extended flat diffused targets, where the broadening of the received pulse is due to the wavefront curvature of the laser beam and for continuously distributed targets in the atmosphere. A computer-generated example of a speckle distorted pulse is shown in Fig. 4.1. This phenomenon is referred to as time-resolved speckle.

For applications like target identification and remote sensing of sea states [4], the waveform of the received pulse is used to characterize the target. Therefore, knowledge of the statistics of time-resolved speckle is important. In some other applications such as laser ranging and the pressure measurement technique considered in Chapter 2, estimation of the arrival time of the returned pulse in the presence of time-resolved speckle is the problem.

In this chapter, we first derive the statistics of the detected signal. Then the problem of estimating the arrival time of laser pulse in the presence of time resolved speckle is considered. In Section 4.5, we study partially developed time-resolved speckle. A specific example is treated to illustrate the approach taken in the analysis.

4.2. Statistics of the Detected Signal

In this section, the statistical properties of the detected signal for laser pulses that have been reflected from a diffuse target are considered. The results are derived for a direct detection-type receiver system, which consists of a receiving telescope followed by a photodetector.

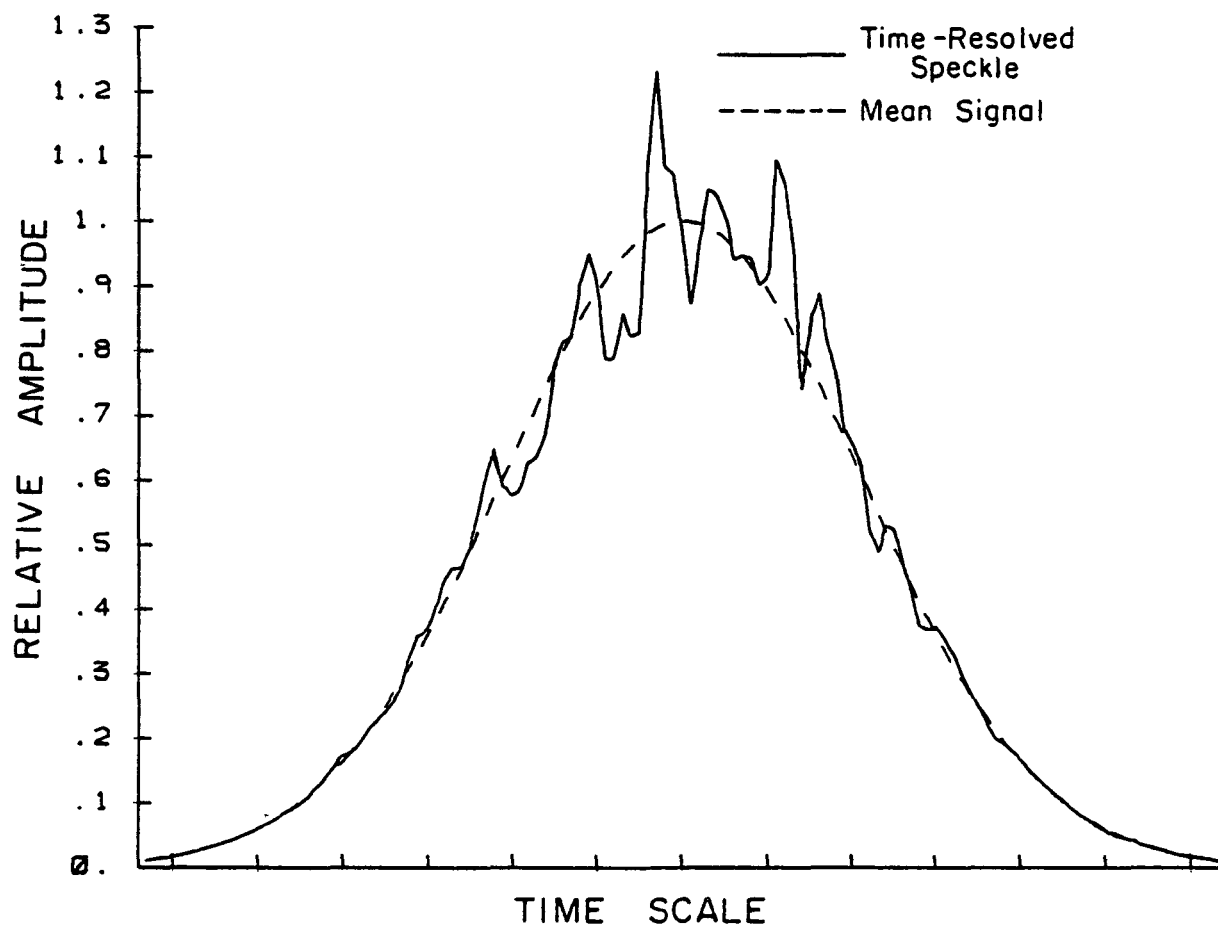


Figure 4.1. Example of time-resolved speckle.

Let the observation interval be $(0, T)$ and the observations be the photoelectron counts in N time bins each with width τ_0 . The observations will be denoted by the photoelectron count vector \vec{k} , and

$$\vec{k} = (k_1, k_2, \dots, k_N) \quad , \quad (4.1)$$

where k_i is the photoelectron count within the i^{th} time bin.

The statistics of k_i are related to the signal field $a_s(\underline{r}, t)$ received over the past τ_0 seconds. Within the i^{th} time bin, the signal energy received by the system is

$$W_i = \int_{(i-1)\tau_0}^{i\tau_0} dt \int_{A_R} d^2\underline{r} |a_s(\underline{r}, t)|^2 \quad , \quad (4.2)$$

where we have assumed a simple aperture weighting function, which takes on the value 1 inside the aperture and 0 outside the aperture. A_R is the receiver aperture area. For reflections from a diffuse target, $a_s(\underline{r}, t)$ follows circular complex Gaussian statistics [10].

We can also write W_i as an infinite sum by performing a modal decomposition on the received field $a_s(\underline{r}, t)$. Using the Karhunen-Loève expansion, we have

$$a_s(\underline{r}, t) = \sum_{m=1}^{\infty} \alpha_m^i \psi_m^i(\underline{r}, t) \quad , \quad (i-1)\tau_0 < t \leq i\tau_0 \quad (4.3)$$

where $\{\psi_m^i\}$ form a complete orthonormal set of basis functions, and α_m^i 's are uncorrelated. Since $a_s(\underline{r}, t)$ has circular complex Gaussian statistics, the coefficients α_m^i 's are circular complex Gaussian variables, which implies that they are independent.

By substituting Eq. (4.3) into Eq. (4.2) and making use of the orthonormal properties of ψ_m^i 's, we have

$$W_i = \sum_{m=1}^{\infty} |\alpha_m^i|^2 . \quad (4.4)$$

This shows that the signal energy received within the i^{th} time bin consists of contributions from infinitely many modes. The energy associated with each mode obeys the negative exponential distribution and is independent of the energies of the other modes. In the absence of photodetector saturation, the following relation holds:

$$k_i = \sum_{m=1}^{\infty} n_m^i , \quad (4.5)$$

where n_m^i is the photoelectron count in the i^{th} bin due to the m^{th} mode.

The distribution of n_m^i when conditioned on $|\alpha_m^i|^2$ is Poisson, and since $|\alpha_m^i|^2$ is negative exponentially distributed, n_m^i is a Bose'-Einstein variable. The probability density function of k_i is then the infinite convolution of the probability density functions of n_m^i , i.e.,

$$p(k_i) = p(n_1^i) * p(n_2^i) * \dots . \quad (4.6)$$

Evaluation of Eq. (4.6) involves solving the eigen equation and carrying out the infinite convolution. Simplifications are possible with some approximations.

For the i^{th} time bin, the observation volume, which is the outer product of the receiver aperture area with the time interval, can be regarded as consisting of M_i subvolumes or correlation cells [10], [13], with the energy density being approximately constant within each cell and statistically independent of the energy densities of all other cells. The energy associated with each correlation cell is assumed to obey the negative exponential distribution, with the mean energy in each subvolume taken to be the same. This is equivalent to assuming the solutions of the eigen

equation in the Karhunen-Loève expansion have only M_1 non-zero eigenvalues, each of the same value [14], [15]. It turns out that for a simple aperture weighting function, this is a reasonable assumption [10].

Under the above assumptions, the energy W_1 received during the i^{th} time bin is gamma distributed, obeying the probability density function

$$p(W_1) = \frac{1}{\Gamma(M_1) \bar{W}_1} \left(M_1 \frac{W_1}{\bar{W}_1} \right)^{M_1} \exp \left[-M_1 \frac{W_1}{\bar{W}_1} \right], \quad (4.7)$$

where \bar{W}_1 is the mean value of the signal energy in the i^{th} bin W_1 .

Mathematically, this is nothing more than matching the actual probability density function of W_1 with a gamma density function. Since in practice, we will only be able to calculate the first and second moments of the intensity of the received signal, the most natural and simple way to choose the parameters of the approximating gamma density function is to match the mean and variance with the actual values.

The expressions for the mean and variance of W_1 can be obtained by using Eq. (4.2) together with the properties of the circular complex Gaussian fields; the results are [4], [6]

$$\bar{W}_1 = \int_{(i-1)\tau_0}^{i\tau_0} dt \int_{A_R} d^2 \underline{r} J_a(\underline{r}, t; \underline{r}, t) \quad (4.8)$$

and

$$\text{var}(W_1) = \int_{(i-1)\tau_0}^{i\tau_0} dt_1 \int_{(i-1)\tau_0}^{i\tau_0} dt_2 \int_{A_R} d^2 \underline{r}_1 \int_{A_R} d^2 \underline{r}_2 |J_a(\underline{r}_1, t_1; \underline{r}_2, t_2)|^2, \quad (4.9)$$

where J_a is the mutual coherence function of the received field.

For reflections from diffuse targets, the mutual coherence function can be calculated using the Fresnel reflection formula together with the

properties of the circular complex Gaussian fields; the results are [4], [6]

$$\int_{A_R} d^2 \underline{r} J_a(\underline{r}, t; \underline{r}, t) = Q \int d^2 \underline{\rho} b_2(\underline{\rho}, z) |f(t - \psi)|^2 \quad (4.10)$$

and

$$\begin{aligned} \int_{A_R} d^2 \underline{r}_1 \int_{A_R} d^2 \underline{r}_2 |J_a(\underline{r}_1, t_1; \underline{r}_2, t_2)|^2 \\ = \frac{Q^2}{K} \int d^2 \underline{\rho} b_4(\underline{\rho}, z) |f(t_1 - \psi)|^2 |f(t_2 - \psi)|^2, \end{aligned} \quad (4.11)$$

where Q is the expected received energy per pulse. The remaining variables were defined previously in Chapter 3.

For a Gaussian shape transmitted pulse intensity with rms width σ_f , we have the following simplified results,

$$\int_{A_R} d^2 \underline{r} J_a(\underline{r}, t; \underline{r}, t) = Q F_1(t) \quad (4.12)$$

and

$$\int_{A_R} d^2 \underline{r}_1 \int_{A_R} d^2 \underline{r}_2 |J_a(\underline{r}_1, t_1; \underline{r}_2, t_2)|^2 = Q^2 K^{-1} G(\sqrt{2} \sigma_f, t_1 - t_2) F_2\left(\frac{t_1 + t_2}{2}\right), \quad (4.13)$$

where

$$F_1(t) = \int d^2 \underline{\rho} b_2(\underline{\rho}, z) G(\sigma_f, t - \psi), \quad (4.14)$$

$$F_2(t) = \int d^2 \underline{\rho} b_4(\underline{\rho}, z) G\left(\frac{\sigma_f}{\sqrt{2}}, t - \psi\right), \quad (4.15)$$

$$G(\sigma, t) = \frac{1}{\sqrt{2\pi} \sigma} \exp\left[-\frac{t^2}{2\sigma^2}\right]. \quad (4.16)$$

$F_1(t)$ is the mean received pulse shape and $F_2(t)$ is the waveform of the variance of the received signal. Both are functions of the target.

By substituting Eq. (4.12) into Eq. (4.8) and making the assumption that τ_0 is much smaller than the width of $F_1(t)$, we have

$$\bar{W}_1 = Q F_1(i\tau_0) \tau_0. \quad (4.17)$$

The variance of W_1 can be calculated from Eqs. (4.9) and (4.13)

$$\begin{aligned} \text{var}(W_1) &= \frac{Q^2}{K} \int_{(i-1)\tau_0}^{i\tau_0} dt_1 \int_{(i-1)\tau_0}^{i\tau_0} dt_2 G(\sqrt{2}\sigma_f, t_1 - t_2) F_2\left(\frac{t_1 + t_2}{2}\right) \\ &= \frac{Q^2}{K} \left\{ \int_0^{\tau_0} dT_1 G(\sqrt{2}\sigma_f, T_1) \int_{(i-1)\tau_0 + \frac{T_1}{2}}^{i\tau_0 - \frac{T_1}{2}} dT_2 F_2(T_2) \right. \\ &\quad \left. + \int_{-\tau_0}^0 dT_1 G(\sqrt{2}\sigma_f, T_1) \int_{(i-1)\tau_0 - \frac{T_1}{2}}^{i\tau_0 + \frac{T_1}{2}} dT_2 F_2(T_2) \right\}, \quad (4.18) \end{aligned}$$

where we made the following changes of variables:

$$T_1 = t_1 - t_2 \quad (4.19)$$

and

$$T_2 = (t_1 + t_2)/2. \quad (4.20)$$

Assuming the width of $F_2(t)$ is long compared with τ_0 , and τ_0 is large compared with σ_f , we have

$$\begin{aligned} \text{var}(W_1) &= \frac{Q^2}{K} F_2(i\tau_0) 2 \left\{ \int_0^{\tau_0} dT_1 G_1(\sqrt{2}\sigma_f, T_1) (\tau_0 - T_1) \right\} \\ &= \frac{Q^2}{K} F_2(i\tau_0) 2 \left\{ \frac{\tau_0}{2} \text{erf}\left(\frac{\tau_0}{2\sigma_f}\right) - \frac{\sigma_f}{\sqrt{\pi}} \left(1 - e^{-\frac{\tau_0^2}{4\sigma_f^2}} \right) \right\} = \frac{Q^2}{K} F_2(i\tau_0) \tau_0. \quad (4.21) \end{aligned}$$

Finally, the parameter M_1 of the gamma density function can be obtained by matching the degree of freedom of the gamma density function with the signal-to-noise ratio,

$$M_1 = \frac{\overline{W_1^2}}{\text{Var}(W_1)} = \frac{KF_1^2(1\tau_0)}{F_2(1\tau_0)} \tau_0 \quad (4.22)$$

M_1 will be referred to as the number of speckle correlation cells in the i^{th} time bin.

If the laser footprint is uniform, or if the target is small compared to the laser footprint and the width of the transmitted laser pulse is small compared to the range spread of the target, $F_1(t)$ and $F_2(t)$ given by Eqs. (4.14) and (4.15) are approximately equal and we have

$$M_1 \cong K F_1(1\tau_0) \tau_0 \quad (4.23)$$

Since $F_1(1\tau_0) \tau_0 < 1$, M_1 is always smaller than K . Equation (4.23) is not a good approximation of Equation (4.22) in the leading and trailing edges of the received pulse where it could predict values of M_1 smaller than one. M_1 should always be greater than one.

For the case when the receiver can not resolve the return waveform so only the energy of the received pulse is observed, the number of speckle correlation cells is simply K [12]. For a target with large-range spread, only part of the target area is illuminated within one time bin and the area available for interference is smaller. As a consequence, the size of the speckle is larger and M_1 is smaller than K .

Since W_1 is gamma distributed with parameter M_1 , the distribution of k_1 can be shown to have a probability density function given by [12]

$$p(k_i) = \frac{\Gamma(k_i + M_i)}{\Gamma(k_i + 1)\Gamma(M_i)} \left(1 + \frac{M_i}{k_i}\right)^{-k_i} \left(1 + \frac{\bar{k}_i}{M_i}\right)^{-M_i} . \quad (4.24)$$

Here

$$\bar{k}_i = \eta \bar{W}_i / h\nu = \langle N \rangle F_1(i\tau_0)\tau_0 , \quad (4.25)$$

η is the quantum efficiency of the photodetector and $\langle N \rangle$ is the expected number of photoelectrons per pulse. When M_i is an integer, Eq. (4.24) is the negative binomial density function.

For most laser receivers τ_0 is longer than the transmitted pulse width. For this case, the photoelectron counts from different time bins are statistically independent. The joint density function of \vec{k} is then

$$p(\vec{k}) = \prod_{i=1}^N p(k_i) . \quad (4.26)$$

This equation forms the basis for the analysis on receiver timing in Section 4.3.

We will look at some specific target configurations. The first example is an extended flat diffuse target that covers the entire laser footprint. For simplicity, we assume the target to have uniform reflectivity. This is a good model for reflections from the ground, sands or walls of large buildings. In this case, the broadening of the received pulse is due to the curvature effects of the laser beam.

Assuming a Gaussian laser cross section with a radius σ_i (exp(-1/2) point), we have

$$K = \pi A_R \left[\frac{2\sigma_i}{\lambda z} \right]^2 . \quad (4.27)$$

For normal incidence, the mean and variance of W_i can be calculated to give

$$\overline{W}_1 = \frac{Qcz\tau_o}{4\sigma_1^2} \exp\left[\frac{c^2 z^2 \sigma_f^2}{8\sigma_1^4} - \frac{czi\tau_o}{2\sigma_1^2}\right] \operatorname{erfc}\left[\frac{cz\sigma_f}{2\sqrt{2}\sigma_1^2} - \frac{i\tau_o}{\sqrt{2}\sigma_f}\right] \quad (4.28)$$

and

$$\operatorname{var}(W_1) = \frac{Q^2 cz\tau_o}{2K\sigma_1^2} \exp\left[\frac{c^2 z^2 \sigma_f^2}{4\sigma_1^4} - \frac{czi\tau_o}{\sigma_1^2}\right] \operatorname{erfc}\left[\frac{cz\sigma_f}{2\sigma_1^2} - \frac{i\tau_o}{\sigma_f}\right]. \quad (4.29)$$

Equations (4.28) and (4.29) are plotted in Figs. 4.2 and 4.3 for three different laser beam divergence angles. The number of speckle cells in the i^{th} time bin is given by

$$M_i = \frac{Kcz\tau_o}{8\sigma_1^2} \operatorname{erfc}^2\left[\frac{cz\sigma_f}{2\sqrt{2}\sigma_1^2} - \frac{i\tau_o}{\sqrt{2}\sigma_f}\right] / \operatorname{erfc}\left[\frac{cz\sigma_f}{2\sigma_1^2} - \frac{i\tau_o}{\sigma_f}\right], \quad (4.30)$$

which is plotted in Fig. 4.4. The figure shows that M_i starts increasing when the leading edge of the laser pulse illuminates the target; it remains constant after the trailing edge of the pulse arrives at the target. This can be seen from the formula of M_i shown in Eq. (4.30). When the entire pulse illuminates the target, i is large and M_i is approximately given by

$$M_i \cong \frac{\pi A_R c \tau_o}{\lambda^2 z}, \quad (4.31)$$

which is constant with time. Equation (4.31) does not depend on σ_1 , so the curves of M_i in Fig. 4.4 for three different beam divergence angles coincide with each other.

For non-normal incidence, additional broadening due to the tilt of the target dominates the pulse shape. Neglecting the curvature effects, we find both the mean and variance of W_1 to be Gaussian in shape; they are

Time Bin Width = 1 cm
Target Distance = 500 km
Receiver Aperture Area = 100 cm²
Laser Wavelength = 1064 nm

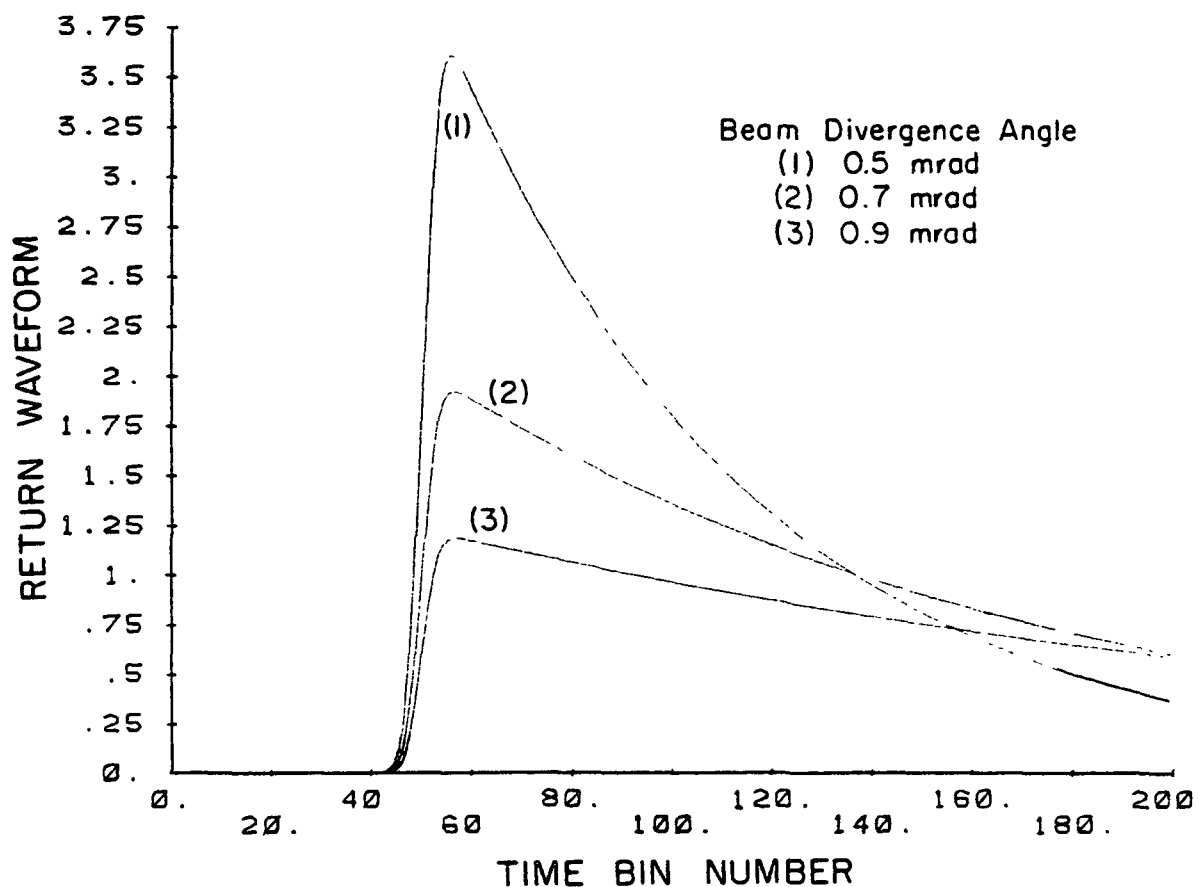


Figure 4.2. Mean received pulse shape for reflection from an infinite flat diffuse target. Normal incidence. Magnitude scale is relative.

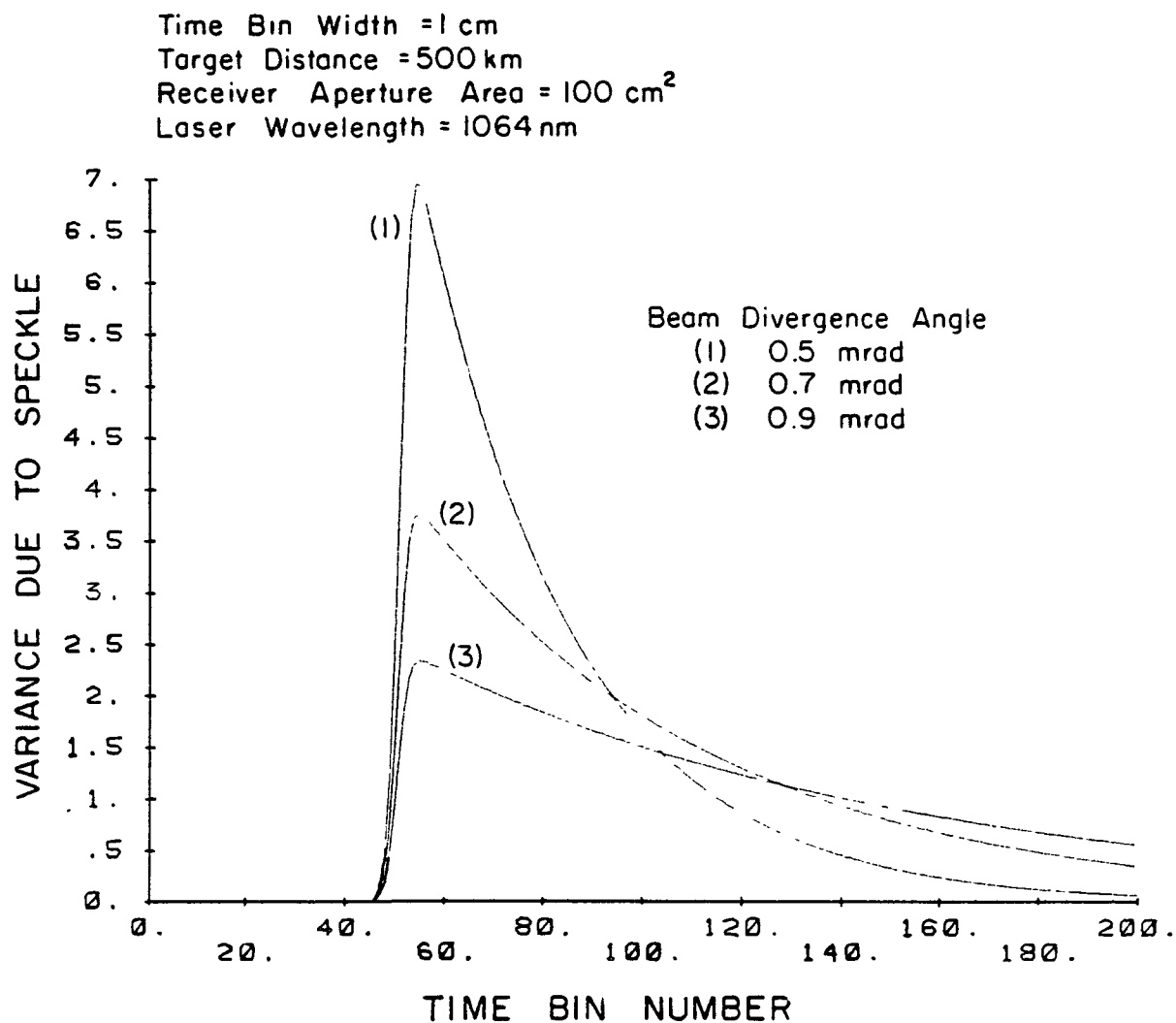


Figure 4.3. Waveform of the variance for reflection from an infinite flat diffuse target. Normal incidence. Magnitude scale is relative.

Time Bin Width = 1 cm
Target Distance = 500 km
Receiver Aperture Area = 100 cm²
Laser Wavelength = 1064 nm

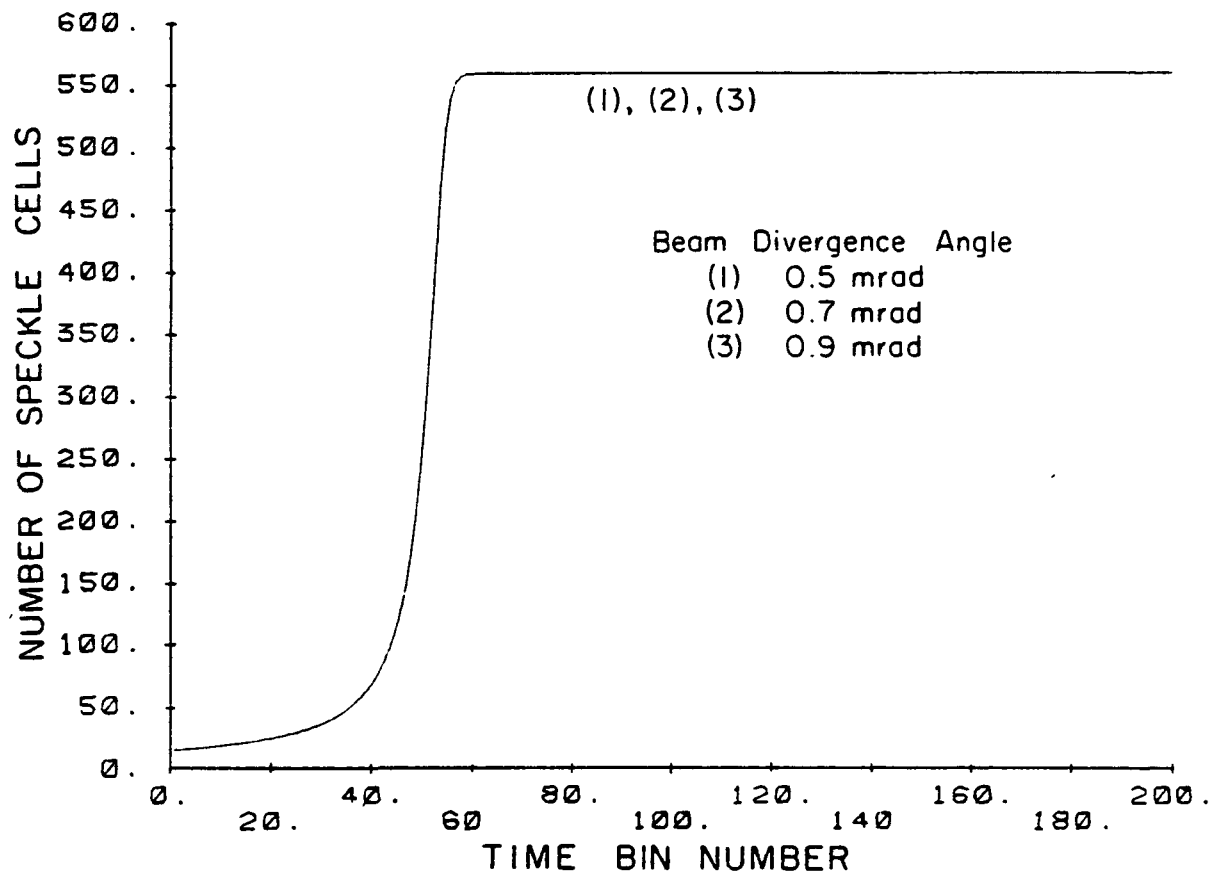


Figure 4.4. Number of speckle correlation cells for reflection from an infinite flat diffuse target. Normal incidence.

plotted in Figs. 4.5 and 4.6. M_i is plotted in Fig. 4.7. M_i is constant in time.

The next target we consider is a finite size flat plate. The geometry of the target is shown in Fig. 4.8. The face of the plate is not normal to the incident beam, instead, the plate is slanted with an angle θ and, therefore, has a non-zero range spread equal to the length of the plate times $\sin \theta$. This model can represent reflections from roofs, billboards or one facet of a vehicle.

We shall assume the center of the plate is situated at the center of the laser footprint. For a rectangular plate of size ℓ m long by h m wide, the mean and variance of W_i can be calculated to give

$$\begin{aligned} \bar{W}_i = & \frac{Qc\tau_0}{\left\{ 4\sqrt{2\pi} \tan \theta \sigma_i \operatorname{erf} \left[\frac{\ell \cos \theta}{2\sqrt{2} \sigma_i} \right] \sqrt{1 + \frac{c^2 \sigma_f^2}{4 \tan^2 \theta \sigma_i^2}} \right\}} \\ & \cdot \exp \left[-\frac{(i\tau_0)^2}{2\sigma_f^2} \left(1 - \frac{1}{1 + \frac{c^2 \sigma_f^2}{4 \tan^2 \theta \sigma_i^2}} \right) \right] \\ & \cdot \left\{ \operatorname{erf} \left(\frac{i\tau_0}{\sqrt{2} \sigma_f \sqrt{1 + \frac{c^2 \sigma_f^2}{4 \tan^2 \theta \sigma_i^2}}} + \frac{\ell \sin \theta \sqrt{1 + \frac{c^2 \sigma_f^2}{4 \tan^2 \theta \sigma_i^2}}}{\sqrt{2} c \sigma_f} \right) \right. \\ & \left. - \operatorname{erf} \left(\frac{i\tau_0}{\sqrt{2} \sigma_f \sqrt{1 + \frac{c^2 \sigma_f^2}{4 \tan^2 \theta \sigma_i^2}}} - \frac{\ell \sin \theta \sqrt{1 + \frac{c^2 \sigma_f^2}{4 \tan^2 \theta \sigma_i^2}}}{\sqrt{2} c \sigma_f} \right) \right\} \quad (4.32) \end{aligned}$$

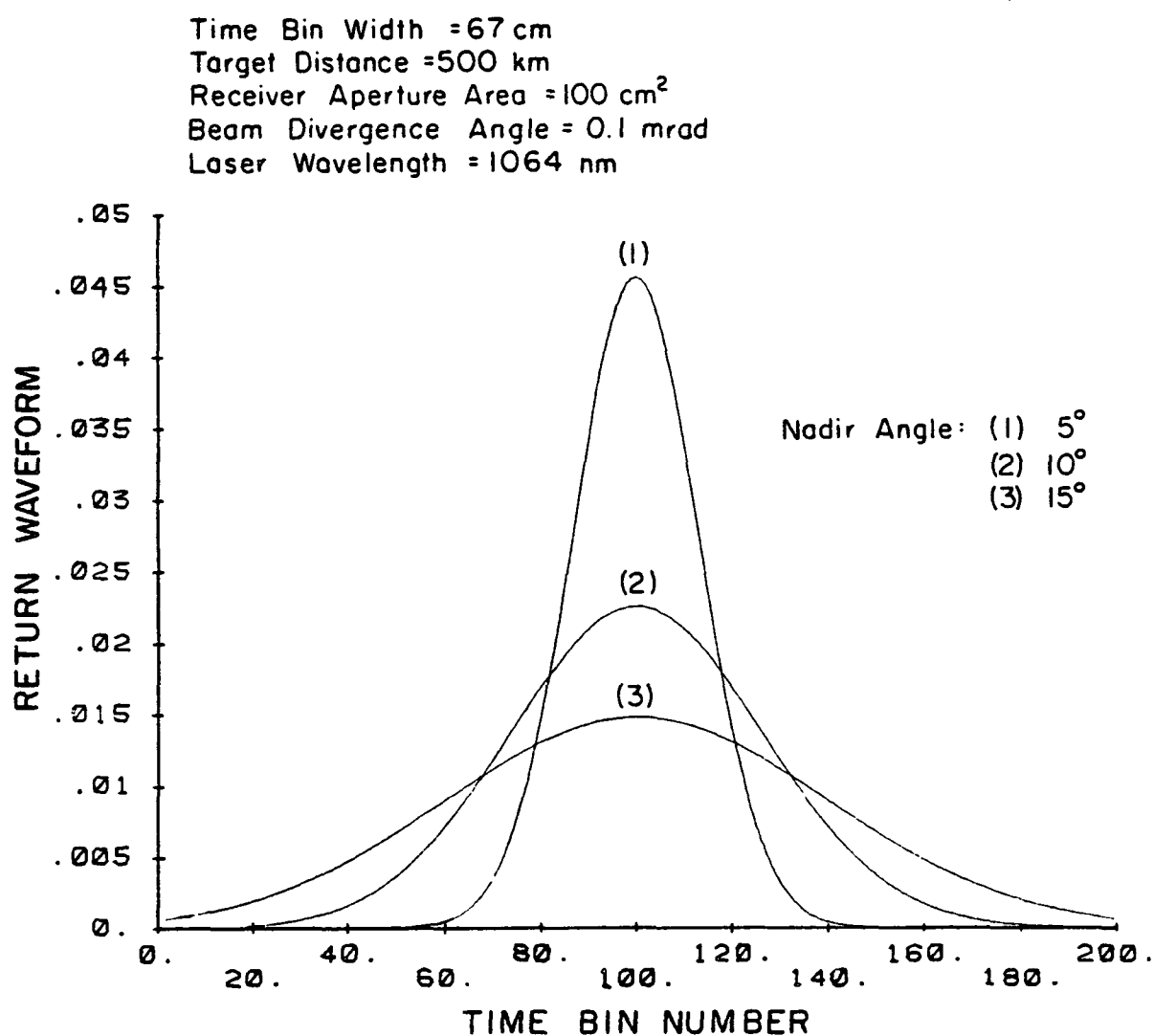


Figure 4.5. Mean received pulse shape for reflection from an infinite flat diffuse target. Non-normal incidence. Magnitude scale is relative.

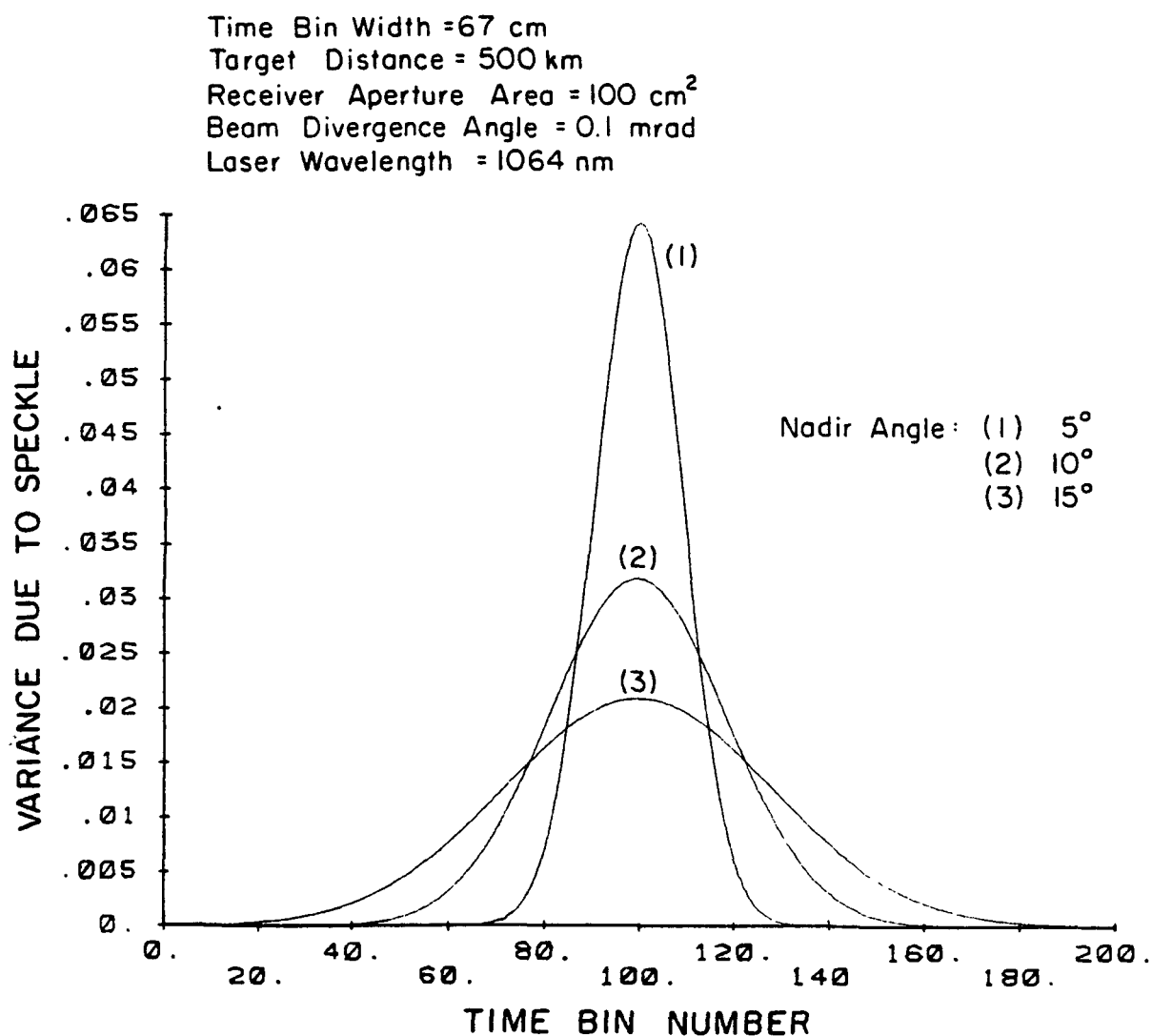


Figure 4.6. Waveform of the variance for reflection from an infinite flat diffuse target. Non-normal incidence. Magnitude scale is relative.

Time Bin Width = 67 cm
Target Distance = 500 km
Receiver Aperture = 100 cm²
Beam Divergence Angle = 0.1 mrad
Laser Wavelength = 1064 nm

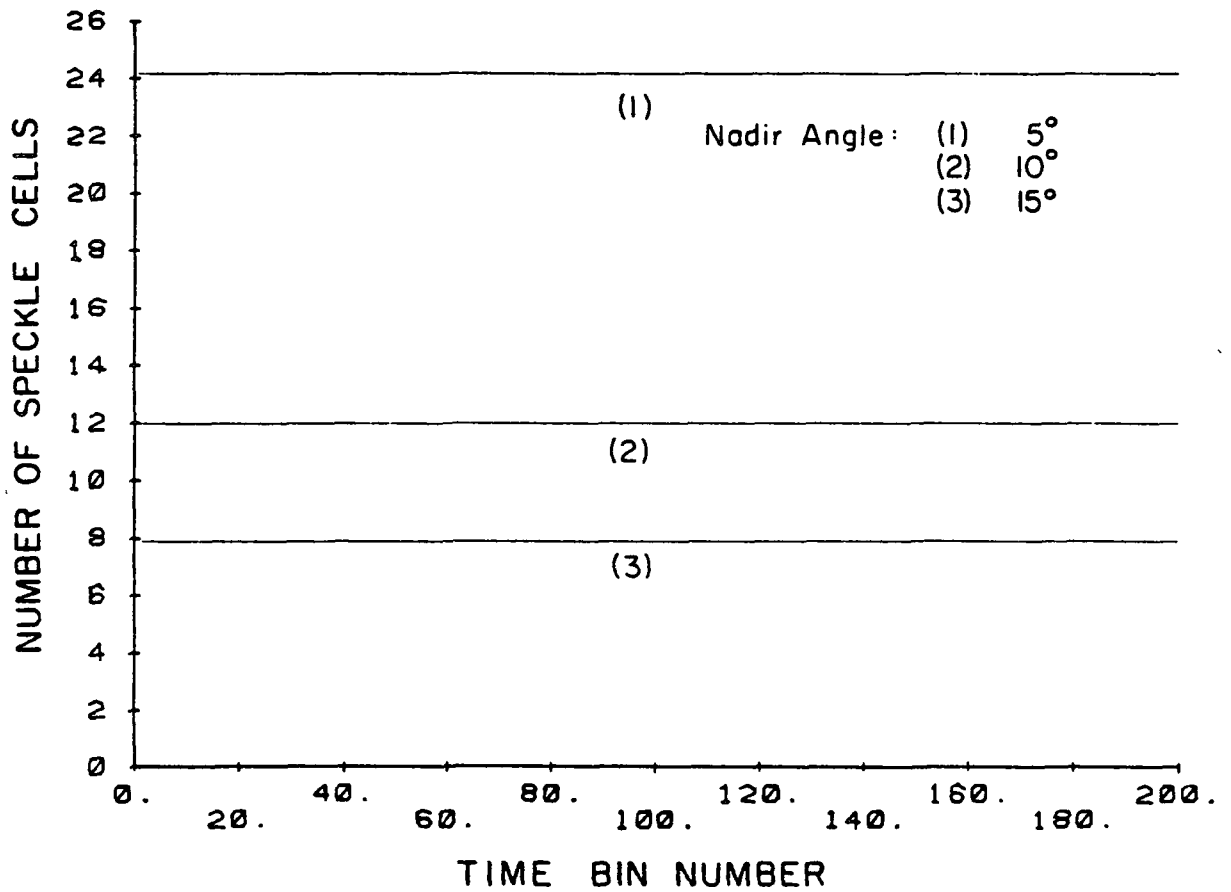


Figure 4.7. Number of speckle correlation cells for reflection from an infinite flat diffuse target. Non-normal incidence.

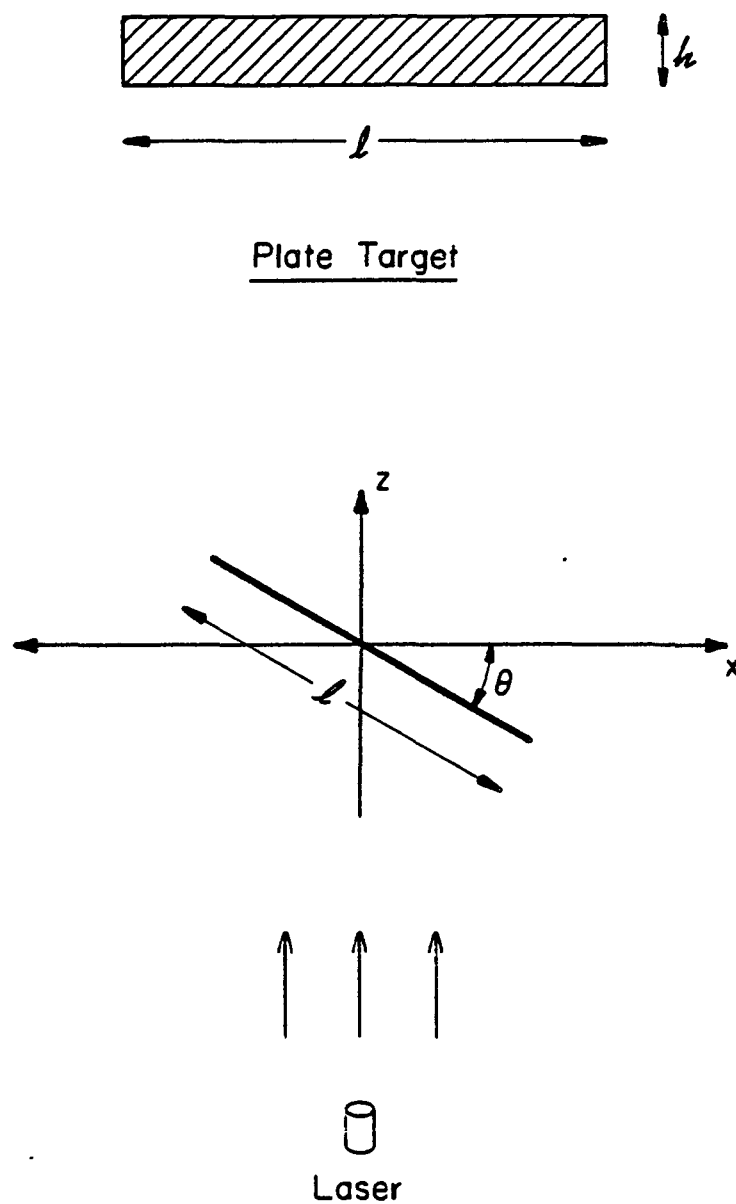


Figure 4.8. Geometry of the finite size plate target.

and

$$\begin{aligned}
 \text{var}(W_1) = & \frac{Q^2 \tau_o}{K \sqrt{\pi} \sigma_i \sigma_f \text{erf} \left[\frac{l \cos \theta}{2 \sigma_i} \right] \sqrt{\frac{4}{\sigma_i^2} + \frac{16 \tan^2 \theta}{c^2 \sigma_f^2}}} \\
 & \cdot \exp \left[-\frac{(i \tau_o)^2}{\sigma_f^2} \left(1 - \frac{1}{1 + \frac{c^2 \sigma_f^2}{4 \tan^2 \theta \sigma_i^2}} \right) \right] \\
 & \left\{ \text{erf} \left(\frac{i \tau_o}{\sigma_f \sqrt{1 + \frac{c^2 \sigma_f^2}{4 \tan^2 \theta \sigma_i^2}}} + \frac{l \sin \theta \sqrt{1 + \frac{c^2 \sigma_f^2}{4 \tan^2 \theta \sigma_i^2}}}{c \sigma_f} \right) \right. \\
 & \left. - \text{erf} \left(\frac{i \tau_o}{\sigma_f \sqrt{1 + \frac{c^2 \sigma_f^2}{4 \tan^2 \theta \sigma_i^2}}} - \frac{l \sin \theta \sqrt{1 + \frac{c^2 \sigma_f^2}{4 \tan^2 \theta \sigma_i^2}}}{c \sigma_f} \right) \right\}, \quad (4.33)
 \end{aligned}$$

with K given by

$$K = \frac{A_R 4 \pi \sigma_i^2 \left(\text{erf} \left[\frac{l \cos \theta}{2 \sqrt{2} \sigma_i} \right] \text{erf} \left[\frac{h}{2 \sqrt{2} \sigma_i} \right] \right)^2}{\lambda^2 z^2 \text{erf} \left[\frac{l \cos \theta}{2 \sigma_i} \right] \text{erf} \left[\frac{h}{2 \sigma_i} \right]}. \quad (4.34)$$

When the plate is small compared to the laser footprint, K is simplified to

$$K \cong \frac{A_R 2h \cos \theta}{\lambda^2 z^2}. \quad (4.35)$$

The mean and variance of W_1 are plotted in Figs. 4.9 and 4.10 for three

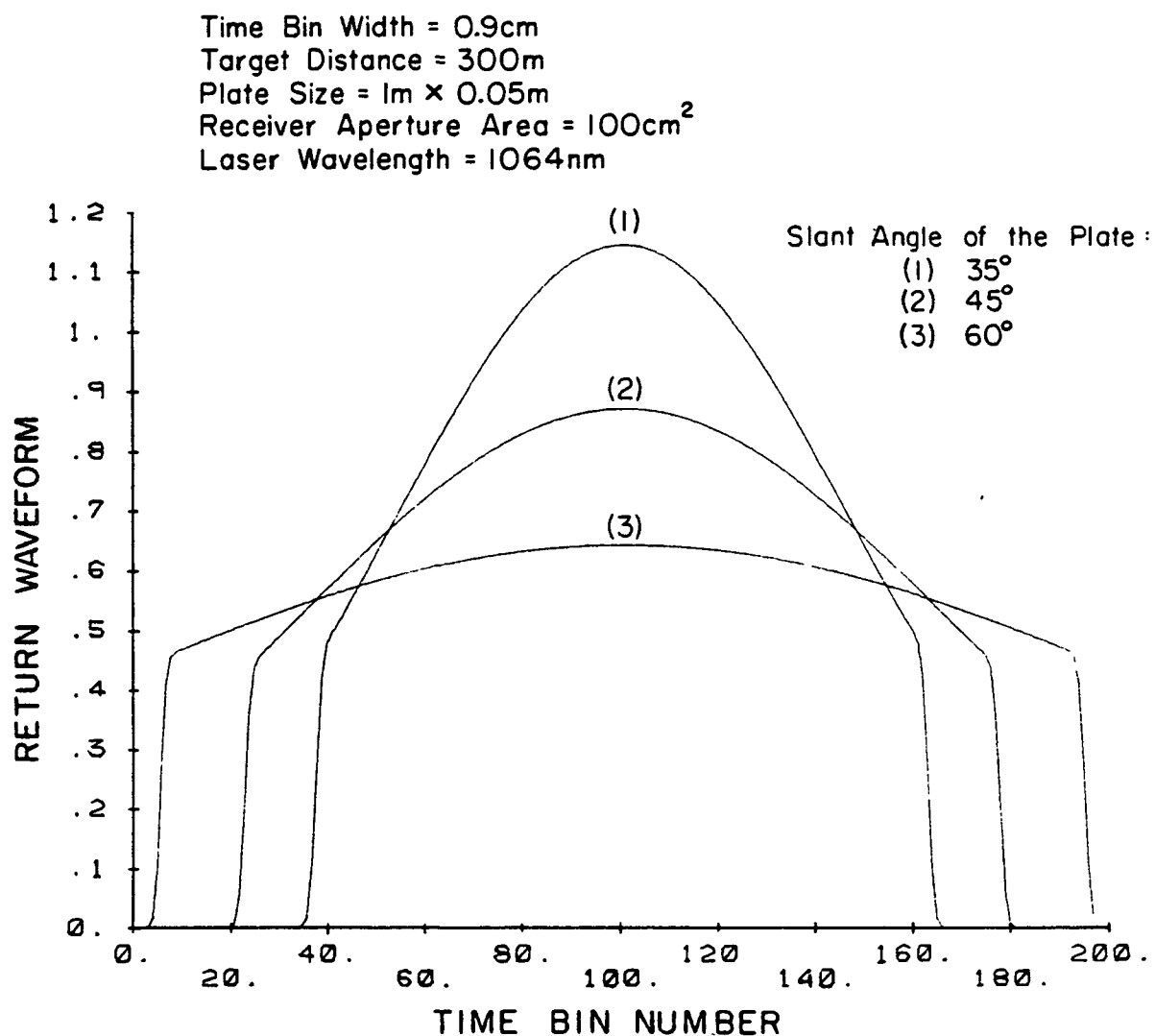


Figure 4.9. Mean received pulse shape for reflection from a finite size plate. Magnitude scale is relative.

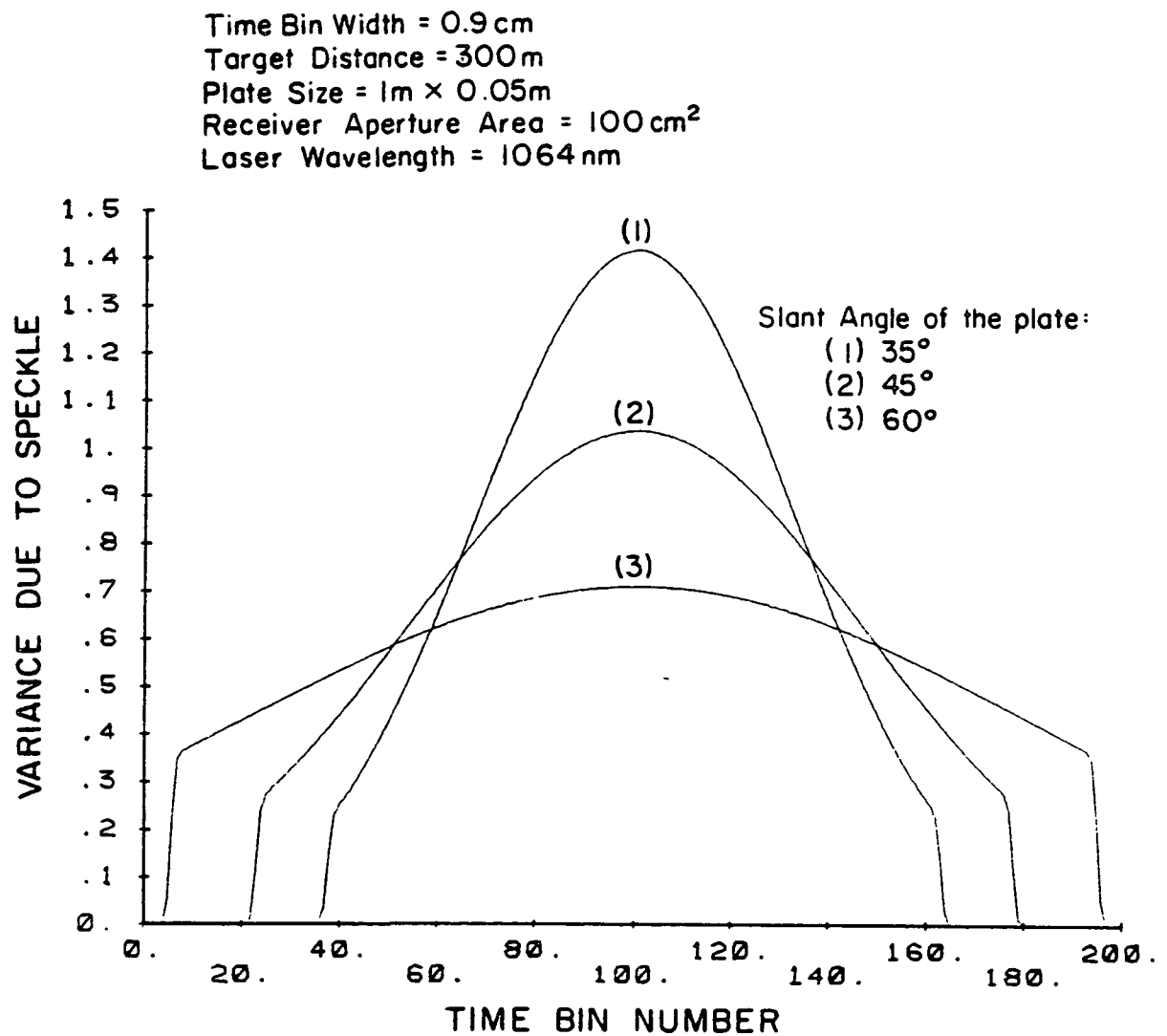


Figure 4.10. Waveform of the variance for reflection from a finite size plate. Magnitude scale is relative.

different slant angles of the plate. The number of speckle cells is plotted in Fig. 4.11. The number of speckle cells starts increasing when the leading edge of the laser pulse illuminates the plate; it reaches a constant value when the trailing edge of the pulse arrives at the plate. The number of speckle cells starts decreasing when the leading edge of the pulse leaves the end of the plate. When the whole laser pulse illuminates the plate, M_1 maintains a constant value given by

$$M_1 = \frac{Kc\tau_o \operatorname{erf}\left[\frac{l \cos \theta}{2\sigma_1}\right]}{4\sqrt{\pi} \tan \theta \sigma_1 \operatorname{erf}^2\left[\frac{l \cos \theta}{2\sqrt{2}\sigma_1}\right]}$$

$$= \frac{\sqrt{\pi} A_R c \tau_o \sigma_1 \operatorname{erf}\left(\frac{h}{2\sqrt{2}\sigma_1}\right)^2}{\lambda^2 z^2 \tan \theta \operatorname{erf}\left(\frac{h}{2\sigma_1}\right)} \quad (4.36)$$

For finite-size targets, the relative sizes of the target and laser footprint are important factors in determining the return pulse shape. For example, if the length of the plate is increased from 1 meter, which is the length of the plate used for Figs. 4.9, 4.10, and 4.11, to 3 meters, the corresponding plots become Figs. 4.12, 4.13, and 4.14, which are similar to the return waveforms from an infinite-size target.

Another target we consider is a Gaussian random surface. This is a good model for reflection of laser pulses from the ocean surface. For negligible curvature effects, the expected received pulse shape is Gaussian [4]. If the transmitted laser pulse is short compared to the surface height variation, $F_1(t)$ and $F_2(t)$ will be approximately equal, and

Time Bin Width = 0.9cm
 Target Distance = 300m
 Plate Size = 1m \times 0.05m
 Receiver Aperture Area = 100cm²
 Laser Wavelength = 1064nm

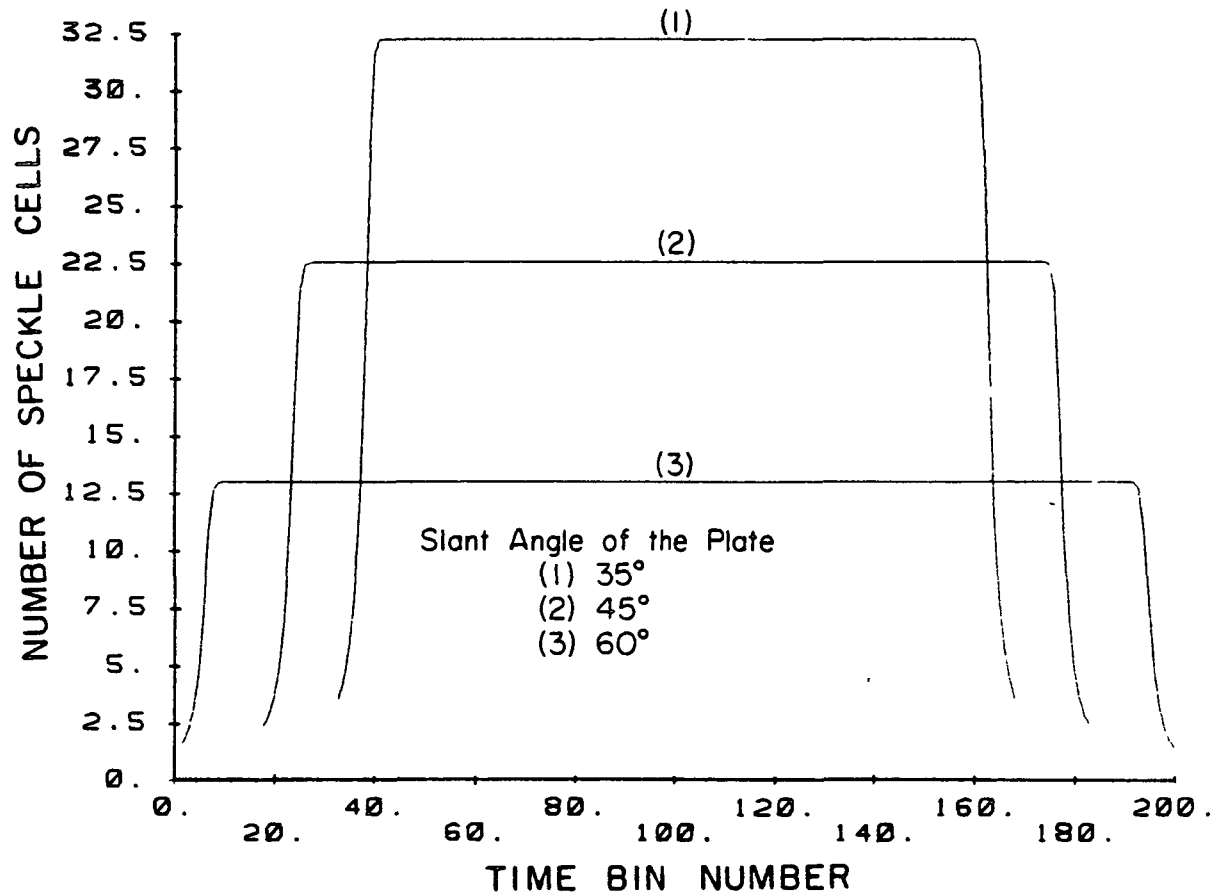


Figure 4.11. Number of speckle correlation cells for reflection from a finite size plate.

Time Bin Width = 2.7cm
Target Distance = 300m
Plate Size = 3m \times 0.05m
Receiver Aperture Area = 100cm²
Laser Wavelength = 1046nm

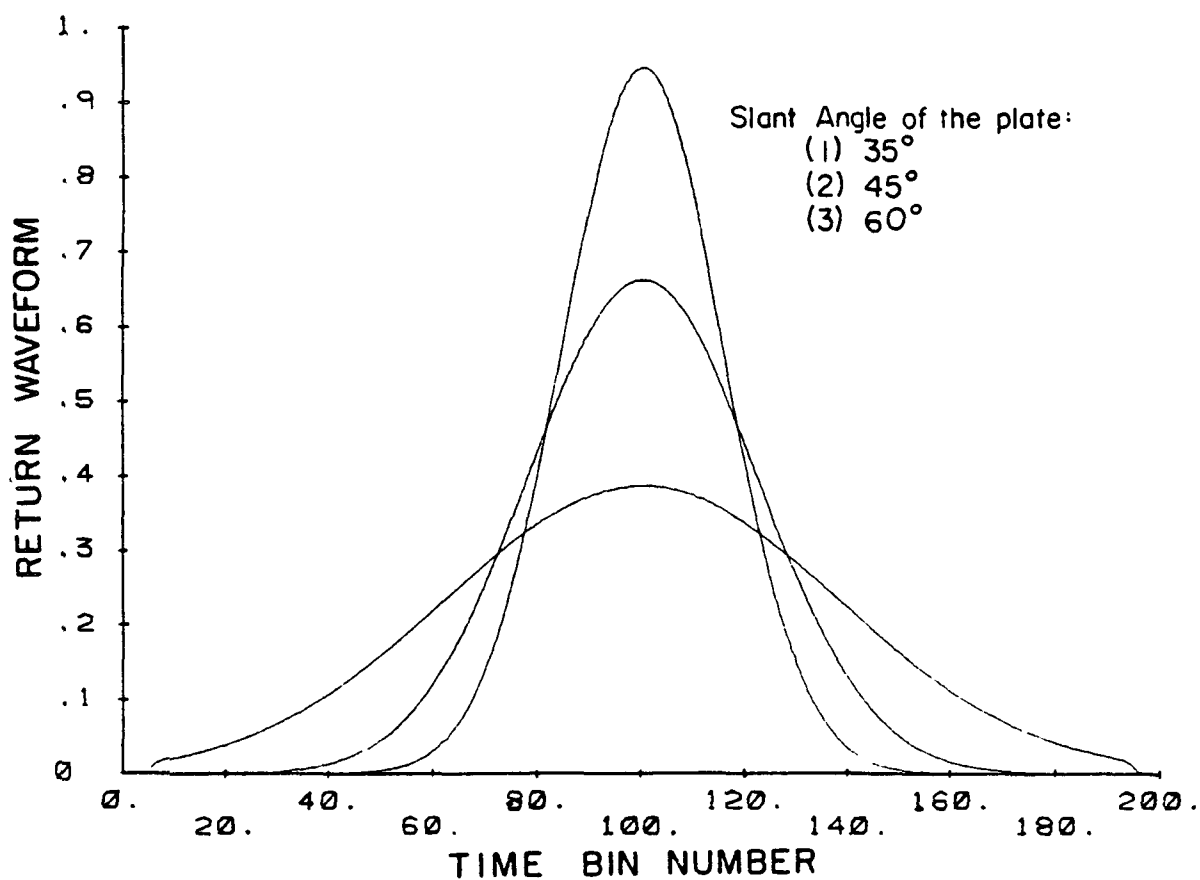


Figure 4.12. Mean received pulse shape for reflection from a finite size plate. Magnitude scale is relative.

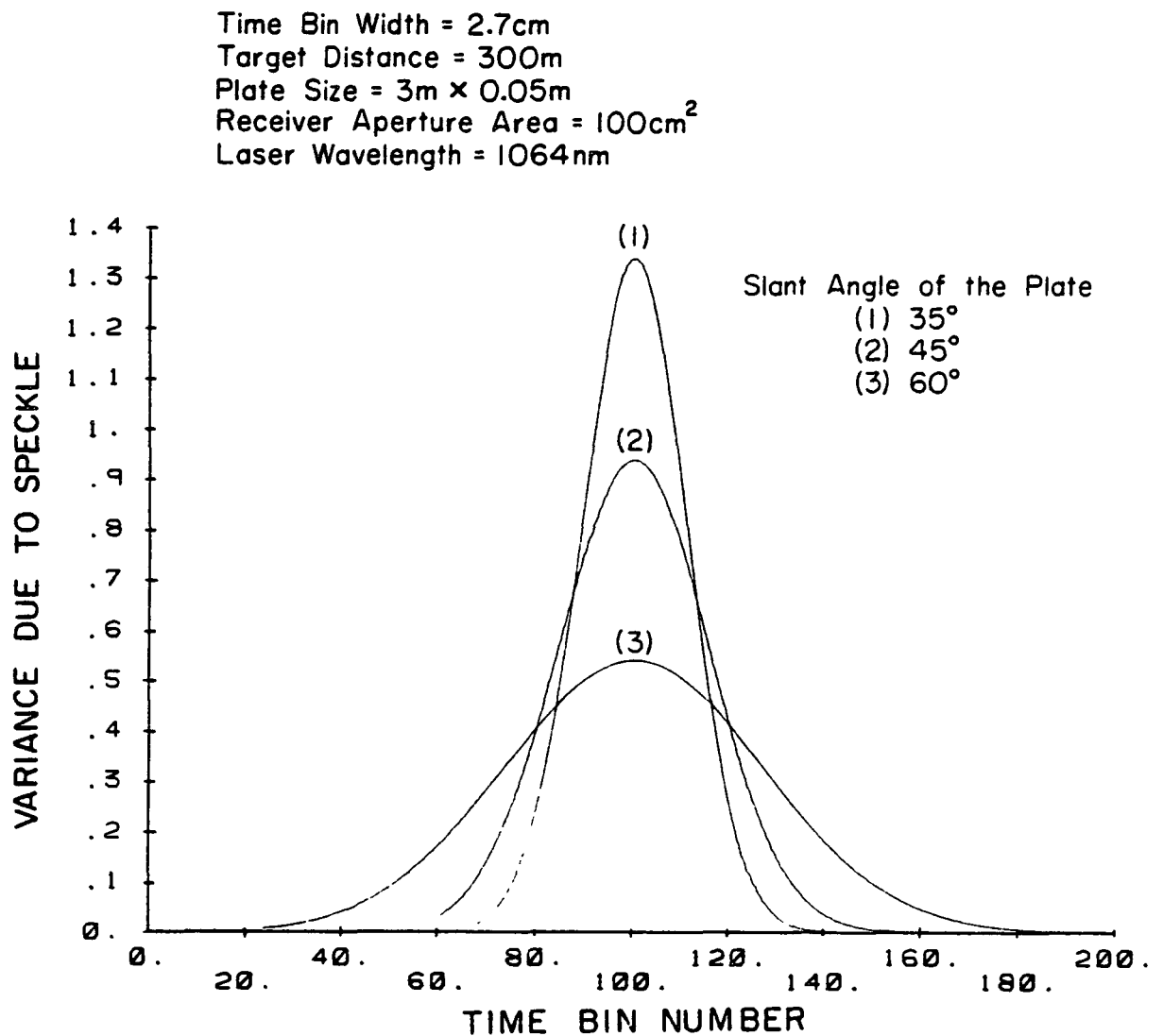


Figure 4.13. Waveform of the variance for reflection from a finite size target. Magnitude scale is relative.

Time Bin Width = 2.7cm
Target Distance = 300m
Plate Size = 3m \times 0.05m
Receiver Aperture Area = 100cm²
Laser Wavelength = 1064nm

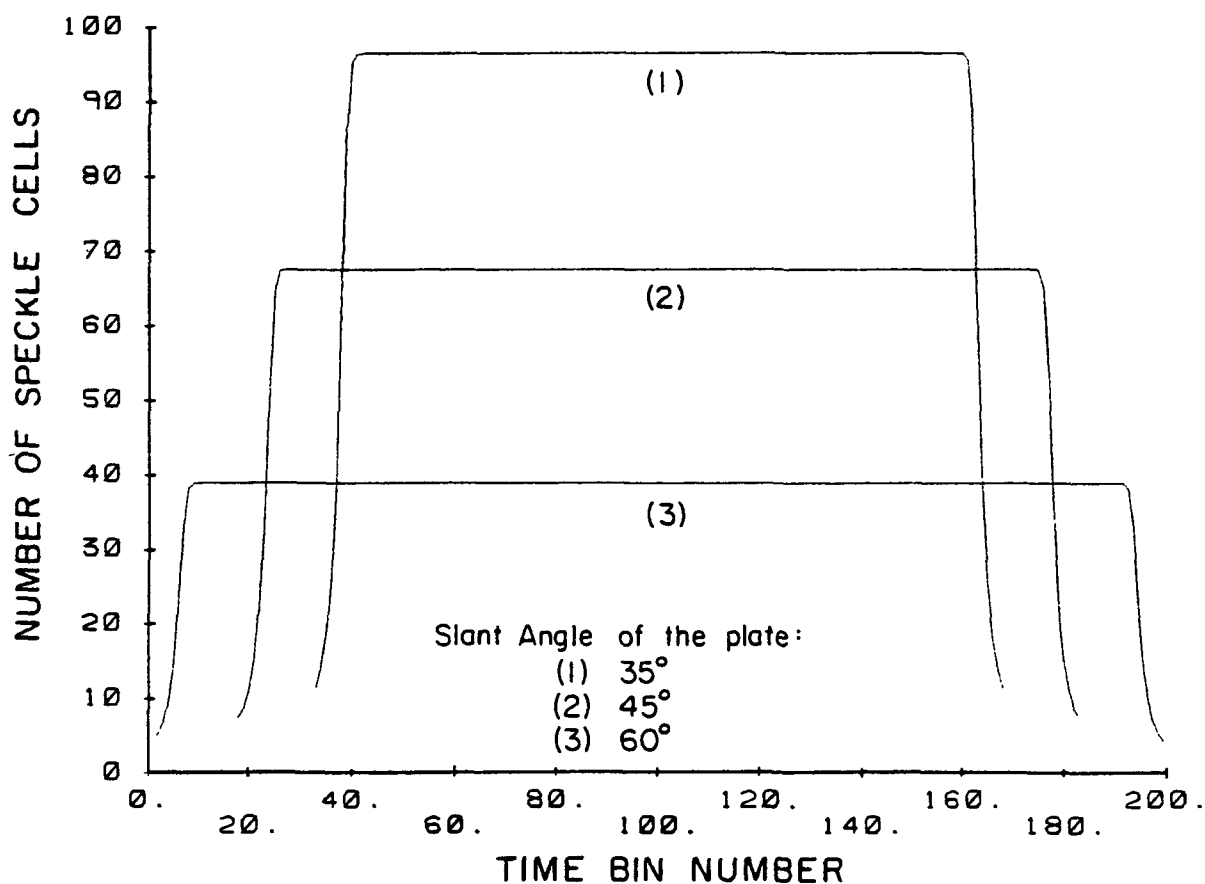


Figure 4.14. Number of speckle correlation cells for reflection from a finite size plate.

$$M_1 \equiv KG \left(\sqrt{\sigma_f^2 + \frac{4\sigma_\xi^2}{c^2}}, i\tau_0 \right) \tau_0, \quad (4.37)$$

where σ_ξ is the rms height of the surface profile. In this case, M_1 is roughly proportional to the pulse shape.

In summary, the received signal in the i^{th} time bin is gamma distributed with parameter M_1 , and when M_1 is an integer, the photoelectron count is negative binomial distributed. M_1 is the signal-to-noise ratio of the received energy and is referred to as the number of speckle correlation cells. From the examples considered, we find that the mean received waveform is closely related to the geometry of the target. The statistics of time-resolved speckle also depend on target geometries.

4.3. Estimation of Arrival Time

In laser ranging and altimetry applications, the arrival time of the returned pulse, denoted by τ_d , is of interest. In this case, Eq. (4.26) can be written explicitly as

$$p(\vec{k}|\tau_d) = \prod_{i=1}^N \frac{\Gamma(k_i + M_1(\tau_d))}{\Gamma(k_i + 1) \Gamma(M_1(\tau_d))} \left(1 + \frac{M_1(\tau_d)}{k_i(\tau_d)}\right)^{-k_i} \left(1 + \frac{\overline{k}_1(\tau_d)}{M_1(\tau_d)}\right)^{-M_1(\tau_d)}. \quad (4.38)$$

The Maximum Likelihood (ML) estimate of the arrival time is the value of τ_d that maximizes the likelihood function $p(\vec{k}|\tau_d)$, i.e.,

$$\begin{aligned} \hat{\tau}_{d, \text{ML}} &= \arg \max_{\tau_d} [p(\vec{k}|\tau_d)] \\ &= \arg \max_{\tau_d} [\ln p(\vec{k}|\tau_d)] \quad , \end{aligned} \quad (4.39)$$

where $\arg \max_x [F(x)]$ denotes the argument x that maximizes $F(x)$. By substituting Eqs. (4.38), (4.25) and (4.22) into Eq. (4.39), we have

$$\begin{aligned} \hat{\tau}_{d_{ML}} = \arg \max_{\tau_d} & \left[\sum_{i=1}^N \ln \Gamma(k_i + M_i(\tau_d)) - \sum_{i=1}^N \ln \Gamma(k_i + 1) - \sum_{i=1}^N \ln \Gamma(M_i(\tau_d)) \right. \\ & \left. - \sum_{i=1}^N k_i \ln \left(1 + \frac{KF_1(i\tau_o - \tau_d)}{\langle N \rangle F_2(i\tau_o - \tau_d)} \right) - \sum_{i=1}^N M_i(\tau_d) \ln \left(1 + \frac{\langle N \rangle F_2(i\tau_o - \tau_d)}{KF_1(i\tau_o - \tau_d)} \right) \right]. \end{aligned} \quad (4.40)$$

Assuming that the received pulse always stays inside the observation interval for all values of τ_d , so that there are no end effects, we obtain

$$\begin{aligned} \hat{\tau}_{d_{ML}} = \arg \max_{\tau_d} & \left[\sum_{i=1}^N \left(k_i + M_i(\tau_d) - \frac{1}{2} \right) \ln(k_i + M_i(\tau_d)) - \sum_{i=1}^N \left(M_i(\tau_d) - \frac{1}{2} \right) \ln(M_i(\tau_d)) \right. \\ & \left. - \sum_{i=1}^N k_i \ln \left(1 + \frac{KF_1(i\tau_o - \tau_d)}{\langle N \rangle F_2(i\tau_o - \tau_d)} \right) - \sum_{i=1}^N M_i(\tau_d) \ln \left(1 + \frac{\langle N \rangle F_2(i\tau_o - \tau_d)}{KF_1(i\tau_o - \tau_d)} \right) \right], \end{aligned} \quad (4.41)$$

where we have made use of the following relation

$$\ln \Gamma(x) \cong \left(x - \frac{1}{2} \right) \ln x - x + \frac{1}{2} \ln 2\pi \quad . \quad x > 1 \quad (4.42)$$

Assuming the summations of $M_i(\tau_d)$ over i to be independent of τ_d , we have

$$\begin{aligned} \hat{\tau}_{d_{ML}} = \arg \max_{\tau_d} & \left[\sum_{i=1}^N \left(k_i + M_i(\tau_d) - \frac{1}{2} \right) \ln(k_i + M_i(\tau_d)) \right. \\ & \left. - \sum_{i=1}^N k_i \ln \left(1 + \frac{KF_1(i\tau_o - \tau_d)}{\langle N \rangle F_2(i\tau_o - \tau_d)} \right) \right]. \end{aligned} \quad (4.43)$$

When the footprint is approximately uniform over the target area and the width of the laser pulse is short compared to the range spread of the target, F_1 and F_2 are approximately equal. Equation (4.43) reduces to

$$\begin{aligned} \hat{\tau}_{d_{ML}} &= \arg \max_{\tau_d} \left[\sum_{i=1}^N \left(k_i + M_i(\tau_d) - \frac{1}{2} \right) \ln(k_i + M_i(\tau_d)) \right] \\ &= \arg \max_{\tau_d} [H(\tau_d)] \quad . \end{aligned} \quad (4.44)$$

The performance of $\hat{\tau}_{d_{ML}}$ will be analyzed based on a procedure similar to that used by Bar-David [16].

If $H(\tau_d)$ is differentiable, we have

$$\left. \frac{d}{d\tau_d} H(\tau_d) \right|_{\hat{\tau}_{d_{ML}}} = \dot{H}(\tau_{d_{ML}}) = 0. \quad (4.45)$$

If the actual arrival time of the pulse is denoted as τ_{do} , then $H(\tau_d)$ can be expanded using the Taylor series expansion centered around τ_{do} as

$$H(\tau_d) = H(\tau_{do}) + \dot{H}(\tau_{do})(\tau_d - \tau_{do}) + \ddot{H}(\tau_{do}) \frac{(\tau_d - \tau_{do})^2}{2!} + \dots \quad (4.46)$$

Differentiating Eq. (4.46) with respect to τ_d and using Eq. (4.45) yield

$$\dot{H}(\tau_{d_{ML}}) = 0 = \dot{H}(\tau_{do}) + (\hat{\tau}_{d_{ML}} - \tau_{do}) \ddot{H}(\tau_{do}) + \dots, \quad (4.47)$$

from which it follows that the error of the estimator is

$$\epsilon = \hat{\tau}_{d_{ML}} - \tau_{do} \cong - \frac{\dot{H}(\tau_{do})}{\ddot{H}(\tau_{do})}, \quad (4.48)$$

provided $\ddot{H}(\tau_{do}) \neq 0$. This constraint excludes strictly rectangular pulses from this analysis.

The bias and variance of the estimator can be written as

$$E[\epsilon] = -E[\dot{H}(\tau_{do})/\ddot{H}(\tau_{do})] \quad (4.49)$$

and

$$\text{var}[\epsilon] = E\left\{ \left[\frac{\dot{H}(\tau_{do})}{\ddot{H}(\tau_{do})} \right]^2 \right\} - E^2[\epsilon], \quad (4.50)$$

where the expectations are over the observation vector \vec{k} .

Assuming $E^2[\ddot{H}(\tau_{do})] \gg \text{var}[\ddot{H}(\tau_{do})]$, such that $\ddot{H}(\tau_{do})$ can be replaced by its expected value, we have

$$E[\varepsilon] \cong - \frac{E\{\dot{H}(\tau_{do})\}}{E\{\ddot{H}(\tau_{do})\}} \quad (4.51)$$

and

$$\text{var}[\varepsilon] \cong \frac{\text{var}[\dot{H}(\tau_{do})]}{E^2\{\ddot{H}(\tau_{do})\}} \quad (4.52)$$

$E[\dot{H}(\tau_{do})]$ is given by

$$\begin{aligned} E[\dot{H}(\tau_{do})] &= \sum_{i=1}^N \dot{M}_i(\tau_{do}) E\{\ln(k_i + M_i(\tau_{do}))\} + E\left\{ \sum_{i=1}^N \frac{k_i + M_i - \frac{1}{2}}{k_i + M_i} \dot{M}_i \right\} \\ &\cong \sum_{i=1}^N \dot{M}_i(\tau_{do}) E\{\ln(k_i + M_i(\tau_{do}))\} \quad (4.53) \end{aligned}$$

To proceed further, we note that

$$\begin{aligned} \ln(k_i + M_i(\tau_{do})) &= \ln(\bar{k}_i + M_i(\tau_{do})) + \ln\left(1 + \frac{\Delta k_i}{\bar{k}_i + M_i(\tau_{do})}\right) \\ &\cong \ln(\bar{k}_i + M_i(\tau_{do})) + \frac{\Delta k_i}{\bar{k}_i + M_i(\tau_{do})} \quad (4.54) \end{aligned}$$

where we have separated k_i into a deterministic part \bar{k}_i and a zero mean random part Δk_i . The validity of Eq. (4.54) requires

$$\Delta k_i \ll \bar{k}_i + M_i(\tau_{do}) \quad (4.55)$$

which is satisfied when the received signal level is high or when the number of speckle cells is large.

Substituting Eq. (4.54) into Eq. (4.53) yields

$$\begin{aligned} E[\dot{H}(\tau_{do})] &\cong K \tau_o \sum_{i=1}^N \dot{F}_1(i\tau_o - \tau_{do}) \ln F_1(i\tau_o - \tau_{do}) \\ &\cong K \tau_o \int_{-\infty}^{\infty} \dot{F}_1 \ln F_1 = 0 ; \end{aligned} \quad (4.56)$$

therefore, the estimator is unbiased. The variance of $\dot{H}(\tau_{do})$ is

$$\text{var}[\dot{H}(\tau_{do})] = \sum_{i=1}^N \left[\frac{\dot{M}_1(\tau_{do})}{\bar{k}_1 + M_1(\tau_{do})} \right]^2 \text{var}(\Delta k_1) . \quad (4.57)$$

From the probability density function of k_1 shown in Eq. (4.24), we have

$$\text{var}[\Delta k_1] = \bar{k}_1 + \frac{\bar{k}_1^2}{M_1} . \quad (4.58)$$

By substituting Eqs. (4.58), (4.25) and (4.23) into Eq. (4.57), we obtain

$$\text{var}[\dot{H}(\tau_{do})] = \left(\frac{1}{\langle N \rangle} + \frac{1}{K} \right)^{-1} \sum_{i=1}^N \frac{\dot{F}_1^2}{F_1} \tau_o . \quad (4.59)$$

$E[\ddot{H}(\tau_{do})]$ is given by

$$\begin{aligned} E[\ddot{H}(\tau_{do})] &= \sum_{i=1}^N \ddot{M}_1(\tau_{do}) \ln(\bar{k}_1 + M_1(\tau_{do})) + E \left\{ \sum_{i=1}^N \frac{\dot{M}_1^2(\tau_{do})}{\bar{k}_1 + M_1(\tau_{do})} \right\} \\ &\cong \sum_{i=1}^N \ddot{M}_1(\tau_{do}) \ln(\bar{k}_1 + M_1(\tau_{do})) + \sum_{i=1}^N \frac{\dot{M}_1^2(\tau_{do})}{\bar{k}_1(\tau_{do}) + M_1(\tau_{do})} \\ &= - \left(\frac{1}{\langle N \rangle} + \frac{1}{K} \right)^{-1} \sum_{i=1}^N \frac{\dot{F}_1^2}{F_1} \tau_o , \end{aligned} \quad (4.60)$$

where use has been made of Eq. (4.54). Finally, by substituting these results into Eq. (4.50), we have for the ML estimator

$$\text{var}[\varepsilon] = \left(\frac{1}{\langle N \rangle} + \frac{1}{K} \right) \frac{1}{\left(\sum_{i=1}^N \frac{\dot{F}_1^2}{F_1} \tau_o \right)} . \quad (4.61)$$

As a comparison, the ML estimator derived for the case of negligible speckle noise is [13], [16],

$$\hat{\tau}_{d_{\text{ML}}} = \arg \max_{\tau_d} \left[\sum_{i=1}^N k_i \ln \bar{k}_i(\tau_d) \right] . \quad (4.62)$$

It will be interesting to see how this estimator performs in the presence of speckle. Employing the same procedure used above, we find it to be unbiased and the variance of its error is given by

$$\text{var}[\varepsilon] = \frac{1}{\langle N \rangle} \frac{1}{\sum_{i=1}^N \frac{\dot{F}_1^2}{F_1} \tau_o} + \frac{1}{K} \frac{\sum_{i=1}^N \left(\frac{\dot{F}_1}{F_1} \right)^2 F_2}{\left(\sum_{i=1}^N \frac{\dot{F}_1^2}{F_1} \right)^2 \tau_o} , \quad (4.63)$$

which reduces to Eq. (4.61) when F_1 and F_2 are equal. This indicates that, under the assumptions made in analyzing the two estimators, i.e., shot noise and speckle noise are not severe, their performances are indistinguishable.

It can be seen from Eq. (4.63) that the timing error is smaller for waveforms with larger first derivative. The effects of signal bandwidth on the timing performance will be further discussed in Chapter 5.

We shall use Eq. (4.63) to calculate the timing performances for the target geometries considered in Section 4.2. For normal incidence from an infinite flat target, the mean received waveform corresponds to Fig. 4.2.

The ranging accuracy is calculated and plotted in Fig. 4.15 versus the average number of photoelectrons. From the figure, we see that in the limit of high signal energy all three curves have the same accuracy limit set by speckle. This is expected because they have the same number of speckle cells as shown in Fig. 4.4. For non-normal incidence, the mean waveform was shown previously in Fig. 4.5 and the ranging accuracy is plotted in Fig. 4.16. For both normal and non-normal incidence cases, geometries that give rise to sharper received pulses result in better timing accuracies.

For the finite-size plate target considered in Section 4.2, the return waveform was found to depend on the relative sizes of the plate and the laser footprint. Therefore, we expect the ranging performance will also depend on the size of the plate. For a plate length of 1 meter, the mean waveform corresponds to Fig. 4.9; the ranging performance is calculated and plotted in Figure 4.17. It is interesting to note that, although for a slant angle of 60° , the return pulse is broader than that of a slant angle of 35° , the ranging performance is actually better for the same signal level. This can be explained by examining the slopes of the return waveforms shown in Fig. 4.18. For the 60° case, the ends of the plate are located closer to the center of the footprint, so when the laser pulse first hits the front end of the plate, the increase of the reflected energy is larger. Therefore, the slope of the leading edge of the reflected pulse is larger. For the 35° case, the ends of the plate are farther away from the center of the footprint, so the slope of the leading edge of the reflected pulse is smaller. From Eq. (4.63), we see that waveforms with larger slopes or bandwidths result in better timing accuracy. We need to keep in mind that in Fig. 4.16 the performance is plotted versus the

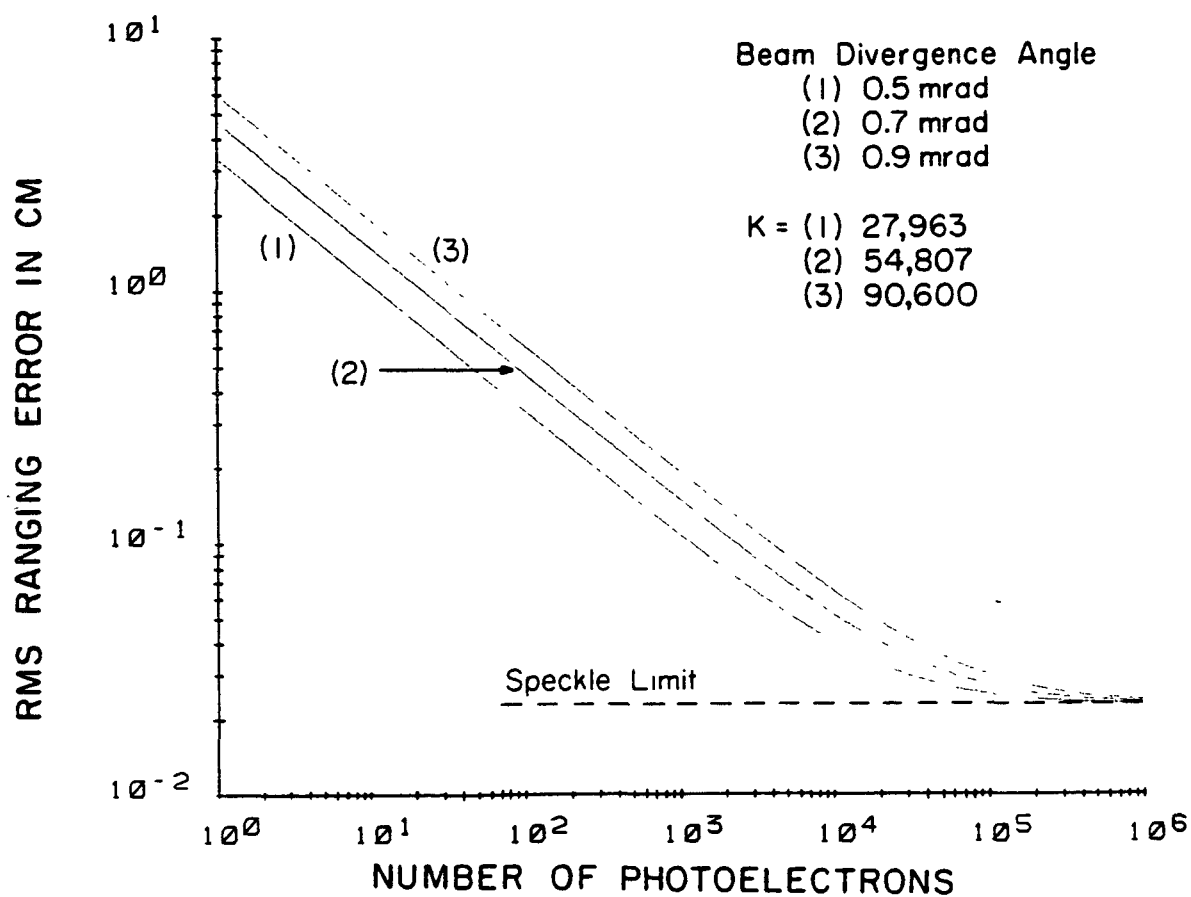


Figure 4.15. Timing performance for reflection from an infinite flat diffuse target calculated using Eq. (4.63). Normal incidence. Mean received pulse shape corresponds to that in Figure 4.2.

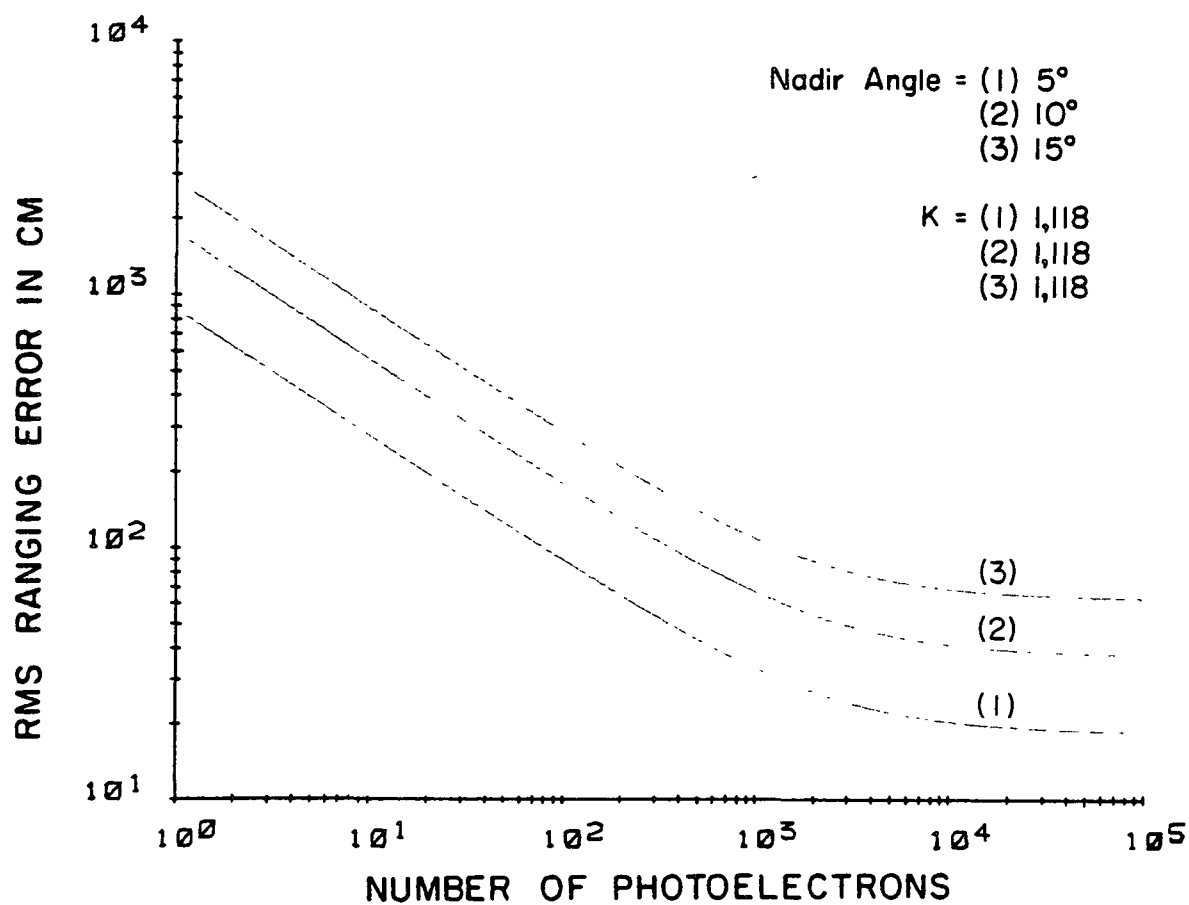


Figure 4.16. Timing performance for reflection from an infinite flat diffuse target calculated using Eq. (4.63). Non-normal incidence. Mean received pulse shape corresponds to that in Figure 4.5.

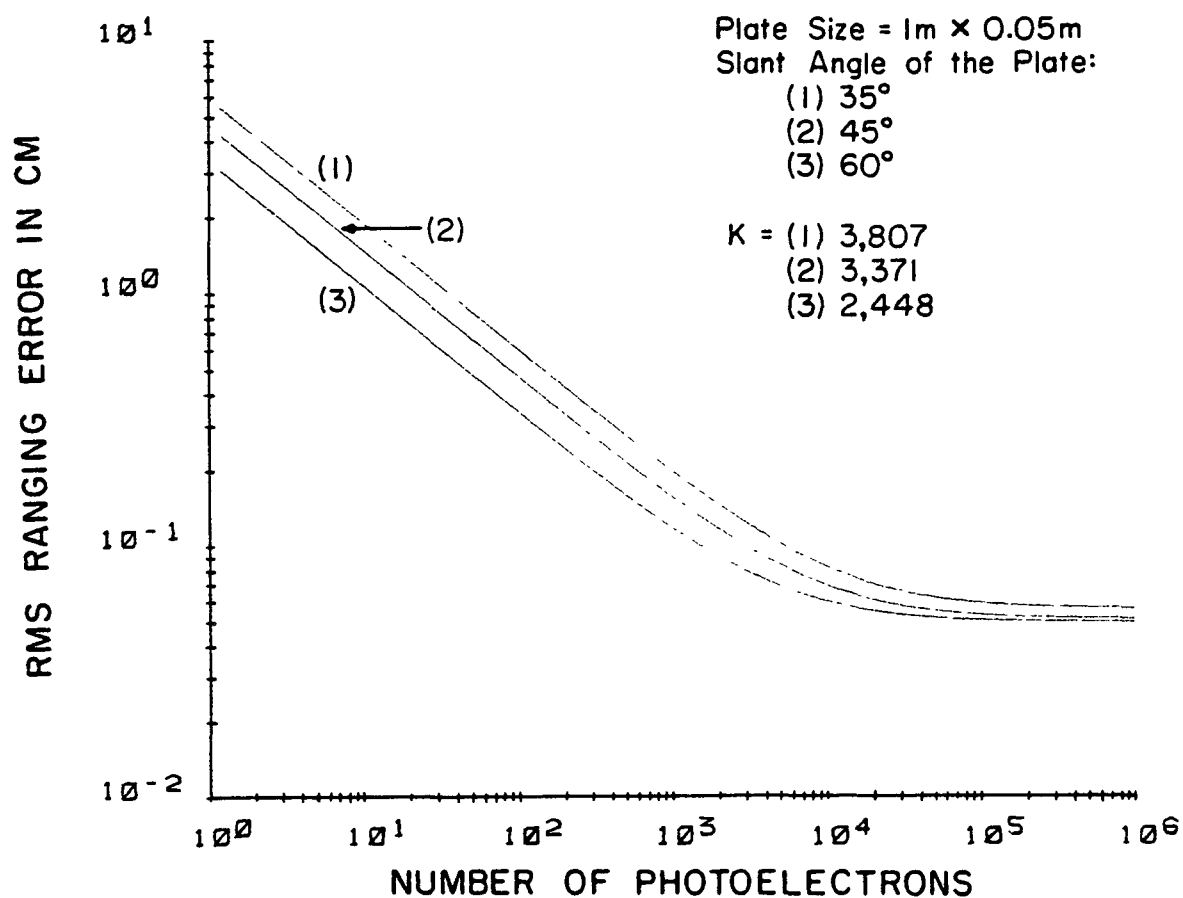


Figure 4.17. Timing performance for reflection from a finite size plate calculated using Eq. (4.63). Mean received pulse shape corresponds to that in Figure 4.9.

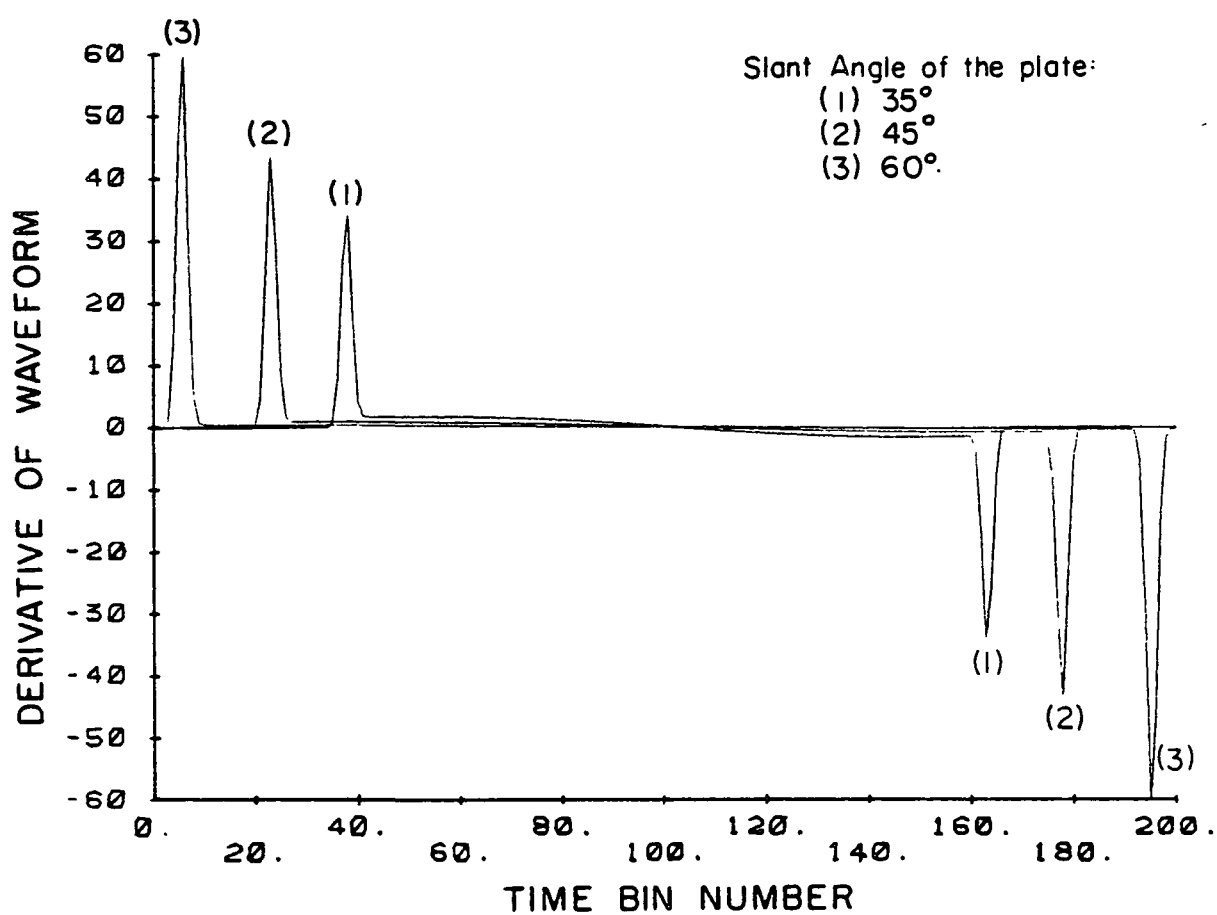


Figure 4.18. Slope of the mean pulse shape shown in Figure 4.9. Magnitude scale is relative.

average number of photoelectrons. For a fixed laser output energy and fixed plate size, the average number of photoelectrons will decrease as the slant angle increases. In practice, this has to be taken into account in comparing the timing performance.

For a 3 m long plate, the return waveform is shown in Fig. 4.12, and the slope of the waveform is plotted in Fig. 4.19. The ranging performance is shown in Fig. 4.20. In this case, a 45° slant angle results in the worst timing performance. Again Figs. 4.21 and 4.22 clearly show that waveforms with larger derivatives permit better timing accuracy.

For a Gaussian received pulse shape with rms width α_T , Eq. (4.63) can be evaluated to give

$$\text{var}[\epsilon] = \left(\frac{1}{\langle N \rangle} + \frac{1}{K} \right) \alpha_T^2, \quad (4.64)$$

where we have approximated the summation by an integral. If $\langle N \rangle \gg K$, then the timing accuracy is limited by speckle; on the other hand, if $K \gg \langle N \rangle$, the timing accuracy of the receiver is shot noise limited.

A suboptimal estimator that could be simpler to implement is

$$\hat{\tau}_{d_c} = \arg \max_{\tau_d} \left[\sum_{i=1}^N k_i \bar{k}_i(\tau_d) \right], \quad (4.65)$$

which is the discrete time analog of the correlation receiver or matched filter. Again, the estimator can be analyzed by Bar-David's [16] method. It is easy to show that the estimator is unbiased, and its error has a variance given by

$$\text{var}[\epsilon] = \frac{\frac{1}{\langle N \rangle} \sum_{i=1}^N \dot{F}_1^2 F_1 \tau_o + \frac{1}{K} \sum_{i=1}^N \dot{F}_1^2 F_2 \tau_o}{\left\{ \sum_{i=1}^N F_1 \ddot{F}_1 \tau_o \right\}^2}. \quad (4.66)$$

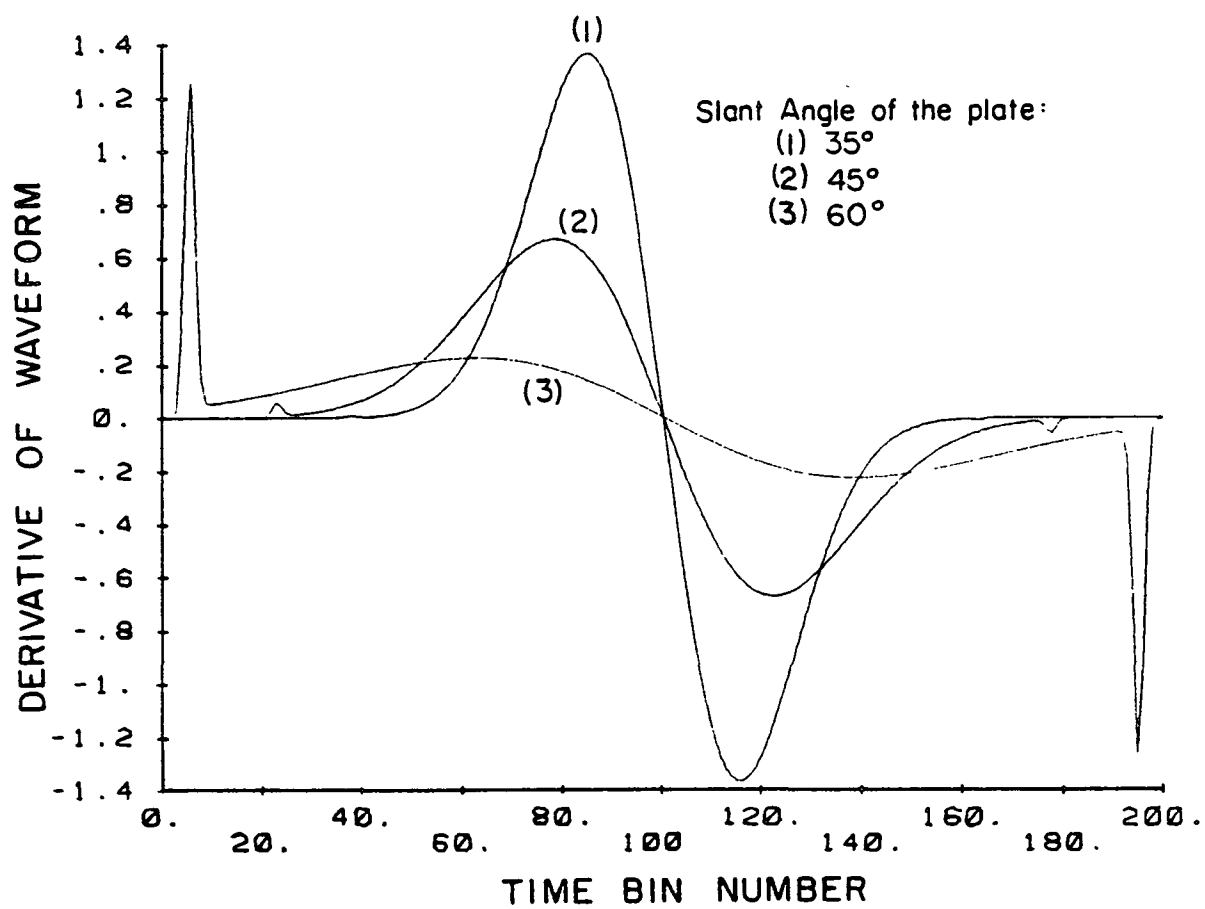


Figure 4.19. Slope of the mean pulse shape shown in Figure 4.12. Magnitude scale is relative.

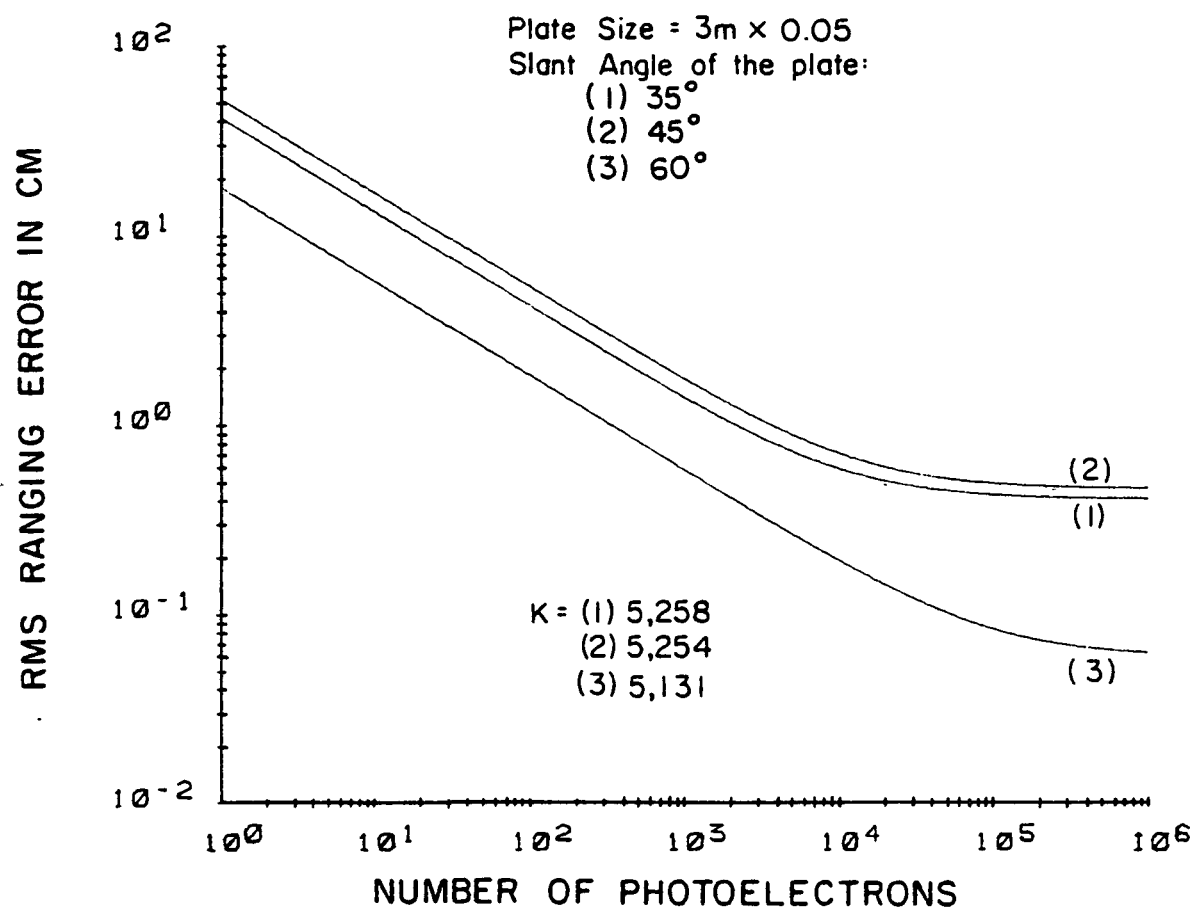


Figure 4.20. Timing performance for reflection from a finite size target. Calculated using Eq. (4.63). Mean received pulse shape corresponds to that in Figure 4.12.

When both F_1 and F_2 are equal to a Gaussian pulse shape with rms width σ_T , we have

$$\text{var}[\epsilon] = \left(\frac{1}{\langle N \rangle} + \frac{1}{K} \right) \frac{8}{3\sqrt{3}} \sigma_T^2 \quad (4.67)$$

Comparing Eq. (4.64) with Eq. (4.67), we find that $\hat{\tau}_{dc}$ has a rms timing error which is about 25% greater. In critical timing applications, it may be necessary to use the better estimator $\hat{\tau}_{d_{ln}}$.

From the above results, we can see the effects of speckle on the receiver timing performance. When speckle is present, the mean-square timing error is increased by a factor of $\langle N \rangle / K$. If K is much larger than $\langle N \rangle$, the effects of speckle on timing are negligible. But if $\langle N \rangle$ is comparable to or even greater than K , speckle will degrade the timing performance significantly.

4.4. Computer Simulation

Since Eqs. (4.63) and (4.66) were derived under the high signal-to-noise assumption, they are not accurate for low signal levels; other methods must be used to determine the estimators' performances for weak signal returns. A computer simulation of maximum likelihood estimators has been developed by J. B. Abshire and J. F. McGarry at NASA Goddard Space Flight Center (GSFC) for this purpose. This simulator was an extension of earlier work [17] used to evaluate the low-level timing performance of estimators with shot noise only. A summary of simulation results was recently presented [18].

The simulation is performed by dividing the observation interval into 512 time bins and using the computer to generate the photoelectron counts in each time bin. The probability density function of the photoelectron

count in the i^{th} time bin $p(k_i)$ was given previously in Eq. (4.24). For an integer value of M_i , $p(k_i)$ becomes

$$p(k_i) = \binom{k_i + M_i - 1}{k_i} \left(\frac{\bar{k}_i}{\bar{k}_i + M_i} \right)^{k_i} \left(\frac{M_i}{\bar{k}_i + M_i} \right)^{M_i}, \quad (4.68)$$

which is the negative binomial or Pascal probability density function.

The negative binomial distribution originates from a sequence of independent Bernoulli trials. In such trials, each trial has a fixed probability of success, p , and fixed probability of failure, q . The probability of k failures prior to the r^{th} success [19] is given by

$$\begin{aligned} p(k) &= \binom{-r}{k} (-q)^k p^r \\ &= \binom{r + k - 1}{k} p^r q^k. \end{aligned} \quad (4.69)$$

This probability density is called negative binomial. The derivation of this formula is straightforward after observing that the r^{th} success occurs on the $(r + k)^{\text{th}}$ trial if and only if $(r - 1)$ successes and k failures occurred in the first $(r + k - 1)$ trials and they are followed by a single success.

Comparing Eq. (4.68) and (4.69), Abshire and McGarry found that the probability of observing k_i photoelectrons in the i^{th} time bin was equal to the probability of k_i failures prior to the M_i^{th} success in a sequence of Bernoulli trials with probability of success equal to $M_i / (M_i + \bar{k}_i)$. Using this analogy, they generated k_i by conducting a sequence of Bernoulli trials and counting the number of failures which occurred before the M_i^{th} success occurs. The advantage of this approach is that the Bernoulli trial can be implemented easily and efficiently on a computer. The computer

generates uniform random numbers between 0 and 1. Whenever the generated number is less than a threshold, the trial is classified as a success. The threshold is chosen to be the same as the probability of success, which is $M_i / (M_i + \bar{k}_i)$ for the i^{th} time bin.

In general situations, M_i may not be an integer and Eq. (4.24) does not reduce to the negative binomial distribution. In these cases the simulator rounds M_i to the nearest integer value. This quantization of M_i only introduces small errors if M_i is large.

The simulator was run for a raised cosine waveform, which can be expressed as

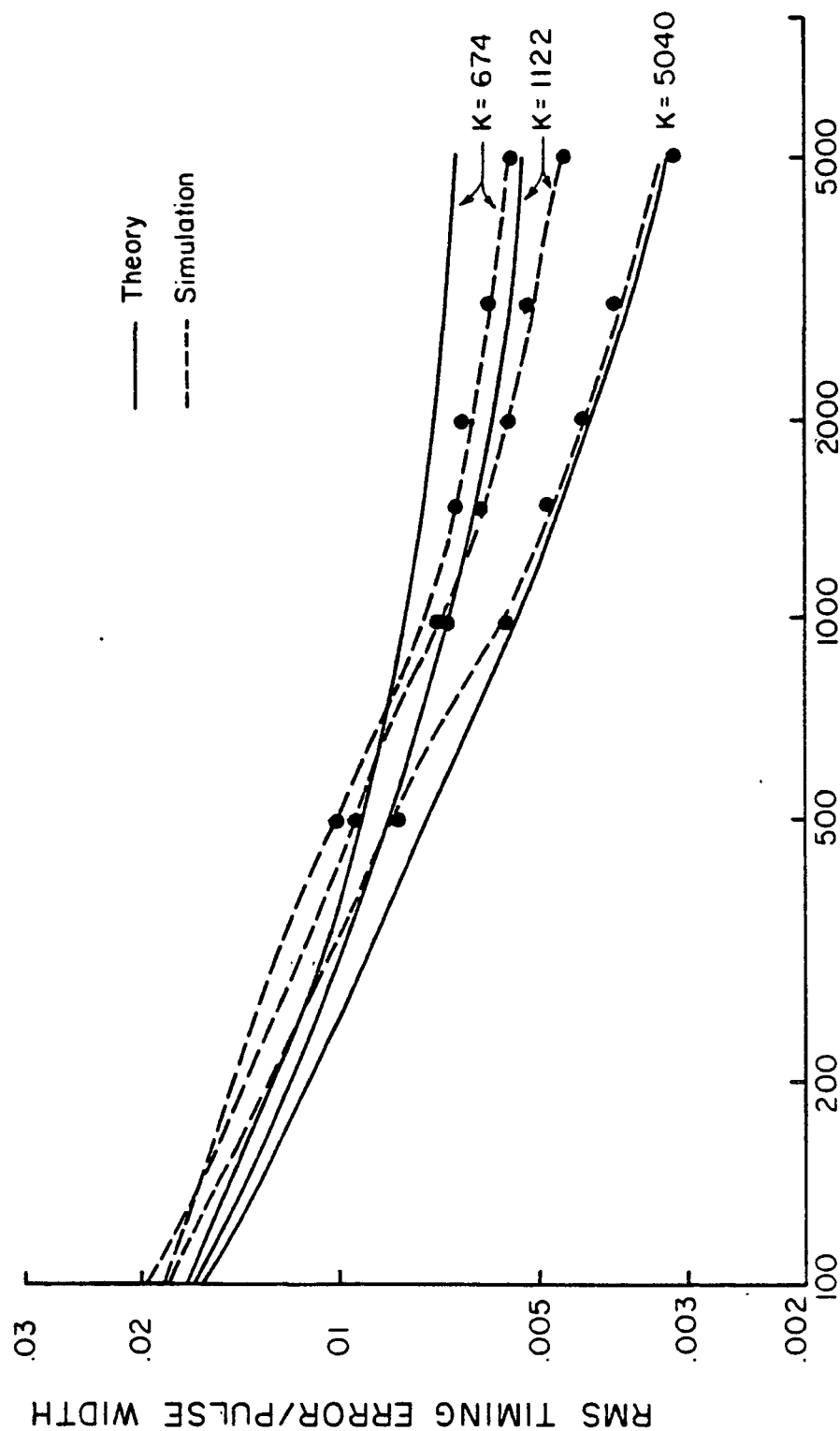
$$F(t) = \frac{1}{D} \left(1 + \cos \frac{2\pi}{D} t \right) ; \quad -\frac{D}{2} \leq t \leq \frac{D}{2} . \quad (4.70)$$

M_i is calculated using Eq. (4.23) and rounded to the nearest integer. If M_i falls below 1, it will be replaced by 1. The results of the simulator are compared with the theory in Fig. 4.21. The agreement between the theory and simulation is better for high-signal level and for large K . This is expected, because in deriving the theory, we have assumed a high signal-to-noise ratio, so that the approximation that leads to Eq. (4.63) is valid.

For K equal to 5040, the transition occurs at signal energy about 1000 photoelectrons, where the simulation and the theory come into agreement. At this signal level, the average number of photoelectrons in each time bin is only about 2. In practice, the signal level is usually higher and the theory is expected to predict the timing performance accurately.

The simulator has two limitations. The first is that in its present form it can only work with integer values of M_i . In principle, we can

TIMING PERFORMANCE SIMULATOR VS. THEORY



RETURN SIGNAL ENERGY IN PHOTOELECTRONS

Figure 4.21. Comparison of simulation and theory.

generate the counts for a non-integer M_1 by first generating a gamma distributed variable, then use it as the mean function in a Poisson random variable generator, and generate the desired variable. Although this approach requires more computer time, it gives more accurate results for low values of M_1 . This extension of the simulator is presently underway at GSFC. The second limitation is that the timing resolution is limited by the finite number of time bins (presently 512) in the simulator. Therefore, the arrival time of each simulated waveform can only be an integer multiple of the width of a time bin.

The error introduced by the timing quantization can be calculated by using the fact that it is uniformly distributed over one time bin. Therefore it has a standard deviation of $0.29 (1/\sqrt{12})$ time bin. This is equivalent to an error of $5.6 \times 10^{-4} (0.29/512)$ when normalized by the pulse width. The quantization noise is not important for the results shown in Fig. 4.21, but it is the limiting factor when the timing error is small. Therefore, if the simulator is to be used for waveforms that result in a normalized timing accuracy better than 0.0005, more time bins are required. Unfortunately, an increase in the number of time bins is usually accompanied by a quadratic increase in the computer execution time. This execution time is the limiting factor with the present simulator.

Since the computer simulation results and the theory are in good agreement for high signal levels, this verifies the theory's validity in that region. The simulator establishes the ML algorithm performance at low signal levels.

4.5. Partially Developed Speckle

In previous treatments of the time resolved speckle, we have assumed a fully developed speckle, i.e., the speckle follows the circular complex

Gaussian statistics, which is generally true for diffuse targets or for targets with many reflection centers. For some targets, the speckle is only partially developed, and the distribution of the speckle is not Gaussian. An example of the partially developed speckle is laser reflections from the LAGEOS.

The Laser Geodynamic Satellite (LAGEOS) was launched in May 1976 and was designed as a passive long-lived target with a well-defined orbit [20]. As such, it functions as a reference point in the inertial space and by ranging to it, sets of ground-based laser systems may recover their individual geometry, their positions with respect to the earth's center of mass, or their positions with respect to an inertial reference. In order to enhance its reflectivity as a laser target, the satellite is covered with optical cube corners which retroreflect any incident optical signal. There are a total of 426 cube corner reflectors. The LAGEOS has a diameter of 60 cm and is orbiting at an altitude of 5000 km. Simple calculations show that, even for a reasonably large receiving telescope, say 1 meter in diameter, the individual retroreflector on the LAGEOS can not be resolved.

During the prelaunch testing at the NASA-GSFC in December 1975 and January 1976, there had been concerns about the pulse-shape fluctuations due to the coherency effects [20]. This is due to the fact that there is a random phase associated with the optical field reflected from each retroreflector. When the reflected fields overlap in time at the receiver, interference causes the returned power to vary randomly. However, receivers with enough resolution to experimentally observe this pulse-shape fluctuation or time-resolved speckle were not available at the time of the prelaunch testing. The purpose of the work here is to provide a theoretical analysis of the statistics of this partially developed time-resolved speckle.

Using the Fresnel diffraction formula, the optical field on the plane of the receiving telescope is

$$a_R(\underline{r}, z, t) = c_o \exp\left[\frac{-ik_o r^2}{2z}\right] \sum_{i=1}^{N_r} A_i(t) \exp\left[\frac{ik_o \underline{\rho}_i \cdot \underline{r}}{z}\right] \exp[i\phi_i] \quad , \quad (4.71)$$

where

$$c_o = (T_a / \lambda_o z) \exp[-i2k_o z] \quad (4.72)$$

and

$$A_i(t) = \beta_i^{1/2} a_T(\underline{\rho}_i, z) f\left(t - \frac{2z}{c} - \frac{\rho_i^2}{cz} + \frac{2\xi_i}{c}\right) \exp\left[-ik_o\left(\frac{\rho_i^2}{2z} - 2\xi_i\right)\right] \quad , \quad (4.73)$$

where $a_T(\underline{r}, z)$ is the complex amplitude cross section of the laser footprint, T_a is the intensity transmittance of the atmosphere, k_o is the wave number, and λ_o is the wavelength of the laser. N_r is the total number of retroreflectors, β_i is the effective reflecting area of the i^{th} retroreflector, which is related to the angle of the incident laser beam and the orientation of the retroreflector. In practice, most of the β_i 's are zero due to the shadowing effects. ϕ_i is the random phase angle associated with the reflection from the i^{th} reflector; we assume ϕ_i 's to be statistically independent of each other and uniformly distributed between 0 and 2π . $\underline{\rho}_i$ is the transverse coordinate of the i^{th} reflector and ξ_i is its displacement relative to the reference plane.

For a direct detection receiver, the received power is given by

$$\begin{aligned} P(t) &= |c_o|^2 \sum_{i=1}^{N_r} \sum_{k=1}^{N_r} A_i(t) A_k^*(t) \exp[i(\phi_i - \phi_k)] \int d^2 \underline{r} W(\underline{r}) \exp(ik_o \underline{r} \cdot (\underline{\rho}_i - \underline{\rho}_k) / z) \\ &= |c_o|^2 \sum_{i=1}^{N_r} \sum_{k=1}^{N_r} A_i(t) A_k^*(t) \exp[i(\phi_i - \phi_k)] \mathcal{Q}_W\left(\frac{k_o}{z} [\underline{\rho}_i - \underline{\rho}_k]\right) \quad , \quad (4.74) \end{aligned}$$

where $\mathcal{F}_W(\underline{\rho})$ is the two-dimensional Fourier transform of $W(r)$, the aperture function.

Since the individual reflectors on the LAGEOS cannot be spatially resolved, Eq. (4.74) can be simplified to

$$P(t) \equiv |c_0|^2 A_R \left| \sum_{i=1}^{N_r} A_i(t) \exp[i\phi_i] \right|^2, \quad (4.75)$$

where we have made use of the following relationship,

$$\mathcal{F}_W\left(\frac{k_0}{z}(\underline{\rho}_i - \underline{\rho}_k)\right) = \mathcal{F}_W(\underline{0}) = A_R. \quad (4.76)$$

Since ϕ_i 's are random, $P(t)$ is also random. This fluctuation of the received power is due to the coherent additions of fields with random phases. Because the number of components is not large enough to warrant the use of the central limit theorem, the statistics are different from that of a fully developed speckle. The probability density function of $P(t)$ is derived in the following.

Let the dummy variables \tilde{x}_i , \tilde{y}_i , \tilde{X} and \tilde{Y} be defined by the following equations,

$$\tilde{x}_i(t) = (|c_0|^2 A_R)^{1/2} A_i(t) \cos \phi_i, \quad (4.77)$$

$$\tilde{y}_i(t) = (|c_0|^2 A_R)^{1/2} A_i(t) \sin \phi_i, \quad (4.78)$$

$$\tilde{X} = \sum_{i=1}^{N_r} \tilde{x}_i \quad (4.79)$$

and

$$\tilde{Y} = \sum_{i=1}^{N_r} \tilde{y}_i. \quad (4.80)$$

Without loss of generality, we shall assume all A_i 's(t) to be real. Since ϕ_i 's are uniformly distributed, the probability density function of \tilde{x}_i can be obtained by a simple change of variable. The results are

$$p_{\tilde{x}_i}(\tilde{x}_i) = \frac{1}{\pi} [|c_o|^2 A_R A_i^2(t) - \tilde{x}_i^2]^{-1/2} ; \quad |\tilde{x}_i| \leq |c_o| A_R^{1/2} |A_i(t)|$$

$$= 0 ; \quad \text{otherwise,} \quad (4.81)$$

the corresponding characteristic function is

$$\phi_{\tilde{x}_i}(\omega) = \int_{-\infty}^{\infty} d\tilde{x}_i p_{\tilde{x}_i}(\tilde{x}_i) \exp[-i\omega\tilde{x}_i] = J_0(|c_o| A_R^{1/2} A_i(t)\omega) , \quad (4.82)$$

where $J_0(\alpha)$ is the Bessel function of the first kind, zeroth order.

Using the fact that ϕ_i 's are independent, we have

$$\phi_{\tilde{X}}(\omega) = \prod_{i=1}^{N_r} \phi_{\tilde{x}_i}(\omega) = \prod_{i=1}^{N_r} J_0(|c_o| A_R^{1/2} A_i(t)\omega) . \quad (4.83)$$

Similarly, we have

$$\phi_{\tilde{Y}}(\omega) = \prod_{i=1}^{N_r} J_0(|c_o| A_R^{1/2} A_i(t)\omega) . \quad (4.84)$$

The joint characteristic function of \tilde{X} and \tilde{Y} is defined as

$$\phi_{\tilde{X}, \tilde{Y}}(u, v) = \int_{-\infty}^{\infty} d\tilde{X} \int_{-\infty}^{\infty} d\tilde{Y} p_{\tilde{X}, \tilde{Y}}(\tilde{X}, \tilde{Y}) \exp[-i(u\tilde{X} + v\tilde{Y})] . \quad (4.85)$$

Making the following changes of variables

$$r = (\tilde{X}^2 + \tilde{Y}^2)^{1/2} , \quad (4.86)$$

$$\theta = \arctan(\tilde{Y}/\tilde{X}) , \quad (4.87)$$

$$\zeta = (u^2 + v^2)^{1/2} \quad (4.88)$$

and

$$\beta = \arctan(v/u) \quad , \quad (4.89)$$

we have

$$\phi_{\tilde{X}\tilde{Y}}(u,v) = \int_0^\infty dr \int_0^{2\pi} d\theta p_{r,\theta}(r,\theta) \exp[-ir\zeta \cos(\beta - \theta)] \quad . \quad (4.90)$$

Since \tilde{X} and \tilde{Y} have the same distribution, it is reasonable to assume that r and θ are circularly symmetric, so that r is independent of θ and θ is uniformly distributed between 0 and 2π . Under this assumption, we have

$$\phi_{\tilde{X}\tilde{Y}}(u,v) = \int_0^\infty dr p_r(r) J_0(\zeta r) = \int_0^\infty dr p_r(r) J_0(r\sqrt{u^2 + v^2}) \quad . \quad (4.91)$$

Letting v equal 0 in Eq. (4.91), we obtain

$$\begin{aligned} \phi_{\tilde{X}\tilde{Y}}(u,0) &= \phi_{\tilde{X}}(u) = \int_0^\infty dr p_r(r) J_0(ur) \\ &= \int_0^\infty dr r [p_r(r)/r] J_0(ur) \quad . \end{aligned} \quad (4.92)$$

$\phi_{\tilde{X}}(u)$ is recognized to be the Hankel transform of $p_r(r)/r$. Using the inverse Hankel transform, we get

$$\begin{aligned} p_r(r) &= r \int_0^\infty du u \phi_{\tilde{X}}(u) J_0(ur) \quad , \quad r \geq 0 \\ &= 0; \quad r < 0 \quad . \end{aligned} \quad (4.93)$$

Finally, since $P(t)$ is the square of $r(t)$, we have

$$\begin{aligned} p_P(P) &= \frac{1}{2} \int_0^\infty du u \phi_{\tilde{X}}(u) J_0(uP^{1/2}) \quad , \quad P \geq 0 \\ &= 0 \quad ; \quad P < 0 \quad , \end{aligned} \quad (4.94)$$

which is equivalent to Eq. (63) of Barakat [21].

Using Eq. (4.83), the probability density function of optical power can be written explicitly as

$$p_P(P) = (1/2) \int_0^\infty du \left[\prod_{i=1}^{N_r} J_0(|c_0| A_R^{1/2} A_i(t) u) \right] u J_0(u P^{1/2}) ; P \geq 0$$

$$= 0 ; P < 0. \quad (4.95)$$

In principle, p_P can be calculated for all t and for all possible ranging geometries, although the computation can be complicated. In practice, we are interested in the statistical properties of the detected signal, and usually knowing the first- and second-order moments of $P(t)$ is sufficient. In this case, it is not necessary to evaluate Eq. (4.95).

The mean power can be obtained from Eq. (4.75) directly:

$$E[P(t)] = |c_0|^2 A_R \sum_{i=1}^{N_r} |A_i(t)|^2. \quad (4.96)$$

The autocovariance function of $P(t)$ is given by

$$C_P(t_1, t_2) = |c_0|^4 \left\{ \sum_{i=1}^{N_r} \sum_{k=1}^{N_r} \left[A_i(t_1) A_i^*(t_2) A_k(t_1) A_k^*(t_2) \mathcal{Q}_W\left(\frac{k_0}{z} (\rho_i - \rho_k)\right) \right. \right.$$

$$\left. \left. \mathcal{Q}_W\left(-\frac{k_0}{z} (\rho_i - \rho_k)\right) \right] - A_R^2 \sum_{i=1}^{N_r} |A_i(t_1)|^2 |A_i(t_2)|^2 \right\}$$

$$\equiv |c_0|^4 A_R^2 \left\{ \left| \sum_{i=1}^{N_r} A_i(t_1) A_i^*(t_2) \right|^2 - \sum_{i=1}^{N_r} |A_i(t_1)|^2 |A_i(t_2)|^2 \right\}, \quad (4.97)$$

where we have made use of the fact that the retroreflectors cannot be spatially resolved by the telescope.

Let the impulse response of the photodetector be $h(t)$ and its quantum efficiency by η ; the mean and covariance functions of the output $S(t)$ are given by

$$E[S(t)] = \frac{\eta}{hf_o} E[P(t)] * h(t) \quad (4.98)$$

and

$$\begin{aligned} C_S(t_1, t_2) &= \frac{\eta}{hf_o} \int_{-\infty}^{\infty} d\tau E[P(\tau)] h(t_1 - \tau) h(t_2 - \tau) \\ &+ \left[\frac{\eta}{hf_o} \right]^2 \int_{-\infty}^{\infty} d\tau_1 \int_{-\infty}^{\infty} d\tau_2 C_P(\tau_1, \tau_2) h(t_1 - \tau_1) h(t_2 - \tau_2) \quad (4.99) \end{aligned}$$

For simplicity, we assume the transmitted laser pulse and the receiver impulse response are both Gaussian in shape, with rms width σ_f and σ_h , respectively. In this case, we have

$$\begin{aligned} E[S(t)] &= \left[\frac{\eta}{hf_o} \right] |c_o|^2 A_R \sum_{i=1}^{N_r} \beta_i |a_T(\underline{\rho}_i, z)|^2 G(\sqrt{\sigma_h^2 + \sigma_f^2}, t - \psi_i) \\ &\cong \left[\frac{\eta}{hf_o} \right] |c_o|^2 A_R |a_T(\underline{\rho}_o, z)|^2 \sum_{i=1}^{N_r} \beta_i G(\sqrt{\sigma_h^2 + \sigma_f^2}, t - \psi_i) \quad (4.100) \end{aligned}$$

and

$$\begin{aligned} C_S(t_1, t_2) &= \left[\frac{\eta}{hf_o} \right] |c_o|^2 A_R G(\sqrt{\sigma_h^2 + \sigma_f^2}, t_1 - t_2) \sum_{i=1}^{N_r} \beta_i |a_T(\underline{\rho}_i, z)|^2 \\ &\cdot G\left(\sqrt{\frac{\sigma_h^2}{2} + \sigma_f^2}, \frac{t_1 + t_2}{2} - \psi_i\right) + \left[\frac{\eta}{hf_o} \right]^2 |c_o|^4 \\ &\cdot G(\sqrt{2} \sqrt{\sigma_h^2 + \sigma_f^2}, t_1 - t_2) \sum_{i=1}^{N_r} \sum_{\substack{j=1 \\ i \neq j}}^{N_r} \beta_i \beta_j |a_T(\underline{\rho}_i, z)|^2 |a_T(\underline{\rho}_j, z)|^2 \\ &\cdot \mathcal{Q}_w^2\left(\frac{k_o}{z} [\underline{\rho}_i - \underline{\rho}_j]\right) \exp[-(\psi_i - \psi_j)^2 / 4 \sigma_f^2] G\left(\sqrt{(\sigma_f^2 + \sigma_h^2)/2}, \frac{t_1 + t_2}{2} - \frac{\psi_i + \psi_j}{2}\right) \end{aligned}$$

$$\begin{aligned}
&\cong \left[\frac{n}{hf_o} \right] |c_o|^2 A_R G(\sqrt{2} \sigma_h, t_1 - t_2) |a_T(\underline{\rho}_o, z)|^2 \sum_{i=1}^{N_r} \beta_i G \left(\sqrt{\frac{\sigma_h^2}{2} + \sigma_f^2}, \frac{t_1 + t_2}{2} - \psi_i \right) \\
&+ \left[\frac{n}{hf_o} \right]^2 |c_o|^4 G(\sqrt{2} \sqrt{\sigma_h^2 + \sigma_f^2}, t_1 - t_2) |a_T(\underline{\rho}_o, z)|^2 A_R^2 \sum_{i=1}^{N_r} \sum_{\substack{j=1 \\ i \neq j}}^{N_r} \beta_i \beta_j \exp \left[-\frac{(\psi_i - \psi_j)^2}{4\sigma_f^2} \right] \\
&\cdot G \left(\sqrt{\frac{\sigma_h^2 + \sigma_f^2}{2}}, \frac{t_1 + t_2}{2} - \frac{\psi_i + \psi_j}{2} \right), \quad (4.101)
\end{aligned}$$

where

$$\psi_i = 2z/c - \frac{\rho_i^2}{cz} + \frac{2\xi_i}{c}. \quad (4.102)$$

$\underline{\rho}_o$ is the coordinate of the center of the satellite. The first term in Eq. (4.101) is due to shot noise while the second term is due to speckle. We see that shot noise has a correlation length of about $2\sqrt{2} \sigma_h$, and speckle has a correlation length of about $2\sqrt{2}(\sigma_h^2 + \sigma_f^2)^{1/2}$. Also, we find that for the second term in Eq. (4.101) the terms inside the double summations are significant only when ψ_i and ψ_j satisfy

$$\psi_i - \psi_j < 2\sqrt{2} \sigma_f \quad (4.103)$$

or

$$-\left(\frac{\rho_i^2}{cz} - \frac{\rho_j^2}{cz} \right) + \frac{2}{c} (\xi_i - \xi_j) < 2\sqrt{2} \sigma_f. \quad (4.104)$$

Since ρ_i^2/cz , the optical beam curvature term, is very small, we have equivalently

$$(\xi_i - \xi_j) < \sqrt{2}c \sigma_f. \quad (4.105)$$

This shows that only the reflections from reflectors that are separated vertically less than the width of the transmitted pulse will interfere with each other. For a transmitted pulse width of 24 psec, only reflectors that

are separated less than 2 cm will cause interference, but for a pulse width of 2 nsec, reflections from reflectors as far as 42 cm apart will interfere. Therefore, to minimize speckle, a shorter laser pulse should be used. In this case, only when two or more retroreflectors happen to lie on the same plane will there be interference.

We plot the waveforms for two possible LAGEOS orientations and the results are shown in Figs. 4.22 and 4.23. In the figure, the rms widths of the transmitted pulse and receiver impulse response are both equal to 1 cm. The time and the magnitude scales in the figures are relative. From the figures we see that, while the variance due to shot noise is proportional to the signal, the variance due to speckle may not be. For example, in Fig. 4.23, the leading edge of the return pulse is caused by the reflection from only the first reflector; no interference occurs so there is no speckle. In Fig. 4.24, we show the results for the same geometry as in Fig. 4.23, but both the widths of the transmitted pulse and receiver impulse response are doubled. In this case, the long transmitted laser pulse smooths out the received pulse, and the return from the individual reflector cannot be temporally resolved.

4.6. Summary

In this chapter, we studied the statistical properties of time-resolved speckle and the effects of time-resolved speckle on the timing performance of the receiver. The results indicate that, in general, the presence of time-resolved speckle causes the mean square timing error to increase roughly by a factor of $\langle N \rangle / K$. If K is smaller than $\langle N \rangle$, the timing accuracy is limited by speckle.

Since the theory is derived under the high signal-to-noise ratio assumption, the timing performance of the receiver in the low signal level

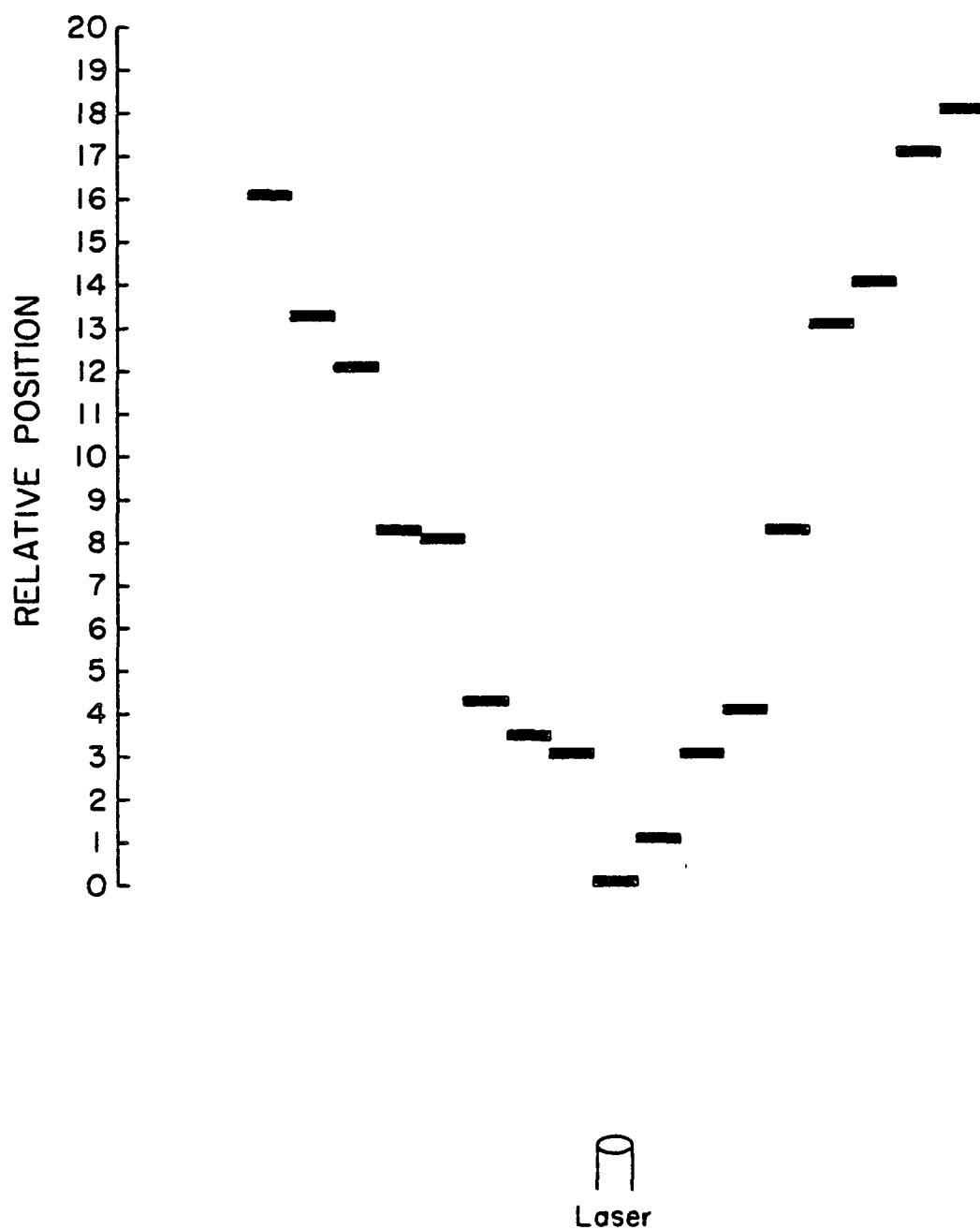


Figure 4.22a. Schematic diagram of the laser and the retroreflectors on LAGEOS. Relative position in units of transmitted pulse width.

Total Number of Illuminated Retroreflectors = 17

reflector #	Cross Section	Relative Position
1	1.000000	0.000000
2	0.950000	1.000000
3	0.900000	3.000000
4	0.900000	3.000000
5	0.900000	3.500000
6	0.850000	4.000000
7	0.850000	4.200000
8	0.800000	8.000000
9	0.700000	8.200000
10	0.700000	8.200000
11	0.300000	12.000000
12	0.300000	13.000000
13	0.400000	15.200000
14	0.350000	14.000000
15	0.300000	16.000000
16	0.200000	17.000000
17	0.150000	18.000000

1. Relative position in units of transmitted pulse width
2. Cross section is relative

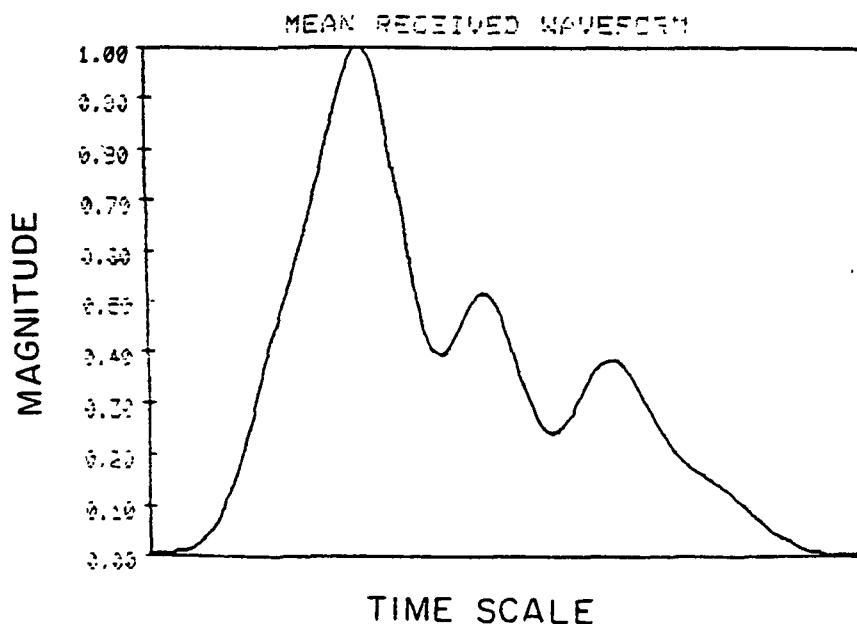


Figure 4.22b. Simulated results for reflection from LAGEOS.

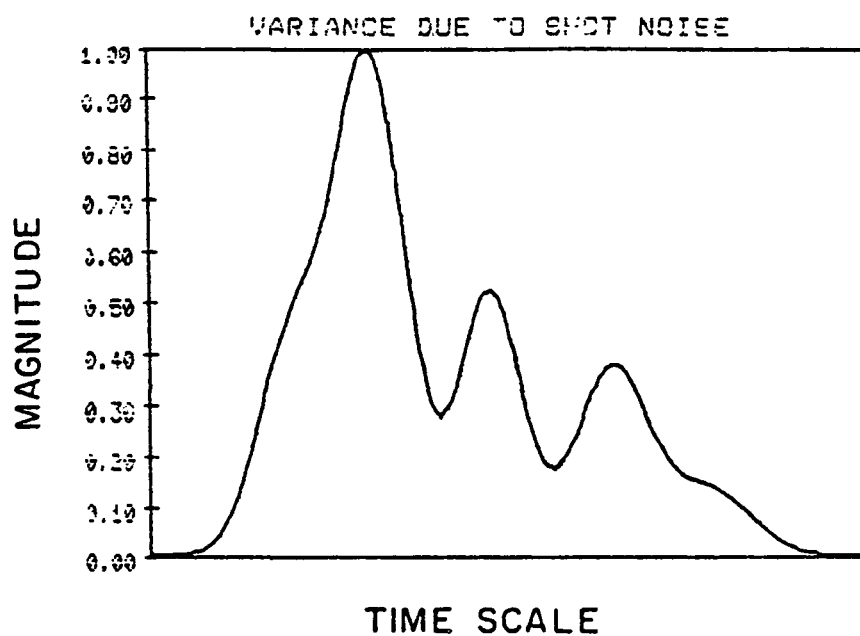


Figure 4.22c. Simulated results for reflection from LAGEOS for variance due to shot noise.

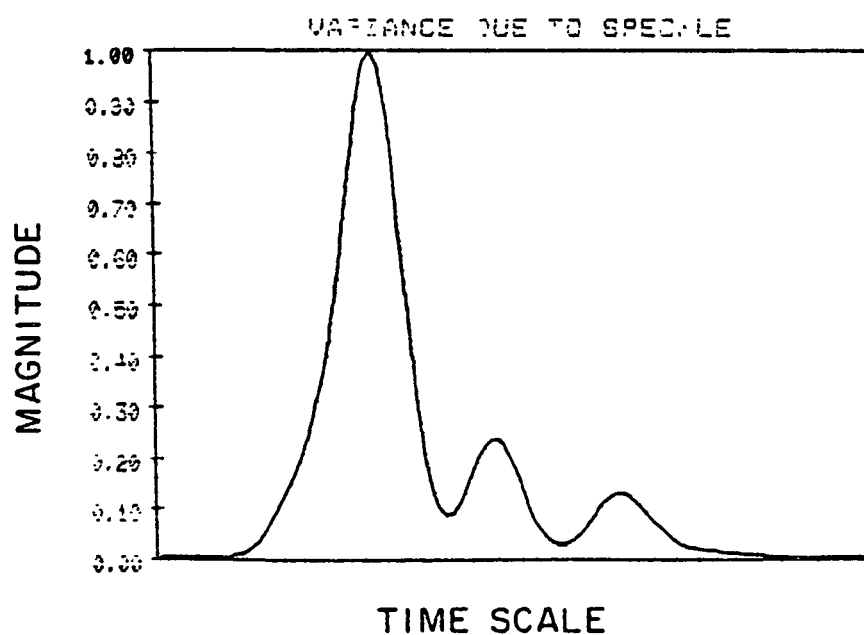


Figure 4.22d. Simulated results for reflection from LAGEOS for variance due to speckle.

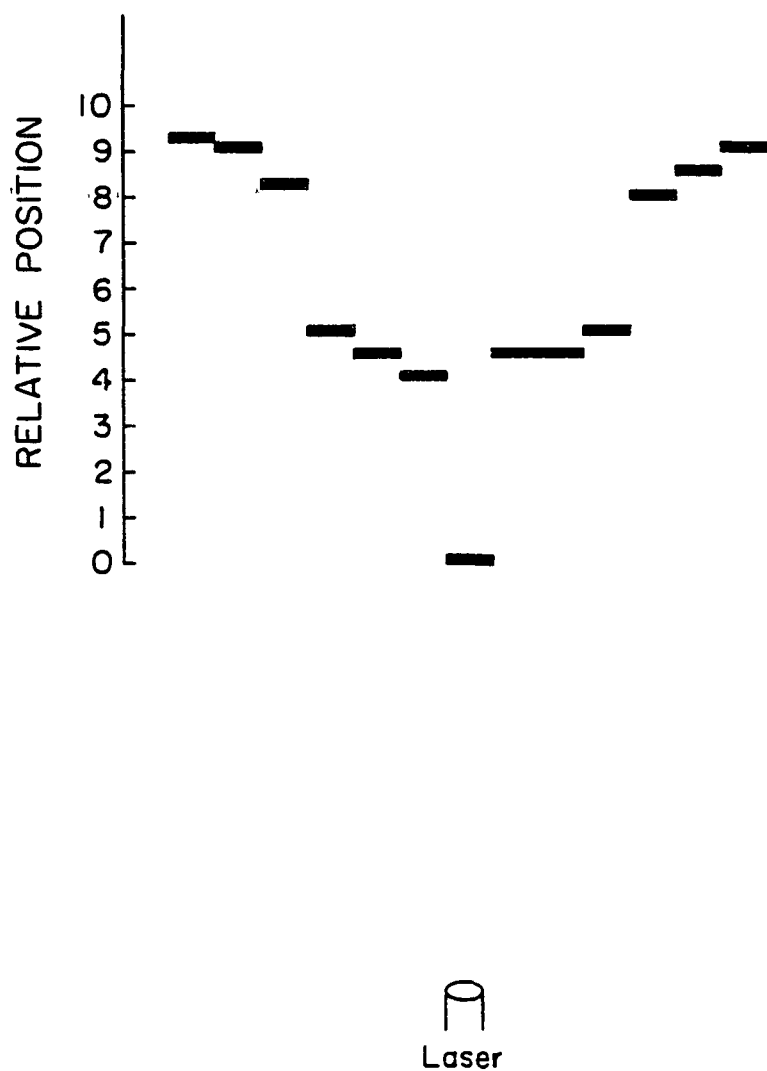


Figure 4.23a. Schematic diagram of the laser and the retroreflectors on LAGEOS. Relative position in units of transmitted pulse width.

total Number of Illuminated Retroreflectors = 13

Reflector #	Cross Section	Relative Position
1	1.000000	0.000000
2	0.800000	1.000000
3	0.800000	4.500000
4	0.800000	4.500000
5	0.750000	4.500000
6	0.750000	5.000000
7	0.750000	5.000000
8	0.400000	8.000000
9	0.400000	8.200000
10	0.350000	8.500000
11	0.300000	9.000000
12	0.200000	9.000000
13	0.200000	9.200000

1. Relative position in units of transmitted pulse width
2. Cross section is relative

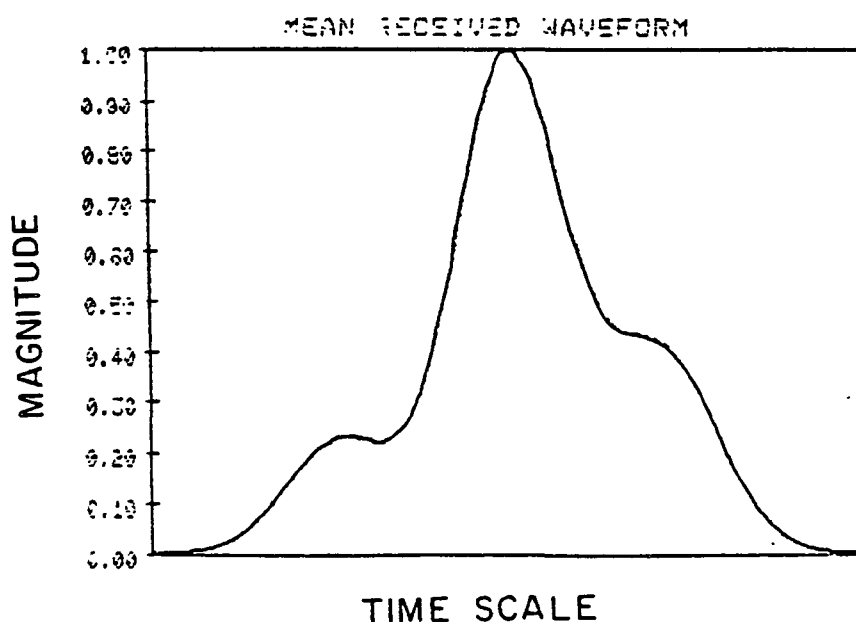


Figure 4.23b. Simulated results for reflection from LAGEOS.

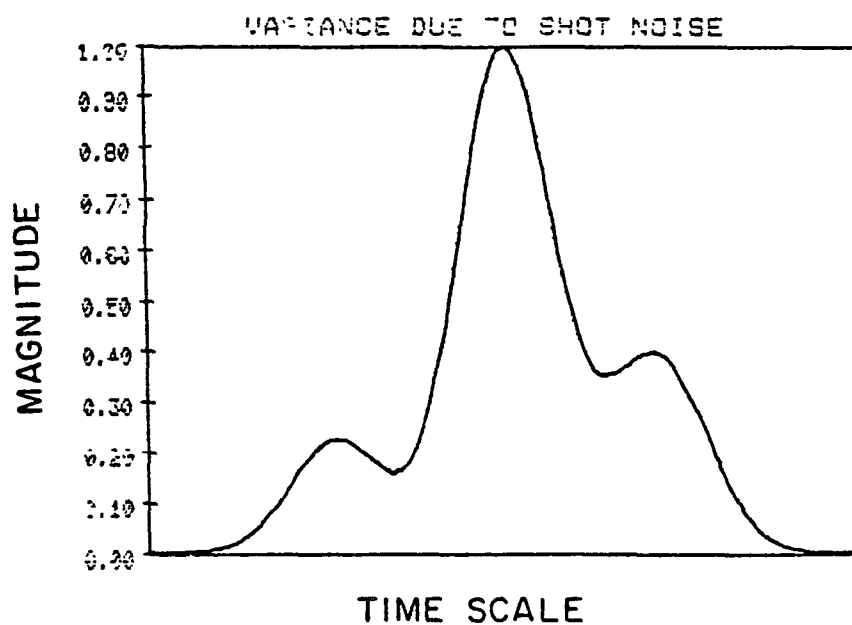


Figure 4.23c. Simulated results for reflection from LAGEOS for variance due to shot noise.

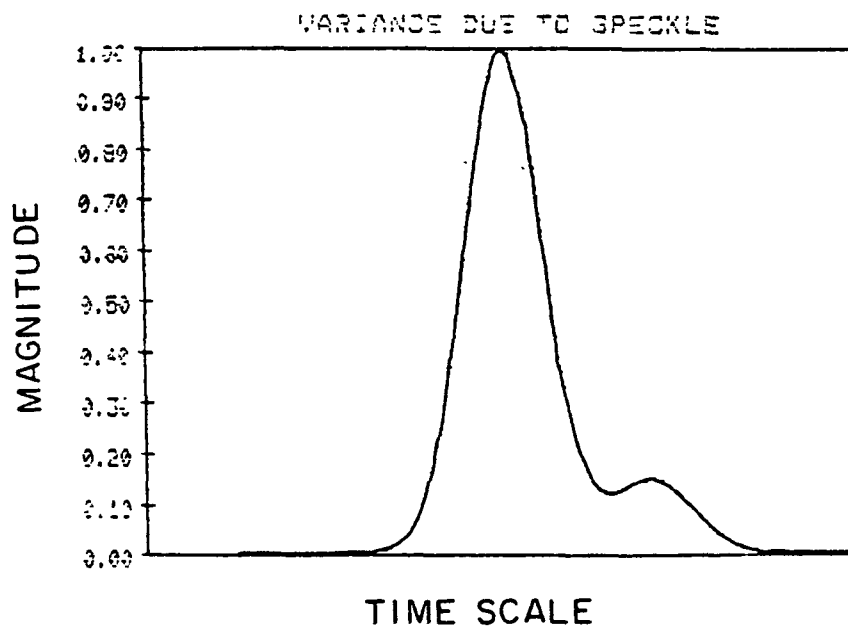


Figure 4.23d. Simulated results for reflection from LAGEOS for variance due to speckle.

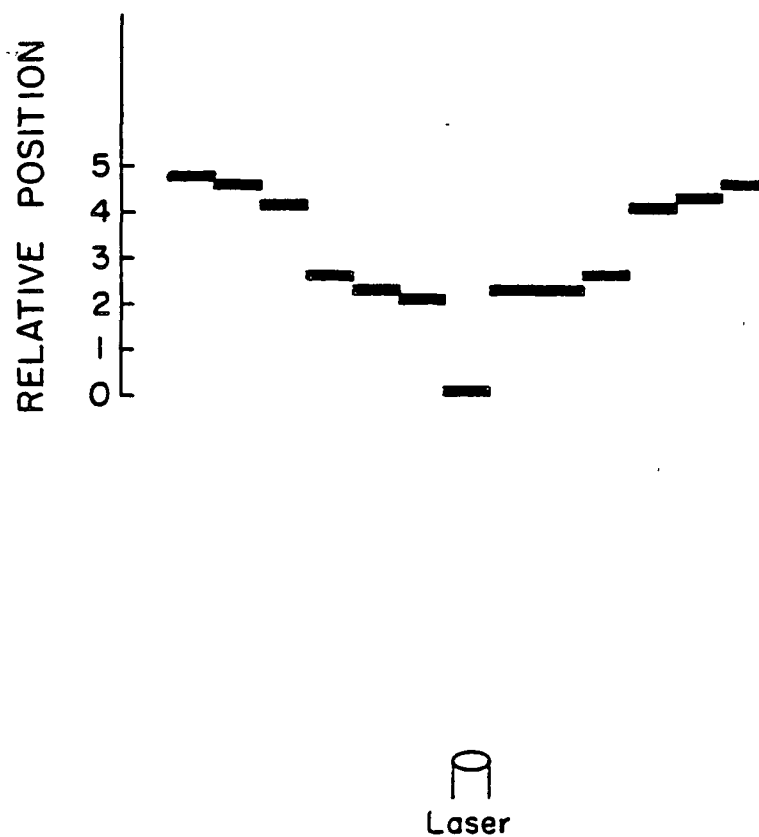


Figure 4.24a. Schematic diagram of the laser and the retroreflector on LAGEOS. Relative position in units of transmitted pulse width.

Total Number of Illuminated Retroreflectors = 10

Reflector #	Cross Section	Relative Position
1	1.000000	0.000000
2	0.800000	2.000000
3	0.800000	2.250000
4	0.800000	2.250000
5	0.750000	2.250000
6	0.750000	2.500000
7	0.750000	2.500000
8	0.400000	4.000000
9	0.400000	4.100000
10	0.350000	4.250000
11	0.300000	4.500000
12	0.200000	4.500000
13	0.200000	4.600000

1. Relative position in units of transmitted pulse width
2. Cross section is relative

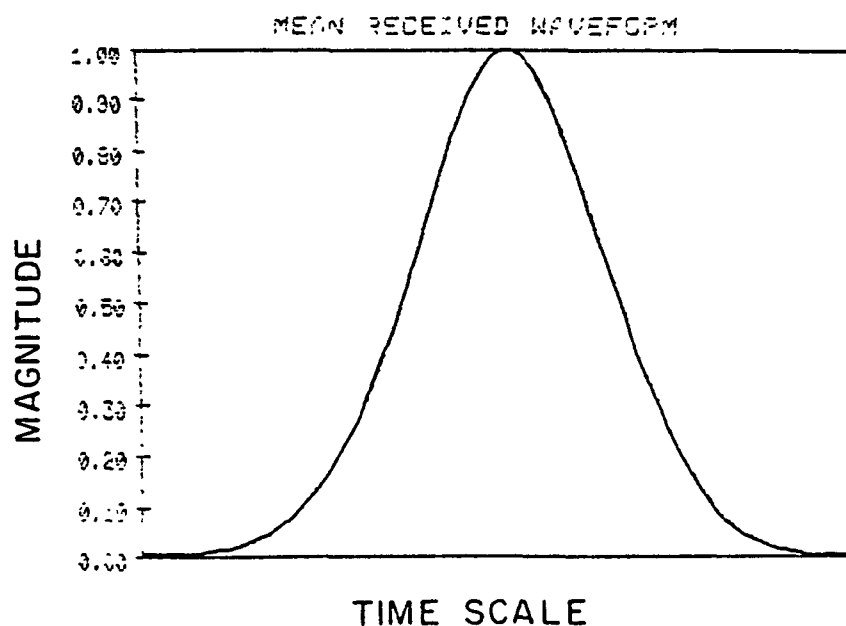


Figure 4.24b. Simulated results for reflection from LAGEOS.

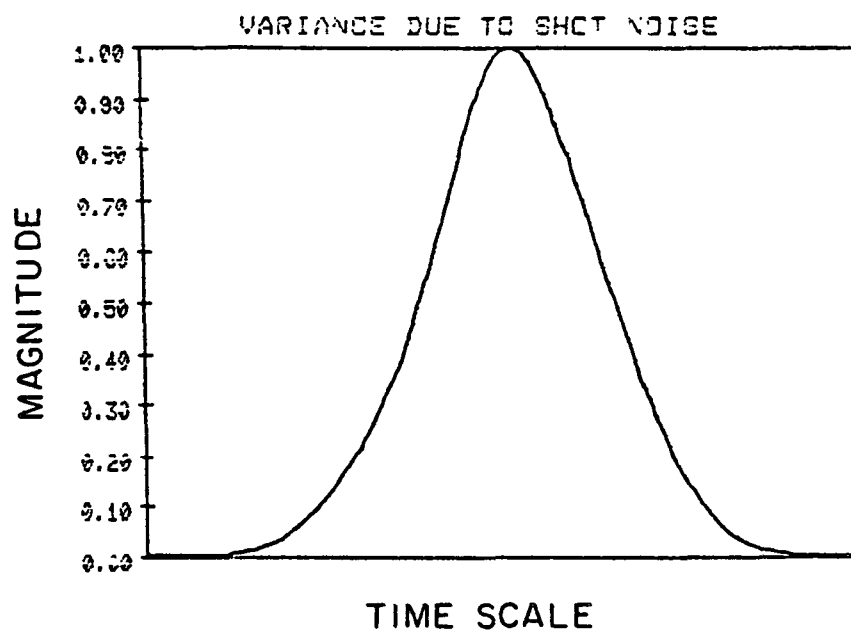


Figure 4.24c. Simulated results for reflection from LAGEOS for variance due to shot noise.

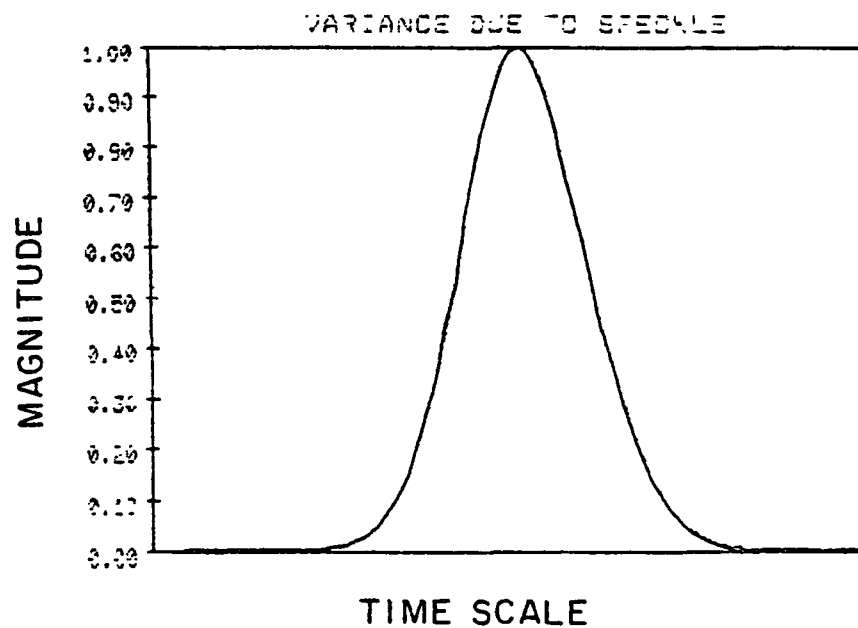


Figure 4.24d. Simulated results for reflection from LAGEOS for variance due to speckle.

case can be more accurately obtained by a computer simulation. The results from the theory and simulation come into good agreement when the signal-to-noise ratio is high.

There are targets that give rise to partially developed speckle. The reflections of laser light from a specific target, the LAGEOS, are investigated to illustrate the approach taken in analyzing partially developed time-resolved speckle.

5. ESTIMATION OF DIFFERENTIAL ARRIVAL TIME

5.1. Introduction

To infer pressure, we need to measure the difference in the round-trip propagation times between two pulses which were transmitted simultaneously at two different wavelengths. In this chapter, we first evaluate and compare the performances of various timing algorithms. The relation between the timing accuracy and signal bandwidth is investigated in Section 5.3. In Section 5.4, timing algorithms are compared for simulated ocean reflected pulse shapes. In Section 5.5, the transmitter effects are considered. The effects of the sampling process are studied in Section 5.6.

5.2. Timing Algorithms

The Maximum Likelihood (ML) estimator for the differential delay can be expressed as

$$\begin{aligned}
 \hat{\tau}_{12_{ML}} &= \widehat{(\tau_2 - \tau_1)}_{ML} \\
 &= \hat{\tau}_{2_{ML_2}} - \hat{\tau}_{1_{ML_2}} \\
 &= \arg \max_{\tau_2} [p(S_1(t), S_2(t) | \tau_2)] - \arg \max_{\tau_1} [p(S_1(t), S_2(t) | \tau_1)] ,
 \end{aligned} \tag{5.1}$$

where τ_1 and τ_2 are the arrival times of the laser pulses at the two wavelengths. In Eq. (5.1) $S_1(t)$ and $S_2(t)$ are the received signals at wavelengths λ_1 and λ_2 , respectively. $\hat{\tau}_{1_{ML_2}}$ and $\hat{\tau}_{2_{ML_2}}$ are the ML estimates of τ_1 and τ_2 when both S_1 and S_2 are observed.

Since the two wavelengths are widely separated, the speckle-induced fluctuations at the two channels are uncorrelated. Also, since the shot noises of the two channels are independent, Eq. (5.1) can be simplified to

$$\begin{aligned}
\hat{\tau}_{12_{ML}} &= \arg \max_{\tau_2} [p(S_2(t) | \tau_2)] - \arg \max_{\tau_1} [p(S_1(t) | \tau_1)] \\
&= \hat{\tau}_{2_{ML}} - \hat{\tau}_{1_{ML}}, \quad (5.2)
\end{aligned}$$

where $\hat{\tau}_{2_{ML}}$ and $\hat{\tau}_{1_{ML}}$ are the ML estimates of individual channels. Equation (5.2) shows that the ML estimate of the differential delay is simply the difference of the single channel ML estimates of the arrival times of the two wavelengths.

The single channel ML estimate of the arrival time when speckle is not severe was given previously in Chapter 4; the integral version of the estimator [13] is written here for convenience

$$\hat{\tau}_{i_{ML}} = \arg \max_{\tau_i} \left[\int_{-\infty}^{\infty} dt S_i(t) \ln \bar{S}_i(t + \tau_i) \right], \quad i = 1, 2 \quad (5.3)$$

where \bar{S}_i is the expected value of S_i . Unfortunately, implementation of the ML estimator requires prior knowledge of the expected received pulse shape. Because of the random and dynamic nature of the ocean surface, the received pulse shapes will change randomly as the surface profile within the footprint changes. Since it is not possible to predict the expected pulse shapes a priori, a suboptimal estimator that does not require knowledge of the pulse shape is needed.

If the laser beams at the two wavelengths are aligned so that their footprints overlap, the reflected pulse shapes will be almost identical. We can write \bar{S}_1 and \bar{S}_2 as

$$\bar{S}_1(t) = \langle N_1 \rangle F(t) \quad (5.4)$$

and

$$\bar{S}_2(t) = \langle N_2 \rangle F(t - \tau_{12}) , \quad (5.5)$$

where $F(t)$ is the normalized mean received waveform. One of the simplest techniques for estimating the differential propagation time is to calculate the peak of the correlation function of the two received pulses

$$\begin{aligned} \hat{\tau}_{12} &= \arg \max_{\tau} \left[\int_{-\infty}^{\infty} dt S_1(t) S_2(t + \tau) \right] \\ &= \arg \max_{\tau} [R_{12}(\tau)] , \end{aligned} \quad (5.6)$$

where R_{12} is the cross correlation function.

Assuming $R_{12}(\tau)$ to be differentiable, we have

$$\dot{R}_{12}(\hat{\tau}_{12}) = 0 . \quad (5.7)$$

By expanding $R_{12}(\tau)$ in terms of the Taylor series expansion centered around the actual differential delay τ_{12} , we can write [16]

$$\epsilon = \hat{\tau}_{12} - \tau_{12} \cong - \frac{\dot{R}_{12}(\tau_{12})}{\ddot{R}_{12}(\tau_{12})} , \quad (5.8)$$

where ϵ is the error of the estimator.

If the shot noise and speckle are not severe so that

$E\{\ddot{R}_{12}(\tau_{12})\}^2 \gg \text{Var}\{\ddot{R}_{12}(\tau_{12})\}$, then the bias and Mean Square Error (MSE) are given by

$$\text{Bias} = E\{\epsilon\} \cong - \frac{E\{\dot{R}_{12}(\tau_{12})\}}{E\{\ddot{R}_{12}(\tau_{12})\}} \quad (5.9)$$

and

$$\text{MSE} = E\{\epsilon^2\} \cong \frac{E\{\dot{R}_{12}^2(\tau_{12})\}}{E\{\ddot{R}_{12}(\tau_{12})\}^2} . \quad (5.10)$$

The numerator on the right-hand side of Eq. (5.9) can be written explicitly as

$$\begin{aligned} E\{\dot{R}_{12}(\tau_{12})\} &= \int_{-\infty}^{\infty} dt \bar{S}_1(t) \frac{\partial}{\partial \tau} \bar{S}_2(t + \tau) \Big|_{\tau=\tau_{12}} \\ &= \langle N_1 \rangle \langle N_2 \rangle \int_{-\infty}^{\infty} dt F(t) \dot{F}(t) . \end{aligned} \quad (5.11)$$

Equation (5.11) is zero if the entire return pulse always stays inside the observation interval. Therefore, the correlation algorithm is unbiased.

The MSE given by Eq. (5.10) can be evaluated as follows:

$$\begin{aligned} E\{\dot{R}_{12}^2(\tau_{12})\} &= E \left\{ \int_{-\infty}^{\infty} dt_1 \int_{-\infty}^{\infty} dt_2 S_1(t_1) S_1(t_2) \frac{\partial}{\partial \tau_1} S_2(t_1 + \tau_1) \right. \\ &\quad \left. \cdot \frac{\partial}{\partial \tau_2} S_2(t_2 + \tau_2) \Big|_{\tau_1=\tau_2=\tau_{12}} \right\} \\ &= \int_{-\infty}^{\infty} dt_1 \int_{-\infty}^{\infty} dt_2 R_{S_1}(t_1, t_2) \frac{\partial^2}{\partial \tau_1 \partial \tau_2} R_{S_2}(t_1 + \tau_1, t_2 + \tau_2) \Big|_{\tau_1=\tau_2=\tau_{12}} \end{aligned} \quad (5.12)$$

and

$$E\{\ddot{R}(\tau_{12})\} = \int_{-\infty}^{\infty} dt \bar{S}_1(t) \frac{\partial^2}{\partial^2 \tau} \bar{S}_2(t + \tau) \Big|_{\tau=\tau_{12}} , \quad (5.13)$$

where

$$R_{S_i}(t_1, t_2) = E\{S_i(t_1) S_i(t_2)\} = C_{S_i}(t_1, t_2) + \bar{S}_i(t_1) \bar{S}_i(t_2) . \quad (5.14)$$

By substituting Eqs. (5.12) and (5.13) into Eq. (5.10), we have

$$\text{MSE} = \frac{\int_{-\infty}^{\infty} dt_1 \int_{-\infty}^{\infty} dt_2 R_{S_1}(t_1, t_2) \frac{\partial^2}{\partial \tau_1 \partial \tau_2} R_{S_2}(t_1 + \tau_1, t_2 + \tau_2) \Big|_{\tau_1=\tau_2=\tau_{12}}}{\int_{-\infty}^{\infty} dt \bar{S}_1(t) \ddot{\bar{S}}_2(t + \tau_{12})^2}$$

$$\begin{aligned}
& \frac{\partial^2}{\partial \tau_1 \partial \tau_2} \left\{ \int_{-\infty}^{\infty} dt_1 \int_{-\infty}^{\infty} dt_2 \bar{s}_1(t_1) \bar{s}_1(t_2) \bar{s}_2(t_1 + \tau_1) \bar{s}_2(t_2 + \tau_2) \right\} \Big|_{\tau_1 = \tau_2 = \tau_{12}} \\
& = \frac{\left\{ \int_{-\infty}^{\infty} dt \bar{s}_1(t) \ddot{\bar{s}}_2(t + \tau_{12}) \right\}^2}{\left\{ \int_{-\infty}^{\infty} dt \bar{s}_1(t) \ddot{\bar{s}}_2(t + \tau_{12}) \right\}^2} \\
& + \frac{\frac{\partial^2}{\partial \tau_1 \partial \tau_2} \left\{ \int_{-\infty}^{\infty} dt_1 \int_{-\infty}^{\infty} dt_2 \bar{s}_1(t_1) \bar{s}_1(t_2) c_{s_2}(t_1 + \tau_1, t_2 + \tau_2) \right\} \Big|_{\tau_1 = \tau_2 = \tau_{12}}}{\left\{ \int_{-\infty}^{\infty} dt \bar{s}_1(t) \ddot{\bar{s}}_2(t + \tau_{12}) \right\}^2} \\
& + \frac{\frac{\partial^2}{\partial \tau_1 \partial \tau_2} \left\{ \int_{-\infty}^{\infty} dt_1 \int_{-\infty}^{\infty} dt_2 c_{s_1}(t_1, t_2) \bar{s}_2(t_1 + \tau_1) \bar{s}_2(t_2 + \tau_2) \right\} \Big|_{\tau_1 = \tau_2 = \tau_{12}}}{\left\{ \int_{-\infty}^{\infty} dt \bar{s}_1(t) \ddot{\bar{s}}_2(t + \tau_{12}) \right\}^2} \\
& + \frac{\frac{\partial^2}{\partial \tau_1 \partial \tau_2} \left\{ \int_{-\infty}^{\infty} dt_1 \int_{-\infty}^{\infty} dt_2 c_{s_1}(t_1, t_2) c_{s_2}(t_1 + \tau_1, t_2 + \tau_2) \right\} \Big|_{\tau_1 = \tau_2 = \tau_{12}}}{\left\{ \int_{-\infty}^{\infty} dt \bar{s}_1(t) \ddot{\bar{s}}_2(t + \tau_{12}) \right\}^2} .
\end{aligned} \tag{5.15}$$

The first term on the right-hand side of Eq. (5.15) equals the square of the bias, which was shown previously to be zero. The second and third terms are the first-order terms. They represent the errors from correlating the received signals with their corresponding mean waveforms. The last term is the second-order term. It is the additional error from correlating two fluctuating pulses. If the mean pulse shape were known in advance and each received pulse were correlated with its mean waveform, then the sum of the second and third terms would be the total error. Since

we do not know the mean pulse shape, we correlate the two received pulses with each other. In this case both pulses are distorted by speckle and shot noise and correlating two distorted pulses gives rise to the additional second-order error term.

For a target that gives rise to a Gaussian shape mean received waveform, Eq. (5.15) can be evaluated in closed form. While the detailed calculations are shown in Appendix A, the results are

$$\begin{aligned}
 \text{MSE} = & \left(\frac{1}{\langle N_1 \rangle} + \frac{1}{\langle N_2 \rangle} \right) \frac{2\sqrt{2}(\sigma_f^2 + \sigma_T^2)(\sigma_h^2 + \sigma_f^2 + \sigma_T^2)^3}{(2\sigma_h^2 + \sigma_f^2 + \sigma_T^2)^{3/2} (\sigma_h^2 + \frac{3}{2}\sigma_f^2 + \frac{3}{2}\sigma_T^2)^{3/2}} \\
 & + \left(\frac{1}{K_1} + \frac{1}{K_2} \right) \frac{2\sqrt{2}\sigma_T^2(\sigma_h^2 + \sigma_f^2 + \sigma_T^2)^3}{(2\sigma_h^2 + 2\sigma_f^2 + \sigma_T^2)^{3/2} (\sigma_h^2 + \frac{3}{2}\sigma_f^2 + 2\sigma_T^2)^{3/2}} \\
 & + \left(\frac{1}{\langle N_1 \rangle K_2} + \frac{1}{\langle N_2 \rangle K_1} \right) \frac{2\sqrt{2}(\sigma_f^2 + 2\sigma_T^2)(\sigma_h^2 + \sigma_f^2 + \sigma_T^2)^3}{(2\sigma_h^2 + \sigma_f^2)^{3/2} (\sigma_h^2 + \frac{3}{2}\sigma_f^2 + 2\sigma_T^2)^{3/2}} \\
 & + \frac{1}{\langle N_1 \rangle \langle N_2 \rangle} \frac{2(\sigma_f^2 + \sigma_T^2)(\sigma_f^2 + \sigma_h^2 + \sigma_T^2)^3}{\sigma_h^3(\sigma_h^2 + 2\sigma_f^2 + 2\sigma_T^2)^{3/2}} \\
 & + \frac{1}{K_1 K_2} \frac{2\sigma_T^2(\sigma_h^2 + \sigma_f^2 + \sigma_T^2)^3}{(\sigma_h^2 + \sigma_f^2)^{3/2} (\sigma_h^2 + \sigma_f^2 + 2\sigma_T^2)^{3/2}} \tag{5.16}
 \end{aligned}$$

where σ_f and σ_h are the rms widths of the transmitted pulse intensity and receiver impulse response, respectively, and σ_T is the rms time spread of the target.

For the case of reflection from a very small or point target, $\sigma_T \approx 0$, Eq. (5.16) reduces to

$$\begin{aligned}
 \text{MSE} = & \left(\frac{1}{\langle N_1 \rangle} + \frac{1}{\langle N_2 \rangle} \right) \frac{2\sqrt{2} \sigma_f^2 (\sigma_h^2 + \sigma_f^2)^3}{(2\sigma_h^2 + \sigma_f^2)^{3/2} (\sigma_h^2 + \frac{3}{2} \sigma_f^2)^{3/2}} \\
 & + \left(\frac{1}{\langle N_1 \rangle K_2} + \frac{1}{\langle N_2 \rangle K_1} \right) \frac{2\sqrt{2} \sigma_f^2 (\sigma_h^2 + \sigma_f^2)^3}{(2\sigma_h^2 + \sigma_f^2)^{3/2} (\sigma_h^2 + \frac{3}{2} \sigma_f^2)^{3/2}} \\
 & + \frac{1}{\langle N_1 \rangle \langle N_2 \rangle} \frac{2\sigma_f^2 (\sigma_f^2 + \sigma_h^2)^3}{\sigma_h^3 (\sigma_h^2 + 2\sigma_f^2)^{3/2}} \quad . \quad (5.17)
 \end{aligned}$$

Here we see that speckle does not contribute to the first-order timing-error terms. In this case, the target does not cause any broadening in the return pulses. Therefore, the speckle-induced fluctuations have a correlation length as wide as the received pulse. The effect of speckle is only to cause the amplitude of the received pulse to fluctuate and not distort the received pulse shape. Since the speckle only affects the amplitude of the received pulse, it will not degrade the correlation. However, shot noise still causes distortion of the received waveforms because it has a correlation length which is smaller than the pulse width.

For reflections from the ocean, the most realistic case is $\sigma_T \gg \sigma_f$ and $\sigma_T \gg \sigma_h$. The MSE for this case is

$$\begin{aligned}
 \text{MSE} = & 1.54 \left(\frac{1}{\langle N_1 \rangle} + \frac{1}{\langle N_2 \rangle} + \frac{1}{K_1} + \frac{1}{K_2} \right) \sigma_T^2 \\
 & + \left(\frac{1}{\langle N_1 \rangle K_2} + \frac{1}{\langle N_2 \rangle K_1} \right) \frac{2\sqrt{2} \sigma_T^2}{\left(2 \frac{\sigma_h^2}{\sigma_T^2} + \frac{\sigma_f^2}{\sigma_T^2} \right)^{3/2}}
 \end{aligned}$$

$$+ \frac{\sigma_T^5}{\sqrt{2} \langle N_1 \rangle \langle N_2 \rangle \alpha_h^3} + \frac{\sigma_T^2}{\sqrt{2} K_1 K_2 \left(\frac{\sigma_h^2}{\sigma_T^2} + \frac{\sigma_f^2}{\sigma_T^2} \right)^{3/2}} . \quad (5.18)$$

From this we see that the second-order terms are roughly proportional to $\frac{\sigma_T^3}{\alpha_h^3}$. To prevent the second-order terms from becoming too large, α_h should not be too small compared to σ_T . This means that the resolution of the receiver should not exceed the bandwidth of the returned signal.

The ML estimator given in Eq. (5.3) correlates the received pulse with the logarithm of the mean pulse shape. It is interesting to consider correlating the received pulse at one wavelength with the logarithm of the received pulse at the other wavelength, i.e.,

$$\hat{\tau}_{12} = \arg \max_{\tau} \left\{ \int_{-\infty}^{\infty} dt S_2(t + \tau) \ln S_1(t) \right\} . \quad (5.19)$$

If S_1 has a high signal-to-noise ratio, we have

$$\begin{aligned} \ln S_1(t) &= \ln \{ \bar{S}_1(t) + \Delta S_1(t) \} \\ &\approx \ln \bar{S}_1(t) + \frac{\Delta S_1(t)}{\bar{S}_1(t)} . \end{aligned} \quad (5.20)$$

Using Eq. (5.20), we find the bias and MSE of the estimator are given by

$$\begin{aligned} \text{Bias} &= \frac{\int_{-\infty}^{\infty} dt \dot{\bar{S}}_2(t + \tau_{12}) \ln \bar{S}_1(t)}{\int_{-\infty}^{\infty} dt \ddot{\bar{S}}_2(t + \tau_{12}) \ln \bar{S}_1(t)} \\ &= \frac{\int_{-\infty}^{\infty} dt \dot{F}(t) \ln F(t)}{\int_{-\infty}^{\infty} dt \ddot{F}(t) \ln F(t)} = 0 , \end{aligned} \quad (5.21)$$

$$\begin{aligned}
\text{MSE} &= \frac{E \left\{ \frac{\partial^2}{\partial \tau_1 \partial \tau_2} \int_{-\infty}^{\infty} dt_1 \int_{-\infty}^{\infty} dt_2 S_2(t_1 + \tau_1) S_2(t_2 + \tau_2) \right. \\
&\quad \left. E \left\{ \frac{\partial^2}{\partial \tau^2} \int_{-\infty}^{\infty} dt S_2(t + \tau) \ln S_1(t) \right|_{\tau=\tau_{12}} \right\}^2 \\
&\quad \left[\ln \bar{S}_1(t_1) + \frac{\Delta S_1(t_1)}{S_1(t_1)} \right] \left[\ln \bar{S}_1(t_2) + \frac{\Delta S_1(t_2)}{S_1(t_2)} \right] \Big|_{\tau_1=\tau_2=\tau_{12}} \Big\}}{E \left\{ \frac{\partial^2}{\partial \tau^2} \int_{-\infty}^{\infty} dt S_2(t + \tau) \ln S_1(t) \right|_{\tau=\tau_{12}} \right\}^2} \\
&= \frac{\int_{-\infty}^{\infty} dt_1 \int_{-\infty}^{\infty} dt_2 \frac{\partial^2}{\partial \tau_1 \partial \tau_2} R_{S_2}(t_1 + \tau_1, t_2 + \tau_2) \Big|_{\tau_1=\tau_2=\tau_{12}}}{\left\{ \int_{-\infty}^{\infty} dt \ddot{\bar{S}}_2(t + \tau_{12}) \ln \bar{S}_1(t) \right\}^2} \\
&\quad \frac{\left[\ln \bar{S}_1(t_1) \ln \bar{S}_1(t_2) + \frac{C_{S_1}(t_1, t_2)}{S_1(t_1) S_1(t_2)} \right]}{\left\{ \int_{-\infty}^{\infty} dt \ddot{\bar{S}}_2(t + \tau_{12}) \ln \bar{S}_1(t) \right\}^2} . \tag{5.22}
\end{aligned}$$

For a Gaussian return pulse shape, we have

$$\begin{aligned}
\text{MSE} &= \left(\frac{1}{\langle N_1 \rangle} + \frac{1}{\langle N_2 \rangle} + \frac{1}{K_1} + \frac{1}{K_2} \right) \sigma_T^2 + \frac{\sigma_f^2}{\langle N_1 \rangle} + \frac{\sigma_f^2}{\langle N_2 \rangle} \\
&\quad + \left(\frac{1}{\langle N_1 \rangle K_2} + \frac{1}{\langle N_2 \rangle K_1} \right) \frac{\sigma_T^6}{\sqrt{2} \left(\sigma_f^2 + \sigma_h^2 \right)^{1/2} \left(2\sigma_h^2 + \sigma_f^2 \right)^{3/2}} \\
&\quad + \frac{\sigma_T^6}{4\sigma_h^4 \langle N_1 \rangle \langle N_2 \rangle} + \frac{\sigma_T^6}{4(\sigma_h^2 + \sigma_f^2)^2 K_1 K_2} , \tag{5.23}
\end{aligned}$$

where we have assumed σ_T to be large compared with σ_f and σ_h . Comparing

Eq. (5.23) with Eq. (5.16), we find correlating with the logarithm of the other pulse has slightly smaller first-order terms, but it has second-order terms that are proportional to σ_T^4/σ_h^4 , which can be much larger than those of the correlation receiver, which are proportional to σ_T^3/σ_h^3 .

One can also find the peaks of both return pulses and use the separation time between the peaks as the estimate, i.e.,

$$\hat{\tau}_{12} = \arg \max_t \{S_2(t)\} - \arg \max_t \{S_1(t)\} . \quad (5.24)$$

The estimator is unbiased because the mean positions of the peaks are identical at two wavelengths. The timing error can be found from Eq. (5.10) to be

$$\begin{aligned} \text{MSE} &= \frac{\text{Var}\left\{\frac{d}{dt} S_2(t) \middle| t=t_{2\max}\right\}}{E\left\{\frac{d^2}{dt^2} S_2(t) \middle| t=t_{2\max}\right\}^2} + \frac{\text{Var}\left\{\frac{d}{dt} S_1(t) \middle| t=t_{1\max}\right\}}{E\left\{\frac{d^2}{dt^2} S_1(t) \middle| t=t_{1\max}\right\}^2} \\ &= \frac{\frac{\partial^2}{\partial t_1 \partial t_2} C_{S_2}(t_1, t_2) \big|_{t_1=t_2=t_{2\max}}}{\bar{S}_2(t_{2\max})^2} + \frac{\frac{\partial^2}{\partial t_1 \partial t_2} C_{S_1}(t_1, t_2) \big|_{t_1=t_2=t_{1\max}}}{\bar{S}_1(t_{1\max})^2} , \end{aligned} \quad (5.25)$$

where $t_{1\max}$ and $t_{2\max}$ are the locations of the peaks of \bar{S}_1 and \bar{S}_2 , respectively. For a Gaussian return pulse shape, this equals

$$\text{MSE} = \left(\frac{1}{\langle N_1 \rangle} + \frac{1}{\langle N_2 \rangle} \right) \frac{(\sigma_h^2 + \sigma_f^2 + \sigma_T^2)^3 (\sigma_f^2 + \sigma_T^2)}{\sigma_h^3 (\sigma_h^2 + 2\sigma_f^2 + 2\sigma_T^2)^{3/2}}$$

$$+ \left(\frac{1}{K_1} + \frac{1}{K_2} \right) \frac{\sigma_T^2 (\sigma_h^2 + \sigma_f^2 + \sigma_T^2)^3}{(\sigma_h^2 + \sigma_f^2)^{3/2} (\sigma_h^2 + \sigma_f^2 + 2\sigma_T^2)^{3/2}} \quad (5.26)$$

For a target with negligible range spread so that $\sigma_T \approx 0$, the MSE reduces to

$$\text{MSE} = \left(\frac{1}{\langle N_1 \rangle} + \frac{1}{\langle N_2 \rangle} \right) \frac{\sigma_f^2 (\sigma_h^2 + \sigma_f^2)^3}{\sigma_h^3 (\sigma_h^2 + 2\sigma_f^2)^{3/2}} \quad (5.27)$$

which is independent of the speckle averaging. This is true because speckle does not distort the received waveforms and, therefore, does not change the positions of the peaks. Comparing Eq. (5.27) with Eq. (5.17), we find the peak-detection algorithm performs about the same as the correlation receiver for point targets. On the other hand, for a target with large-range spread, the performance of the peak detection algorithm is

$$\text{MSE} = \left(\frac{1}{\langle N_1 \rangle} + \frac{1}{\langle N_2 \rangle} \right) \frac{\sigma_T^5}{2\sqrt{2} \sigma_h^3} + \left(\frac{1}{K_1} + \frac{1}{K_2} \right) \frac{\sigma_T^5}{2\sqrt{2} (\sigma_h^2 + \sigma_f^2)^{3/2}} \quad (5.28)$$

which when compared with Eq. (5.18) shows that peak detection is inferior to the correlation receiver. The difference is large when σ_T is large. This difference occurs because when σ_T is larger than σ_h and σ_f , shot noise and speckle will cause fluctuations within the received pulse, which make the peak position shift back and forth.

We can also use the separation between the centroids of the two pulses as the estimate, i.e.,

$$\begin{aligned} \hat{\tau}_{12} &= (\text{Centroid of } S_2(t)) - (\text{Centroid of } S_1(t)) \\ &= \frac{\int_{-\infty}^{\infty} dt \, t \, S_2(t)}{\int_{-\infty}^{\infty} dt \, S_2(t)} - \frac{\int_{-\infty}^{\infty} dt \, t \, S_1(t)}{\int_{-\infty}^{\infty} dt \, S_1(t)} \quad (5.29) \end{aligned}$$

It can be shown that, under the assumption that S_1 and S_2 have the same waveform, the estimator is unbiased and has a MSE given by

$$\begin{aligned} \text{MSE} &= \frac{\int_{-\infty}^{\infty} dt_1 \int_{-\infty}^{\infty} dt_2 t_1 t_2 C_{S_1}(t_1, t_2)}{\langle N_1 \rangle^2} + \frac{\int_{-\infty}^{\infty} dt_1 \int_{-\infty}^{\infty} dt_2 t_1 t_2 C_{S_2}(t_1, t_2)}{\langle N_2 \rangle^2} \\ &= \left(\frac{1}{\langle N_1 \rangle} + \frac{1}{\langle N_2 \rangle} + \frac{1}{K_1} + \frac{1}{K_2} \right) \sigma_T^2 + \left(\frac{1}{\langle N_1 \rangle} + \frac{1}{\langle N_2 \rangle} \right) \sigma_f^2, \end{aligned} \quad (5.30)$$

which is true for general waveforms if σ_T is taken to be the rms width of the time spread of the target. The MSE of the centroid algorithm depends only on the time spread of the received pulse while the performance of the correlation receiver depends on the slope of the received pulse. For a given time spread of the received pulse, the correlation algorithm can be better or worse depending on the bandwidth of the pulse. This will be further discussed in Section 5.4.

In Table 5.1, we list the estimators considered above and their performances for the Gaussian mean pulse shape in the $\sigma_T \gg \sigma_f$ and $\sigma_T \gg \sigma_h$ case. Comparing the performances of these estimators for the Gaussian mean pulse shape, we find computing the centroids performs best. The correlation receiver follows. This is reasonable because for Gaussian pulse shape, the implementation of the ML estimator shown in Eq. (5.3) reduces to calculating the centroids. This can be seen from the following derivations:

$$\begin{aligned} \hat{\tau}_{i_{ML}} &= \arg \max_{\tau_i} \left\{ \int_{-\infty}^{\infty} dt S_i(t) \ln \bar{S}_i(t + \tau_i) \right\} \\ &= \arg \max_{\tau_i} \left\{ \int_{-\infty}^{\infty} dt S_i(t) \ln G(\sigma, t + \tau_i) \right\} \end{aligned}$$

TABLE 5.1.

PERFORMANCES OF TIMING ALGORITHMS FOR GAUSSIAN MEAN PULSE SHAPE, ASSUMING
 $\sigma_T \gg \sigma_h$ AND $\sigma_T \gg \sigma_f$.

Timing Algorithm	Mean-Square Timing Error
<p>Correlation Algorithm</p> $\hat{\tau}_{12} = \arg \max_{\tau} \left[\int_{-\infty}^{\infty} dt S_1(t) S_2(t+\tau) \right]$	$1.54 (\langle N_1 \rangle^{-1} + K_1^{-1} + \langle N_2 \rangle^{-1} + K_2^{-1}) \frac{\sigma_T^2}{\sigma_h^2}$ $+ \frac{\sigma_T^5}{\sqrt{2} \langle N_1 \rangle \langle N_2 \rangle \sigma_h^3} + \frac{\sigma_T^5}{\sqrt{2} K_1 K_2 (\sigma_h^2 + \sigma_f^2)^{3/2}}$ $+ (K_1^{-1} \langle N_2 \rangle^{-1} + K_2^{-1} \langle N_1 \rangle^{-1}) \frac{2\sqrt{2} \sigma_T^5}{(2\sigma_h^2 + \sigma_f^2)^{3/2}}$
<p>Correlation Algorithm (pulse shape known a priori)</p> $\hat{\tau}_{12} = \arg \max_{\tau} \left[\int_{-\infty}^{\infty} dt S_2(t) \bar{S}_2(t+\tau) \right]$ $- \arg \max_{\tau} \left[\int_{-\infty}^{\infty} dt S_1(t) \bar{S}_1(t+\tau) \right]$	$1.54 (\langle N_1 \rangle^{-1} + K_1^{-1} + \langle N_2 \rangle^{-1} + K_2^{-1}) \frac{\sigma_T^2}{\sigma_h^2}$
<p>Correlation with Log Waveform</p> $\hat{\tau}_{12} = \arg \max_{\tau} \left[\int_{-\infty}^{\infty} dt S_2(t+\tau) \ln S_1(t) \right]$	$(\langle N_1 \rangle^{-1} + K_1^{-1} + \langle N_2 \rangle^{-1} + K_2^{-1}) \frac{\sigma_T^2}{\sigma_h^2}$ $+ \frac{\sigma_T^6}{4 \sigma_h^4 \langle N_1 \rangle \langle N_2 \rangle} + \frac{\sigma_T^6}{4 (\sigma_h^2 + \sigma_f^2)^2 K_1 K_2}$ $+ (K_1^{-1} \langle N_2 \rangle^{-1} + K_2^{-1} \langle N_1 \rangle^{-1}) \frac{\sigma_T^6}{\sqrt{2} (2\sigma_h^2 + \sigma_f^2)^2}$
<p>Correlation with log pulse shape (Optimum) (pulse shape known a priori)</p> $\hat{\tau}_{12} = \arg \max_{\tau} \left[\int_{-\infty}^{\infty} dt S_2(t) \ln \bar{S}_2(t+\tau) \right]$ $- \arg \max_{\tau} \left[\int_{-\infty}^{\infty} dt S_1(t) \ln \bar{S}_1(t+\tau) \right]$	$(\langle N_1 \rangle^{-1} + K_1^{-1} + \langle N_2 \rangle^{-1} + K_2^{-1}) \frac{\sigma_T^2}{\sigma_h^2}$
<p>Peak Detection</p> $\hat{\tau}_{12} = \arg \max_c [S_2(t)] - \arg \max_c [S_1(t)]$	$(\langle N_1 \rangle^{-1} + \langle N_2 \rangle^{-1}) \frac{\sigma_T^5}{2\sqrt{2} \sigma_h^3}$ $+ (K_1^{-1} + K_2^{-1}) \frac{\sigma_T^5}{2\sqrt{2} (\sigma_h^2 + \sigma_f^2)^{2/3}}$
<p>Centroid Method</p> $\hat{\tau}_{12} = (\text{Centroid of } S_2) - (\text{Centroid of } S_1)$ $= \frac{\int_{-\infty}^{\infty} dt t S_2(t)}{\int_{-\infty}^{\infty} dt S_2(t)} - \frac{\int_{-\infty}^{\infty} dt t S_1(t)}{\int_{-\infty}^{\infty} dt S_1(t)}$	$(\langle N_1 \rangle^{-1} + K_1^{-1} + \langle N_2 \rangle^{-1} + K_2^{-1}) \frac{\sigma_T^2}{\sigma_h^2}$

$$= \arg \max_{\tau_i} \left\{ \int_{-\infty}^{\infty} dt [-(t + \tau_i)^2 S_i(t)/2\sigma^2] \right\}, \quad (5.31)$$

which means $\hat{\tau}_{i_{ML}}$ satisfies

$$\frac{d}{d\tau_i} \left\{ \int_{-\infty}^{\infty} dt (t + \tau_i)^2 S_i(t)/2\sigma^2 \right\} \Big|_{\tau_i = \hat{\tau}_{i_{ML}}} = 0, \quad (5.32)$$

which is equivalent to calculating the centroid,

$$\hat{\tau}_{i_{ML}} = \frac{\int_{-\infty}^{\infty} dt t S_i(t)}{\int_{-\infty}^{\infty} dt S_i(t)}. \quad (5.33)$$

However, for general waveforms, calculating the centroids could be far from optimal.

5.3. Frequency Domain Representation of Timing Error

From the above results, we restrict our attention to the correlation and centroid algorithms. For general waveforms, the performance of the correlation receiver has to be calculated numerically. The MSE can be expressed in terms of the bandwidth of the received signal. Equation (5.13) can be written as

$$\begin{aligned} \int_{-\infty}^{\infty} dt \bar{S}_1(t) \frac{\partial^2}{\partial \tau^2} \bar{S}_2(t + \tau) \Big|_{\tau = \tau_{12}} &= \frac{1}{2\pi} \int_{-\infty}^{\infty} d\omega \mathcal{Q}[\bar{S}_1(t)] \mathcal{Q}[\bar{S}_2(t + \tau_{12})]^* \\ &= - \frac{\langle N_1 \rangle \langle N_2 \rangle}{2\pi} \int_{-\infty}^{\infty} d\omega \omega^2 |\phi_s(\omega)|^2, \end{aligned} \quad (5.34)$$

where

$$\begin{aligned} \phi_s(\omega) &= \int_{-\infty}^{\infty} dt F(t) e^{-i\omega t} \\ &= \int d^2 \underline{\rho} b_2(\underline{\rho}, z) \exp \left[-\frac{\omega^2}{2} (\sigma_h^2 + \sigma_f^2) \right] \exp[i\omega \psi]. \end{aligned} \quad (5.35)$$

$\phi_s(\omega)$ is the Fourier transform of the mean received pulse shape. For any function $a(t)$ we use $\mathcal{Q}\{a(t)\}$ to denote its Fourier transform. In arriving at Eq. (5.34), we have made use of the following Fourier transform relationship

$$\int_{-\infty}^{\infty} dt a(t)b(t) = \frac{1}{2\pi} \int_{-\infty}^{\infty} d\omega \mathcal{Q}\{a(t)\} \mathcal{Q}\{b(t)\}^* \quad (5.36)$$

Equation (5.12) can be written as

$$\begin{aligned} & \int_{-\infty}^{\infty} dt_1 \int_{-\infty}^{\infty} dt_2 R_{S_1}(t_1, t_2) \frac{\partial^2}{\partial \tau_1 \partial \tau_2} R_{S_2}(t_1 + \tau_1, t_2 + \tau_2) \Big|_{\tau_1 = \tau_2 = \tau_{12}} \\ &= \frac{1}{4\pi^2} \int_{-\infty}^{\infty} d\omega_1 \int_{-\infty}^{\infty} d\omega_2 \mathcal{Q}\{R_{S_1}(t_1, t_2)\} \mathcal{Q}\left\{\frac{\partial^2}{\partial \tau_1 \partial \tau_2} R_{S_2}(t_1 + \tau_1, t_2 + \tau_2) \Big|_{\tau_1 = \tau_2 = \tau_{12}}\right\}^* \\ &= -\frac{1}{4\pi^2} \int_{-\infty}^{\infty} d\omega_1 \int_{-\infty}^{\infty} d\omega_2 \hat{R}_{S_1}(\omega_1, \omega_2) \omega_1 \omega_2 \hat{R}_{S_2}(\omega_1, \omega_2) e^{i\omega_1 \tau_{12}} e^{i\omega_2 \tau_{12}} \end{aligned} \quad (5.37)$$

where

$$\hat{R}_{S_1}(\omega_1, \omega_2) = \int_{-\infty}^{\infty} dt_1 \int_{-\infty}^{\infty} dt_2 R_{S_1}(t_1, t_2) e^{-i\omega_1 t_1} e^{-i\omega_2 t_2} \quad (5.38)$$

$\hat{R}_{S_1}(\omega_1, \omega_2)$ is the two-dimensional Fourier transform of $R_{S_1}(t_1, t_2)$. In arriving at Eq. (5.37), we have made use of the following Fourier transform relationship,

$$\int_{-\infty}^{\infty} dt_1 \int_{-\infty}^{\infty} dt_2 a(t_1, t_2) b(t_1, t_2) = \frac{1}{4\pi^2} \int_{-\infty}^{\infty} d\omega_1 \int_{-\infty}^{\infty} d\omega_2 \mathcal{Q}\{a(t_1, t_2)\} \mathcal{Q}\{b(t_1, t_2)\}^* \quad (5.39)$$

which is the two-dimensional version of Eq. (5.36). Using Eqs. (5.34) and (5.37), we have

$$\text{MSE} = - \frac{\int_{-\infty}^{\infty} d\omega_1 \int_{-\infty}^{\infty} d\omega_2 \omega_1 \omega_2 \hat{R}_{S_1}(\omega_1, \omega_2) \hat{R}_{S_2}(\omega_1, \omega_2) e^{i\omega_1 \tau_{12}} e^{i\omega_2 \tau_{12}}}{\left\{ \int_{-\infty}^{\infty} d\omega \omega^2 |\phi_s(\omega)|^2 \right\}^2} . \quad (5.40)$$

The Fourier transform can be calculated using the FFT algorithm and the integrations can be done digitally, although the computation time can be substantial due to the presence of two-dimensional transforms and integrations. However, by considering Eq. (5.40) alone, it is not clear what is the relationship between the timing error and the characteristics of the received signal. By substituting the explicit expressions for R_S , we can express the timing error in terms of the bandwidth of the received signal. The intermediate steps are shown in Appendix B; the results are

$$\begin{aligned} \text{MSE} = & \left(\frac{1}{\langle N_1 \rangle} + \frac{1}{\langle N_2 \rangle} + \frac{1}{K_1} + \frac{1}{K_2} \right) \frac{\alpha}{2B^2} \\ & + \frac{\sqrt{\pi}}{4\sqrt{2} \int_{-\infty}^{\infty} d\omega |\phi_s(\omega)|^2 B^4} \left\{ \frac{\frac{1}{\sigma_h^2} - B^2}{\langle N_1 \rangle \langle N_2 \rangle \sigma_h} + \frac{\frac{1}{\sigma_h^2 + \sigma_f^2} - B^2}{K_1 K_2 \sqrt{\sigma_h^2 + \sigma_f^2}} \right. \\ & \left. + \frac{2\sqrt{2} \left\{ \frac{1}{2\sigma_h^2 + \sigma_f^2} - B^2 \right\}}{\langle N_1 \rangle K_2 \sqrt{2\sigma_h^2 + \sigma_f^2}} + \frac{2\sqrt{2} \left\{ \frac{1}{2\sigma_h^2 + \sigma_f^2} - B^2 \right\}}{\langle N_2 \rangle K_1 \sqrt{2\sigma_h^2 + \sigma_f^2}} \right\} , \end{aligned} \quad (5.41)$$

where

$$B^2 = \frac{\int_{-\infty}^{\infty} d\omega \omega^2 |\phi_s(\omega)|^2}{\int_{-\infty}^{\infty} d\omega |\phi_s(\omega)|^2} \quad (5.42)$$

and

$$\alpha = \frac{\int_{-\infty}^{\infty} d\omega \omega^2 \phi_s^*(\omega) [\phi_s(\omega) * \phi_s(\omega)]}{\int_{-\infty}^{\infty} d\omega \omega^2 |\phi_s(\omega)|^2 \int_{-\infty}^{\infty} d\omega |\phi_s(\omega)|^2} \quad (5.43)$$

B is the RMS bandwidth of the received pulses, and α is a dimensionless factor which typically varies between 1 and 2, depending on the surface profile. For Gaussian-pulse shape, α equals 1.54. Since the second-order terms are roughly proportional to $(1/\alpha_h)^3$, to keep the second-order terms from becoming very large, the resolution of the receiver $(1/\alpha_h)$ should not be too large. Equation (5.4) shows that timing error is inversely proportional to the signal bandwidth. This is expected since high-bandwidth signals will contain fine structures which improve the performance of the correlation timing algorithm.

5.4. Comparison of the Correlation and Centroid Algorithms

We will evaluate the performance of the correlation and centroid algorithms numerically for a set of simulated ocean return waveforms. The waveforms we use are a raised cosine superimposed with smaller scale modulations. That is

$$F(t) = (1 + \cos(2\pi t/D)) + A(1 - \cos(2\pi t/d))^n, \quad -D/2 \leq t \leq D/2, \quad (5.44)$$

where d is smaller than D . Here the variable n is used to control the sharpness of the modulation. The larger the value of n , the sharper the peaks. This approximates the ocean return signal plotted in Fig. 3.5 for off-nadir pointing.

We first compute the results for a smooth raised cosine, which is obtained by letting A equal zero. The rms timing error is plotted versus expected photocounts in Fig. 5.1 for a speckle number $K_1 = K_2 = 50,000$.

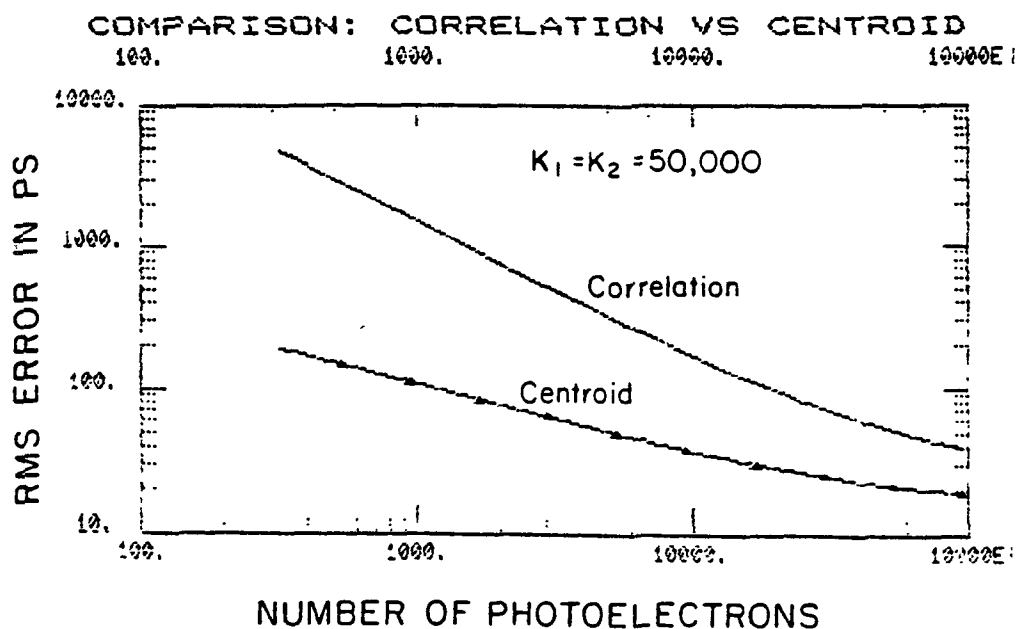
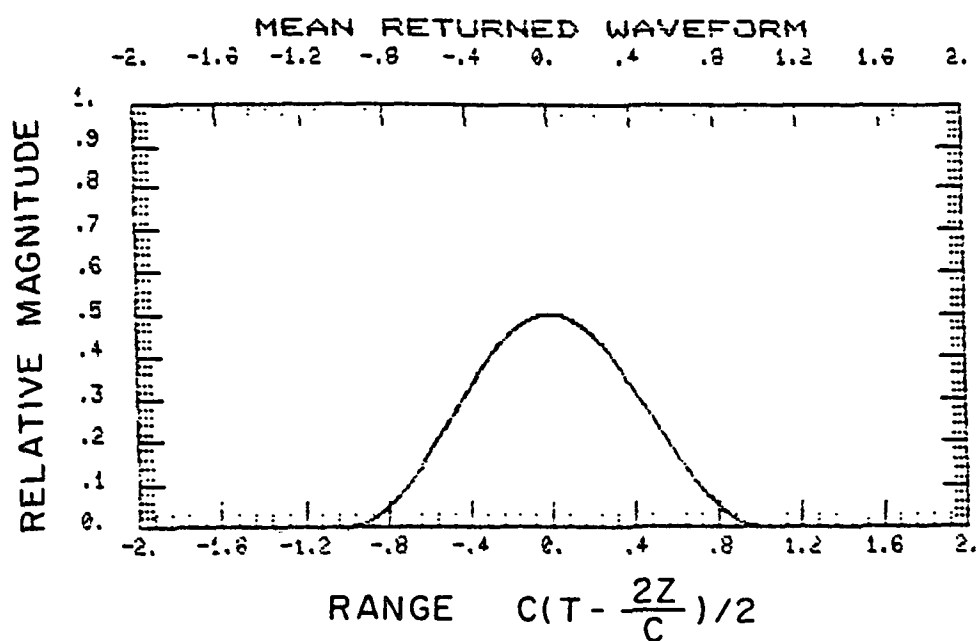


Figure 5.1. Comparison of the correlation and centroid algorithms for a simulated received pulse shape from a Gaussian ocean surface.

The centroid algorithm performs better in this case, which is expected because the centroid algorithm performs better for the Gaussian pulse shape and the raised cosine resembles the Gaussian.

Next, we use a waveform that approximates the return from a sinusoidal ocean shown previously in Fig. 3.5. The approximation is done by letting n equal 4, A equal 0.94 and D/d equal 12. The results are shown in Fig. 5.2; the performance of the correlation receiver is significantly better, because the waveform has a relatively large bandwidth due to the presence of the sharp structures. The rms bandwidths of the waveforms shown in Figs. 5.1 and 5.2 are calculated to be 0.272 and 2.717 GHz, respectively. In Fig. 5.3, the power spectra of the two waveforms are plotted. Indeed, the waveforms shown in Fig. 5.2 have more high-frequency energy. While the performance of the centroid algorithm remains nearly the same for both waveforms, because the mean square widths of both waveforms are approximately equal, the performance of the correlation algorithm improves significantly with the increase of the signal bandwidth. From the above results, we conclude that, to achieve picosecond timing accuracy with ocean reflected pulses, the correlation algorithm should be used. In Chapter 6, we consider the effects of the footprint on the bandwidth of the received signal.

In Fig. 5.4, we show the performance of the correlation receiver for three different values of speckle number. At the strong signal limit, the performance is limited by speckle. The amount of speckle averaging determines the timing error. At the weak signal limit, the performance is limited by shot noise and the timing error is less sensitive to the number of speckle cells. In all cases, the timing accuracy improves as the signal strength and speckle number increase. Single shot accuracies of ~ 10 psec

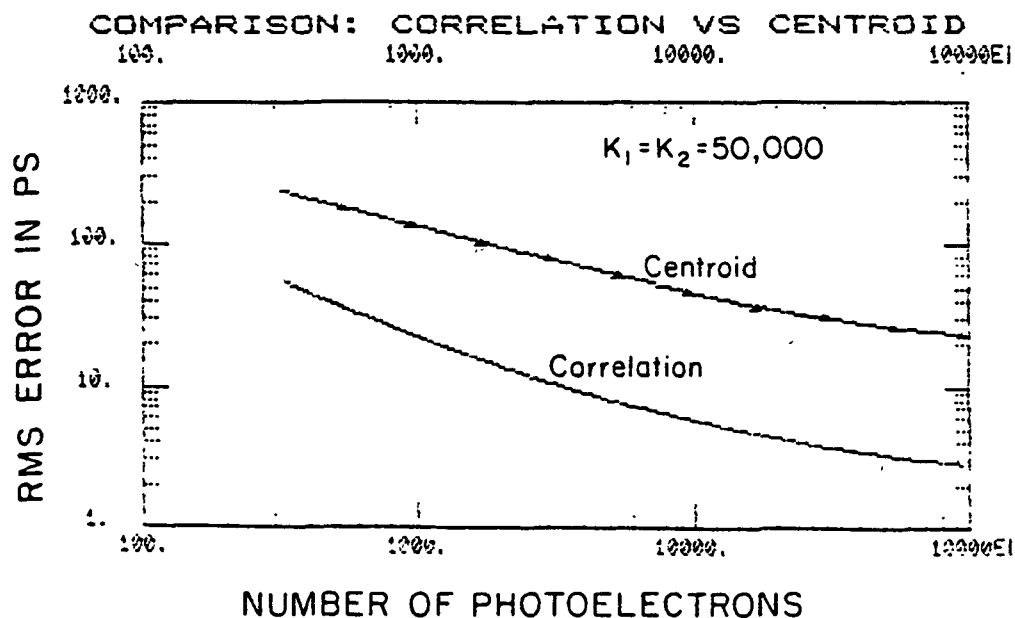
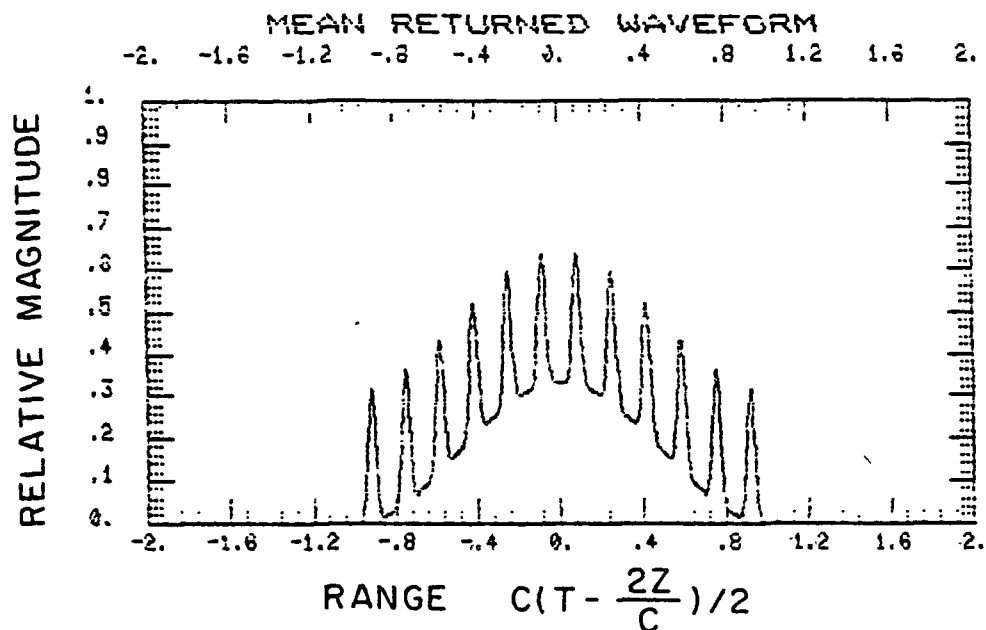


Figure 5.2. Comparison of the correlation and centroid algorithms for a simulated received pulse shape from a sinusoidal ocean surface.

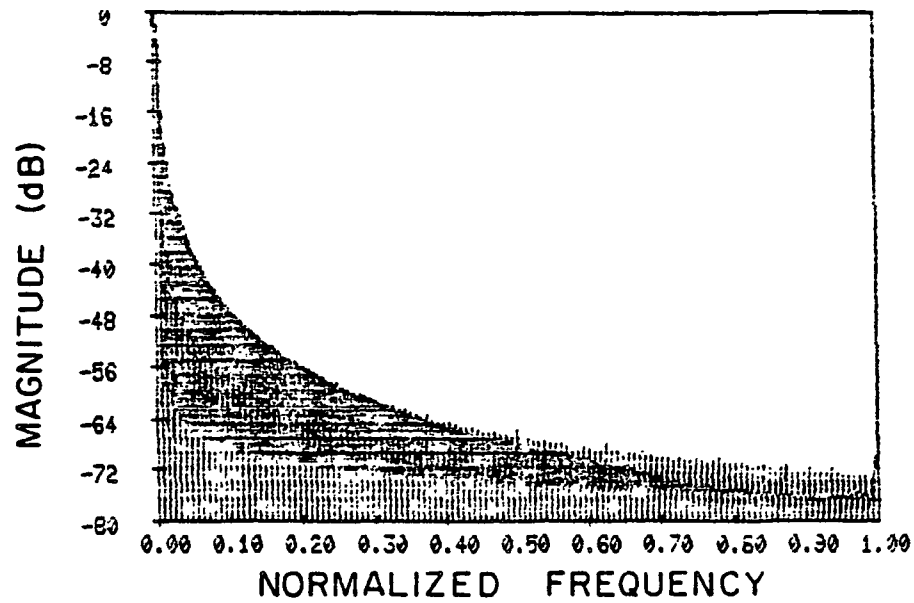


Figure 5.3a. Power spectra of the mean received pulse shape shown in Figure 5.1.

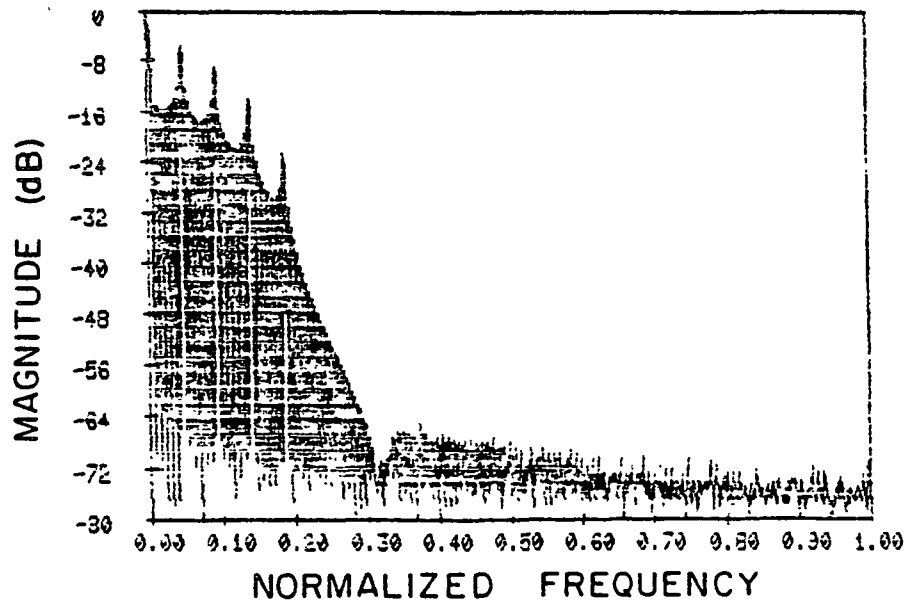


Figure 5.3b. Power spectra of the mean received pulse shape shown in Figure 5.2.

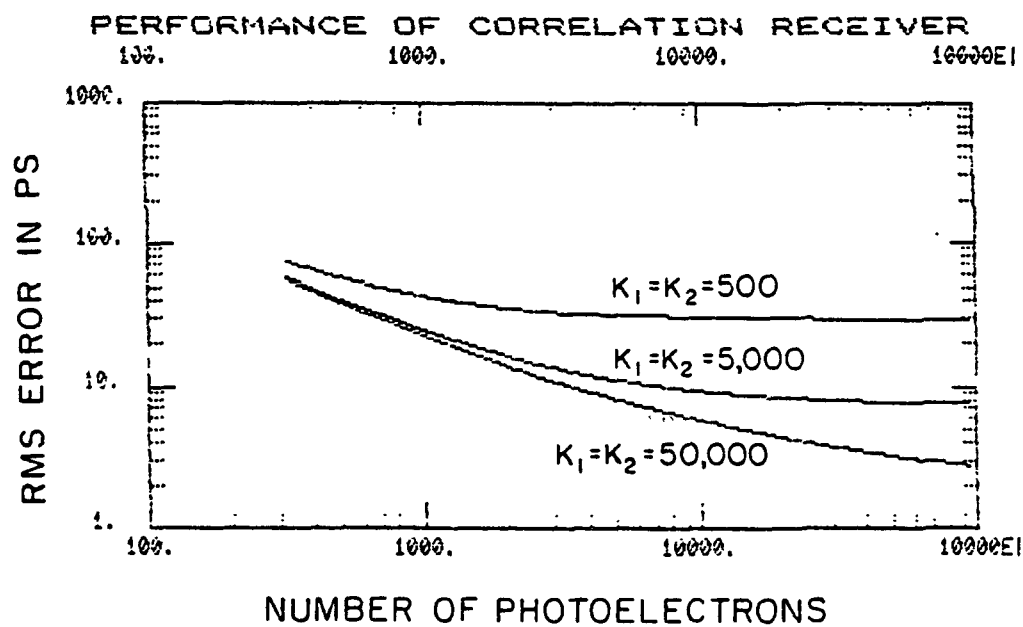


Figure 5.4. Effects of speckle averaging on the correlation algorithm.
The mean pulse shape corresponds to Figure 5.2.

appear to be feasible with ocean surface targets when the expected photo-counts for both pulses approach a few thousand. The timing accuracy can be improved further by averaging the measurements from many shots.

5.5. Transmitter Effects

In practice, the expected waveforms at the two wavelengths may not be exactly the same. This can be due to misalignment of the transmitted laser beams and different beam divergence due to the diffraction effects or due to turbulence. When the mean waveforms at the two wavelengths are not the same, the correlation receiver can become biased, with a bias given by

$$\text{Bias} = - \frac{E\{\dot{R}_{12}(\tau_{12})\}}{E\{\ddot{R}_{12}(\tau_{12})\}} = - \frac{\int_{-\infty}^{\infty} dt \bar{S}_1(t) \dot{\bar{S}}_2(t + \tau_{12})}{\int_{-\infty}^{\infty} dt \bar{S}_1(t) \ddot{\bar{S}}_2(t + \tau_{12})}$$

$$= \frac{\int_{-\infty}^{\infty} d\omega i\omega \phi_{S1}^*(\omega) \phi_{S2}(\omega)}{\int_{-\infty}^{\infty} d\omega \omega^2 \phi_{S1}^*(\omega) \phi_{S2}(\omega)}, \quad (5.45)$$

and the MSE given previously by Eq. (5.40) becomes

$$\text{MSE} = - \frac{\int_{-\infty}^{\infty} d\omega_1 \int_{-\infty}^{\infty} d\omega_2 \omega_1 \omega_2 \hat{R}_{S1}(\omega_1, \omega_2) \hat{R}_{S2}(\omega_1, \omega_2) e^{i\omega_1 \tau_{12}} e^{i\omega_2 \tau_{12}}}{\left(\int_{-\infty}^{\infty} d\omega \omega^2 \phi_{S1}^*(\omega) \phi_{S2}(\omega) \right)^2}. \quad (5.46)$$

This result is expanded into a form suitable for numerical computation in Appendix C. As an example, suppose one channel has a very large footprint, so that it has a mean pulse shape which looks like Fig. 5.1. Suppose the other channel has a small footprint and a mean pulse shape that looks like Fig. 5.2. The bias of the correlation algorithm is found to be zero

because although the waveforms are different they are not shifted with respect to each other. The timing error can be evaluated and the results are shown in Fig. 5.5. Compared with Figs. 5.1 and 5.2, we see a degradation in the performance, which is expected, because the correlation between the two waveforms has decreased.

5.6. Sampling Effects

In practice, the output of the receiver or photodetector is usually sent into a waveform digitizer and the sampled and digitized data are recorded by a computer for future processing. If the waveforms are sampled at a fixed interval, τ_0 , then the output of the waveform digitizer can be modeled as

$$Y_i = \int_{(i-1)\tau_0}^{i\tau_0} dt S(t) + n_i \quad (5.47)$$

and

$$E\{n_i n_j\} = \text{Var}\{n_i\} \delta_{ij} \quad (5.48)$$

where Y_i is the i -th sampled data point, n_i is the additive noise introduced in the sampling and digitizing processes. Here n_i is due to the quantization in the digitizing process and the noise of the waveform digitizer. To avoid losses in the high frequency content of the signal, usually τ_0 is chosen to be short compared to the impulse response of the receiver. In this case, we have

$$Y_i \cong S(i\tau_0) \tau_0 + n_i \quad (5.49)$$

Next, we consider the effects of n_i on various timing algorithms. Since the analyses of timing algorithms usually involve differentiations, a discrete process like Y_i can not be readily analyzed. To overcome this

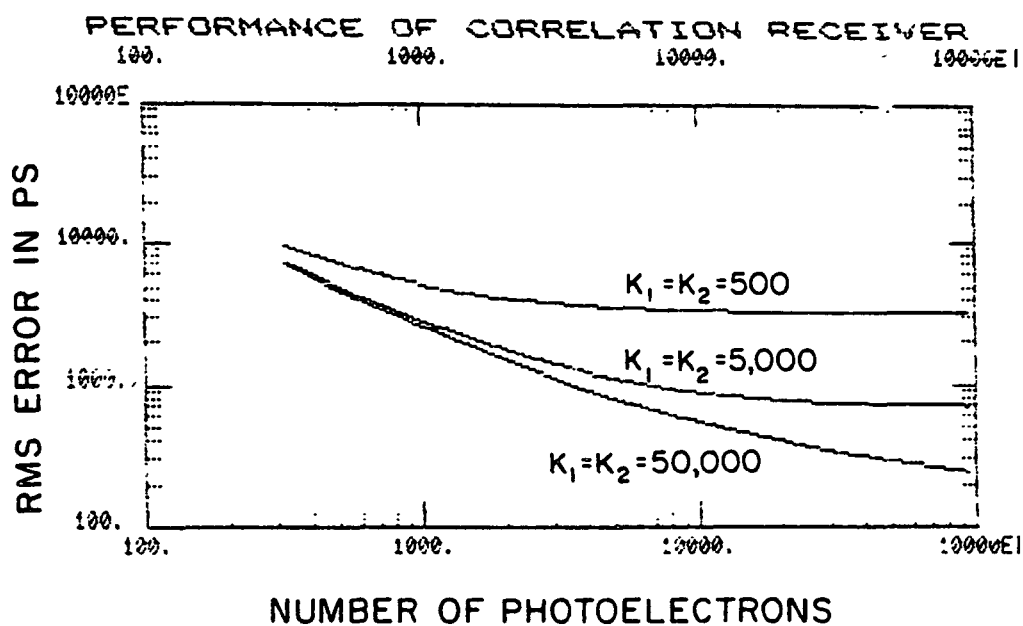


Figure 5.5. Performance of the correlation algorithm when the mean pulse shapes at two wavelengths are different. One wavelength has mean pulse shape corresponding to that in Figure 5.1. The other wavelength has mean pulse shape corresponding to that in Figure 5.2.

difficulty, we can approximate Y_1 with a continuous process $Y(t)$,

$$Y(t) = S(t) + n(t) \quad (5.50)$$

and

$$\begin{aligned} R_Y(t_1, t_2) &= R_S(t_1, t_2) + R_n(t_1, t_2) \\ &= R_S(t_1, t_2) + N_0 G(\sigma_1, t_1 - t_2) G\left(\sigma_2, \frac{t_1 + t_2}{2}\right), \end{aligned} \quad (5.51)$$

where σ_1 is the correlation length of the noise, which is on the order of the width of the digitizer element spacing τ_0 , N_0 is the noise energy. The function $G(\sigma_2, \frac{t_1 + t_2}{2})$ is introduced to keep the total noise energy finite in the correlation process, and σ_2 is chosen to be large compared to the support of $S(t)$, so that the noise power is essentially uniform.

By substituting $R_S(t_1, t_2)$ with $R_Y(t_1, t_2)$ into the previous equations, we find additional error terms are introduced. The MSE of the correlation receiver, given previously in Eq. (5.15), is increased by an additional amount MSE' , which is given by

$$\begin{aligned} MSE' &= \frac{\frac{\partial^2}{\partial \tau_1 \partial \tau_2} \int_{-\infty}^{\infty} dt_1 \int_{-\infty}^{\infty} dt_2 \bar{S}_1(t_1) \bar{S}_1(t_2) R_n(t_1 + \tau_1, t_2 + \tau_2)}{\left\{ \int_{-\infty}^{\infty} dt \bar{S}_1(t) \bar{S}_2(t + \tau_{12}) \right\}^2} \\ &\quad + \frac{R_n(t_1, t_2) \bar{S}_2(t_1 + \tau_1) \bar{S}_2(t_2 + \tau_2) \Big|_{\tau_1 = \tau_2 = \tau_{12}}}{\left\{ \int_{-\infty}^{\infty} dt \bar{S}_1(t) \bar{S}_2(t + \tau_{12}) \right\}^2} \end{aligned} \quad (5.52)$$

In Eq. (5.52), we have neglected the higher-order terms which are generally very small. By substituting the expression for R_n into Eq. (5.52), we obtain

$$\text{MSE}' = \left(\frac{1}{\langle N_1 \rangle^2} + \frac{1}{\langle N_2 \rangle^2} \right) \frac{\sqrt{2\pi} N_o}{\sigma_2} \frac{1}{\int_{-\infty}^{\infty} d\omega \omega^2 |\phi_s(\omega)|^2} . \quad (5.53)$$

The computation leading to Eq. (53) is given in Appendix D. For a Gaussian-pulse shape, MSE' becomes

$$\text{MSE}' = \left(\frac{1}{\langle N_1 \rangle^2} + \frac{1}{\langle N_2 \rangle^2} \right) \frac{2\sqrt{2} N_o (\sigma_f^2 + \sigma_h^2 + \sigma_T^2)^{3/2}}{\sigma_2} . \quad (5.54)$$

From Eq. (5.54), we see that for the correlation receiver the additional timing error introduced by the sampling-digitizing process is usually small, because it is proportional to N_o/σ_2 and σ_2 is very large.

For the peak detection algorithm, the additional error can be found from Eq. (5.25) to be

$$\text{MSE}' = \frac{\frac{\partial^2}{\partial t_1 \partial t_2} R_n(t_1, t_2) \Big|_{t_1=t_2=t_{2\max}}}{\{\ddot{S}_2(t_{2\max})\}^2} + \frac{\frac{\partial^2}{\partial t_1 \partial t_2} R_n(t_1, t_2) \Big|_{t_1=t_2=t_{1\max}}}{\{\ddot{S}_1(t_{1\max})\}^2} . \quad (5.55)$$

For a Gaussian received pulse shape, Eq. (5.55) becomes

$$\begin{aligned} \text{MSE}' &= \left(\frac{1}{\langle N_1 \rangle^2} + \frac{1}{\langle N_2 \rangle^2} \right) \frac{N_o (4\sigma_2^2 - \sigma_1^2) (\sigma_f^2 + \sigma_h^2 + \sigma_T^2)^3}{4\sigma_1^3 \sigma_2^3} \\ &\equiv \left(\frac{1}{\langle N_1 \rangle^2} + \frac{1}{\langle N_2 \rangle^2} \right) \frac{N_o (\sigma_f^2 + \sigma_h^2 + \sigma_T^2)^3}{\sigma_1^3 \sigma_2} , \end{aligned} \quad (5.56)$$

which is proportional to $N_o/\sigma_1^3 \sigma_2$. N_o/σ_1^3 can be large and the additional

error for the peak detection algorithm can be significant when the signal levels $\langle N_1 \rangle$ and $\langle N_2 \rangle$ are not very large. If peak detection is to be used, it is advisable to make the correlation length of the noise σ_1 larger. This can be done by smoothing or low-pass filtering the sampled sequence.

For the centroid algorithm, we find the sampling-digitizing process introduces an additional timing error which can be found from Eq. (5.30) to

be given by

$$\begin{aligned} \text{MSE}' &= \frac{\int_{-\infty}^{\infty} dt_1 \int_{-\infty}^{\infty} dt_2 t_1 t_2 R_n(t_1, t_2)}{\langle N_1 \rangle^2} + \frac{\int_{-\infty}^{\infty} dt_1 \int_{-\infty}^{\infty} dt_2 t_1 t_2 R_n(t_1, t_2)}{\langle N_2 \rangle^2} \\ &= \left(\frac{1}{\langle N_1 \rangle^2} + \frac{1}{\langle N_2 \rangle^2} \right) N_0 \left(\frac{\sigma_2^2}{2} - \frac{\sigma_1^2}{4} \right). \end{aligned} \quad (5.57)$$

This value is usually small for a reasonable signal strength.

The effects of sampling on the timing accuracy for a Gaussian mean pulse shape are summarized in Table 5.2. We conclude that correlation and centroid algorithms are not sensitive to the noise introduced by the sampling-digitizing process, but peak detection is more sensitive. For peak detection, it is advantageous to first smooth the sampled data.

5.7. Summary

The ML estimator for differential arrival time cannot be implemented due to the lack of prior knowledge of the mean pulse shape. Among the suboptimal estimators investigated, the correlation algorithm can achieve a signal shot accuracy of ~ 10 psec if the reflected pulse has time structure or glints. The performance of the correlation algorithm is found to improve with the bandwidth of the received pulse.

If the mean received pulse shape at the two wavelengths is not the same, bias and additional error are introduced into the correlation

TABLE 5.2.
ADDITIONAL TIMING ERROR DUE TO SAMPLING NOISE

Timing Algorithm	Additional Mean-Square Timing Error
Correlation Algorithm	$(\langle N_1 \rangle^{-2} + \langle N_2 \rangle^{-2}) 2\sqrt{2} N_o (\sigma_f^2 + \sigma_h^2 + \sigma_T^2)^{3/2} / \sigma_2$
Centroid Algorithm	$(\langle N_1 \rangle^{-2} + \langle N_2 \rangle^{-2}) N_o (\sigma_2^2 - 0.25 \sigma_1^2)$
Peak Detection	$(\langle N_1 \rangle^{-2} + \langle N_2 \rangle^{-2}) N_o (\sigma_f^2 + \sigma_h^2 + \sigma_T^2)^3 / \sigma_1^3 \sigma_2$

algorithm. Therefore, the laser beams at the two wavelengths should be carefully aligned.

The sampling of the receiver output can introduce additional noise. The correlation algorithm is found to be less sensitive to the sampling noise than the peak detection algorithm.

6. BANDWIDTH OF THE OCEAN REFLECTED PULSE

From Chapter 5 we found that the timing accuracy of the receiver depends on the bandwidth of the received signal. In this chapter, we study the effects of the surface profile and altimeter parameters on the bandwidth of the received signal. The expected bandwidth of the received pulse that has been reflected by a Gaussian distributed ocean surface is evaluated under the conditions that the profile correlation length is much less or much greater than the footprint radius.

The bandwidth of the received signal defined previously in Chapter 5 has an expected value given by

$$E\{B^2\} = E\left\{\frac{\int_{-\infty}^{\infty} d\omega \omega^2 |\phi_s(\omega)|^2}{\int_{-\infty}^{\infty} d\omega |\phi_s(\omega)|^2}\right\} \\ = \frac{\int_{-\infty}^{\infty} d\omega \omega^2 E\{|\phi_s(\omega)|^2\}}{\int_{-\infty}^{\infty} d\omega E\{|\phi_s(\omega)|^2\}}, \quad (6.1)$$

where the expectation is with respect to the Gaussian surface profile.

From Eq. (5.35), we have

$$E\{|\phi(\omega)|^2\} = \int d^2 \underline{\rho}_1 \int d^2 \underline{\rho}_2 b_2(\underline{\rho}_1, z) b_2(\underline{\rho}_2, z) e^{-\omega^2(\alpha_h^2 + \sigma_f^2)} E\{e^{i\omega(\psi_1 - \psi_2)}\} \\ = \frac{e^{-\omega^2(\alpha_h^2 + \sigma_f^2)}}{4\pi z^4 \tan^4 \theta_T} \int d^2 \underline{\rho}_1 \int d^2 \underline{\rho}_2 e^{-\frac{(\rho_1^2 + \rho_2^2)}{2z^2 \tan^2 \theta_T}} e^{i\omega \frac{(\rho_1^2 - \rho_2^2)}{cz}} \\ \cdot E\left\{e^{-i\frac{2\omega}{c} [\xi(\underline{\rho}_1) - \xi(\underline{\rho}_2)]}\right\}, \quad (6.2)$$

where we have assumed a Gaussian laser footprint with a radius of $z \tan \theta_T$ at the $\exp(-1/2)$ point. For a Gaussian surface profile with rms surface height σ_ξ , we have

$$E\left\{e^{-i\frac{2\omega}{c} [\xi(\underline{\rho}_1) - \xi(\underline{\rho}_2)]}\right\} = e^{-\frac{4}{c^2} \omega^2 \sigma_\xi^2 [1 - R_\xi(\underline{\rho}_1, \underline{\rho}_2)]} \quad (6.3)$$

where $R_{\xi}(\rho_1, \rho_2)$ is the normalized autocorrelation function of the surface profile ξ .

We first assume $L \gg z \tan \theta_T$ and a quadratic autocorrelation function with $R_{\xi}(\rho_1, \rho_2)$ given by

$$R_{\xi}(\rho_1, \rho_2) = 1 - \frac{|\rho_1 - \rho_2|^2}{2L^2}, \quad (6.4)$$

where L is the correlation length of the surface profile. The case of $L \ll z \tan \theta_T$ is treated later.

By substituting Eqs. (6.3) and (6.4) into (6.2) and making the following changes of variables

$$\rho_d = \rho_1 - \rho_2 \quad (6.5)$$

and

$$\rho_s = \frac{\rho_1 + \rho_2}{2}, \quad (6.6)$$

we have

$$\begin{aligned} E\{|\phi_s(\omega)|^2\} &= \frac{e^{-\omega^2(\sigma_h^2 + \sigma_f^2)}}{4\pi(z^4 \tan^4 \theta_T)} \int d^2 \rho_s \int d^2 \rho_d e^{-\frac{2\rho_s^2 + \frac{1}{2}\rho_d^2}{2z^2 \tan^2 \theta_T}} \\ &\quad \cdot e^{-\frac{2\omega^2 \sigma_{\xi}^2}{c^2 L^2} \rho_d^2} e^{i \frac{2\omega}{cz} \rho_s \cdot \rho_d} \\ &= \frac{\gamma^2 e^{-\omega^2(\sigma_f^2 + \sigma_h^2)}}{\gamma^2 + (\sigma_h^2 + \sigma_f^2)\omega^2}. \end{aligned} \quad (6.7)$$

Here

$$\gamma = \frac{c(\sigma_h^2 + \sigma_f^2)^{1/2}}{2z \tan \theta_T \left[\frac{2\sigma_{\xi}^2}{L^2} + \tan^2 \theta_T \right]^{1/2}}. \quad z \tan \theta_T \ll L \quad (6.8)$$

By substituting Eq. (6.7) into Eq. (6.1), we obtain

$$E\{B^2\} = \frac{\gamma e^{-\gamma^2}}{\sqrt{\pi}(\sigma_h^2 + \sigma_f^2) \operatorname{erfc}[\gamma]} - \frac{\gamma^2}{\sigma_h^2 + \sigma_f^2} \quad z \tan \theta_T \ll L \quad (6.9)$$

For the case when $L \ll z \tan \theta_T$, the autocorrelation function can be approximated by a delta function. Therefore,

$$\begin{aligned} E\{|\phi_s(\omega)|^2\} &= \frac{e^{-\omega^2(\sigma_h^2 + \sigma_f^2 + \frac{4}{c^2}\sigma_\xi^2)}}{4\pi z^4 \tan^4 \theta_T} \int d^2 \underline{\rho}_s \int d^2 \underline{\rho}_d e^{-\frac{2\rho_s^2 + \frac{1}{2}\rho_d^2}{2z^2 \tan^2 \theta_T}} e^{i \frac{2\omega}{cz} \underline{\rho}_s \cdot \underline{\rho}_d} \\ &= \frac{\gamma^2 e^{-\omega^2(\sigma_f^2 + \sigma_h^2 + \frac{4}{c^2}\sigma_\xi^2)}}{\gamma^2 + (\sigma_f^2 + \sigma_h^2 + \frac{4}{c^2}\sigma_\xi^2)\omega^2}, \end{aligned} \quad (6.10)$$

where

$$\gamma = \frac{c(\sigma_h^2 + \sigma_f^2 + \frac{4}{c^2}\sigma_\xi^2)^{1/2}}{2z \tan \theta_T} \quad L \ll z \tan \theta_T \quad (6.11)$$

In this case, the expected bandwidth is

$$E\{B^2\} = \frac{\gamma e^{-\gamma^2}}{\sqrt{\pi}(\sigma_h^2 + \sigma_f^2 + \frac{4}{c^2}\sigma_\xi^2) \operatorname{erfc}[\gamma]} - \frac{\gamma^2}{(\sigma_h^2 + \sigma_f^2 + \frac{4}{c^2}\sigma_\xi^2)} \quad (6.12)$$

$$L \ll z \tan \theta_T$$

Combining the results for both $L \gg z \tan \theta_T$ and $L \ll z \tan \theta_T$, we can write

$$E\{B^2\} = \begin{cases} \frac{\Delta}{\sigma_h^2 + \sigma_f^2} & L \gg z \tan \theta_T \\ \frac{\Delta}{\sigma_h^2 + \sigma_f^2 + \frac{4}{c^2} \sigma_\xi^2} & L \ll z \tan \theta_T \end{cases} \quad (6.13)$$

where

$$\Delta = \frac{\gamma e^{-\gamma^2}}{\sqrt{\pi} \operatorname{erfc}[\gamma]} - \gamma^2, \quad (6.14)$$

and

$$\gamma = \begin{cases} \frac{c(\sigma_h^2 + \sigma_f^2)^{1/2}}{2z \tan \theta_T} \left(\frac{2\sigma_\xi^2}{L^2} + \tan^2 \theta_T \right)^{-1/2} & L \gg z \tan \theta_T \\ \frac{c}{2z \tan^2 \theta_T} \left(\sigma_h^2 + \sigma_f^2 + \frac{4}{c^2} \sigma_\xi^2 \right)^{1/2} & L \ll z \tan \theta_T \end{cases} \quad (6.15)$$

The results for a flat surface can be computed by letting σ_ξ equal zero. When $L \gg z \tan \theta_T$, if the received pulse shapes are dominated by beam curvature ($\tan \theta_T$ is large) or surface effects (σ_ξ is large), γ will be small. If the curvature and surface effects are negligible, γ will be large. On the other hand, when $L \ll z \tan \theta_T$, γ will be large when σ_ξ is large. In these two limiting cases, Δ simplifies to

$$\Delta = \begin{cases} \frac{\gamma}{\sqrt{\pi}} & \gamma \ll 1 \\ \frac{1}{2} & \gamma \gg 1 \end{cases} \quad (6.16)$$

To evaluate the expression for the bandwidth and timing error, we assumed $c(\sigma_h^2 + \sigma_f^2)^{1/2} \ll \sigma_\xi < z \tan \theta_T$. This means that the surface rms height is large compared to the point target response width but small compared to the radius of the footprint. For small footprints, the solution for $L \gg z \tan \theta_T$ is probably the most applicable so that

$$\text{MSE} \cong \left(\frac{1}{\langle N_1 \rangle} + \frac{1}{\langle N_2 \rangle} + \frac{1}{K_1} + \frac{1}{K_2} \right) \frac{\sqrt{2\pi} \alpha (\sigma_h^2 + \sigma_f^2)^{1/2} \sigma_\xi z \tan \theta_T}{cL} \quad L \gg z \tan \theta_T \quad (6.17)$$

For large footprints the solution for $L \ll z \tan \theta_T$ is the most applicable, and

$$\text{MSE} \cong \left(\frac{1}{\langle N_1 \rangle} + \frac{1}{\langle N_2 \rangle} + \frac{1}{K_1} + \frac{1}{K_2} \right) \frac{4\alpha\sigma_\xi^2}{c^2} \quad L \ll z \tan \theta_T \quad (6.18)$$

where we have given only the first-order terms of Eq. (5.41) for simplicity.

Because the wave height is typically of the order of tens of centimeters, σ_ξ/c will usually be a few nanoseconds or larger. Picosecond time resolution is probably not feasible when the footprint is large. However, when the footprint is small and the surface correlation length is large, picosecond accuracy is possible if the system parameters are properly chosen. The requirement for a large correlation length is equivalent to requiring a glint within the footprint.

7. LINK EQUATIONS

In this chapter, we use the results obtained from previous chapters to estimate the expected timing accuracies of realistic system designs and to estimate the corresponding accuracies of the barometric measurements.

The expected number of received signal photons was calculated in Ref. 4 for Gaussian ocean wave statistics:

$$\langle N \rangle = \frac{\eta}{hf_o} Q T_a^2 \frac{A_R}{z^2} \frac{|R(0)|^2}{4\pi(S^2 + 2 \tan^2 \theta_T)} . \quad (7.1)$$

η is the receiving system efficiency, hf_o is the signal photon energy, Q is the total transmitted energy, and T_a^2 is the two-way atmospheric transmittance. The ocean reflectance $|R(0)|^2$ depends on wavelength and water composition. From the near IR to the near UV, the ocean reflectance is ~2 % [22]. The factor $(S + 2 \tan^2 \theta_T)$ in Eq. (1) is related to the solid angle of the reflected signal. In a perfectly calm sea $S^2 \approx 0$, so the solid angle of the back-scattered signal is equal to the solid angle of the laser beam. For an isotropic surface, S^2 is related to the MS surface roughness and profile correlation length (L):

$$S^2 = 2 \sigma_\xi^2 / L^2 . \quad (7.2)$$

Buften et al. [23] recently reported measurements of $\beta_r = |R(0)|^2 / 4\pi S^2$ for a variety of sea states, nadir angles, and laser wavelengths. Their measurements were obtained at wavelengths of 337 nm, 532 nm, and 9.5 μ m using an airborne lidar. At the visible and near UV wavelengths, the ocean reflectance (β_r) for low wind speeds was ~6%. Equations (3.8) and (3.9) of Chapter 3 are consistent with these results.

If we use this value for β_r in Eq. (7.1) and the parameters listed in Table 7.1 for a satellite-based altimeter, the expected signal photocount

is $\langle N \rangle \approx 1300$. The speckle number calculated using Eq. (3.17) is $K = 50,000$. In this case, speckle is negligible, and the shot noise is the dominant source of timing error. From the data plotted in Fig. 5.4, we see that the single shot timing error for this case is ~ 18 psec. The error can be reduced to ~ 2 psec by averaging the timing measurements from 100 shots. If the fundamental (1064 nm) and tripled (353 nm) YAG laser frequencies are used, a 2 psec timing error results in a pressure error of ~ 1 mbar (see Fig. 2.1).

TABLE 7.1.
PARAMETERS OF A SATELLITE-BASED LASER ALTIMETER

Receiving System Efficiency	:	10%
Receiver Aperture Area	:	0.1 m^2
Two-way Atmospheric Transmittance:		0.5
Altitude of the Satellite	:	400 km
Laser Beam Divergence Angle	:	100 μrad
Total Transmitted Energy	:	250 mJ

8. AIRBORNE ALTIMETER EXPERIMENT DATA ANALYSIS

8.1. Introduction

An aircraft experiment was conducted on September 7 and 9, 1983, at the NASA facility on Wallops Island, VA. The experiment was to test the flight performance of the instrumentation and to measure the correlation properties of the multiwavelength ocean reflected return pulses. GSFC personnel including Abshire, McGarry and Rowe conducted the flight experiment, while the data reduction and analysis were performed at the University of Illinois.

The experiment was performed on board the NASA WFF Electra airplane. A picture of the airplane is shown in Fig. 8.1. The laser ranging system used in this experiment, including the laser, computer, waveform digitizer and other electronics, is the same equipment used in previous horizontal-path experiments [24], [25], [26]. Figure 8.2 is a picture of the computer system on board the aircraft. Figure 8.3 is a picture of the equipment rack on the aircraft. Figure 8.4 is a picture of the arrangement of the equipment on the aircraft.

On September 7, before the flight, the altimeter was first tested by ranging horizontally to a cube corner reflector. The system worked well on the ground. However, after the aircraft took off and ascended to the ranging altitude, the receiver did not detect any reflected laser pulses. After the flight, the ranging system was carefully examined. The problem was caused by the vibrations that occurred during the flight which caused a misalignment between the receiving telescope and the detector.

On September 8, before the aircraft took off, two ground calibration data sets data were collected by ranging to a white plate. Then the aircraft took off, headed east over the ocean, and the altimeter started



Figure 8.1. A picture of the NASA Electra airplane.

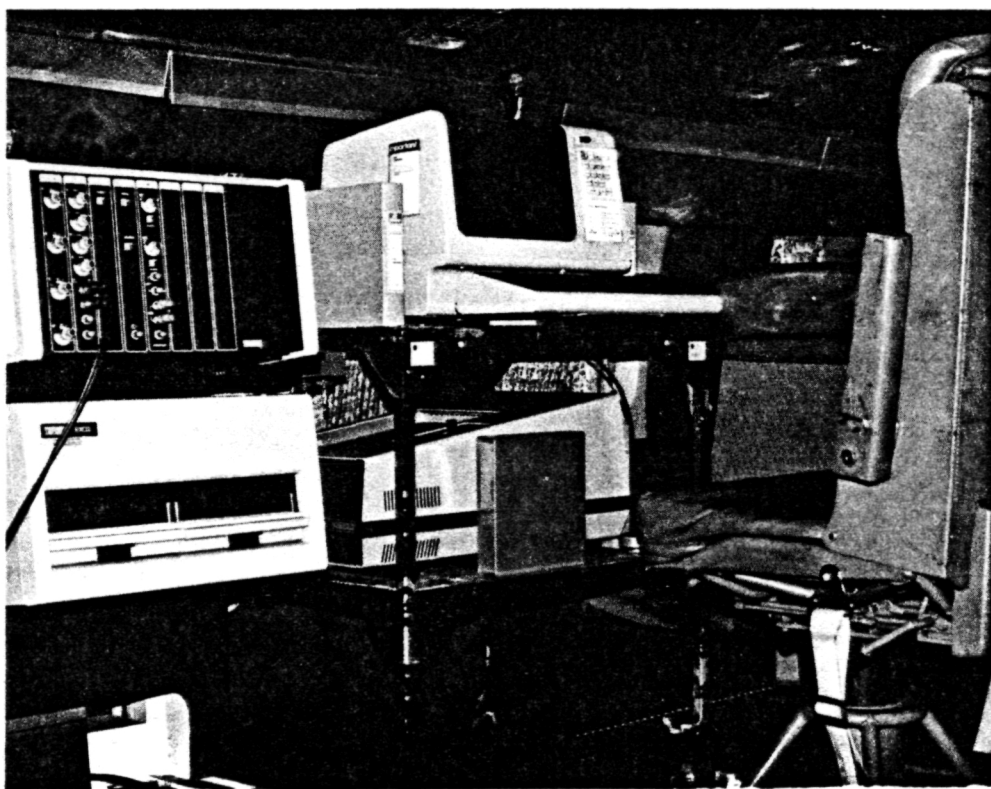


Figure 8.2. A picture of the computer system on board the airplane.

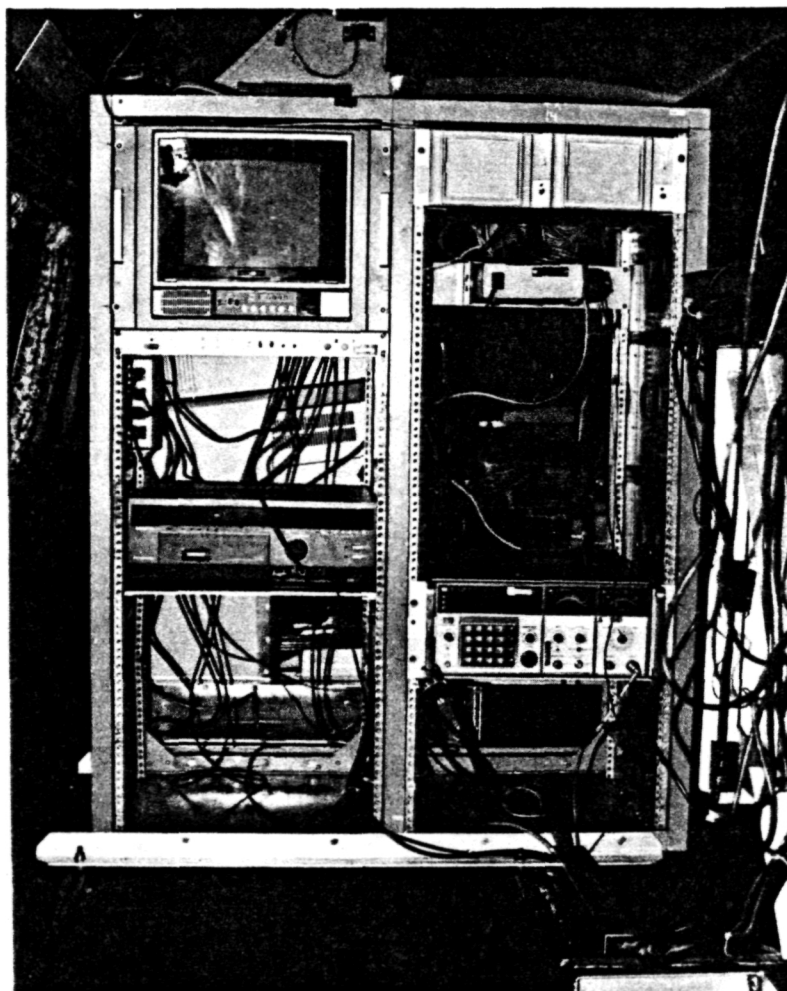


Figure 8.3. A picture of the equipment rack on board the airplane.

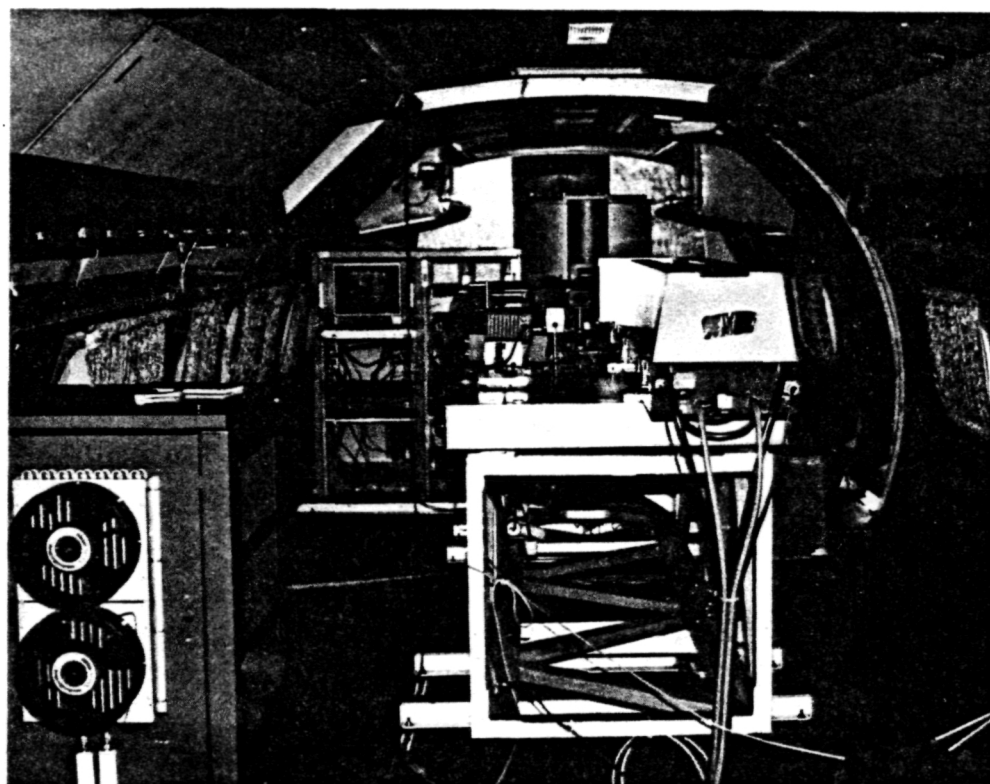


Figure 8.4. A picture of the interior of the airplane showing the laser power supply, the laser and the transmitting optics.

collecting data. During the three-hour flight, the system operated smoothly except for a temporary computer failure due to a loose circuit board. The problem was fixed during the flight. In this flight, data were taken over the ocean at both 305 m (1000 ft) and 1219 m (4000 ft) altitudes. They are the first data that furnish information on ocean reflection properties with 8 cm height resolution [27].

8.2. Data Analysis

A typical recorded waveform collected at 305 m altitude is shown in Fig. 8.5. The pulse on the left corresponds to the return at 355 nm (UV), and the pulse on the right is the return at 532 nm (Green). The time scale in the plot is the number of digitizer elements. The temporal spacing between the elements is 39 picoseconds so that the full scale range is 20 nsec. The actual flight time of the green pulse is shorter, but it is passed through an electrical delay line so that both pulses can be recorded on the waveform digitizer side by side. Due to this arrangement, the separation time between the two pulses will decrease with altitude, instead of increase.

On some of the recorded waveforms, double peaks in both return pulses were observed. An example is shown in Fig. 8.6. This occurred in some of the returns from the ocean at both 305 m and 1219 m altitude and also in some of the returns from the white plate. The separation between the closely spaced two peaks exceeds 1 nsec in some returns.

Because a separation of 1 nsec is equivalent to a target range spread of 15 cm, which is not the case for the white plate target, and unlikely for the ocean target. The laser has a beam divergence angle of approximately 500 μ rad (full width at 10% points); therefore, the footprint has a size of ~15 cm at 305 m altitude and ~60 cm at 1219 m altitude. An ocean-wave

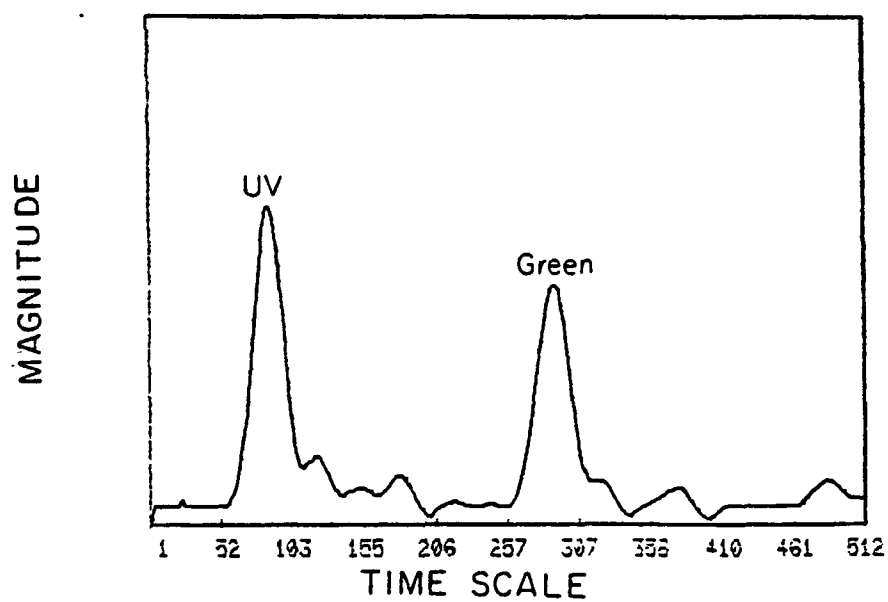


Figure 8.5. A waveform recorded at 305 m (1000 ft) altitude.

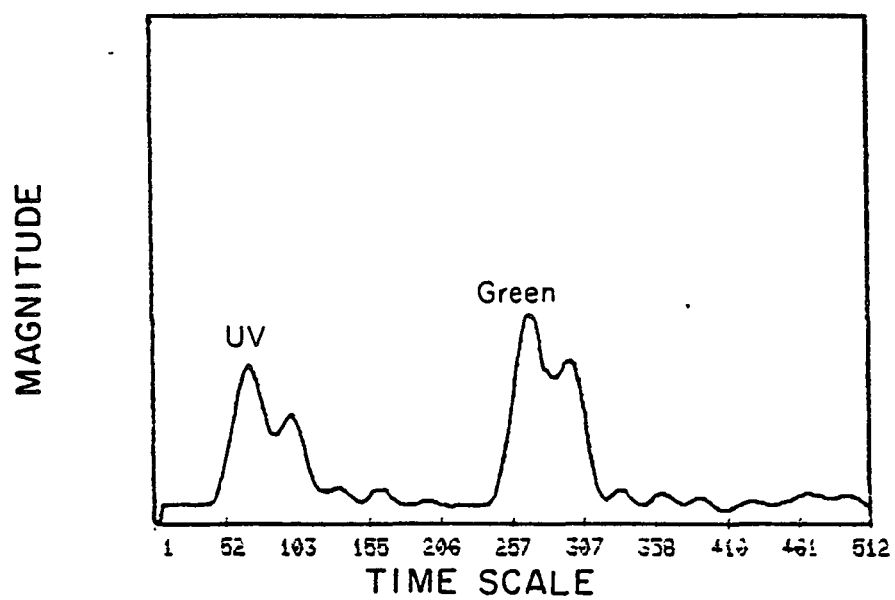


Figure 8.6. A waveform recorded at 305 m (1000 ft) altitude.

height difference of 15 cm within a 60 cm footprint is possible, but is much less likely within a 15 cm footprint. We conclude that double pulsing of the laser is probably the cause of the double peaks in the return pulse. In future experiments, the resolution of the receiver will be increased so that this ambiguity will no longer exist.

After the flight, the collected data were first run through a sorting program, in which every waveform was scrutinized to reject unsatisfactory ones. A waveform is rejected if any of the following conditions occur: signal level too low (no energy detected at one or two wavelengths), signal level too large (outside the dynamic range of the waveform digitizer), and signal not recorded completely due to a triggering problem. The good waveforms are then processed to extract the differential arrival time between the two pulses.

The first technique used for timing was the correlation technique. This was done by first calculating the correlation coefficient of the two return pulses. The correlation coefficient ρ is defined as

$$\rho(j) = \frac{\sum_{i=1}^N x(i) x(i+j)}{\left\{ \sum_{i=1}^N x(i)^2 \right\}^{1/2} \left\{ \sum_{i=j+1}^{j+N} x(i)^2 \right\}^{1/2}}, \quad (8.1)$$

where $x(i)$ represents the output of the i^{th} digitizer element and N is the number of points used in the correlation. $\rho(j)$ is normalized so that if the two pulses have exactly the same shape it achieves its maximum value of one. We calculated the correlation coefficient instead of just the correlation function because the correlation coefficient also furnishes information on the degree of similarity of the pulse shapes at two wavelengths. The delay value that maximizes ρ was then used as the differential arrival time estimate. That is,

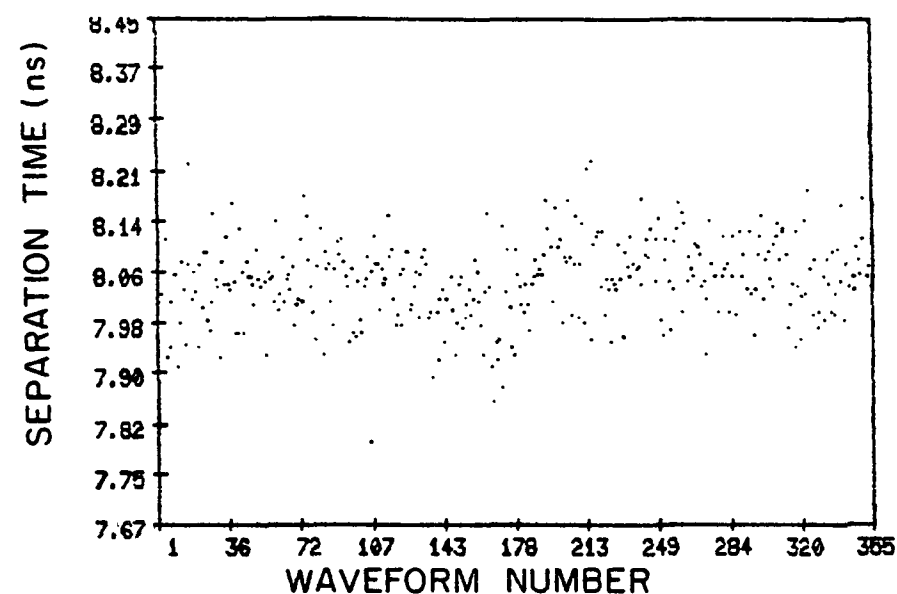
$$\hat{\tau}_{12} = [\arg \max_j \rho(j)] \tau_0, \quad (8.2)$$

where τ_0 is the temporal spacing of the digitizer elements. For this experiment τ_0 is 39 picoseconds for all the data. Therefore, $\hat{\tau}_{12}$ can only assume quantized values in integer multiples of τ_0 . In retrospect, the experiment could have been improved by using a faster digitizer sweep speed. However, at the time of the experiment, there was no way of knowing how wide the return pulse would be. Therefore, a slower sweep speed was used to make sure the entire return waveform could be recorded.

The quantization problem can be partially remedied by fitting a curve through the correlation function and finding the peak of the fitted curve. A second-order polynomial was chosen as the fitting curve, because most return pulses resemble Gaussian pulses and a Gaussian is well approximated by a quadratic near its peak. We first tried using 5 or more points to perform the least square curve fitting. However, because the fitted curve did not pass through all data points, there were cases when the peak of the fitted curve was smaller than the original correlation peak. Therefore, we decided to use only 3 points around the correlation peaks for curve fitting. In this case, the fitted parabola will pass through all 3 points. The success of the 3-point curve fitting requires a high signal-to-noise ratio for the data points used. This requirement holds for the points near the correlation peaks.

A history plot and histogram of the timing and the correlation coefficient are shown in Figs. 8.7 and 8.8 for the 305 m altitude data.

In Fig. 8.9, two recorded waveforms collected at 1219 m altitude are shown. The timing results are shown in Fig. 8.10. Statistics of the correlation coefficient are shown in Fig. 8.11.



OF POINTS GREATER THAN 8.448 ns = 0
 # OF POINTS SMALLER THAN 7.667 ns = 0

TOTAL NUMBER OF WAVEFORMS = 355
 AVERAGE SEPARATION TIME = 204.6 ELEMENTS
 = 7.994 NANO SEC
 STANDARD DEVIATION = 1.612 ELEMENTS
 = 63 PICO SEC

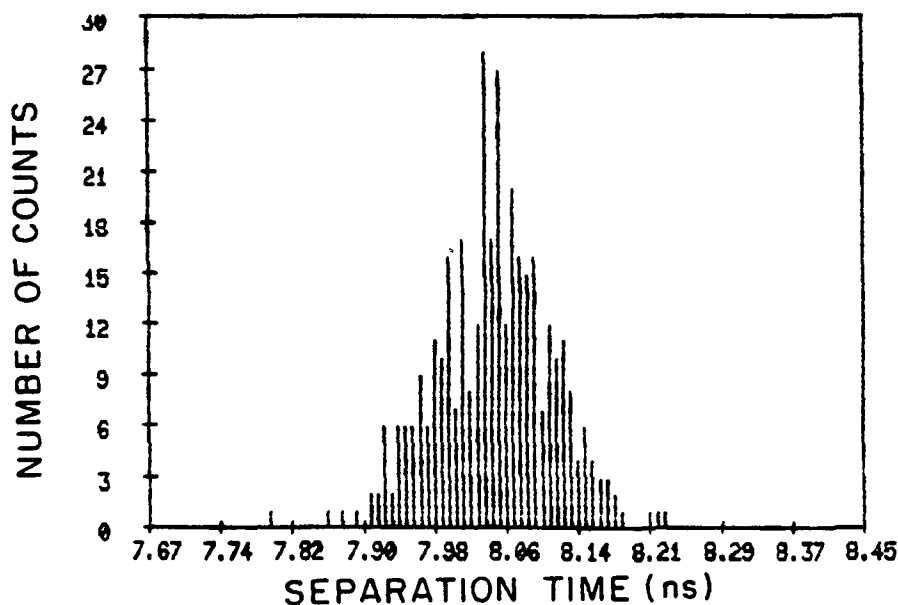


Figure 8.7. Timing history and timing histograms for the 305 m altitude data, using the correlation algorithm. Correlation coefficient is curve fitted around its peak.

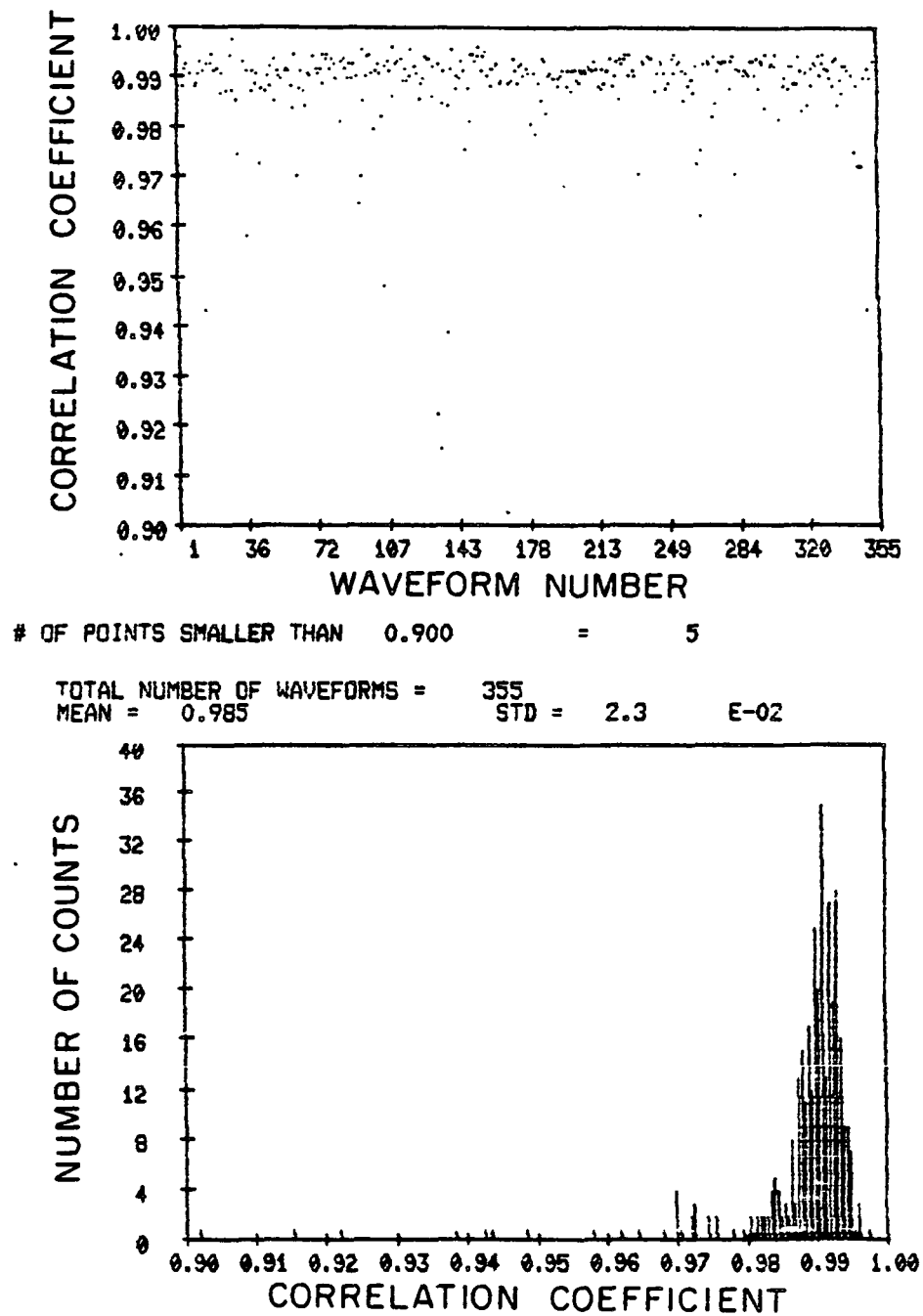


Figure 8.8. History plot and histogram of the correlation coefficient for the 305 m altitude data. Correlation coefficient is curve fitted around its peak.

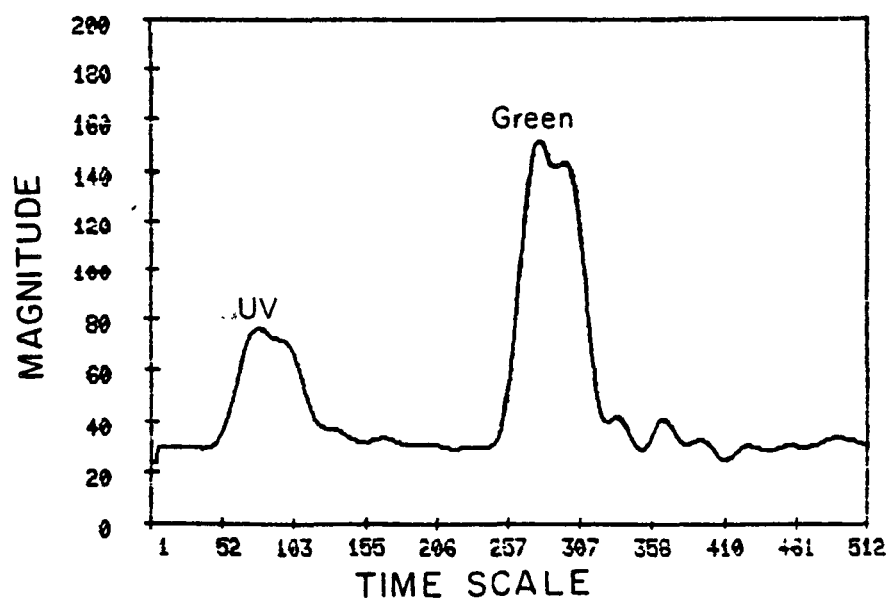
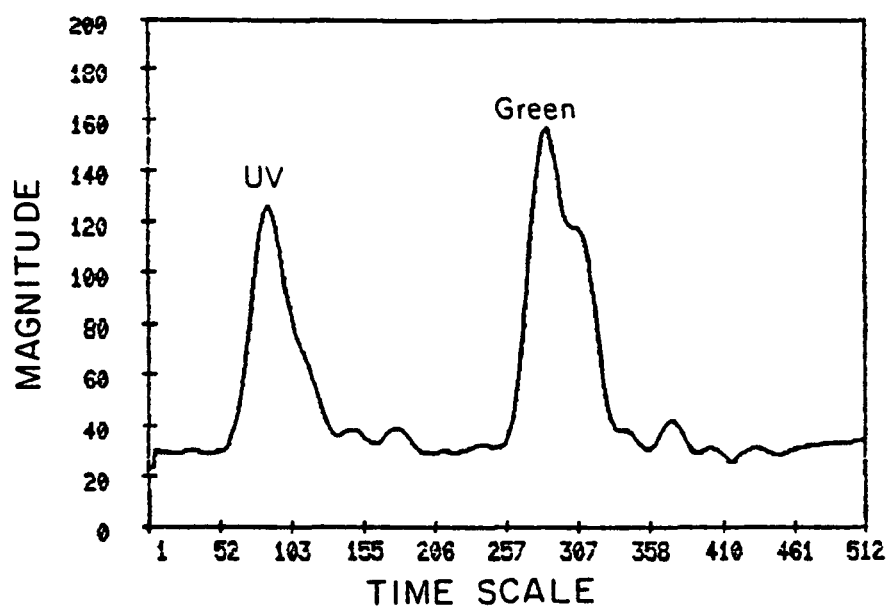
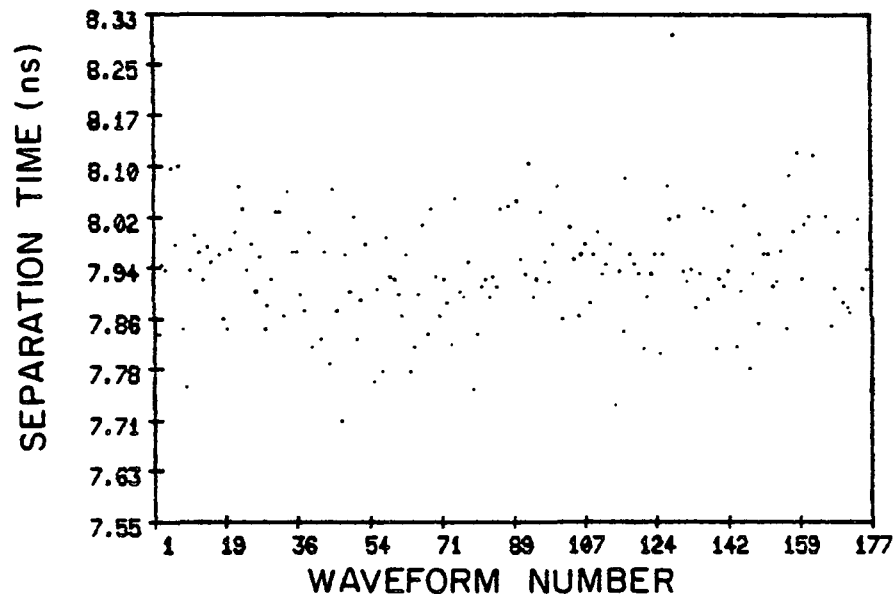


Figure 8.9. Two recorded waveforms at 1219 m (4000 ft) altitude.



# OF POINTS GREATER THAN	8.331	ns =	1
# OF POINTS SMALLER THAN	7.550	ns =	0
TOTAL NUMBER OF WAVEFORMS = 177			
AVERAGE SEPARATION TIME =	201.9	ELEMENTS	
	7.888	NANO SEC	
STANDARD DEVIATION =	2.331	ELEMENTS	
	91	PICO SEC	

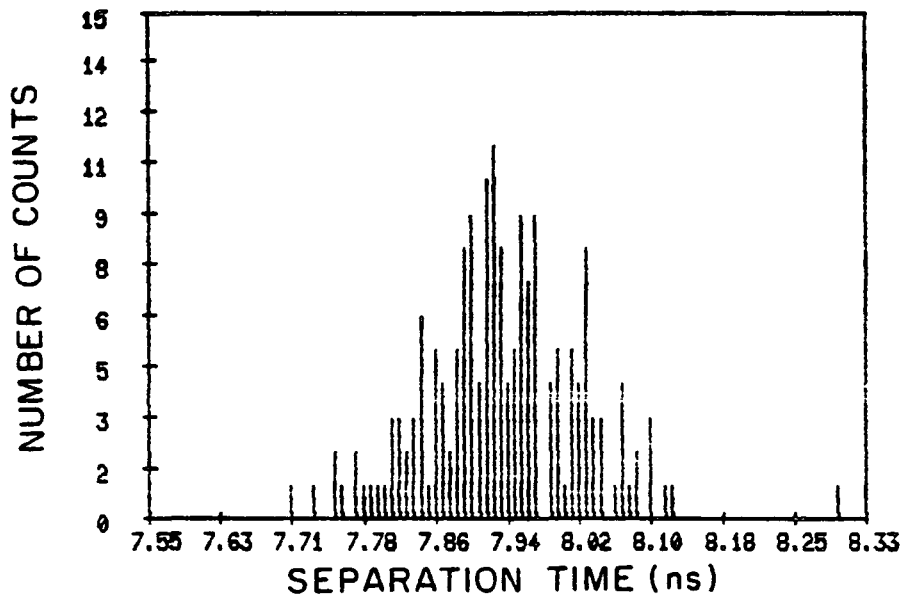


Figure 8.10. Timing history and timing histogram for the 1219 m altitude data, using the correlation algorithm. Correlation coefficient is curve fitted around its peak.

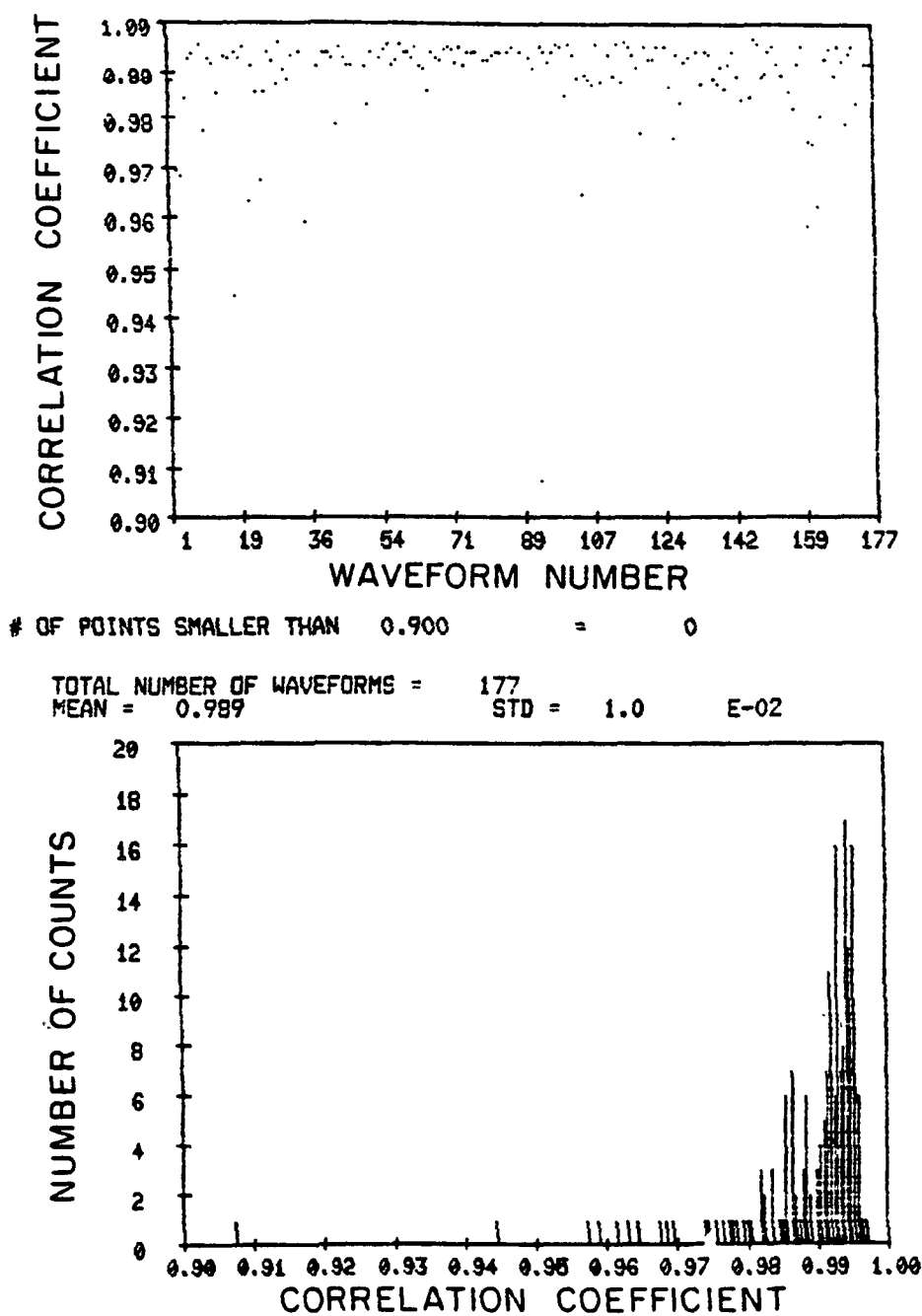


Figure 8.11. History plot and histogram of the correlation coefficient for the 1219 m altitude data. Correlation coefficient is curve fitted around its peak.

For both 305 m and 1219 m altitude data, the correlation coefficient has average values approaching 0.99. This high average value of the correlation coefficient indicates that the pulse shapes at the two wavelengths are very similar even on the pulse-to-pulse basis. This is encouraging for the pressure measurement technique because similar waveforms are essential.

In Fig. 8.12, two recorded waveforms from a white plate target are shown. The corresponding timing and correlation coefficient results are given in Figs. 8.13 and 8.14. In Fig. 8.15, we plot two recorded waveforms from a cube corner reflector. The timing results are shown in Fig. 8.16 and the results for the correlation coefficient are given in Fig. 8.17.

In Table 8.1, we summarize the above results. From the results, we find the data obtained from ranging to the white plate have the smallest timing fluctuations, the highest mean correlation coefficient and also the smallest standard deviation of the correlation coefficient. It is reasonable that the returns from the white plate would have a higher signal-to-noise ratio than the returns from the ocean, but it seems that the returns from the cube corner reflector should have an even higher signal-to-noise ratio. This was not the case, probably because the ranging to the cube corner reflector was performed in daytime with the presence of a strong turbulence during the experiment.

The data obtained at 305 m and 1219 m altitudes can be used to verify the pressure measurement concept. From Appendix E, the differential arrival time measured at 1219 m and 305 m should differ approximately by

$$\Delta\tau = 1326(e^{-305/h_s} - e^{-1219/h_s})$$

$$= 126.6 \text{ psec} ,$$

$$(8.3)$$

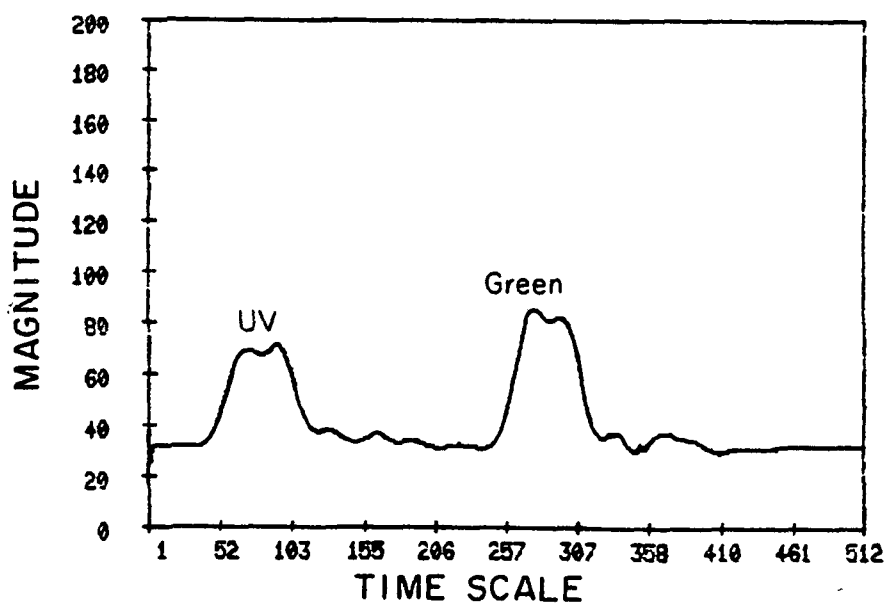
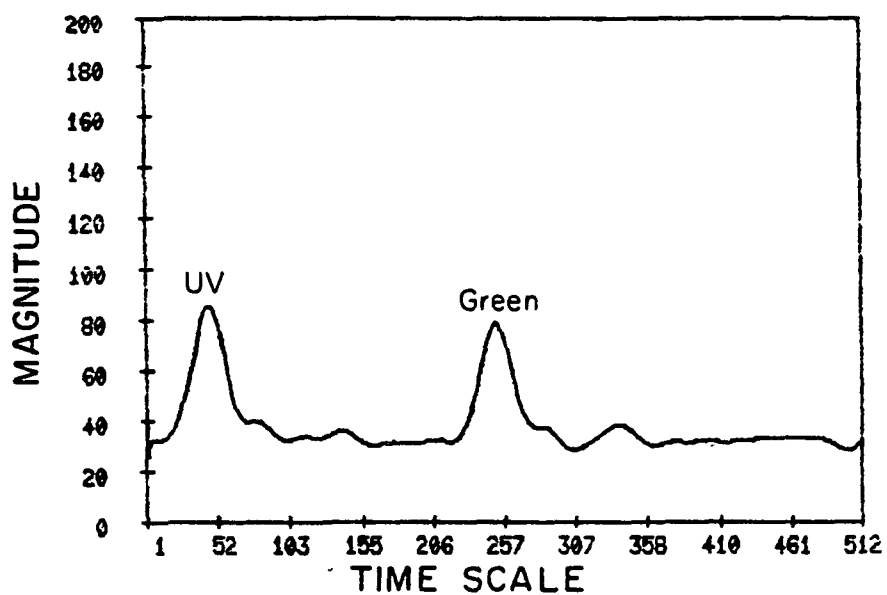
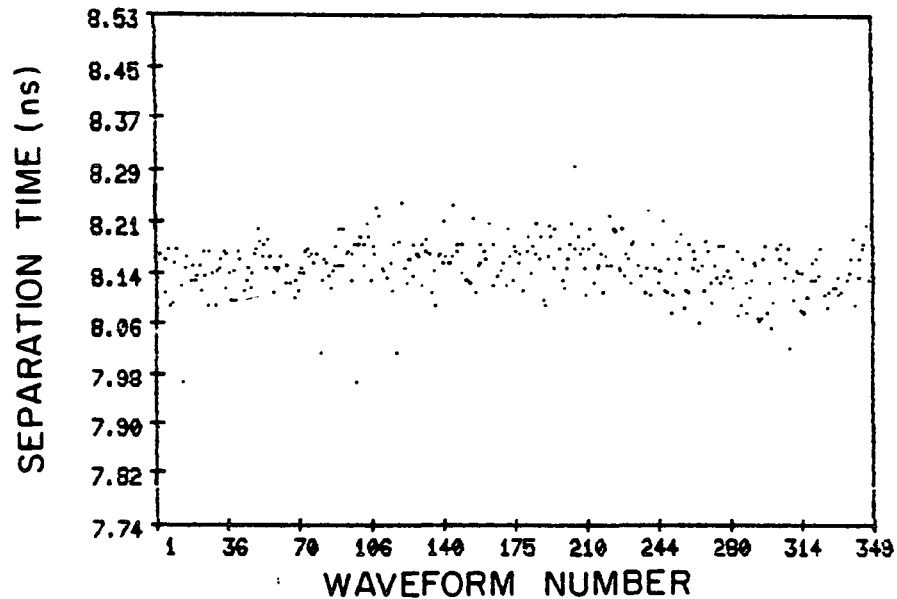


Figure 8.12. Two recorded waveforms obtained from ranging to a white plate.



# OF POINTS GREATER THAN	8.526	ns =	0
# OF POINTS SMALLER THAN	7.745	ns =	0
TOTAL NUMBER OF WAVEFORMS = 349			
AVERAGE SEPARATION TIME =	207.1	ELEMENTS	
	8.093	NANO SEC	
STANDARD DEVIATION =	1.030	ELEMENTS	
	40	PICO SEC	

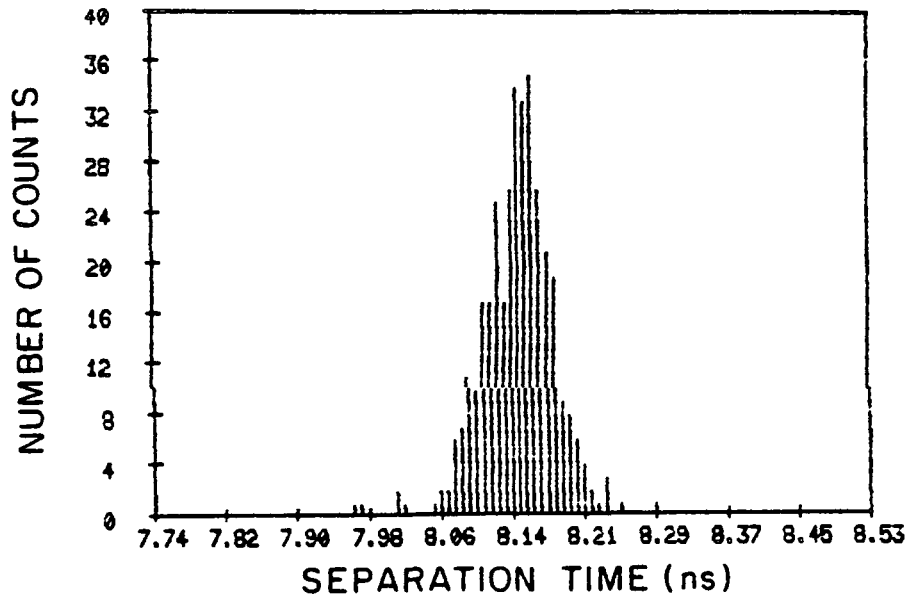


Figure 8.13. Timing history and timing histogram for the data obtained from ranging to a white plate, using the correlation algorithm. Correlation coefficient is curve fitted around its peak.

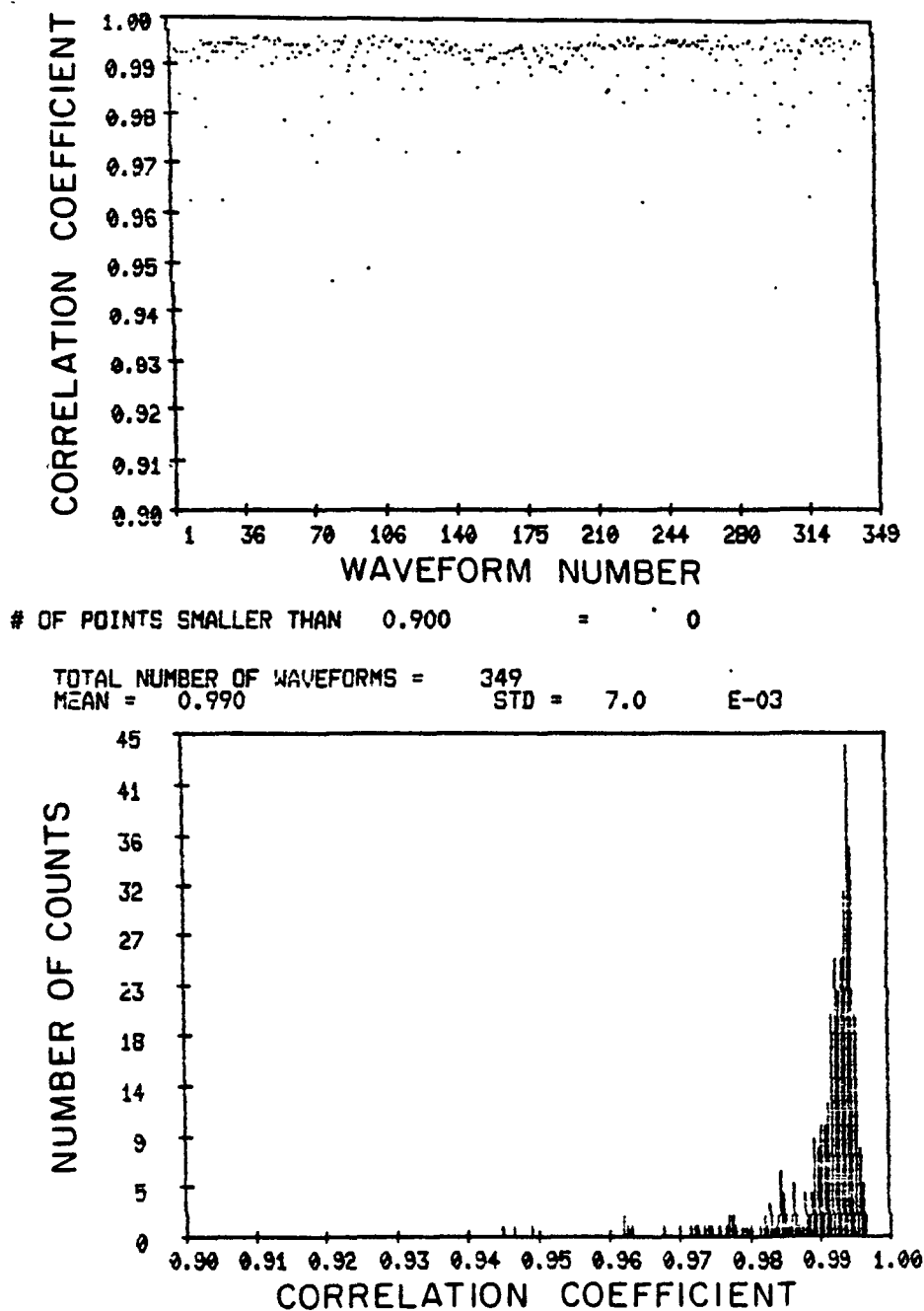


Figure 8.14. History plot and histogram of the correlation coefficient for the data obtained from ranging to a white plate. Correlation coefficient is curve fitted around its peak.

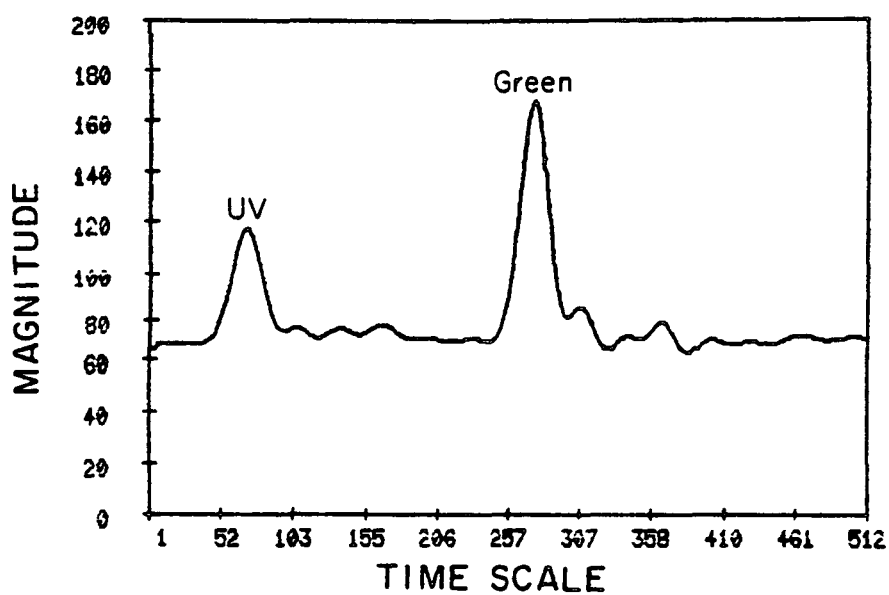
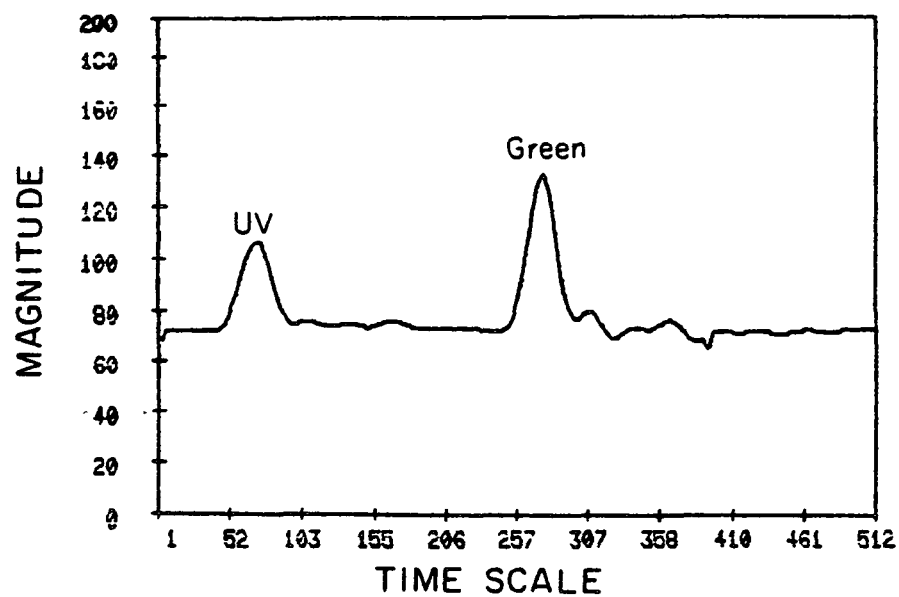
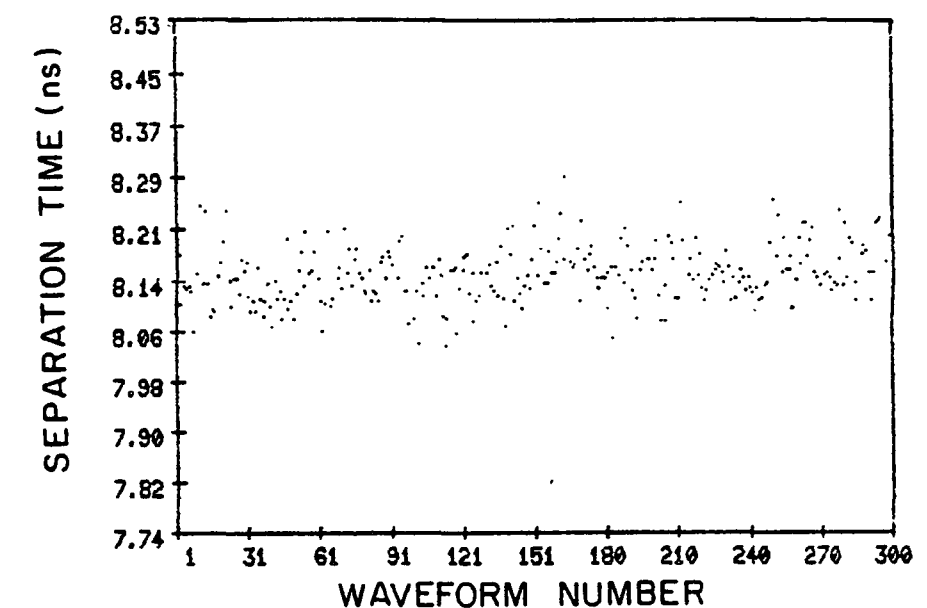


Figure 8.15. Two recorded waveforms obtained from ranging to a cube corner reflector.



OF POINTS GREATER THAN 8.526 ns = 0
 # OF POINTS SMALLER THAN 7.745 ns = 0

TOTAL NUMBER OF WAVEFORMS = 300
 AVERAGE SEPARATION TIME = 207.2 ELEMENTS
 = 8.093 NANO SEC
 STANDARD DEVIATION = 1.125 ELEMENTS
 = 43 PICO SEC

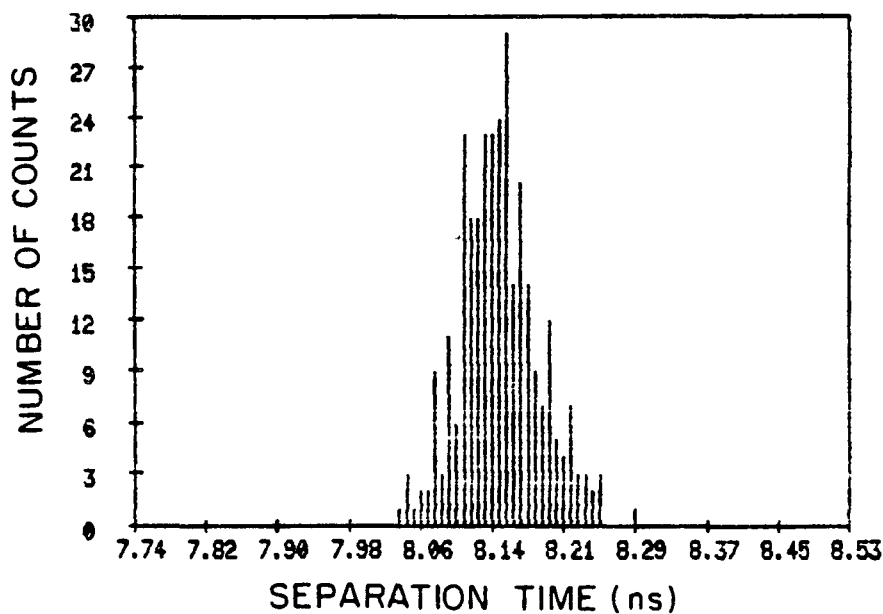


Figure 8.16. Timing history and timing histogram for the data obtained from ranging to a cube corner reflector, using the correlation algorithm. Correlation coefficient is curve fitted around its peak.

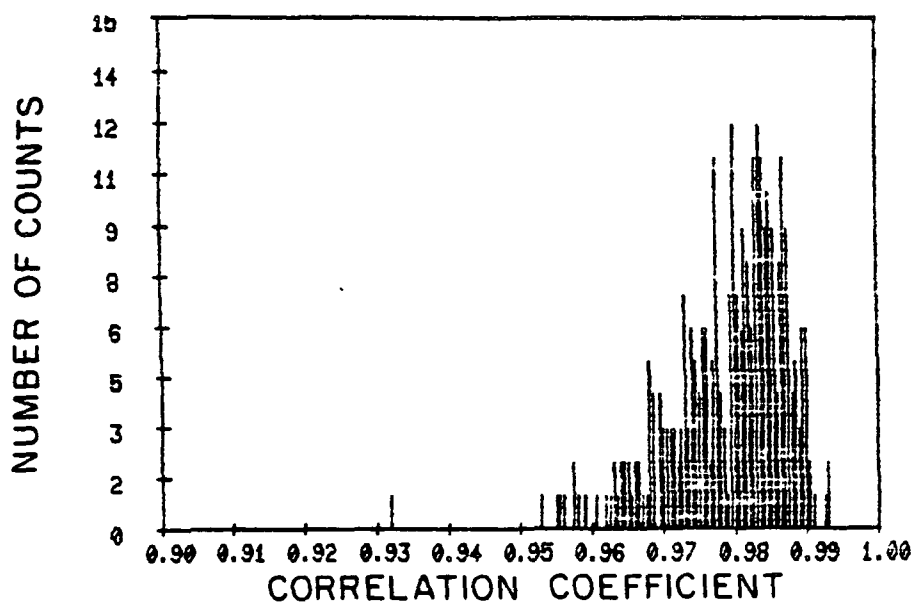
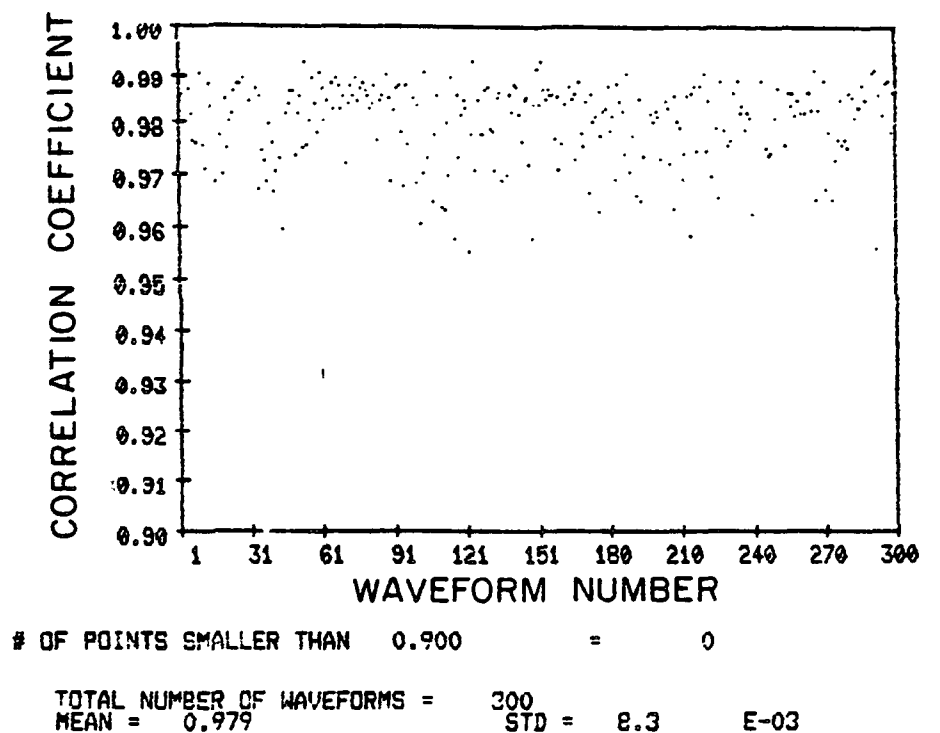


Figure 8.17. History plot and histogram of the correlation coefficient for the data obtained from ranging to a cube corner reflector. Correlation coefficient is curve fitted around its peak.

TABLE 8.1.

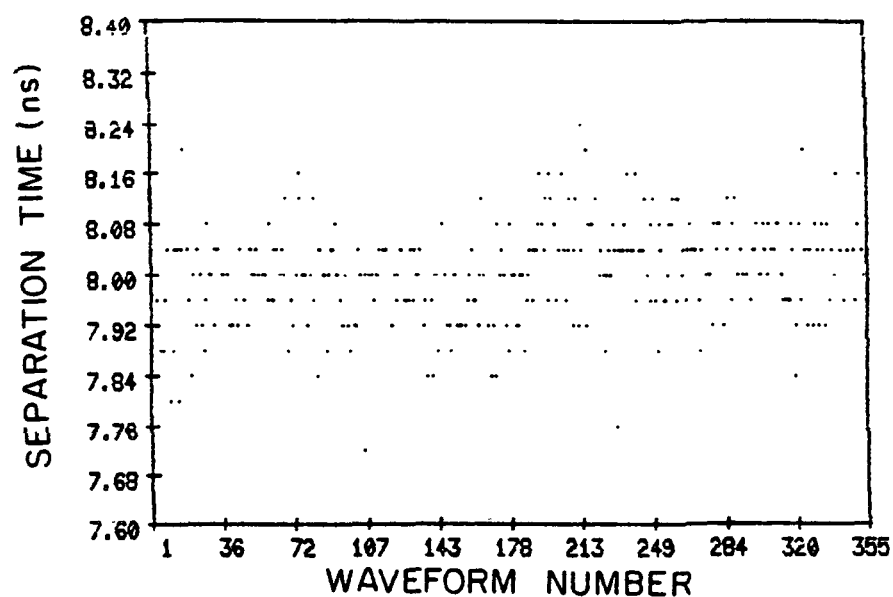
SUMMARY OF THE RESULTS OBTAINED FROM THE CORRELATION TECHNIQUE. THE
90 % CONFIDENCE INTERVALS OF MEAN AND STANDARD DEVIATIONS ARE SHOWN.

Data Set	Separation Time		Correlation Coefficient	
	Mean	STD	Mean	STD
305m altitude data	7995 psec [7989,8001]	63 psec [60,67]	0.986 [.984,.988]	0.023 [.022,.025]
1219 m altitude data	7888 psec [7877,7899]	91 psec [84,101]	0.989 [.988,.990]	0.010 [.009,.011]
White plate target	8093 psec [8089,8097]	40 psec [38,43]	0.991 [.990,.992]	0.007 [.006,.008]
Cube corner target	8094 psec [8090,8098]	43.95 psec [41,47]	0.979 [.978,.980]	0.008 [.007,.009]

where h_s is the atmospheric scale height, taken to be 8787 m. From the experimental data, the difference in differential arrival time is 106 picoseconds. Taking into account the fluctuations in the aircraft altitude and the quantization in the waveform digitizer, the 20 psec difference between the theory and the experiment is considered to be within the accuracy of the experiment.

For comparison, we processed the data collected at 305 m altitude and the data collected from ranging to a cube corner reflector using other estimation schemes. These two sets of data are chosen for comparison because the ocean is an example of a target with range spread, while the cube corner reflector is an example of a point target.

From Chapter 5, we know one of the simplest techniques for estimating differential arrival time is to find the separation time between the peaks of the two pulses. For the 305 m altitude data, the results are shown in Fig. 8.18. The standard deviation of timing is 176 picoseconds, much larger than that of the correlation algorithm. For the cube corner reflector data, the results are shown in Fig. 8.19. The peak detection yields a timing error of 49 picoseconds, which is not far from the 44 picoseconds of the correlation algorithm. This is consistent with the theory derived in Chapter 5, which states that, for range spread targets, the peak detection performs significantly worse than the correlation algorithm, while for point targets, the performances of the two estimators are close. Also, from Chapter 5, we know that the peak detection algorithm is more sensitive to noise introduced by the waveform digitizer than the correlation algorithm. This partially explains the slightly inferior performance of the peak detection algorithm for the cube corner reflector data.



OF POINTS GREATER THAN 8.400 ns = 0
 # OF POINTS SMALLER THAN 7.600 ns = 4

TOTAL NUMBER OF WAVEFORMS = 355
 AVERAGE SEPARATION TIME = 203.6 ELEMENTS
 = 7.956 NANO SEC
 STANDARD DEVIATION = 4.507 ELEMENTS
 = 176 PICO SEC

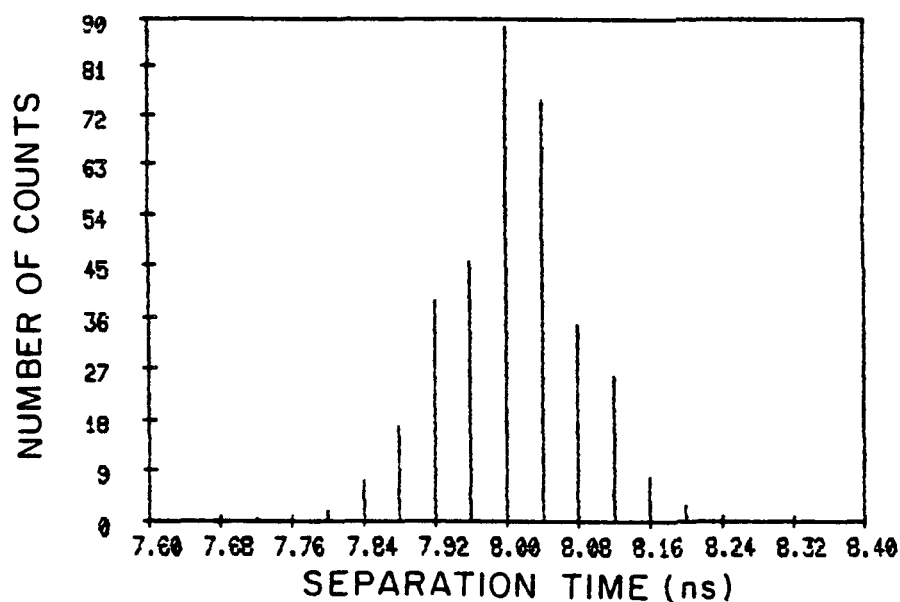
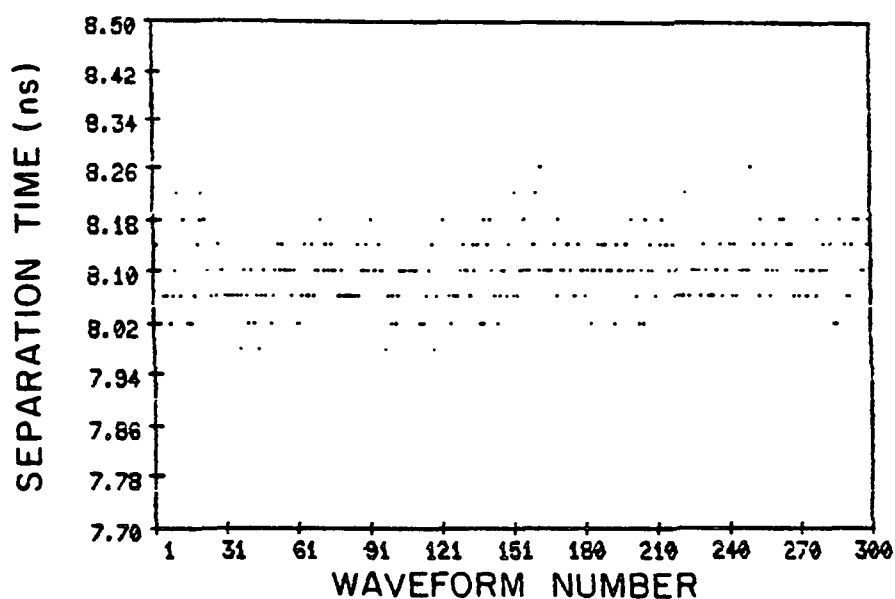


Figure 8.18. Timing history and timing histogram for the data obtained at 305 m altitude, using the separation between the two peaks as the differential arrival time estimate.



OF POINTS GREATER THAN 8.500 ns = 0
 # OF POINTS SMALLER THAN 7.700 ns = 0

TOTAL NUMBER OF WAVEFORMS = 300

AVERAGE SEPARATION TIME = 206.9
 = 8.083

STANDARD DEVIATION = 1.257
 = 49

ELEMENTS
 NANO SEC
 ELEMENTS
 PICO SEC

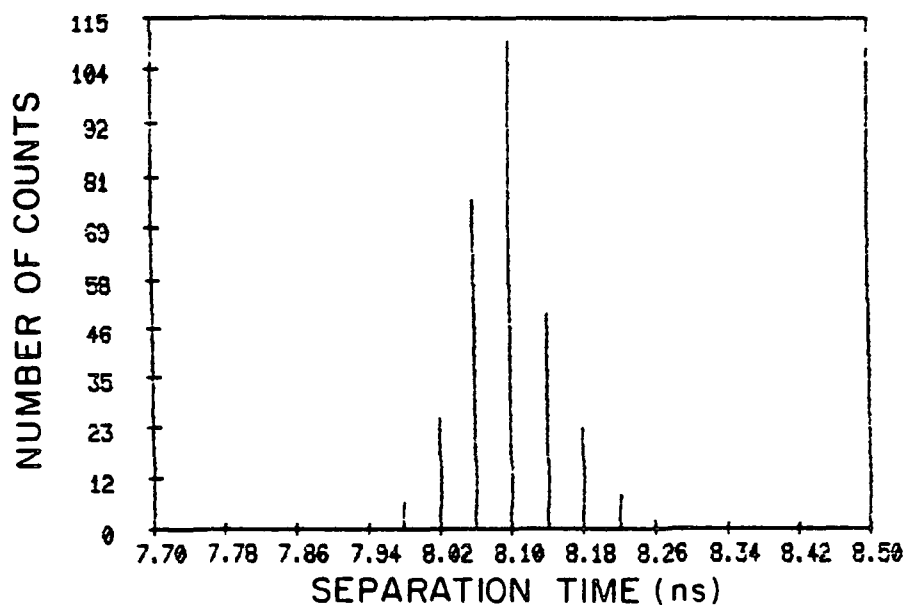


Figure 8.19. Timing history and timing histogram for the data obtained from ranging to a cube corner reflector, using the separation between the two peaks as the differential arrival time estimate.

The centroid detection algorithm was also used to calculate the differential delay. We used a total of 75 points around the peaks to calculate the centroids, and the timing results for the 305 m altitude data are shown in Figure 8.20. Compared to peak detection, the timing error is improved; it is 118.7 picoseconds. The corresponding results for the cube corner reflector are shown in Fig. 8.21. The timing error is 50 picoseconds, which is slightly larger than the 49.1 picoseconds of the peak detection algorithm. This is recognized to be caused by the inclusion of the ringing noise of the waveform digitizer in calculating the centroids. The return pulse from the cube corner reflector occupied a width narrower than 75 points, so using 75 points in calculating the centroids includes the undesirable data points that correspond to the ringing of the digitizer. We then used only 50 points in calculating the centroids. The results are shown in Fig. 8.22; the timing performance is improved to 46 picoseconds.

From Chapter 5, we know that the ML estimator correlates the received pulse with the logarithm of its mean pulse shape. Because the mean pulse shape is not available, the ML estimator can not be implemented. Correlating one return pulse with the logarithm of the other return pulse will not be optimum, but it is interesting to see how it performs. We first correlated the UV pulse with the logarithm of the green pulse. The results are shown in Fig. 8.23 for the 305 m altitude data. The standard deviation of timing is 84 picoseconds, which is not as good as the 63 picoseconds of the correlation algorithm. In Fig. 8.24, two recorded waveforms and their logarithms are shown. Taking the logarithm enhances the small amplitude fluctuations, which are mostly due to ringing and digitizer noise. The quantization effects also become more apparent after taking the

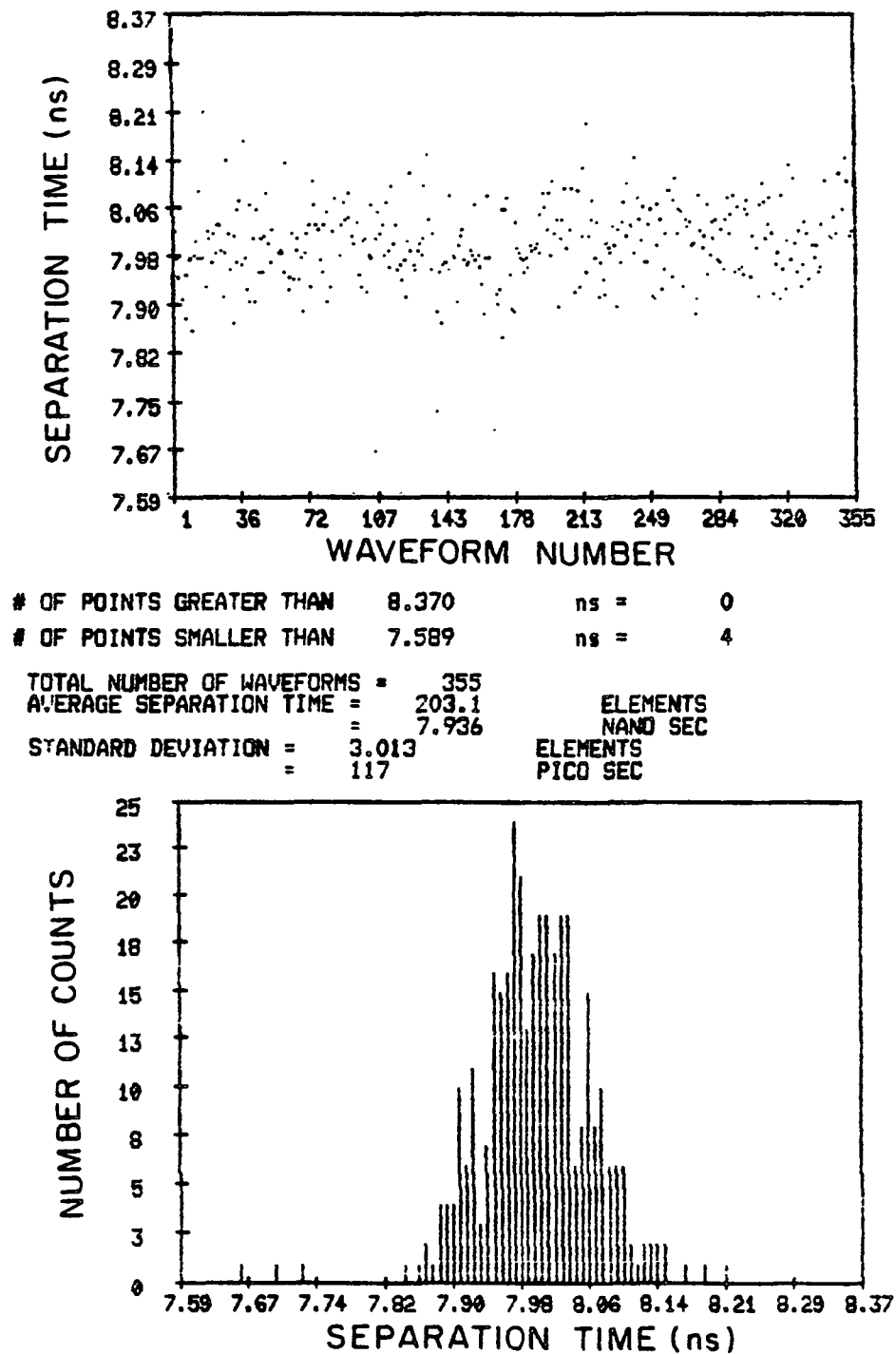
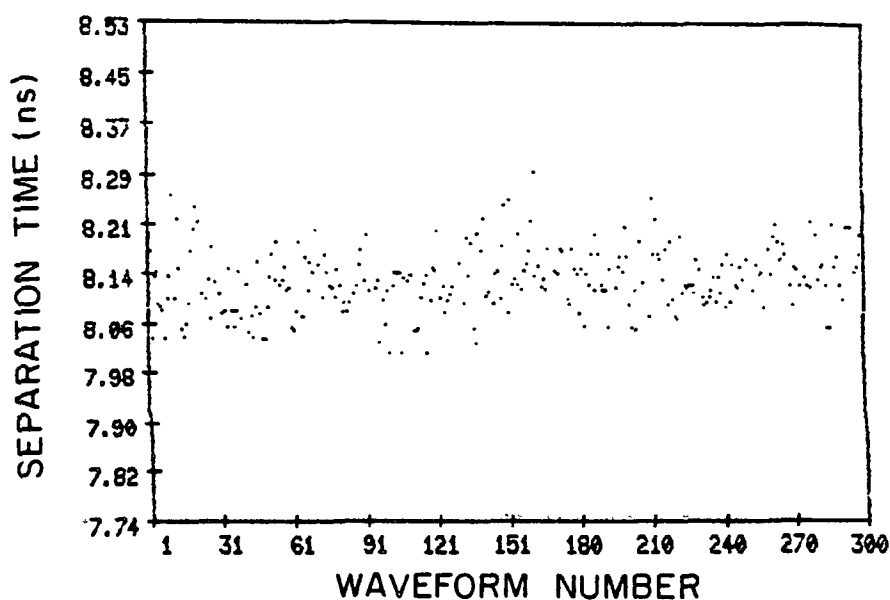


Figure 8.20. Timing history and timing histogram for the data collected at 305 m altitude. Results obtained by calculating the centroids of 75 points around the peaks.



OF POINTS GREATER THAN 8.526 ns = 0
 # OF POINTS SMALLER THAN 7.745 ns = 0

TOTAL NUMBER OF WAVEFORMS = 300
 AVERAGE SEPARATION TIME = 206.8 ELEMENTS
 = 8.080 NANO SEC
 STANDARD DEVIATION = 1.291 ELEMENTS
 = 50 PICO SEC

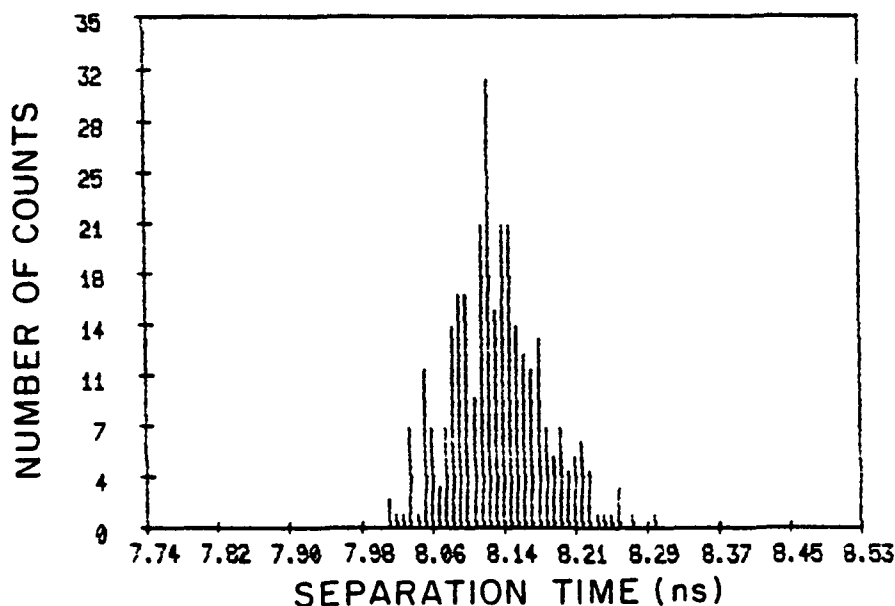
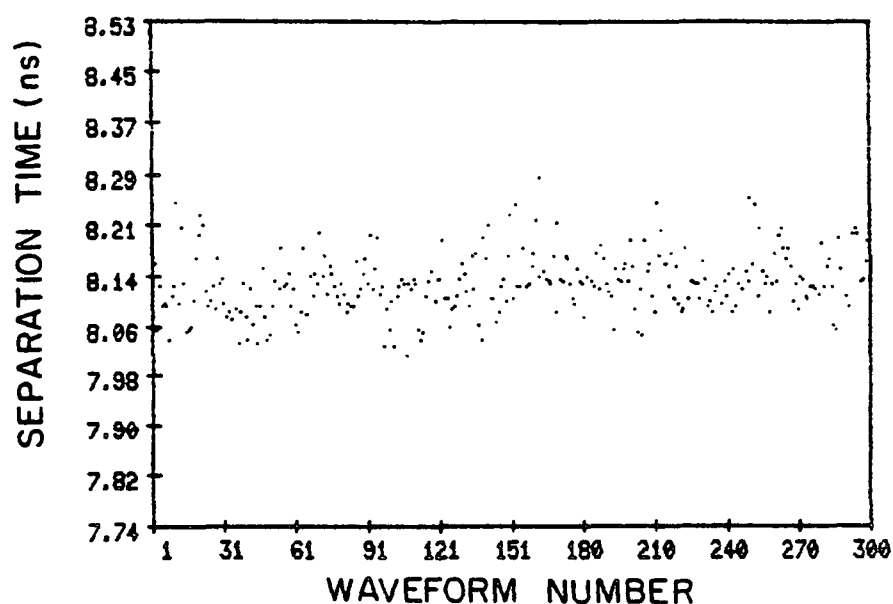


Figure 8.21. Timing history and timing histogram for the data collected from ranging to a cube corner reflector. Results obtained by calculating the centroids of 75 points around the peaks.



# OF POINTS GREATER THAN	8.526	ns =	0
# OF POINTS SMALLER THAN	7.745	ns =	0

```

TOTAL NUMBER OF WAVEFORMS =      300
AVERAGE SEPARATION TIME =      206.6      ELEMENTS
                        =      8.073      NANO SEC
STANDARD DEVIATION =      1.184      ELEMENTS
                        =      46      PICO SEC

```

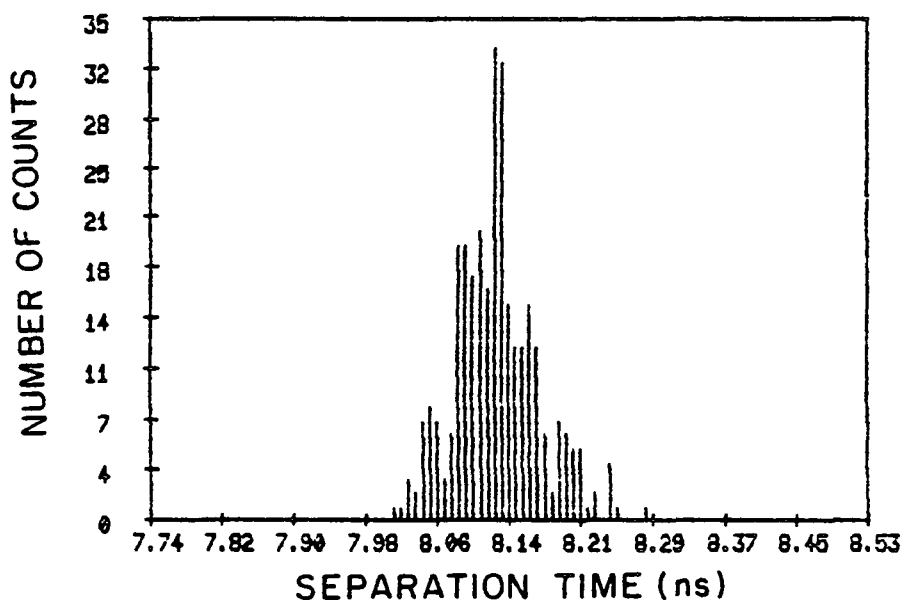
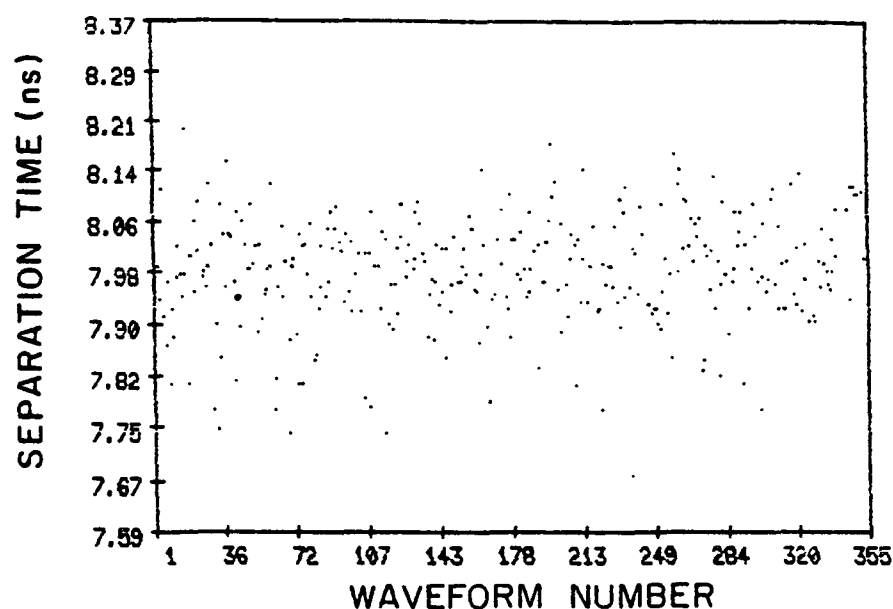


Figure 8.22. Timing history and timing histogram for the data collected from ranging to a cube corner reflector. Results obtained by calculating the centroids of 50 points around the peaks.



OF POINTS GREATER THAN 8.370 ns = 0
 # OF POINTS SMALLER THAN 7.589 ns = 0

TOTAL NUMBER OF WAVEFORMS = 355
 AVERAGE SEPARATION TIME = 202.9 ELEMENTS
 = 7.928 NANO SEC
 STANDARD DEVIATION = 2.160 ELEMENTS
 = 84 PICO SEC

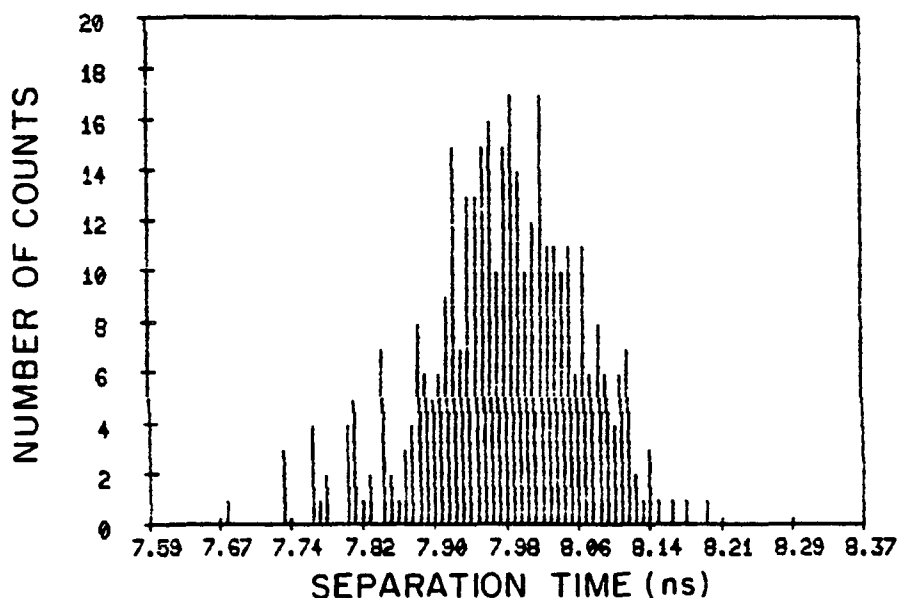


Figure 8.23. Timing history and timing histogram for the data collected at 305 m altitude. Results obtained by correlating the UV pulse with the logarithm of the green pulse.

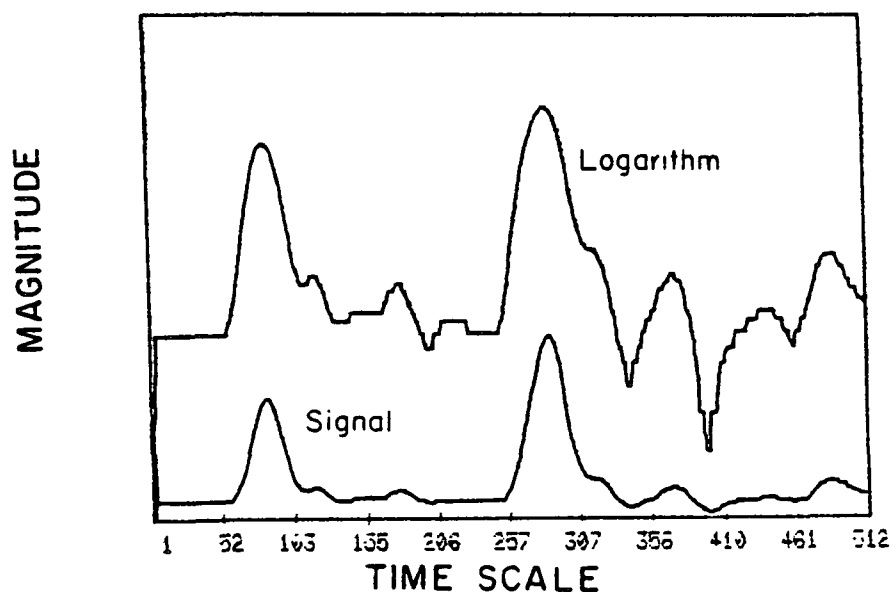
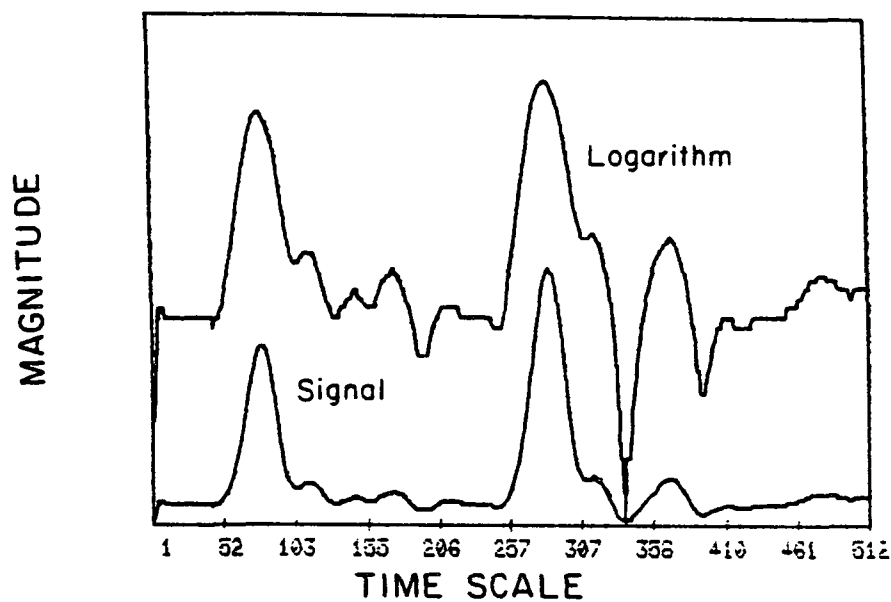
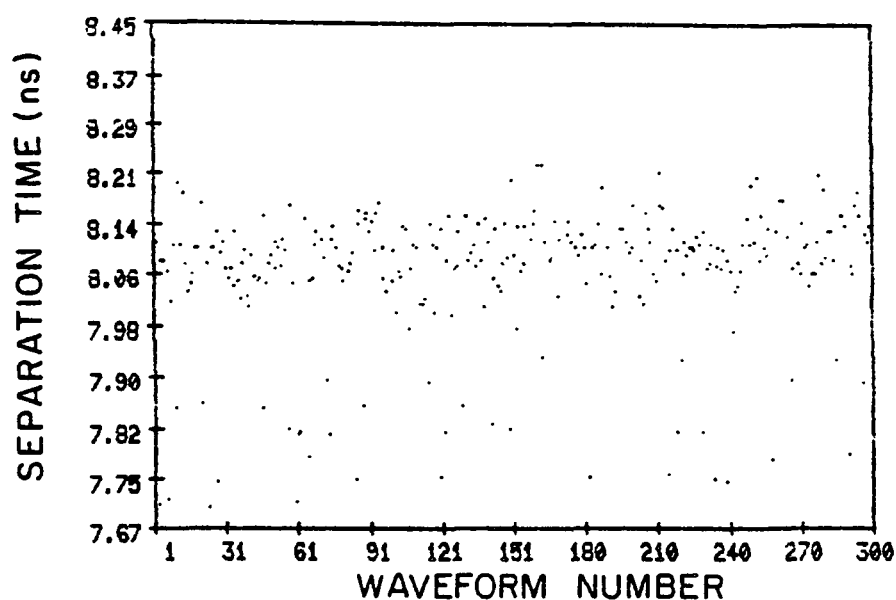


Figure 8.24. Two recorded waveforms and their logarithms. 305 m altitude data.

logarithm. The corresponding results for the cube corner reflector data are shown in Fig. 8.25; the timing error is a large 105 picoseconds. Looking at the timing histogram in Fig. 8.25, we find the poor timing performance is caused by the presence of a few estimates that are significantly below mean. Two recorded waveforms and their logarithms are shown in Fig. 8.26. Again, we find ringing becomes very pronounced after taking the logarithm.

We then correlated the logarithm of the UV pulse with the green pulse; the results are shown in Fig. 8.27 for the 305 m altitude data. The timing error is 68 picoseconds, better than the previous case, but still not as good as the correlation algorithm. The results for the cube corner reflector data are shown in Fig. 8.28; the timing error is reduced to only 43 picoseconds, which is close to the 44 picoseconds of the correlation algorithm. This can be explained by noting the fact that, for a point target, the individual received pulse has the same shape as the mean pulse shape, which is just the impulse response of the system. The difference is that the individual return is corrupted by ringing and noise of the digitizer. Therefore, for a point target, if ringing is not severe, correlating one received pulse with the logarithm of the other pulse is a good approximation of the ML estimator. This explains why it performs quite well. For both data sets, we find the algorithm that takes the logarithm of the UV pulse performs better than those taking the log of the green pulse, probably because the UV pulse has less of a ringing problem than the green pulse.

Finally, we correlated the logarithms of both received pulses. The results for the 305 m altitude data are shown in Fig. 29; the timing error



OF POINTS GREATER THAN 8.448 ns = 0
 # OF POINTS SMALLER THAN 7.667 ns = 0

TOTAL NUMBER OF WAVEFORMS = 300
 AVERAGE SEPARATION TIME = 204.9
 = 8.007

STANDARD DEVIATION = 2.698
 = 105

ELEMENTS
 NANO SEC
 ELEMENTS
 PICO SEC

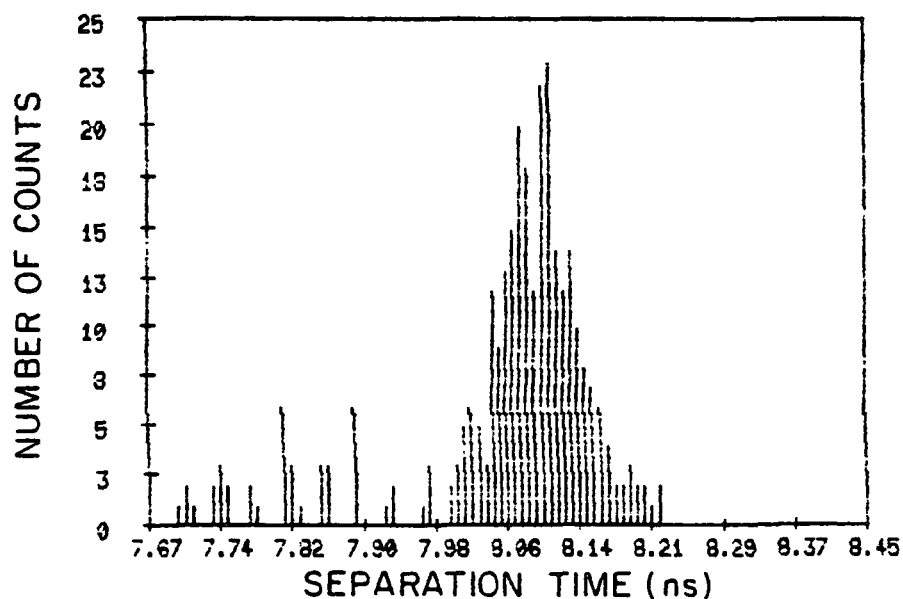


Figure 8.25. Timing history and timing histogram for the data collected from ranging to a cube corner reflector. Results obtained by correlating the UV pulse with the logarithm of the green pulse.

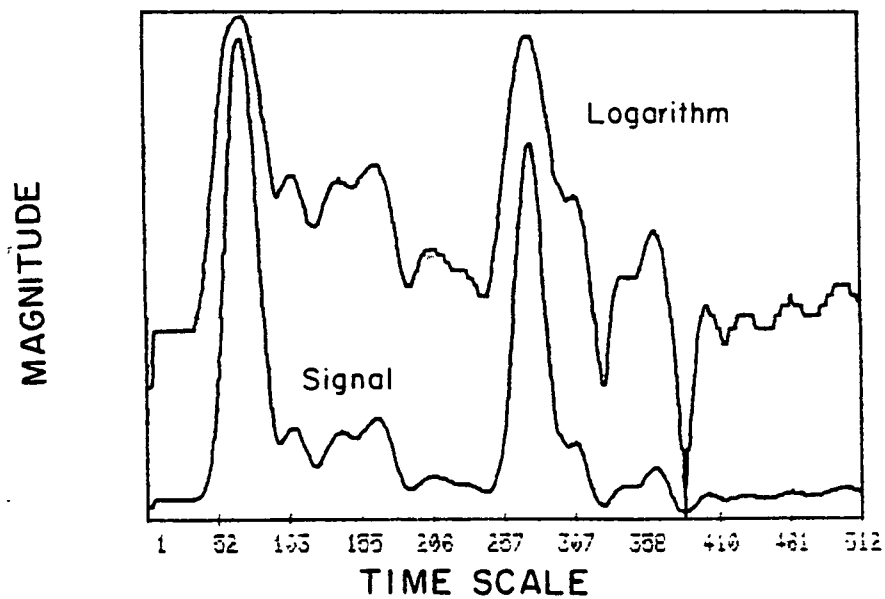
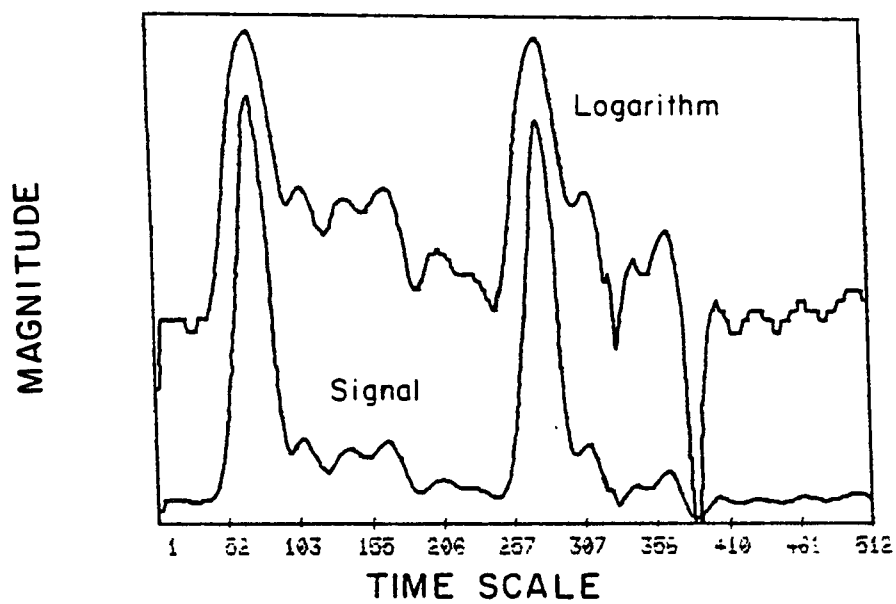
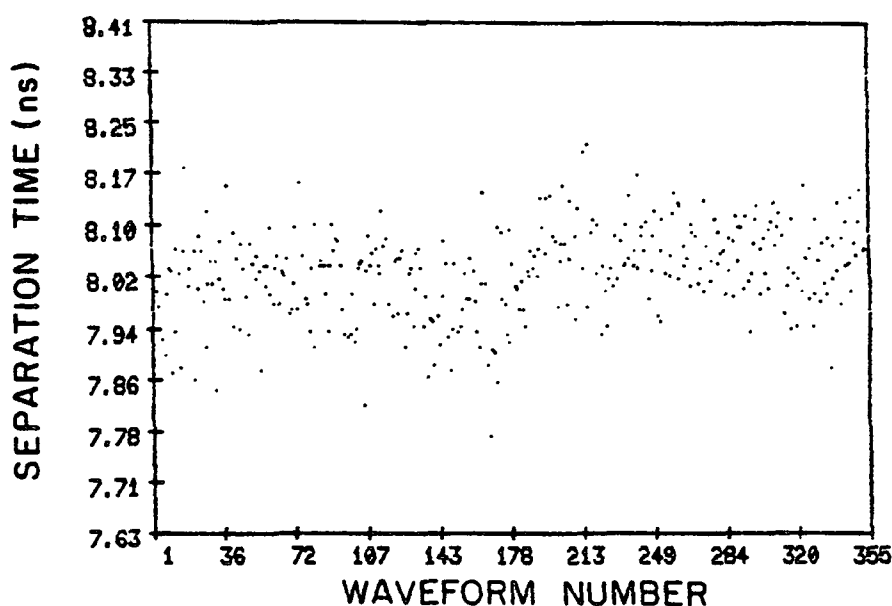


Figure 8.26. Two recorded waveforms and their logarithms. Cube corner reflector data.



OF POINTS GREATER THAN 8.408999 ns = 0
 # OF POINTS SMALLER THAN 7.628000 ns = 0

TOTAL NUMBER OF WAVEFORMS = 355
 AVERAGE SEPARATION TIME = 204.0896 ELEMENTS
 = 7.972250 NANO SEC
 STANDARD DEVIATION = 1.764449 ELEMENTS
 = 68.92381 PICO SEC

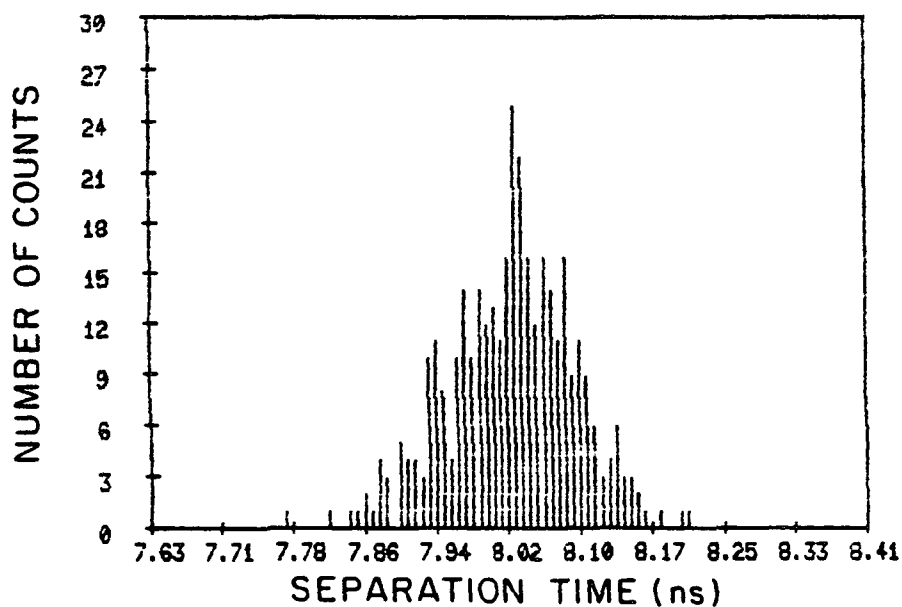
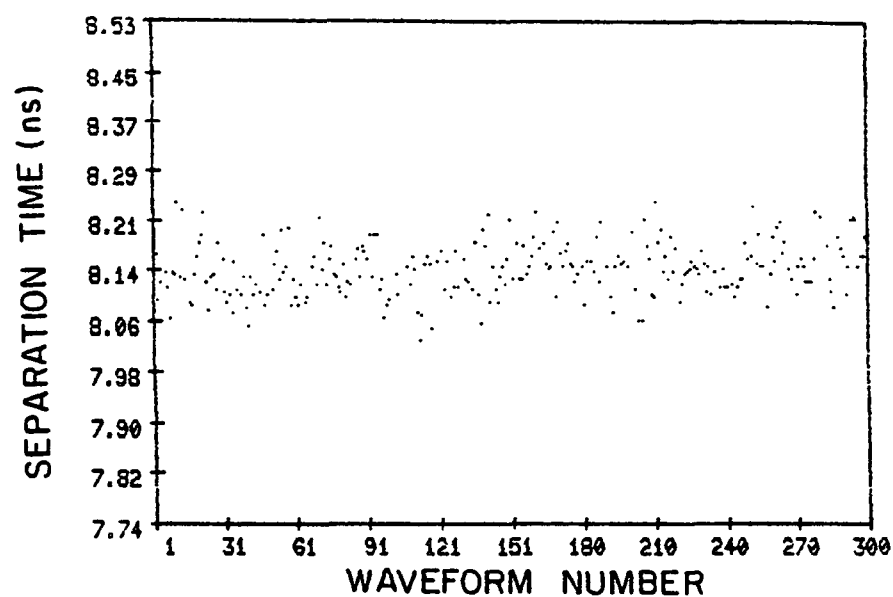


Figure 8.27. Timing history and timing histogram for the data collected at 305 m altitude. Results obtained by correlating the logarithm of the UV pulse with the green pulse.



OF POINTS GREATER THAN 8.526 ns = 0
 # OF POINTS SMALLER THAN 7.745 ns = 0

TOTAL NUMBER OF WAVEFORMS = 300
 AVERAGE SEPARATION TIME = 206.9 ELEMENTS
 = 8.084 NANO SEC
 STANDARD DEVIATION = 1.098 ELEMENTS
 = 42 PICO SEC

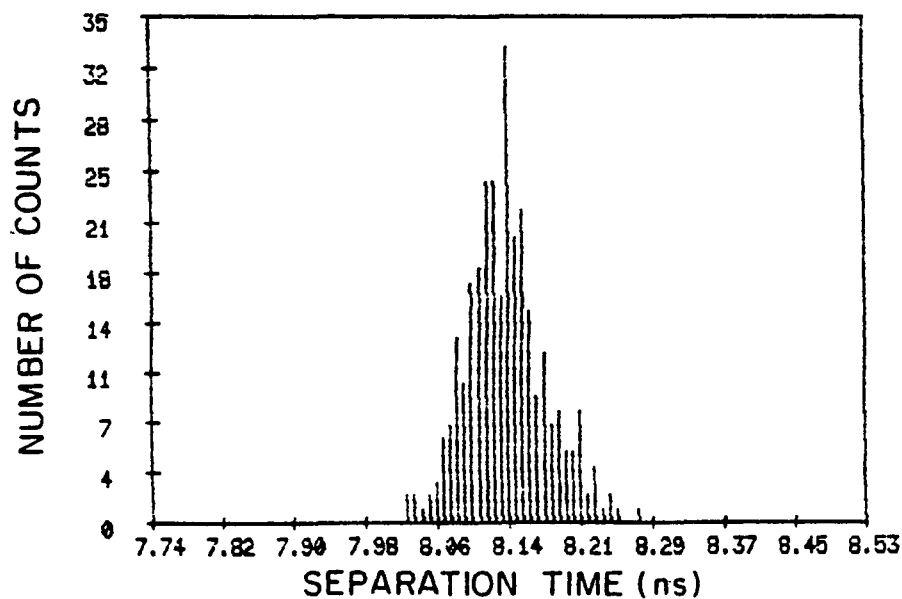
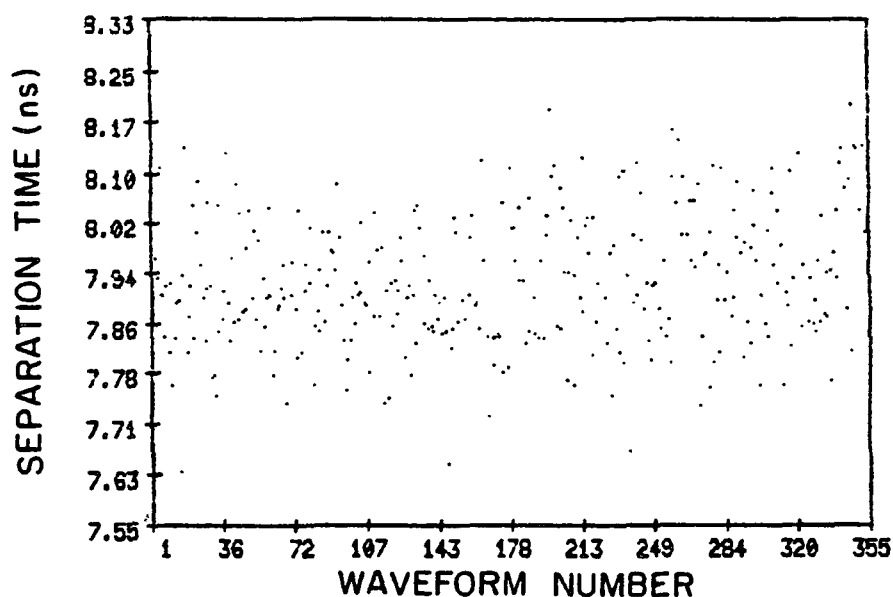


Figure 8.28. Timing history and timing histogram for the data collected from ranging to a cube corner reflector. Results obtained by correlating the logarithm of the UV pulse with the green pulse.



OF POINTS GREATER THAN 8.331 ns = 0
 # OF POINTS SMALLER THAN 7.550 ns = 0

TOTAL NUMBER OF WAVEFORMS = 355
 AVERAGE SEPARATION TIME = 201.6 ELEMENTS
 = 7.878 NANO SEC
 STANDARD DEVIATION = 2.651 ELEMENTS
 = 103 PICO SEC

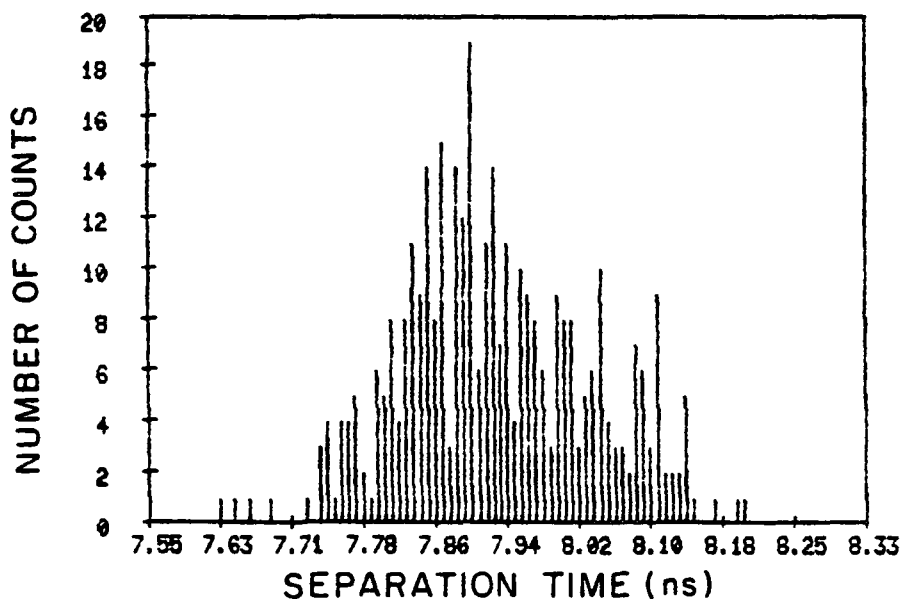


Figure 8.29. Timing history and timing histogram for the data collected at 305 m altitude. Results obtained by correlating the logarithms of both pulses.

is 104 picoseconds. The corresponding results for the cube corner reflector are shown in Fig. 8.30; the timing error is 100 picoseconds. After taking the logarithms, the correlation between the two pulses decreases, because the uncorrelated noises are emphasized by the logarithm. From the above results, we conclude that the logarithm algorithms should be applied only to mean waveforms, or signals with very high signal-to-noise ratios. The results from the different algorithms are summarized in Table 8.2.

8.3. Altitude Dependence of the Received Signal Energy

During the experiment, it was found that the return signal level remained about the same when the altitude of the aircraft was increased from 305 m (1000 ft) to 1219 m (4000 ft). According to the link equation, the signal level should vary inversely with the altitude squared (z^{-2}). Therefore, the signal level at the 305 m altitude should be 16 times the signal level at 1219 m.

This deviation of the signal level in lidar systems from z^{-2} dependence has been studied by Harms [28], [29]. He found there are two mechanisms that cause power loss at small-to-medium target distances. First, in a system with shadowing of the main mirror by a central obstruction, such as a secondary mirror, the overlap of the transmitted beam with the receiver field of view is often incomplete. Second, because the telescope is usually focused at infinity, the light backscattered from a target at small-to-medium distances is not completely focused onto the detector. Both effects cause power losses that can be significant at small target distances.

In Appendix F, the received signal level is derived taking into account both effects. In Fig. 8.31, the relative signal level is plotted versus altitude for four different detector sizes. The detector is assumed

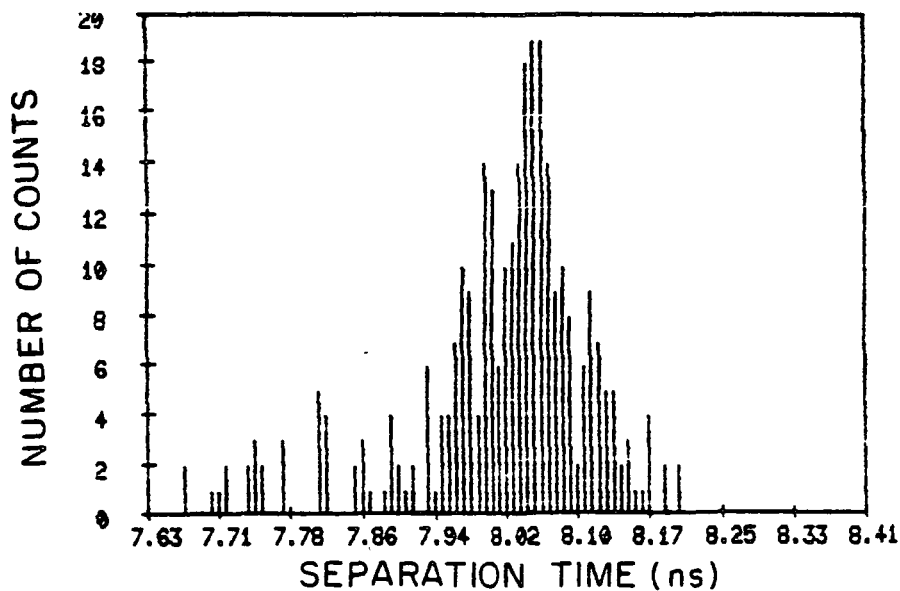
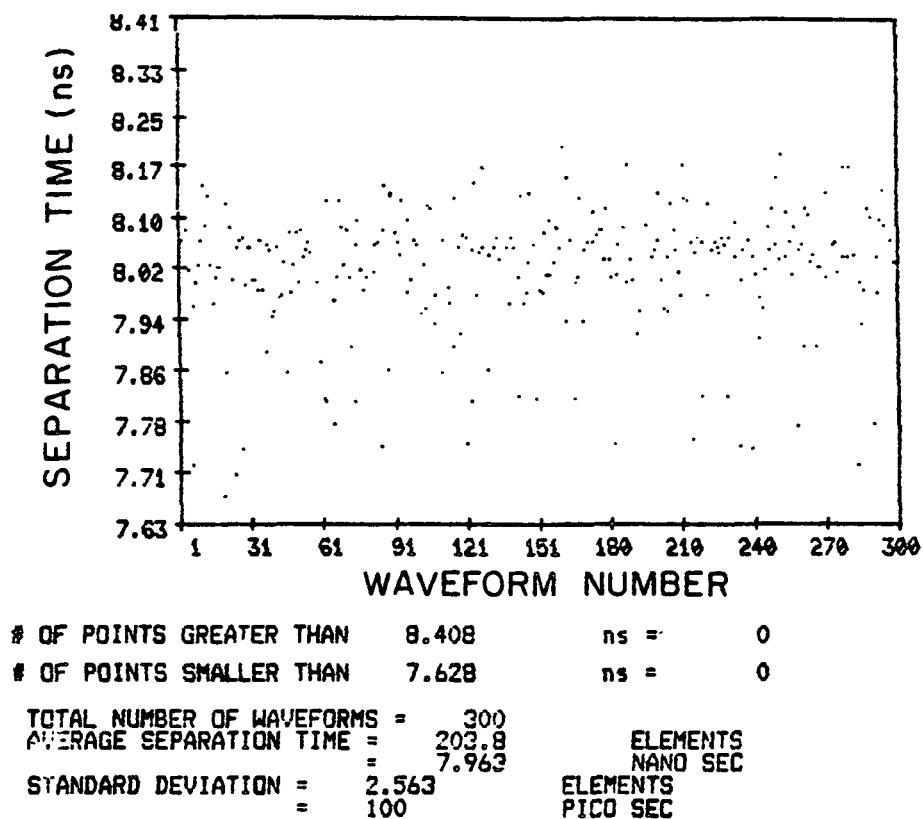


Figure 8.30. Timing history and timing histogram for the data collected from ranging to a cube corner reflector. Results obtained by correlating the logarithms of both pulses.

TABLE 8.2.

COMPARISON OF THE RESULTS FROM DIFFERENT TIMING ALGORITHMS. THE 90 %
CONFIDENCE INTERVALS OF THE TIMING ERRORS OF THE ALGORITHMS ARE SHOWN.

Algorithm	Timing Accuracy	
	305 m Altitude Data	Cube Corner Data
Correlation	63 psec [60,67]	44 psec [41,47]
Peak detection	176 psec [166,188]	49 psec [46,53]
Calculate centroid	118 psec [111,126]	46 psec [44,50]
Correlate the UV pulse with log of the green pulse	84 psec [80,90]	105 psec [99,114]
Correlate log of the UV pulse with the green pulse	69 psec [65,74]	43 psec [40,46]
Correlate log of both pulses	104 psec [98,111]	100 psec [94,108]

RMS Laser Beam Width = 0.117 mrad
 Telescope Focal Length = 14.47m (570 inch)
 Primary Lens Radius = 20.32 cm (8 inch)
 Central Obstruction Radius = 5.08 cm (2 inch)
 Telescope is Focused at Infinity

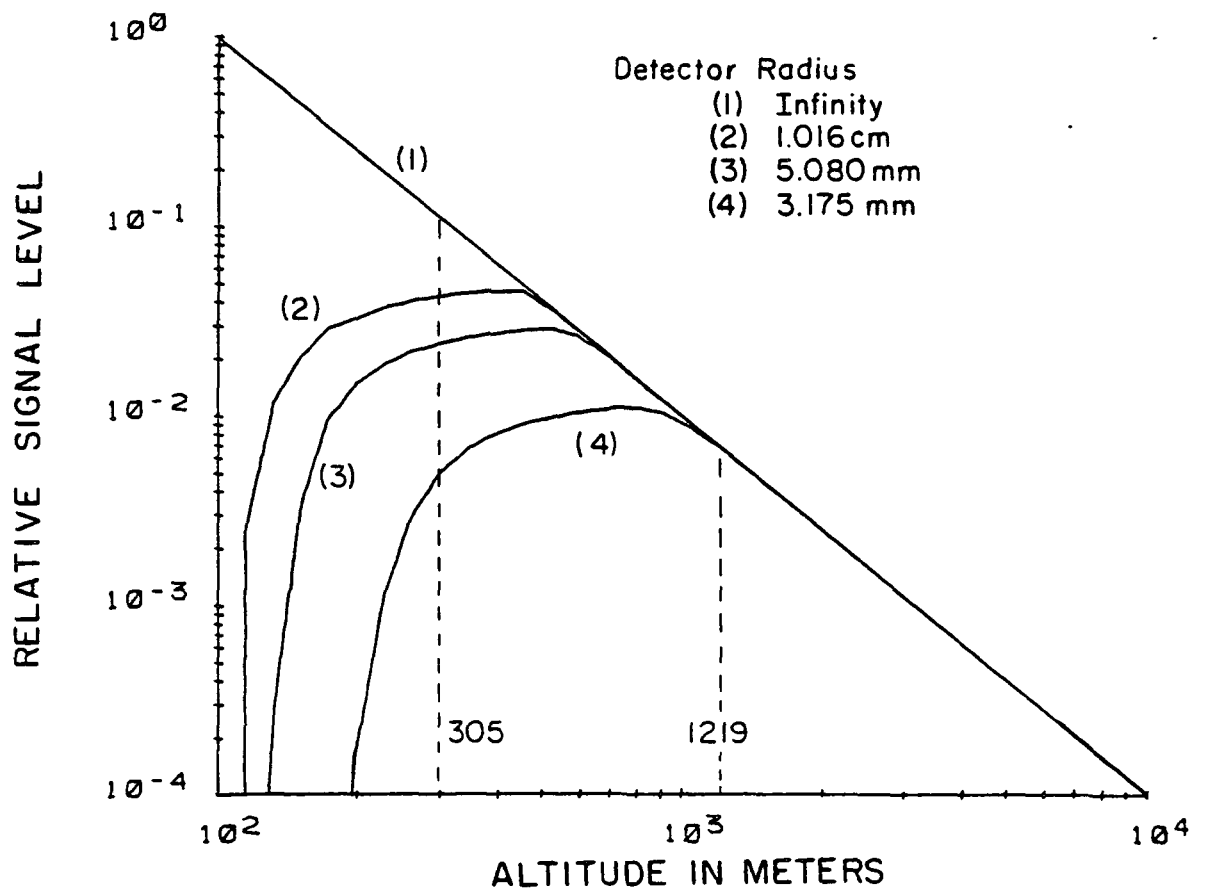


Figure 8.31. Received signal level versus altitude for a telescope with central obstruction.

to be at the focal plane, or the telescope is focused at infinity. From the figure we see that, if the detector is very large, the z^{-2} dependence is maintained, because all the energy collected by the telescope is detected and the assumption behind the link equation is valid. For the aircraft experiment, the detector is situated at the focal point of a telescope with an effective focal length of 14.47 m. The detector of interest has a 3.175 mm (1/8 inch) radius. From Fig. 8.31, we see the theory does predict a nearly equal signal strength at 305 m (1000 ft) and 1219 m (4000 ft) altitudes. When calculating the maximum allowable altitude based on ground-based tests over short paths, the effects must be taken into account.

In Fig. 8.32 we show the results for the case of no central obstruction. In this case, light loss at close distances is due to the fact that the target is not focused onto the detector. The out-of-focus intensity pattern spreads out over a larger area, and only a portion of it is sensed by the detector. In Fig. 8.33, we show the effects of the telescope focusing on the relative signal level. In the figures, when the telescope is focused at 305 m, the detector is the position where the image of a target 305 m away will form. In the figure, we see that the maximum received energy is obtained at a given altitude when the target is focused onto the detector. As a comparison, in Fig. 8.34, we plot the results for a telescope without the central obstruction.

From the above results, we see that the altitude dependence of the received signal energy observed in the experiment can be accounted for by the central obstruction of the telescope and the finite size of the detector. For future experiments, these results can be used to more accurately predict the received signal level.

RMS Laser Beam Width = 0.117 mrad
 Telescope Focal Length = 14.47 m (570 inch)
 Primary Lens Radius = 20.32 cm (8 inch)
 Telescope is Focused at Infinity

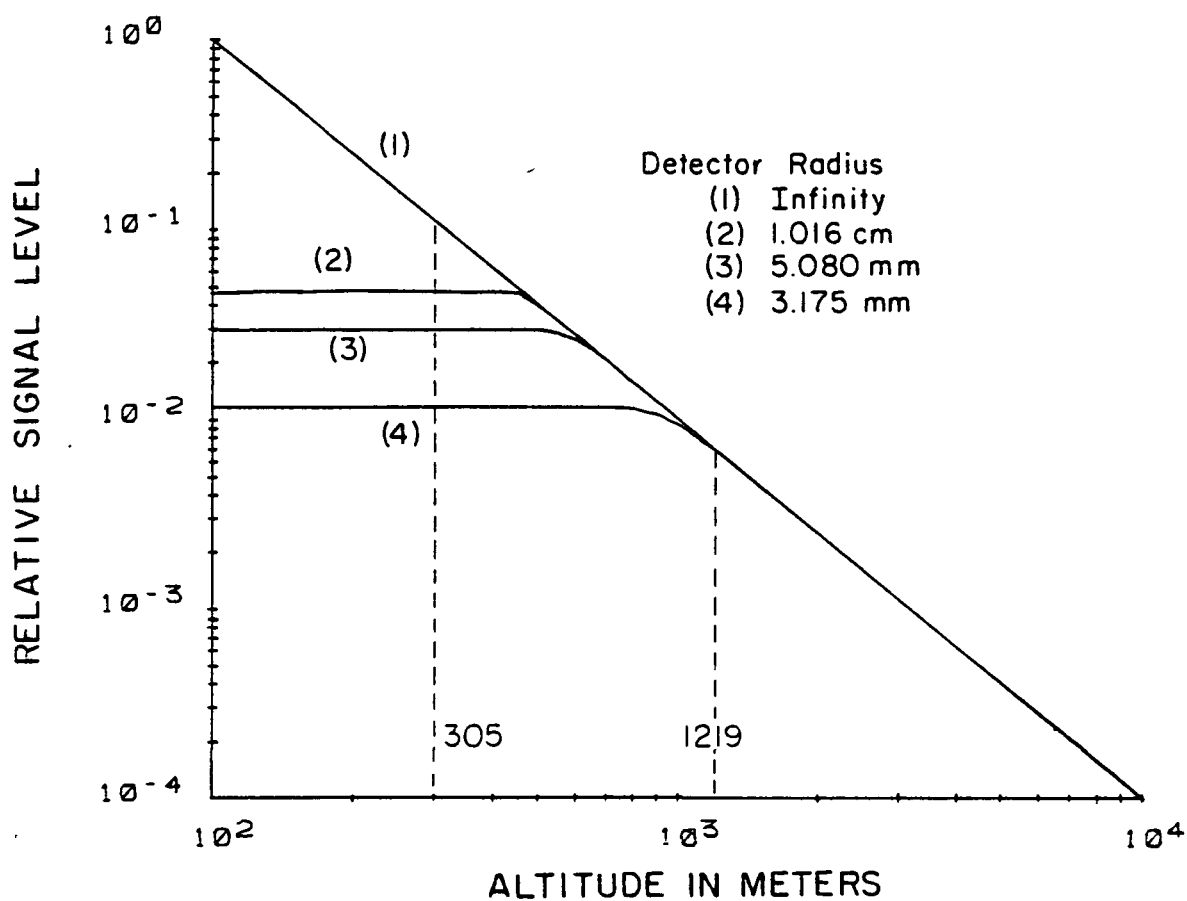


Figure 8.32. Received signal level versus altitude for a telescope without central obstruction.

RMS Laser Beam Radius = 0.117 mrad
 Telescope Focal Length = 14.47m (570 inch)
 Primary Lens Radius = 20.32 cm (8 inch)
 Central Obstruction Radius = 5.08 cm (2 inch)
 Detector Radius = 3.175 mm (0.125 inch)

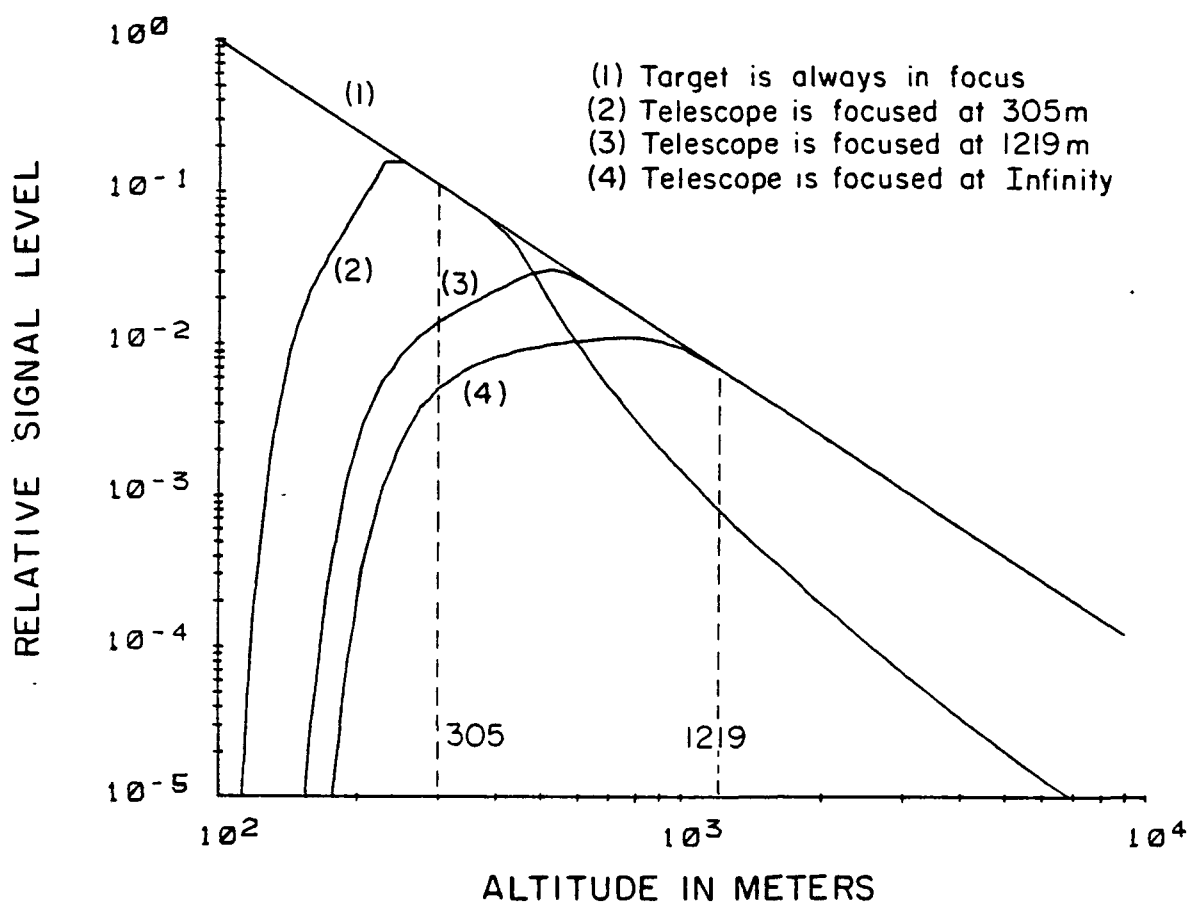


Figure 8.33. Effects of telescope focusing on the received signal level.
 Telescope has central obstruction.

RMS Laser Beam Radius = 0.117 mrad
 Telescope Focal Length = 14.47m (570 inch)
 Primary Lens Radius = 20.32 cm (8 inch)
 Detector Radius = 3.175 mm (0.125 inch)

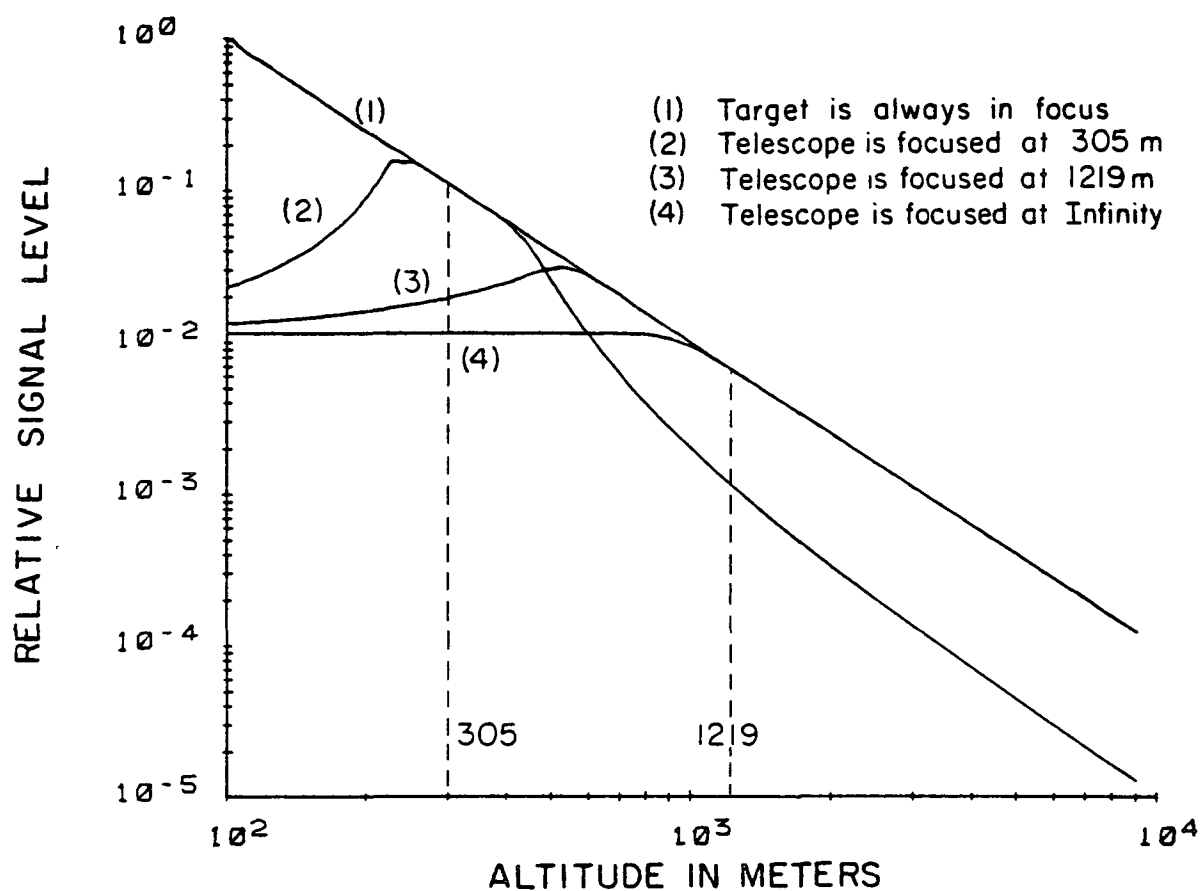


Figure 8.34. Effects of telescope focusing on the received signal level.
 Telescope has no central obstruction.

8.4. Summary

In this chapter, we analyzed the data obtained from the first airborne multiwavelength altimeter experiment. The data were processed with different timing algorithms. Taking into account the confidence intervals of the results obtained, we found that the correlation algorithm probably has the best timing accuracy.

A study was done on the altitude dependence of the received signal level. The results obtained explained the signal level observed during the experiment.

9. CONCLUSIONS

Atmospheric pressure can be measured from a satellite by observing the change with frequency in the optical path length from the satellite to the earth's surface. Because the optical path-length difference is relatively insensitive to surface temperature and water vapor pressure, only rough estimates of these parameters are required. Therefore, the major error source is likely to be the differential path-length measurement. For a nadir viewing altimeter using the fundamental and tripled YAG laser frequencies, the differential propagation delay is approximately 52 cm. For a pressure accuracy of 1 mbar the differential delay must be measured with an accuracy of 0.5 mm or 2 psec. Instrumentation such as the streak tube camera which is capable of meeting these timing requirements is currently available.

To achieve the high timing accuracy needed, the receiver has to cope with not only shot noise but also time-resolved speckle. Time-resolved speckle causes fluctuation of the received energy, distorts the received pulse shape and degrades the timing performance. This study showed that generally the mean square timing error is increased by a factor of $\langle N \rangle / K$, due to the presence of time-resolved speckle. Fortunately, for realistic altimeter systems, K is usually very large ($\sim 50,000$).

Among the timing algorithms considered, we found the correlation algorithm to be most promising. The accuracy of the correlation technique improves as the bandwidth of the received signal increases. The success of the technique depends on the presence of specular reflections or "glints" within the footprint which preserve the high-frequency content of the transmitted pulses. Under this condition, we found that, by using the correlation algorithm to determine the differential propagation delay,

single shot accuracies of ~ 10 picoseconds can be achieved when the expected signal photocount approaches a few thousand.

As for the surface profile, we found that for glints to occur within the footprint, the profile should have a long correlation length, so there will be large areas where the surface elevation remains nearly constant. The condition is satisfied by sinusoidal and trochoidal waves.

Experimental results from the first airborne altimeter experiment conducted at Goddard's Wallop Flight Facility show a high degree of correlation between the received pulse shapes at the visible and UV wavelengths. This is essential to the success of the pressure measurement technique. Although this initial experiment was not designed to provide data of sufficient accuracy to permit actual barometric measurements, they were used to verify the concept of the pressure measurement technique. We processed the data with various timing algorithms. The results show a general agreement with the theoretical performances of these algorithms. The results also indicate the superiority of the correlation technique.

Currently, work is underway at NASA-Goddard to upgrade the altimeter system. An image intensified streak tube camera with timing resolution of ~ 2 picoseconds will be used to replace the waveform digitizer used in the initial experiments. Extensive airborne experiments using the new system are scheduled for the summer of 1984. With the much higher timing accuracy of the new system, the data collected will be used to demonstrate the feasibility of the technique for the pressure measurement over the ocean.

This dissertation work began with the study of the statistics and waveforms of the ocean reflected laser pulses. The results are not only essential to the pressure measurement technique, but also have applications

in remote sensing of sea states. Then, the statistical properties of time-resolved speckle and estimation of arrival times in the presence of both shot noise and speckle were studied. The study was done in the general context of laser altimetry and the results obtained are new in the area. For completeness, an example of partially developed time-resolved speckle was also studied.

The central problem of the dissertation work is the estimation of differential arrival time. Various algorithms were proposed and studied. The relation between timing accuracy and bandwidth of the received signal was established. These results enable the prediction of the accuracy of a realistic pressure measurement system.

Data analysis was also a major part of the dissertation work. The data were processed with different timing algorithms and the results were compared with the theory.

APPENDIX A

EVALUATION OF THE PERFORMANCE OF THE CORRELATION ALGORITHM
FOR A GAUSSIAN MEAN RECEIVED PULSE SHAPE

From Chapter 4, the mean and covariance functions of the received signal can be written explicitly as

$$\overline{S}_1(t) = \langle N_1 \rangle G(\sqrt{\alpha_h^2 + \sigma_f^2 + \alpha_T^2}, t), \quad (A.1)$$

$$\overline{S}_2(t) = \langle N_2 \rangle G(\sqrt{\alpha_h^2 + \sigma_f^2 + \alpha_T^2}, t - \tau_{12}) \quad (A.2)$$

$$\begin{aligned} C_{S_1}(t_1, t_2) = & \langle N_1 \rangle G(\sqrt{2}\alpha_h, t_1 - t_2) G(\sqrt{\alpha_h^2/2 + \sigma_f^2 + \alpha_T^2}, (t_1 + t_2)/2) \\ & + \frac{\langle N_1 \rangle^2}{K_1} G(\sqrt{2}\sqrt{\alpha_h^2 + \sigma_f^2}, t_1 - t_2) G(\sqrt{\alpha_h^2/2 + \sigma_f^2/2 + \alpha_T^2}, (t_1 + t_2)/2) \end{aligned} \quad (A.3)$$

and

$$\begin{aligned} C_{S_2}(t_1, t_2) = & \langle N_1 \rangle G(\sqrt{2}\alpha_h, t_1 - t_2) G(\sqrt{\alpha_h^2/2 + \sigma_f^2 + \alpha_T^2}, (t_1 + t_2)/2 - \tau_{12}) \\ & + \frac{\langle N_2 \rangle^2}{K_2} G(\sqrt{2}\sqrt{\alpha_h^2 + \sigma_f^2}, t_1 - t_2) \\ & \cdot G(\sqrt{\alpha_h^2/2 + \sigma_f^2/2 + \alpha_T^2}, (t_1 + t_2)/2 - \tau_{12}). \end{aligned} \quad (A.4)$$

The denominator on the right-hand side of Eq. (5.15) can be calculated by making use of Eqs. (A.1) - (A.4),

$$\begin{aligned} \left\{ \int_{-\infty}^{\infty} dt \overline{S}_1(t) \frac{\partial^2}{\partial \tau^2} \overline{S}_2(t + \tau) \right\}_{\tau=\tau_{12}}^2 = & \left\{ \int_{-\infty}^{\infty} dt \langle N_1 \rangle \langle N_2 \rangle \left[-\frac{1}{\alpha_h^2 + \sigma_f^2 + \alpha_T^2} \right. \right. \\ & \left. \left. + \frac{\tau^2}{(\alpha_h^2 + \sigma_f^2 + \alpha_T^2)^2} \right] G(\sqrt{\alpha_h^2 + \sigma_f^2 + \alpha_T^2}, t) \right\}^2 \end{aligned}$$

$$= \frac{\langle N_1 \rangle^2 \langle N_2 \rangle^2}{16\pi(\alpha_h^2 + \sigma_f^2 + \alpha_T^2)^3} \quad (A.5)$$

The numerators of the four terms on the right-hand side of Eq. (5.15) are evaluated as follows:

$$\begin{aligned} & \frac{\partial^2}{\partial \tau_1 \partial \tau_2} \int_{-\infty}^{\infty} dt_1 \int_{-\infty}^{\infty} dt_2 \bar{S}_1(t_1) \bar{S}_1(t_2) \bar{S}_2(t_1 + \tau_1) \bar{S}_2(t_2 + \tau_2) \Big|_{\tau_1 = \tau_2 = \tau_{12}} \\ &= \langle N_1 \rangle^2 \langle N_2 \rangle^2 \frac{\partial^2}{\partial \tau_1 \partial \tau_1} \left\{ \int_{-\infty}^{\infty} dt_1 \int_{-\infty}^{\infty} dt_2 G(\sqrt{\alpha_h^2 + \sigma_f^2 + \alpha_T^2}, t_1) \right. \\ & \quad \cdot G(\sqrt{\alpha_h^2 + \sigma_f^2 + \alpha_T^2}, t_2) G(\sqrt{\alpha_h^2 + \sigma_f^2 + \alpha_T^2}, t_1 + \tau_1 - \tau_{12}) \\ & \quad \cdot G(\sqrt{\alpha_h^2 + \sigma_f^2 + \alpha_T^2}, t_2 + \tau_2 - \tau_{12}) \Big\} \Big|_{\tau_1 = \tau_2 = \tau_{12}} \\ &= \langle N_1 \rangle^2 \langle N_2 \rangle^2 \frac{\partial^2}{\partial \tau_1 \partial \tau_2} \left\{ G(\sqrt{2}\sqrt{\alpha_h^2 + \sigma_f^2 + \alpha_T^2}, \tau_1 - \tau_{12}) \right. \\ & \quad \cdot G(\sqrt{2}\sqrt{\alpha_h^2 + \sigma_f^2 + \alpha_T^2}, \tau_2 - \tau_{12}) \Big\} \Big|_{\tau_1 = \tau_2 = \tau_{12}} \\ &= 0 \end{aligned} \quad (A.6)$$

$$\begin{aligned} & \frac{\partial^2}{\partial \tau_1 \partial \tau_2} \left\{ \int_{-\infty}^{\infty} dt_1 \int_{-\infty}^{\infty} dt_2 \bar{S}_1(t_1) \bar{S}_1(t_2) C_{S_2}(t_1 + \tau_1, t_2 + \tau_2) \right\} \Big|_{\tau_1 = \tau_2 = \tau_{12}} \\ &= \langle N_1 \rangle^2 \langle N_2 \rangle \frac{\partial^2}{\partial \tau_1 \partial \tau_2} \left\{ \int_{-\infty}^{\infty} dt_1 \int_{-\infty}^{\infty} dt_2 G(\sqrt{2}\sqrt{\alpha_h^2 + \sigma_f^2 + \alpha_T^2}, t_1 - t_2) \right. \\ & \quad \cdot G\left(\frac{1}{\sqrt{2}}\sqrt{\alpha_h^2 + \sigma_f^2 + \alpha_T^2}, \frac{t_1 + t_2}{2}\right) G(\sqrt{2}\alpha_h, t_1 - t_2 + \tau_1 - \tau_2) \\ & \quad \cdot G(\sqrt{\alpha_h^2/2 + \sigma_f^2 + \alpha_T^2}, (t_1 + t_2)/2 + (\tau_1 + \tau_2)/2 - \tau_{12}) \Big\} \Big|_{\tau_1 = \tau_2 = \tau_{12}} \end{aligned}$$

$$\begin{aligned}
& + \frac{\langle N_1 \rangle^2 \langle N_2 \rangle^2}{K_2} \frac{\partial^2}{\partial \tau_1 \partial \tau_2} \left\{ \int_{-\infty}^{\infty} dt_1 \int_{-\infty}^{\infty} dt_2 G(\sqrt{2} \sqrt{\alpha_h^2 + \sigma_f^2 + \alpha_T^2}, t_1 - t_2) \right. \\
& \cdot G\left(\frac{1}{\sqrt{2}} \sqrt{\alpha_h^2 + \sigma_f^2 + \alpha_T^2}, \frac{t_1 + t_2}{2}\right) G(\sqrt{2} \sqrt{\alpha_h^2 + \sigma_f^2}, t_1 - t_2 + \tau_1 - \tau_2) \\
& \cdot G\left(\sqrt{\alpha_h^2/2 + \sigma_f^2/2 + \alpha_T^2}, (t_1 + t_2)/2 + (\tau_1 + \tau_2)/2 - \tau_{12}\right) \Bigg\} \Big|_{\tau_1 = \tau_2 = \tau_{12}} \\
& = \langle N_1 \rangle \langle N_2 \rangle \frac{\partial^2}{\partial \tau_1 \partial \tau_2} \left\{ G(\sqrt{2} \sqrt{\alpha_h^2 + \sigma_f^2 + \alpha_T^2}, \tau_1 - \tau_2) \right. \\
& \cdot G\left(\sqrt{\alpha_h^2 + \frac{3}{2} \sigma_f^2 + \frac{3}{2} \alpha_T^2}, \frac{\tau_1 + \tau_2}{2} - \tau_{12}\right) \Bigg\} \Big|_{\tau_1 = \tau_2 = \tau_{12}} \\
& + \frac{\langle N_1 \rangle^2 \langle N_2 \rangle^2}{K_2} \frac{\partial^2}{\partial \tau_1 \partial \tau_2} \left\{ G(\sqrt{2} \sqrt{\alpha_h^2 + 2\sigma_f^2 + \alpha_T^2}, \tau_1 - \tau_2) \right. \\
& \cdot G\left(\sqrt{\alpha_h^2 + \sigma_f^2 + \frac{3}{2} \alpha_T^2}, \frac{\tau_1 + \tau_2}{2} - \tau_{12}\right) \Bigg\} \Big|_{\tau_1 = \tau_2 = \tau_{12}} \\
& = \frac{\langle N_1 \rangle^2 \langle N_2 \rangle (\sigma_f^2 + \alpha_T^2)}{2(2\alpha_h^2 + \sigma_f^2 + \alpha_T^2)^{3/2} (\alpha_h^2 + \frac{3}{2} \sigma_f^2 + \frac{3}{2} \alpha_T^2)^{3/2}} \\
& + \frac{\langle N_1 \rangle^2 \langle N_2 \rangle^2 \alpha_T^2}{K_2 4\pi\sqrt{2} (2\alpha_h^2 + 2\sigma_f^2 + \alpha_T^2)^{3/2} (\alpha_h^2 + \sigma_f^2 + \frac{3}{2} \alpha_T^2)^{3/2}} . \tag{A.7}
\end{aligned}$$

Following the same derivations, we have

$$\frac{\partial^2}{\partial \tau_1 \partial \tau_2} \left\{ \int_{-\infty}^{\infty} dt_1 \int_{-\infty}^{\infty} dt_2 \bar{S}_2(t_1 + \tau_1) \bar{S}_2(t_2 + \tau_2) C_{S_1}(t_1, t_2) \right\} \Big|_{\tau_1 = \tau_2 = \tau_{12}}$$

$$\begin{aligned}
&= \frac{\langle N_1 \rangle \langle N_2 \rangle^2 (\sigma_f^2 + \sigma_T^2)}{2(2\sigma_h^2 + \sigma_f^2 + \sigma_T^2)^{3/2} (\sigma_h^2 + \frac{3}{2}\sigma_f^2 + \frac{3}{2}\sigma_T^2)^{3/2}} \\
&+ \frac{\langle N_1 \rangle^2 \langle N_2 \rangle^2 \sigma_T^2}{K_1 4\pi\sqrt{2}(2\sigma_h^2 + 2\sigma_f^2 + \sigma_T^2)^{3/2} (\sigma_h^2 + \sigma_f^2 + \frac{3}{2}\sigma_T^2)^{3/2}} . \quad (A.8)
\end{aligned}$$

The last term is

$$\begin{aligned}
&\frac{\partial^2}{\partial \tau_1 \partial \tau_2} \left\{ \int_{-\infty}^{\infty} dt_1 \int_{-\infty}^{\infty} dt_2 C_{S_1}(t_1, t_2) C_{S_2}(t_1 + \tau_1, t_2 + \tau_2) \right\} \Big|_{\tau_1 = \tau_2 = \tau_{12}} \\
&= \langle N_1 \rangle \langle N_2 \rangle \frac{\partial^2}{\partial \tau_1 \partial \tau_2} \left\{ \int_{-\infty}^{\infty} dt_1 \int_{-\infty}^{\infty} dt_2 G(\sqrt{2}\sigma_h, t_1 - t_2) G(\sqrt{\sigma_h^2/2 + \sigma_f^2 + \sigma_T^2}, (t_1 + t_2)/2) \right. \\
&\quad \cdot G(\sqrt{2}\sigma_h, t_1 - t_2 + \tau_1 - \tau_2) G(\sqrt{\sigma_h^2/2 + \sigma_f^2 + \sigma_T^2}, (t_1 + t_2)/2) \\
&\quad \left. + \frac{(\tau_1 + \tau_2)}{2} - \tau_{12} \right\} \Big|_{\tau_1 = \tau_2 = \tau_{12}} \\
&+ \frac{\langle N_1 \rangle \langle N_2 \rangle^2}{K_2} \frac{\partial^2}{\partial \tau_1 \partial \tau_2} \left\{ \int_{-\infty}^{\infty} dt_1 \int_{-\infty}^{\infty} dt_2 G(\sqrt{2}\sigma_h, t_1 - t_2) \right. \\
&\quad \cdot G(\sqrt{\sigma_h^2/2 + \sigma_f^2 + \sigma_T^2}, (t_1 + t_2)/2) G(\sqrt{2}\sigma_h, t_1 - t_2 + \tau_1 - \tau_2) \\
&\quad \cdot G(\sqrt{\sigma_h^2/2 + \sigma_f^2/2 + \sigma_T^2}, (t_1 + t_2)/2 - \tau_{12} + \frac{(\tau_1 + \tau_2)}{2}) \Big\} \Big|_{\tau_1 = \tau_2 = \tau_{12}} \\
&+ \frac{\langle N_1 \rangle^2 \langle N_2 \rangle}{K_1} \frac{\partial^2}{\partial \tau_1 \partial \tau_2} \left\{ \int_{-\infty}^{\infty} dt_1 \int_{-\infty}^{\infty} dt_2 G(\sqrt{2}\sigma_h, t_1 - t_2) \right. \\
&\quad \cdot G(\sqrt{\sigma_h^2/2 + \sigma_f^2/2 + \sigma_T^2}, (t_1 + t_2)/2) G(\sqrt{2}\sigma_h, t_1 - t_2 + \tau_1 - \tau_2)
\end{aligned}$$

$$\begin{aligned}
& \cdot G(\sqrt{\alpha_h^2/2 + \sigma_f^2 + \alpha_T^2}, (t_1 + t_2)/2 + (\tau_1 + \tau_2)/2 - \tau_{12}) \Big|_{\tau_1=\tau_2=\tau_{12}} \\
& + \frac{\langle N_1 \rangle^2 \langle N_2 \rangle^2}{K_1 K_2} \frac{\partial^2}{\partial \tau_1 \partial \tau_2} \left\{ \int_{-\infty}^{\infty} dt_1 \int_{-\infty}^{\infty} dt_2 G(\sqrt{2\alpha_h^2 + \sigma_f^2}, t_1 - t_2) \right. \\
& \cdot G(\sqrt{\alpha_h^2/2 + \sigma_f^2/2 + \alpha_T^2}, (t_1 + t_2)/2) G(\sqrt{2\alpha_h^2 + \sigma_f^2}, t_1 - t_2 + \tau_1 - \tau_2) \\
& \cdot G(\sqrt{\alpha_h^2/2 + \sigma_f^2/2 + \alpha_T^2}, (t_1 + t_2)/2 + (\tau_1 + \tau_2)/2 - \tau_{12}) \Big|_{\tau_1=\tau_2=\tau_{12}} \\
& = \langle N_1 \rangle \langle N_2 \rangle \frac{\partial^2}{\partial \tau_1 \partial \tau_2} \left\{ G(2\alpha_h, \tau_1 - \tau_2) G(\sqrt{\alpha_h^2 + 2\sigma_f^2 + 2\alpha_T^2}, (\tau_1 + \tau_2)/2 \right. \\
& \left. - \tau_{12}) \Big|_{\tau_1=\tau_2=\tau_1} + \frac{\langle N_1 \rangle \langle N_2 \rangle^2}{K_2} \frac{\partial^2}{\partial \tau_1 \partial \tau_2} \left\{ G(\sqrt{2\alpha_h^2 + \sigma_f^2}, \tau_1 - \tau_2) \right. \right. \\
& \left. \cdot G(\sqrt{\alpha_h^2 + \frac{3}{2}\sigma_f^2 + 2\alpha_T^2}, (\tau_1 + \tau_2)/2 - \tau_{12}) \Big|_{\tau_1=\tau_2=\tau_{12}} \right. \\
& \left. + \frac{\langle N_1 \rangle^2 \langle N_2 \rangle}{K_1} \frac{\partial^2}{\partial \tau_1 \partial \tau_2} \left\{ G(\sqrt{2\alpha_h^2 + \sigma_f^2}, \tau_1 - \tau_2) \right. \right. \\
& \left. \cdot G(\sqrt{\alpha_h^2 + \frac{3}{2}\sigma_f^2 + 2\alpha_T^2}, (\tau_1 + \tau_2)/2 - \tau_{12}) \Big|_{\tau_1=\tau_2=\tau_{12}} \right. \\
& \left. + \frac{\langle N_1 \rangle^2 \langle N_2 \rangle^2}{K_1 K_2} \frac{\partial^2}{\partial \tau_1 \partial \tau_2} \left\{ G(2\sqrt{\alpha_h^2 + \sigma_f^2}, \tau_1 - \tau_2) \right. \right. \\
& \left. \cdot G(\sqrt{\alpha_h^2 + \sigma_f^2 + 2\alpha_T^2}, (\tau_1 + \tau_2)/2 - \tau_{12}) \Big|_{\tau_1=\tau_2=\tau_{12}} \right. \\
& = \frac{\langle N_1 \rangle \langle N_2 \rangle (\sigma_f^2 + \alpha_T^2)}{8\pi \alpha_h^3 (\alpha_h^2 + 2\sigma_f^2 + 2\alpha_T^2)^{3/2}} + \left(\frac{\langle N_1 \rangle^2 \langle N_2 \rangle}{K_1} + \frac{\langle N_2 \rangle^2 \langle N_1 \rangle}{K_2} \right) \\
& \cdot \frac{\sigma_f^2 + 2\alpha_T^2}{4\pi \sqrt{2} (2\alpha_h^2 + \sigma_f^2)^{3/2} (\alpha_h^2 + \frac{3}{2}\sigma_f^2 + 2\alpha_T^2)^{3/2}}
\end{aligned}$$

$$+ \frac{\langle N_1 \rangle^2 \langle N_2 \rangle^2 \alpha_T^2}{K_1 K_2 8\pi (\alpha_h^2 + \sigma_f^2)^{3/2} (\alpha_h^2 + \sigma_f^2 + 2\alpha_T^2)^{3/2}} \quad (\text{A.9})$$

Finally, by using Eqs. (A.5 - A.9), we obtain

$$\begin{aligned} \text{MSE} \approx & \left(\frac{1}{\langle N_1 \rangle} + \frac{1}{\langle N_2 \rangle} \right) \frac{2\sqrt{2} (\sigma_f^2 + \alpha_T^2) (\sigma_f^2 + \alpha_h^2 + \alpha_T^2)^3}{(2\alpha_h^2 + \sigma_f^2 + \alpha_T^2)^{3/2} (\alpha_h^2 + \frac{3}{2}\sigma_f^2 + \frac{3}{2}\alpha_T^2)^{3/2}} \\ & + \left(\frac{1}{K_1} + \frac{1}{K_2} \right) \frac{2\sqrt{2} \alpha_T^2 (\alpha_h^2 + \sigma_f^2 + \alpha_T^2)^3}{(2\alpha_h^2 + 2\sigma_f^2 + \alpha_T^2)^{3/2} (\alpha_h^2 + \sigma_f^2 + \frac{3}{2}\alpha_T^2)^{3/2}} \\ & + \left(\frac{1}{\langle N_1 \rangle K_2} + \frac{1}{\langle N_2 \rangle K_1} \right) \frac{2\sqrt{2} (\sigma_f^2 + 2\alpha_T^2) (\alpha_h^2 + \sigma_f^2 + \alpha_T^2)^3}{(2\alpha_h^2 + \sigma_f^2)^{3/2} (\alpha_h^2 + \frac{3}{2}\sigma_f^2 + 2\alpha_T^2)^{3/2}} \\ & + \frac{1}{\langle N_1 \rangle \langle N_2 \rangle} \frac{2(\sigma_f^2 + \alpha_T^2) (\sigma_f^2 + \alpha_h^2 + \alpha_T^2)^3}{\alpha_h^3 (\alpha_h^2 + 2\sigma_f^2 + 2\alpha_T^2)^{3/2}} \\ & + \frac{1}{K_1 K_2} \frac{2\alpha_T^2 (\alpha_h^2 + \sigma_f^2 + \alpha_T^2)^3}{(\alpha_h^2 + \sigma_f^2)^{3/2} (\alpha_h^2 + \sigma_f^2 + 2\alpha_T^2)^{3/2}} \end{aligned}$$

The results are used in Chapter 5.

APPENDIX B

DERIVATIONS LEADING TO THE FREQUENCY DOMAIN REPRESENTATION OF TIMING ERROR

From Chapter 4, for a general mean waveform $F(t)$, we have

$$\bar{S}_1(t) = \langle N_1 \rangle F(t) \quad , \quad (B.1)$$

$$\bar{S}_2(t) = \langle N_2 \rangle F(t - \tau_{12}) \quad , \quad (B.2)$$

$$\begin{aligned} C_{S_1}(t_1, t_2) = \langle N_1 \rangle G(\sqrt{2} \sigma_h, t_1 - t_2) F\left(\frac{t_1 + t_2}{2}\right) \\ + \frac{\langle N_1 \rangle^2}{K_1} G(\sqrt{2} \sqrt{\sigma_h^2 + \sigma_f^2}, t_1 - t_2) F\left(\frac{t_1 + t_2}{2}\right) \end{aligned} \quad (B.3)$$

and

$$\begin{aligned} C_{S_2}(t_1, t_2) = \langle N_2 \rangle G(\sqrt{2} \sigma_h, t_1 - t_2) F\left(\frac{t_1 + t_2}{2} - \tau_{12}\right) \\ + \frac{\langle N_2 \rangle^2}{K_2} G(\sqrt{2} \sqrt{\sigma_h^2 + \sigma_f^2}, t_1 - t_2) F\left(\frac{t_1 + t_2}{2} - \tau_{12}\right) \end{aligned} \quad (B.4)$$

where we have assumed the width of $F(t)$ to be much larger than σ_h and σ_f .

The mean square error is written here for convenience:

$$\begin{aligned} \text{MSE} = \frac{\frac{\partial^2}{\partial \tau_1 \partial \tau_2} \left\{ \int_{-\infty}^{\infty} dt_1 \int_{-\infty}^{\infty} dt_2 (\bar{S}_1(t_1) \bar{S}_1(t_2) + C_{S_1}(t_1, t_2)) \right.}{\frac{\langle N_1 \rangle^2 \langle N_2 \rangle^2}{4\pi^2} \left\{ \int_{-\infty}^{\infty} d\omega \omega^2 |\phi_S(\omega)|^2 \right\}^2} \\ \left. (\bar{S}_2(t_1 + \tau_1) \bar{S}_2(t_2 + \tau_2) C_{S_2}(t_1 + \tau_1, t_2 + \tau_2)) \right\} \Big|_{\tau_1 = \tau_2 = \tau_{12}}}{\frac{\langle N_1 \rangle^2 \langle N_2 \rangle^2}{4\pi^2} \left\{ \int_{-\infty}^{\infty} d\omega \omega^2 |\phi_S(\omega)|^2 \right\}^2} \end{aligned} \quad (B.5)$$

The numerator on the right-hand side is calculated as follows:

$$\begin{aligned}
 & \frac{\partial^2}{\partial \tau_1 \partial \tau_2} \int_{-\infty}^{\infty} dt_1 \int_{-\infty}^{\infty} dt_2 c_{S_1}(t_1, t_2) \bar{S}_2(t_1 + \tau_1) \bar{S}_2(t_2 + \tau_2) \Big|_{\tau_1 = \tau_2 = \tau_{12}} \\
 &= \langle N_1 \rangle \langle N_2 \rangle^2 \int_{-\infty}^{\infty} dt_1 \int_{-\infty}^{\infty} dt_2 G(\sqrt{2} \sigma_h, t_1 - t_2) F\left(\frac{t_1 + t_2}{2}\right) \dot{F}(t_1) \dot{F}(t_2) \\
 &+ \frac{\langle N_1 \rangle^2 \langle N_2 \rangle^2}{K_1} \int_{-\infty}^{\infty} dt_1 \int_{-\infty}^{\infty} dt_2 G(\sqrt{2} \sqrt{\sigma_h^2 + \sigma_f^2}, t_1 - t_2) F\left(\frac{t_1 + t_2}{2}\right) \dot{F}(t_1) \dot{F}(t_2) . \quad (B.6)
 \end{aligned}$$

By assuming σ_h and σ_f to be small, we have

$$\begin{aligned}
 & \frac{\partial^2}{\partial \tau_1 \partial \tau_2} \int_{-\infty}^{\infty} dt_1 \int_{-\infty}^{\infty} dt_2 c_{S_1}(t_1, t_2) \bar{S}_2(t_1 + \tau_1) \bar{S}_2(t_2 + \tau_2) \Big|_{\tau_1 = \tau_2 = \tau_{12}} \\
 &= \left(\langle N_1 \rangle \langle N_2 \rangle^2 + \frac{\langle N_1 \rangle^2 \langle N_2 \rangle^2}{K_1} \right) \int_{-\infty}^{\infty} dt_1 \dot{F}^2(t_1) F(t_1) \\
 &= \frac{1}{2} \left(\langle N_1 \rangle \langle N_2 \rangle^2 + \frac{\langle N_1 \rangle^2 \langle N_2 \rangle^2}{K_1} \right) \left\{ \dot{F}(t) F^2(t) \Big|_{-\infty}^{\infty} - \int_{-\infty}^{\infty} dt \ddot{F}(t) F^2(t) \right\} \\
 &= -\frac{1}{4\pi} \left\{ \langle N_1 \rangle \langle N_2 \rangle^2 + \frac{\langle N_1 \rangle^2 \langle N_2 \rangle^2}{K_1} \right\} \int_{-\infty}^{\infty} d\omega \mathcal{Q}\{\ddot{F}(t)\}^* \mathcal{Q}\{F^2(t)\} \\
 &= \frac{1}{4\pi} \left\{ \langle N_1 \rangle \langle N_2 \rangle^2 + \frac{\langle N_1 \rangle^2 \langle N_2 \rangle^2}{K_1} \right\} \int_{-\infty}^{\infty} d\omega \omega^2 \phi_s^*(\omega) \frac{1}{2\pi} \{\phi_s(\omega) * \phi_s(\omega)\} . \quad (B.7)
 \end{aligned}$$

By the same reasoning, we have

$$\begin{aligned}
 & \frac{\partial^2}{\partial \tau_1 \partial \tau_2} \int_{-\infty}^{\infty} dt_1 \int_{-\infty}^{\infty} dt_2 \bar{S}_1(t_1) \bar{S}_1(t_2) c_{S_2}(t_1 + \tau_1, t_2 + \tau_2) \Big|_{\tau_1 = \tau_2 = \tau_{12}} \\
 &= \frac{1}{4\pi} \left\{ \langle N_1 \rangle^2 \langle N_2 \rangle + \frac{\langle N_1 \rangle^2 \langle N_2 \rangle^2}{K_2} \right\} \int_{-\infty}^{\infty} d\omega \omega^2 \phi_s^*(\omega) \frac{1}{2\pi} \{\phi_s(\omega) * \phi_s(\omega)\} . \quad (B.8)
 \end{aligned}$$

The other non-zero term is

$$\begin{aligned}
& \frac{\partial^2}{\partial \tau_1 \partial \tau_2} \int_{-\infty}^{\infty} dt_1 \int_{-\infty}^{\infty} dt_2 C_{S_1}(t_1, t_2) C_{S_2}(t_1 + \tau_1, t_2 + \tau_2) \Big|_{\tau_1 = \tau_2 = \tau_{12}} \\
&= \frac{\partial^2}{\partial \tau_1 \partial \tau_2} \left\{ \langle N_1 \rangle \langle N_2 \rangle G(2\sigma_h, \tau_1 - \tau_2) \int_{-\infty}^{\infty} dT F(T) F\left(T + \frac{\tau_1 + \tau_2}{2} - \tau_{12}\right) \right. \\
&\quad + \left(\frac{\langle N_1 \rangle \langle N_2 \rangle^2}{K_2} + \frac{\langle N_1 \rangle^2 \langle N_2 \rangle}{K_1} \right) G(\sqrt{2}\sqrt{\sigma_h^2 + \sigma_f^2}, \tau_1 - \tau_2) \\
&\quad \cdot \int_{-\infty}^{\infty} dT F(T) F\left(T + \frac{\tau_1 + \tau_2}{2} - \tau_{12}\right) \\
&\quad \left. + \frac{\langle N_1 \rangle^2 \langle N_2 \rangle^2}{K_1 K_2} G(2\sqrt{\sigma_h^2 + \sigma_f^2}, \tau_1 - \tau_2) \int_{-\infty}^{\infty} dT F(T) F\left(T + \frac{\tau_1 + \tau_2}{2} - \tau_{12}\right) \right\} \Big|_{\tau_1 = \tau_2 = \tau_{12}} \\
&= \langle N_1 \rangle \langle N_2 \rangle \left\{ -\ddot{G}(2\sigma_h, 0) \int_{-\infty}^{\infty} dT F^2(T) + \frac{1}{4} G(2\sigma_h, 0) \int_{-\infty}^{\infty} dT F(T) \ddot{F}(T) \right\} \\
&\quad + \left(\frac{\langle N_1 \rangle^2 \langle N_2 \rangle}{K_1} + \frac{\langle N_1 \rangle \langle N_2 \rangle^2}{K_2} \right) \left\{ -\ddot{G}(\sqrt{2}\sqrt{2\sigma_h^2 + \sigma_f^2}, 0) \int_{-\infty}^{\infty} dT F^2(T) \right. \\
&\quad \left. + \frac{1}{4} G(\sqrt{2}\sqrt{2\sigma_h^2 + \sigma_f^2}, 0) \int_{-\infty}^{\infty} dT F(T) \ddot{F}(T) \right\} \\
&\quad + \frac{\langle N_1 \rangle^2 \langle N_2 \rangle^2}{K_1 K_2} \left\{ -\ddot{G}(2\sqrt{\sigma_h^2 + \sigma_f^2}, 0) \int_{-\infty}^{\infty} dT F^2(T) \right. \\
&\quad \left. + \frac{1}{4} G(2\sqrt{\sigma_h^2 + \sigma_f^2}, 0) \int_{-\infty}^{\infty} dT F(T) \ddot{F}(T) \right\} \\
&= \frac{\langle N_1 \rangle \langle N_2 \rangle}{16\pi \sqrt{2\pi} \sigma_h} \left\{ \frac{1}{\sigma_h^2} \int_{-\infty}^{\infty} d\omega |\phi_s(\omega)|^2 - \int_{-\infty}^{\infty} d\omega \omega^2 |\phi_s(\omega)|^2 \right\} \\
&\quad + \frac{1}{8\pi \sqrt{\pi} \sqrt{2\sigma_h^2 + \sigma_f^2}} \left(\frac{\langle N_1 \rangle^2 \langle N_2 \rangle}{K_1} + \frac{\langle N_1 \rangle \langle N_2 \rangle^2}{K_2} \right) \\
&\quad \cdot \left\{ \frac{1}{2\sigma_h^2 + \sigma_f^2} \int_{-\infty}^{\infty} d\omega |\phi_s(\omega)|^2 - \frac{1}{2} \int_{-\infty}^{\infty} d\omega \omega^2 |\phi_s(\omega)|^2 \right\}
\end{aligned}$$

$$+ \frac{\langle N_1 \rangle^2 \langle N_2 \rangle^2}{16\pi\sqrt{2\pi}\sqrt{\sigma_h^2 + \sigma_f^2} K_1 K_2} \left(\frac{1}{\sigma_h^2 + \sigma_f^2} \int_{-\infty}^{\infty} d\omega |\phi_s(\omega)|^2 - \int_{-\infty}^{\infty} d\omega \omega^2 |\phi_s(\omega)|^2 \right).$$

(B.9)

By substituting Eqs. (B.6-B.9) into Eq. (B.5), we obtain Eq. (5.41).

APPENDIX C

EXPANSION OF EQUATION (5.46)

Following the same derivations shown in Appendix B, and making changes for the difference in mean waveforms, we have

$$\begin{aligned}
 & \int_{-\infty}^{\infty} d\omega_1 \int_{-\infty}^{\infty} d\omega_2 \omega_1 \omega_2 \hat{R}_{S_1}(\omega_1, \omega_2) \hat{R}_{S_2}(\omega_1, \omega_2) e^{i\omega\tau_1} e^{i\omega\tau_2} \\
 &= -\frac{\langle N_1 \rangle^2 \langle N_2 \rangle^2}{4\pi^2} \left\{ \int_{-\infty}^{\infty} d\omega \omega \phi_{S_1}(\omega) \phi_{S_2}^*(\omega) \right\}^2 \\
 &+ \frac{1}{2\pi} \left\{ \langle N_1 \rangle^2 \langle N_2 \rangle + \frac{\langle N_1 \rangle^2 \langle N_2 \rangle^2}{K_2} \right\} \int_{-\infty}^{\infty} d\omega \frac{1}{2\pi} \left\{ (i\omega \phi_{S_1}(\omega)) * (i\omega \phi_{S_1}(\omega)) \right\} \phi_{S_2}^*(\omega) \\
 &+ \frac{1}{2\pi} \left\{ \langle N_2 \rangle^2 \langle N_1 \rangle + \frac{\langle N_1 \rangle^2 \langle N_2 \rangle^2}{K_1} \right\} \int_{-\infty}^{\infty} d\omega \frac{1}{2\pi} \left\{ [i\omega \phi_{S_2}(\omega)] * [i\omega \phi_{S_2}(\omega)] \right\} \phi_{S_1}^*(\omega) \\
 &+ \frac{\langle N_1 \rangle \langle N_2 \rangle}{16\pi\sqrt{2\pi} \alpha_h} \left\{ \frac{1}{\alpha_h^2} \int_{-\infty}^{\infty} d\omega \phi_{S_2}^*(\omega) \phi_{S_1}(\omega) - \int_{-\infty}^{\infty} d\omega \omega^2 \phi_{S_2}^*(\omega) \phi_{S_1}(\omega) \right\} \\
 &+ \frac{1}{8\pi\sqrt{\pi} \sqrt{2\alpha_h^2 + \sigma_f^2}} \left(\frac{\langle N_1 \rangle \langle N_2 \rangle^2}{K_2} + \frac{\langle N_1 \rangle^2 \langle N_1 \rangle}{K_1} \right) \left\{ \frac{1}{2\alpha_h^2 + \sigma_f^2} \int_{-\infty}^{\infty} d\omega \phi_{S_2}^*(\omega) \phi_{S_1}(\omega) \right. \\
 &\quad \left. - \frac{1}{2} \int_{-\infty}^{\infty} d\omega \omega^2 \phi_{S_2}^*(\omega) \phi_{S_1}(\omega) \right\} \\
 &+ \frac{\langle N_1 \rangle^2 \langle N_2 \rangle^2}{16\pi\sqrt{2\pi} \sqrt{\alpha_h^2 + \sigma_f^2} K_1 K_2} \left\{ \frac{1}{\sqrt{\alpha_h^2 + \sigma_f^2}} \right. \\
 &\quad \left. \cdot \int_{-\infty}^{\infty} d\omega \phi_{S_2}^*(\omega) \phi_{S_1}(\omega) - \int_{-\infty}^{\infty} d\omega \omega^2 \phi_{S_2}^*(\omega) \phi_{S_1}(\omega) \right\}. \tag{C.1}
 \end{aligned}$$

This result is used in Chapter 5.

APPENDIX D

DERIVATIONS LEADING TO EQUATION (5.53)

$$\begin{aligned}
& \frac{\partial^2}{\partial \tau_1 \partial \tau_2} \int_{-\infty}^{\infty} dt_1 \int_{-\infty}^{\infty} dt_2 \bar{S}_1(t_1) \bar{S}_1(t_2) R_n(t_1 + \tau_1, t_2 + \tau_2) \\
& \quad \frac{\left\{ \int_{-\infty}^{\infty} dt \bar{S}_1(t) \frac{\partial^2}{\partial \tau^2} \bar{S}_2(t + \tau) \right\}^2}{\tau = \tau_{12}} \\
& \quad + \bar{S}_2(t_1 + \tau_1) \bar{S}_2(t_2 + \tau_2) R_n(t_1, t_2) \Big|_{\tau_1 = \tau_2 = \tau_{12}} \\
& \quad \frac{\left\{ \int_{-\infty}^{\infty} dt \bar{S}_1(t) \frac{\partial^2}{\partial \tau^2} \bar{S}_2(t + \tau) \right\}^2}{\tau = \tau_{12}} \\
& = \frac{N_0 (\langle N_1 \rangle^2 + \langle N_2 \rangle^2) \int_{-\infty}^{\infty} dt_1 \int_{-\infty}^{\infty} dt_2 \dot{F}(t_1) \dot{F}(t_2) G(\sigma_1, t_1 - t_2) G\left(\sigma_2, \frac{t_1 + t_2}{2}\right)}{\langle N_1 \rangle^2 \langle N_2 \rangle^2 \left\{ \int_{-\infty}^{\infty} dt F(t) \ddot{F}(t) \right\}^2} \\
& = \frac{N_0 (\langle N_1 \rangle^2 + \langle N_2 \rangle^2) \int_{-\infty}^{\infty} dt \dot{F}^2(t) G(\sigma_2, t)}{\langle N_1 \rangle^2 \langle N_2 \rangle^2 \left\{ \int_{-\infty}^{\infty} dt F(t) \ddot{F}(t) \right\}^2} \\
& = \frac{N_0 (\langle N_1 \rangle^2 + \langle N_2 \rangle^2) G(\sigma_2, 0) \frac{1}{2\pi} \int_{-\infty}^{\infty} d\omega \omega^2 |\phi_s(\omega)|^2}{\langle N_1 \rangle^2 \langle N_2 \rangle^2 \left\{ \frac{1}{2\pi} \int_{-\infty}^{\infty} d\omega \omega^2 |\phi_s(\omega)|^2 \right\}^2} \\
& = \frac{N_0 \sqrt{2\pi}}{\sigma_2} \left(\frac{1}{\langle N_1 \rangle^2} + \frac{1}{\langle N_2 \rangle^2} \right) \frac{1}{\int_{-\infty}^{\infty} d\omega \omega^2 |\phi_s(\omega)|^2} . \tag{D.1}
\end{aligned}$$

where we have made use of the fact that σ_1 is very small and σ_2 is large compared to the width of the received waveform.

APPENDIX E

EXPECTED DIFFERENTIAL DELAY FOR THE AIRCRAFT EXPERIMENT

For the aircraft experiment, we can write the atmospheric correction as

$$AC \cong 2 \int_{r_{\text{ocean}}}^{r_{\text{aircraft}}} \frac{10^{-6} N_g}{\sin E} dr, \quad (\text{E.1})$$

where we have neglected the term due to the difference between the geometric lengths of the ray and straight-line path.

From Ref. [30], the group refractivity is given by

$$N_g \cong 80.343 f(\lambda) \frac{P}{T}. \quad (\text{E.2})$$

If a zero temperature lapse rate is assumed [31] the pressure P will vary exponentially with altitude:

$$P = P_S \exp \left[-\frac{h}{h_s} \right], \quad (\text{E.3})$$

where

$$h_s = \frac{RT_s}{MG} \quad (\text{E.4})$$

h_s is the atmospheric scale height and

P_S = surface pressure,

h = altitude of the aircraft,

M = molecular weight of air,

R = universal gas constant,

T_s = surface temperature ($^{\circ}\text{K}$),

G = acceleration of gravity.

By substituting Eqs (E.2) and (E.3) into Eq. (E.4), we have

$$AC \cong \frac{2 \times 10^{-6}}{\sin E} N_s h_s \left(1 - \exp \left[-\frac{h}{h_s} \right] \right) , \quad (E.5)$$

where

$$N_s = 80.343 f(\lambda) \frac{P}{T_s} . \quad (E.6)$$

For $E = 90^\circ$, $P = 1010$ mb and $T = 300^\circ K$, the scale height equals 8787 m and the difference of the atmospheric correction at two wavelengths is

$$\Delta AC \cong 4.76(m)(1 - \exp[-h/h_s])(f(\lambda_1) - f(\lambda_2)) . \quad (E.7)$$

For the aircraft experiment, $\lambda_1 = 0.532 \mu m$ and $\lambda_2 = 0.355 \mu m$ which results in

$$\begin{aligned} \Delta AC &= 0.3978(m) (1 - \exp[-h/h_s]) \\ &= 1326(ps) (1 - \exp[-h/h_s]) . \end{aligned} \quad (E.8)$$

The results are used in Chapter 8.

APPENDIX F

EFFECTS OF TELESCOPE CENTRAL OBSTRUCTIONS ON RECEIVED SIGNAL LEVEL

To study the effects of the central obstruction of the telescope on the received signal level, we assume a target with uniform reflectivity and negligible range spread. The analyses here closely follow that of Refs. [28] and [29].

Let r_p and r_b be the radius of the primary mirror and central obstruction (secondary mirror), respectively. Referring to Fig. F.1, the detector is situated on the optical axis, at a distance D behind the primary lens, while the obstruction or secondary mirror of the telescope is located at a distance S_b in front of the lens. The primary lens forms an image of the target on to the image plane. For a target at distance z , if the lens has a focal length f , the image is located at distance $I(z)$ behind the lens, where $I(z)$ is related to f and z by the thin lens formula:

$$1/I(z) + 1/z = 1/f \quad . \quad (F.1)$$

The light back scattered from a point r_o of the target is focused onto the image plane and causes an irradiance $dS(r_i, z)$ at point r_i , where $r_i = r_o \frac{I(z)}{z}$. A pencil of light back scattered to a surface element dA around r_i will illuminate an annulus in the detector plane around r_d with an irradiance of

$$dS(r_d, z) = \frac{dS(r_i, z) dA}{\pi r_c^2 \left(1 - \frac{r_b^2}{r_p^2} \right)} \quad , \quad (F.2)$$

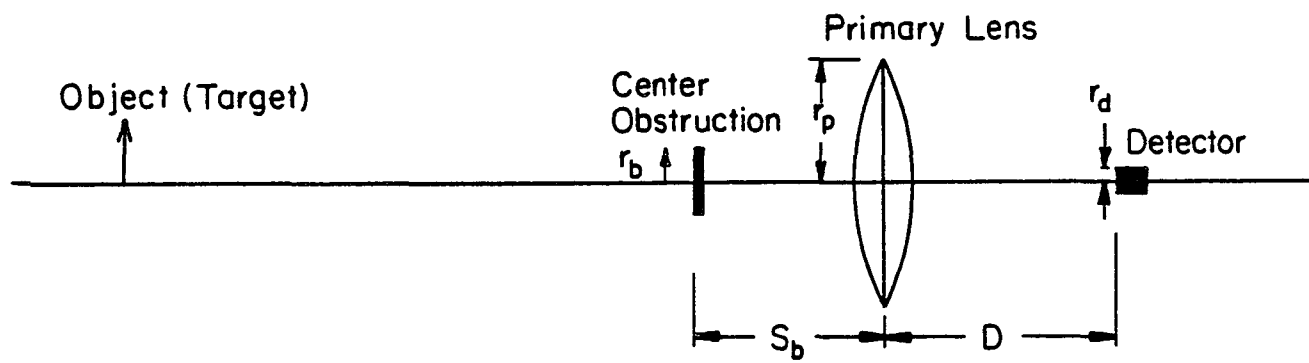


Figure F.1. Geometry of the optical setup.

where $S(r_d, z)$ and $S(r_i, z)$ are the irradiances in the detector and image plane, respectively. r_d is related to r_i by $r_d = \frac{D}{I(z)} r_i$. r_c is the outer radius of the annulus, which is related to r_p by

$$r_c = r_p \frac{I(z) - D}{I(z)} . \quad (F.3)$$

Equation (F.3) can be obtained from observing the geometry shown in Fig. F.2. Equation (F.3) is still valid when $D > I(z)$ if we replace $(I(z) - D)$ by its absolute value.

The total irradiance at r_d is provided by all the pencils of rays for which the principal rays intersect the detector plane within a circle around r_d with radius r_c excluding those rays within a circle with radius $r_c \frac{r_b}{r_p}$. The corresponding marginal points in the image plane form an annulus with an outer radius r_m given by

$$r_m = r_c \frac{I(z)}{D} , \quad (F.4)$$

and an inner radius equal to $r_m \frac{r_b}{r_p}$. This can be seen from the geometry shown in Fig. F.3.

Assuming a Gaussian footprint with a radius at $\exp(-1/2)$ point equal to $z \tan \theta_T$, the irradiance at the image plane is given by

$$S(r_i, z) = \frac{\pi(r_p^2 - r_b^2)}{z^2} \frac{1}{2\pi\sigma_I^2} e^{-\frac{r_i^2}{2\sigma_I^2}} , \quad (F.5)$$

where

$$\sigma_I = z \tan \theta_T \frac{I(z)}{D} = I(z) \tan \theta_T . \quad (F.6)$$

Since we are only interested in the relative signal level, in Eq. (F.5)

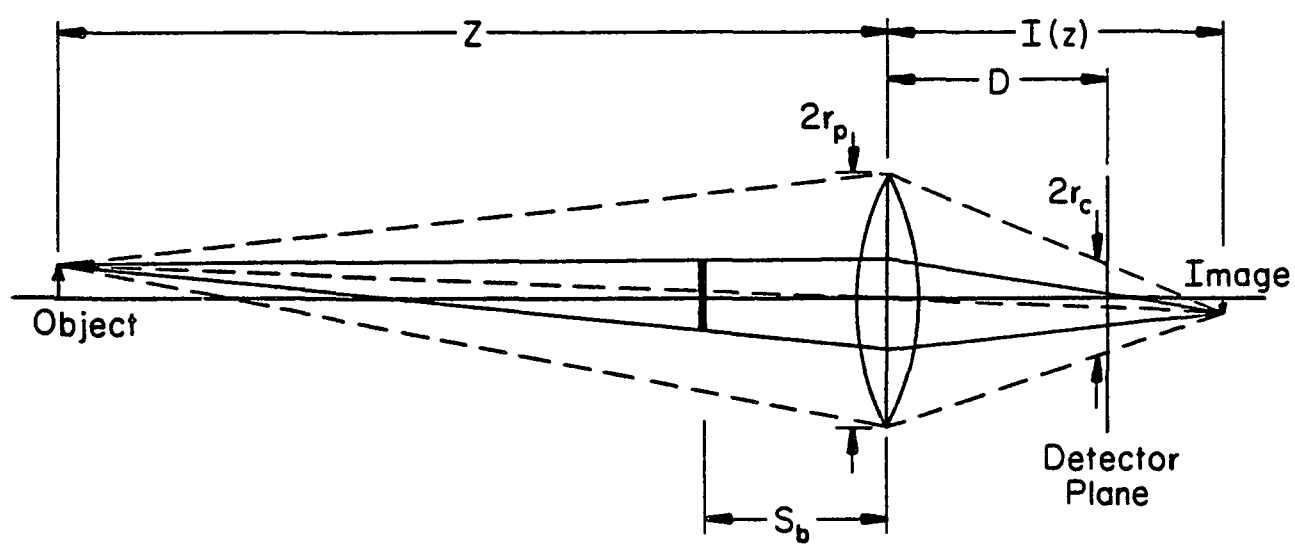


Figure F.2. Ray tracing of the telescope.

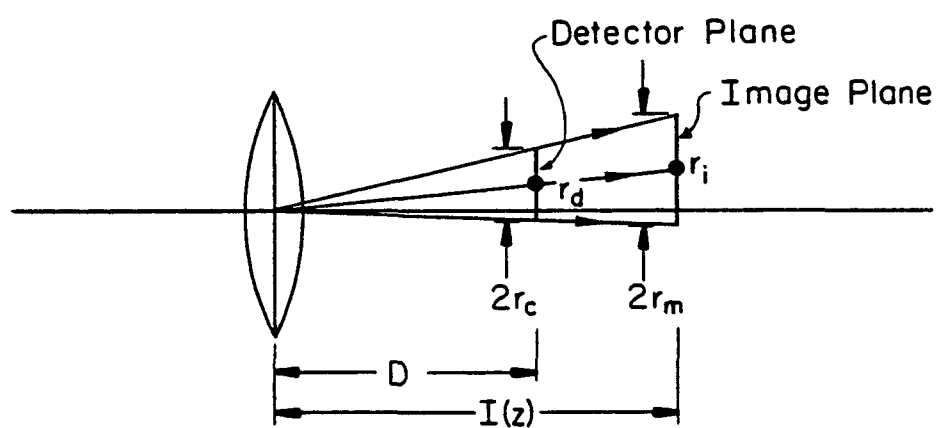


Figure F.3. Geometry of the detector plane and image plane.

we have omitted a proportional constant for simplicity. The constant takes into account transmitted laser power, reflectivity of the target and atmospheric transmittance.

By making use of Eqs. (F.5) and (F.2), we can express the irradiance at the detector plane as

$$S(r_d, z) = \frac{1}{\pi r_c^2 \left(1 - \frac{r_b^2}{r_p^2}\right)} \int_{A(r_m, \frac{I}{D} r_d) / A(r_m \frac{r_b}{r_p}, \frac{I}{D} r_d)} d^2 r \frac{\pi(r_p^2 - r_b^2)}{z^2} \frac{1}{2\pi\sigma_I^2} e^{-\frac{r^2}{2\sigma_I^2}}, \quad (F.7)$$

where $A(r_m, \frac{I}{D} r_d) / A(r_m \frac{r_b}{r_p}, \frac{I}{D} r_d)$ denotes the integration region, an annulus with outer radius r_m , and inner radius $r_m \frac{r_b}{r_p}$ centered around $\frac{I}{D} r_d$.

By making changes of variables, we can write

$$S(r_d, z) = \frac{r_p^2}{r_c^2 z^2} \frac{1}{2\pi\sigma_I^2} \int_{A(r_m, 0) / A(r_m \frac{r_b}{r_p}, 0)} d^2 r \exp\left[-\frac{|\underline{r} - \frac{I}{D} \underline{r}_d|^2}{2\sigma_I^2}\right] \\ = \frac{r_p^2}{r_c^2 z^2 \sigma_I^2} e^{-\frac{I^2 r_d^2}{2\sigma_I^2 D^2}} \int_{r_m \frac{r_b}{r_p}}^{r_m} \frac{r_b}{r_p} dr r e^{-\frac{r^2}{2\sigma_I^2}} I_0\left(\frac{I r r_d}{D \sigma_I^2}\right), \quad (F.8)$$

where I_0 is the modified Bessel function of the first kind, zeroth order.

The total power received by the detector $E(z)$ can be obtained by integrating $S(r_d, z)$ over the detector area,

$$\begin{aligned}
E(z) &= 2\pi \int_0^{R_d} dr_d r_d S(r_d, z) \\
&= \frac{2\pi p^2}{r_c^2 z^2 \alpha_I^2} \int_0^{R_d} dr_d r_d e^{-\frac{I^2 r_d^2}{2\sigma_I^2 D^2}} \int_{r_m \frac{r_b}{r_p}}^{r_m} dr r e^{-\frac{r^2}{2\sigma_I^2}} I_0\left(\frac{I r r_d}{D \alpha_I^2}\right). \quad (F.9)
\end{aligned}$$

Again by making changes of variables, we can write $E(z)$ as

$$\begin{aligned}
E(z) &= \frac{2\pi}{\left(1 - \frac{z}{f} + \frac{z}{b}\right)^2 z^4 \tan^2 \theta_T} \int_0^{R_d \frac{z}{D}} dr r e^{-\frac{r^2}{2z^2 \tan^2 \theta_T}} \\
&\quad \cdot \int_{r_b \left|1 - \frac{z}{f} + \frac{z}{D}\right|}^{r_p \left|1 - \frac{z}{f} + \frac{z}{D}\right|} d\rho \rho e^{-\frac{\rho^2}{2z^2 \tan^2 \theta_T}} I_0\left(\frac{\rho r}{z^2 \tan^2 \theta_T}\right). \quad (F.10)
\end{aligned}$$

If the radius of the detector R_d is very large, i.e., $R_d \gg z \tan \theta_T$, Eq. (F.10) can be simplified to

$$\begin{aligned}
E(z) &= \frac{2\pi}{\left(1 - \frac{z}{f} + \frac{z}{b}\right)^2 z^2} \int_{r_b \left|1 - \frac{z}{f} + \frac{z}{D}\right|}^{r_p \left|1 - \frac{z}{f} + \frac{z}{D}\right|} d\rho \rho \\
&= \frac{\pi(r_p^2 - r_b^2)}{z^2} \quad (F.11)
\end{aligned}$$

which is inversely proportional to the distance squared. This functional dependence is expected when all the energy collected by the telescope is intercepted by the detector. On the other hand, if the detector is very small so that $R_d \ll z \tan \theta_T$, I_0 in Eq. (F.10) can be approximated by 1 and $E(z)$ simplifies to

$$E(z) = \frac{2\pi \tan^2 \theta_T}{\left(1 - \frac{z}{f} + \frac{z}{D}\right)^2} \left[1 - e^{-\frac{R_d^2}{2 \tan^2 \theta_T D^2}} \right] \left[e^{-\frac{r_b^2 \left(1 - \frac{z}{f} + \frac{z}{D}\right)^2}{2z^2 \tan^2 \theta_T}} - e^{-\frac{r_p^2 \left(1 - \frac{z}{f} + \frac{z}{D}\right)^2}{2z^2 \tan^2 \theta_T}} \right] . \quad (F.12)$$

When the detector is situated at the image plane, i.e., when the target is focused onto the detector, the power received by the detector is

$$E(z) = 2\pi \int_0^{R_d} dr_i r_i S(r_i, z) \\ = \frac{\pi(r_p^2 - r_b^2)}{z^2} \left[1 - e^{-\frac{R_d^2}{2\theta_T^2 I^2(z)}} \right] , \quad (F.13)$$

which is generally larger than the power obtained when the detector is at any other position.

REFERENCES

- [1] C. L. Korb, and C. Y. Weng, Appl. Opt. 22, 3759 (1983).
- [2] C. S. Gardner, Appl. Opt. 18, 3184 (1979).
- [3] J. B. Abshire, Appl. Opt. 19, 3436 (1980).
- [4] B. M. Tsai and C. S. Gardner, Appl. Opt. 21, 3932 (1982).
- [5] C. Prabhakara, H. D. Chang and A. T. C. Chang, J. Appl. Meteorol. 21, 59 (1982).
- [6] C. S. Gardner, Appl. Opt. 21, 448 (1982).
- [7] C. S. Gardner, B. M. Tsai, and K. E. Im, Appl. Opt. 22, 2571 (1983).
- [8] C. Cox and W. Munk, J. Opt. Soc. Am. 44, 838 (1954).
- [9] B. Kinsman, Wind Waves (Prentice Hall, Englewood Cliffs, 1965), p. 242.
- [10] J. W. Goodman, "Statistical Properties of Laser Speckle Pattern," in Laser Speckle and Related Phenomena, J. C. Dainty, Ed. (Springer, New York, 1975), pp. 9-65.
- [11] J. W. Goodman, In Remote Techniques for Capillary Wave Measurement, ed. by K. S. Krishnan and N. A. Peppers (Stanford Research Inst. Rep., Stanford, Calif. 1973).
- [12] J. W. Goodman, Proc. IEEE 53, 1688 (1965).
- [13] R. M. Gagliardi and S. Karp, Optical Communication (John Wiley & Sons, New York, 1976).
- [14] R. Barakat, Opt. Acta 20, 729 (1973).
- [15] A. A. Scribot, Opt. Commun. 11, 238 (1974).
- [16] I. Bar-David, IEEE Trans. Inf. Thy., IT-15, 31 (1969).
- [17] J. B. Abshire, Nasa Tech. Paper 1315, Sept. 1978.
- [18] C. S. Gardner, B. M. Tsai, K. E. Im, J. B. Abshire, and J. F. McGarry, 1983 OSA Annual Mtg.
- [19] B. W. Lindgren, Statistical Theory (Macmillan Company, New York, 1965), p. 141.
- [20] M. W. Fitzmaurice, P. O. Minott, J. B. Abshire, and H. E. Rowe, "Prelaunch Testing of the Laser Geodynamic Satellite (LAGEOS)," NASA Technical Paper 1062, Oct. 1977.

- [21] R. Barakat, Opt. Acta 21, 903 (1974).
- [22] R. C. Smith and K. S. Baker, Appl. Opt. 20, 177 (1981).
- [23] J. Bufton, F. E. Hoge and R. N. Swift, Appl. Opt. 22, 2603 (1983).
- [24] J. B. Abshire, "Pulsed Multiwavelength Laser Ranging System," NASA Tech. Memo. 839/7, March 1982.
- [25] J. B. Abshire and J. E. Kalshoven, Jr., Appl. Opt. 22, 2578 (1983).
- [26] K. E. Im, B. M. Tsai and C. S. Gardner, "Analysis of Short Pulse Laser Altimetry Data Obtained over Horizontal Path," RRL Publication 526, Radio Research Laboratory, Department of Electrical Engineering, U. Illinois, Urbana-Champaign.
- [27] J. B. Abshire, J. F. McGarry, B. Tsai and C. S. Gardner, 1983 CLEO Mtg.
- [28] J. Harms, W. Lahmann, and C. Weitkamp, Appl. Opt. 17, 1131 (1978).
- [29] J. Harms, Appl. Opt. 18, 1559 (1979).
- [30] J. Marini and C. Murray, "Correction of Laser Tracking Data for Atmospheric Refraction at Elevations Above 10 Degrees," NASA Technical Report X-591-73-351 (1973).
- [31] J. M. Wallace, P. V. Hobbs, "Atmospheric Science: An Introductory Survey," (Academic Press, New York, 1977).

CUMULATIVE LIST OF RADIO RESEARCH LABORATORY REPORTS

PREPARED UNDER NASA GRANT NSG-5049

- RRL Rep. No. 469 - Gardner, C. S. (December 1975), The Effects of Random Path Fluctuations on the Accuracy of Laser Ranging Systems.
- RRL Rep. No. 471 - Zanter, D. L., C. S. Gardner and N. N. Rao (January 1976), The Effects of Atmospheric Refraction on the Accuracy of Laser Ranging Systems.
- RRL Rep. No. 477 - Gardner, C. S. and J. R. Rowlett (November 1976), Atmospheric Refraction Errors in Laser Ranging Data.
- RRL Rep. No. 478 - Gardner, C. S. and B. E. Hendrickson (December 1976), Correction of Laser Ranging Data for the Effects of Horizontal Refractivity Gradients.
- RRL Rep. No. 481 - Gardner, C. S. (January 1977), Statistics of the Residual Refraction Errors in Laser Ranging Data.
- RRL Rep. No. 486 - Gardner, C. S. (June 1977), Comparison Between the Refraction Error Covariance Model and Ray Tracing.
- RRL Rep. No. 488 - Gardner, C. S. (December 1977), Speckle Noise in Satellite Based Lidar Systems.
- RRL Rep. No. 495 - Gardner, C. S. and G. S. Mercherle (April 1978), Speckle Noise in Direct-Detection Lidar Systems.
- RRL Rep. No. 496 - Gardner, C. S. and A. M. Saleh (October 1978), Speckle Noise in Differential Absorption Lidar Systems.
- RRL Rep. No. 499 - Gardner, C. S. (January 1979), A Technique for Remotely Measuring Surface Pressure from a Satellite Using a Multicolor Laser Ranging System.

- RRL Rep. No. 502 - Palluch, E., J. Shelton and C. S. Gardner (May 1979),
Operating Manual for the RRL 8 Channel Data Logger.
- RRL Rep. No. 505 - Gardner, C. S. and R. Axford, Jr. (March 1980),
Regression Models for Multicolor Satellite Laser Ranging.
- RRL Rep. No. 510 - Gardner, C. S. (April 1981), Analysis of Target
Signatures for Laser Altimeters.
- RRL Rep. No. 514 - Tsai, B. and C. S. Gardner (December 1981), Remote
Sensing of Sea State by Laser Altimeters.
- RRL Rep. No. 518 - Gardner, C. S. (August 1982), Optical Communications.
- RRL Rep. No. 519 - Im, K. E. and C. S. Gardner (September 1982),
Atmospheric Refraction Effects on Baseline Error in Satellite
Laser Ranging Systems.
- RRL Rep. No. 526 - Im, K. E., B. M. Tsai, and C. S. Gardner (September 1983),
Analysis of Short Pulse Laser Altimetry Data Obtained Over Horizontal
Path.
- RRL Rep. No. 527 - Tsai, B. M. and C. S. Gardner (March 1984),
Theoretical and Experimental Analysis of Laser Altimeters for
Barometric Measurements Over the Ocean.

PAPERS PUBLISHED

- C. S. Gardner, "Effects of Random Path Fluctuations on the Accuracy of Laser Ranging Data," Applied Optics, 15, 2539-2545, October 1976.
- C. S. Gardner, "Effects of Horizontal Refractivity Gradients on the Accuracy of Laser Ranging to Satellites," Radio Science, 11, 1037-1044, December 1976.
- C. S. Gardner, "Correction of Laser Tracking Data for the Effects of Horizontal Refractivity Gradients," Applied Optics, 16, 2427-2432, September 1977.
- C. S. Gardner, J. R. Rowlett, and B. E. Hendrickson, "Ray Tracing Evaluation of a Technique for Correcting the Refraction Errors in Satellite Tracking Data," Applied Optics, 17, 3143-3145, October 1978.
- C. S. Gardner, "Technique for Remotely Measuring Surface Pressure from a Satellite Using a Multicolor Laser Ranging System," Applied Optics, 18, 3184-3189, September 15, 1979.
- C. S. Gardner, "Target Signatures for Laser Altimeters: An Analysis," Applied Optics, 21, 448-453, February 1, 1982.
- B. M. Tsai and C. S. Gardner, "Remote Sensing of Sea State Using Laser Altimeters," Applied Optics, 21, 3932-3940, November 1, 1982.
- C. S. Gardner, B. M. Tsai and J. B. Abshire, "Remote Sensing of Atmospheric Pressure and Sea State from Satellites Using Short-Pulse Multicolor Laser Altimeters," Proceedings of NATO-AGARD Symposium on Propagation Factors Affecting Remote Sensing by Radio Waves, Oberammergau, FRG, May 24-28, 1983.
- C. S. Gardner, B. M. Tsai and K. E. Im, "Multicolor Laser Altimeters for Barometric Measurements over the Ocean: Theoretical," Applied Optics, 22, September, 1983.